

Viscoelastic Flow in a Collapsible Channel

A THESIS

SUBMITTED TO THE DEPARTMENT OF CHEMICAL ENGINEERING
AND THE COMMITTEE ON GRADUATE STUDIES

by
Debadi Chakraborty

Department of Chemical Engineering
Monash University
Clayton, Australia

May 31, 2011

This thesis, contains no material which has been accepted for the award of any other degree or diploma in any university or other institution. I affirm that, to the best of my knowledge, the thesis contains no material previously published or written by another person, except where due reference is made in the text of the thesis.

Debadi Chakraborty

To my family

Acknowledgements

The work presented in this thesis was carried out under the direct supervision of Dr. J. Ravi Prakash, Prof. James Friend and Dr. Leslie Yeo. I express my sincere gratitude to them for their guidance and constant encouragement during the last four years. Their enthusiasm and integral view on research with logical thinking, and aim for providing only high quality work and not less have made a deep impression on me. I thank them further for their guidance in writing this thesis.

My research in this area of free surface viscoelastic flows would have been very difficult without the most valuable inputs and the computational code from Dr. Matteo Pasquali at Rice University. I shall forever owe Matteo a debt of gratitude for sharing his deep knowledge and insight in the area of computational rheology.

My PhD would not have been possible without the scholarships from MRGS and the Department of Chemical Engineering at Monash University.

This work was supported by an award under the Merit Allocation Scheme on the NCI National Facility at the Australian National University (ANU). I would also like to thank the VPAC (Australia), and SUNGRID (Monash University, Australia) for the allocation of computing time on their supercomputing facilities.

I am grateful to all the former and current members of molecular rheology group, specially Dr. Prabhakar, Dr. Mohit Bajaj and Dr. Tri Pham, for introducing me to the world of molecular rheology and for many stimulating technical discussions. Many thanks to my other colleagues from MNRL group, Brett, Cheol-ho, David, Daniel, Devendra, Jeremy, Ming, Richie, Ricky, Rohan, Sasi, and Yuejun, for their kind help and valuable opinions during these years.

A special thanks to the staff in the Department of Chemical Engineering, in particular Lilyanne Price, Jill Crisfield, Garry Thunder, Wren Shoppe, Kim Phu and Kate Malcom for their help and advice on administrative matters, and Roy Harrip and Gamini for their help in various technical issues.

I would also like to thank my best friends Aashish, Chiranjib and Mandar for

their constant support and encouragement throughout my PhD. It is my pleasure to thank Mohidus, Sumaiya, Swaradata, Lokesh, Mahesh, Abhishek, Sarvesh, Rajeev and Noman.

Finally, I would like to thank the most important people of my life, my wife Parama, both of our parents, brothers Raj, Sarbartha and Rintu for always being there when I needed them the most, and for supporting me throughout.

Abstract

A numerical method based on a fluid-structure interaction formulation is used to understand the role of viscoelasticity on flow in a two-dimensional collapsible channel. Three different viscoelastic fluid models have been considered - the Oldroyd-B, the FENE-P and Owens model for blood [R. G. Owens, A new microstructure-based constitutive model for human blood, *J. Non-Newtonian Fluid Mech.* 140 (2006), 57-70]. Initially the collapsible wall is considered as a zero thickness membrane model. Subsequently the collapsible wall is modelled as an incompressible neo-Hookean solid. Experiments in micro collapsible channels have also been performed.

At present, there are no models in the literature that simultaneously account for the elastic nature of the collapsible wall and the non-Newtonian rheology of the flowing fluid. In this study, for the first time, a viscoelastic fluid-structure interaction model has been developed that accounts for a viscoelastic fluid and a finite thickness elastic wall, and the resulting governing equations are solved with a sophisticated finite element method. The rheological behaviour of the viscoelastic fluids is described in terms of a conformation tensor model. The mesh equation and transport equations are discretized by using the DEVSS-TG/SUPG mixed finite element method. The computational method developed in this work is validated by comparing with the available analytical and numerical results.

While considering viscoelastic flow in a two-dimensional collapsible channel with a zero-thickness membrane, a distinct difference has been observed in the collapse wall profile for the Oldroyd-B, FENE-P and Owens model as compared to a Newtonian fluid at low values of membrane tension. The shape change of the collapsible wall depends on the Weissenberg number (Wi) for the Oldroyd-B and FENE-P fluids. The shape change in Owens model is essentially due to its shear thinning property. There is a limiting Weissenberg number beyond which computations fail, which increases with mesh refinement and decreases with decrease in membrane tension.

One of the major outcomes of the zero-thickness membrane model study is that the

significant differences that arise amongst the different viscoelastic fluids in the predicted value of the tangential shear stress on the membrane surface, has no influence on the shape of the deformable membrane, because of the boundary condition adopted in the model. Essentially it is assumed that the shape of the membrane is governed only by the normal stresses acting on it. In order to use a more realistic model for the collapsible wall, the zero-thickness membrane model has been replaced by a deformable finite thickness elastic solid which accounts for the effect of shear stress on membrane shape. The limiting Weissenberg number beyond which computations fail to converge is found to be sensitive to the choice of viscoelastic model and depends on a dimensionless solid elasticity parameter Γ . The shape of the fluid-solid interface and the stress and velocity fields in the channel, for the three viscoelastic fluids, are compared with predictions for a Newtonian fluid, and the observed differences are related to individual fluid rheological behaviour. Predictions with a finite thickness elastic solid model for the deformable wall differ considerably from those in which it is modelled as a zero-thickness membrane.

Experiments have been carried out in a micro-collapsible channel made of polydimethylsiloxane (PDMS) that mimics the numerically simulated geometry. The experiments show that the channel width perpendicular to the flow must be significant in order for wall effects to be negligible (an assumption that is made in the 2D simulation). As a consequence, the commercial software ANSYS has been used to develop a full 3D model of the channel which captures the deformation of the flexible membrane in the absence of flow. The elastic properties of PDMS have been extracted by comparing the load-displacement curves obtained from the FEM simulations with the experiments. Preliminary comparison has been made between simulations and experiments for the flow of a Newtonian fluid in the micro-collapsible channel.

Contents

Acknowledgements	i
Abstract	iii
1 Introduction	1
1.1 Blood rheology and modelling	2
1.2 Artery wall rheology and modelling	4
1.3 Fluid-structure interaction	5
1.4 Flow in collapsible channels	7
1.5 Experiments on flow in a collapsible microchannel	8
2 Finite Element Formulation for the Interaction of a Viscoelastic Fluid and a Finite-Thickness Elastic Wall	12
2.1 Governing equations	15
2.1.1 Governing equations for fluid	15
2.1.1.1 Viscoelastic fluid models	16
2.1.2 Governing equations for the solid	18
2.1.3 Mesh generation technique for moving boundaries	20
2.1.4 Finite element formulation of the problem	21
2.1.4.1 Weighted residual form of governing equations for fluid	21
2.1.4.2 Weighted residual form of the equilibrium equation for solid	23
2.1.5 Boundary conditions	24
2.1.6 Solution procedure with Newton's method	24
2.2 Conclusion	25
3 Viscoelastic flow in a two-dimensional collapsible channel	26
3.1 Introduction	26

3.2	Problem formulation	27
3.2.1	Boundary conditions	27
3.2.2	Dimensionless numbers and choice of parameter values	29
3.3	Results and Discussions	30
3.3.1	Code validation	30
3.3.2	Mesh convergence and the limiting Weissenberg number	31
3.3.3	Velocity fields and molecular shear and extension rates	38
3.3.4	Flexible membrane shape, and pressure and stress fields	43
3.4	Conclusions	56
4	The influence of shear thinning on viscoelastic fluid-structure interaction in a two-dimensional collapsible channel	58
4.1	Introduction	58
4.2	Results and discussion	59
4.2.1	Mesh convergence and the limiting Weissenberg number	60
4.2.2	Flow field and flexible membrane shape	61
4.2.3	Pressure and stresses	63
4.3	Conclusions	68
5	Viscoelastic fluid–elastic wall interaction in a two-dimensional collapsible channel	70
5.1	Introduction	70
5.2	Problem formulation	71
5.2.1	Governing Equations	71
5.2.2	Boundary conditions	73
5.3	Results and discussions	74
5.3.1	Validation of the finite-element formulation	74
5.3.1.1	Couette flow past a finite thickness solid	74
5.3.1.2	Two-dimensional collapsible channel flow: Elastic beam model	76
5.3.1.3	Two-dimensional collapsible channel flow: Zero-thickness membrane model	76
5.3.2	Fluid models and choice of parameters	79
5.3.3	Mesh convergence and the high Weissenberg number problem	82
5.3.4	Velocity fields and interface shape	88
5.3.5	Pressure and stresses	91

5.4	Conclusions	99
6	Collapsible microchannel	100
6.1	Introduction	100
6.2	Method	101
6.2.1	Design of a PDMS collapsible microchannel	101
6.2.2	Analytical solution for pressure drop	103
6.2.3	ANSYS formulation	105
6.3	Results and discussions	106
6.3.1	Deformation of the PDMS membrane without fluid flow	106
6.3.2	Deformation of the PDMS membrane with fluid flow	113
6.4	Conclusions	115
7	Overall conclusions and future work	117
7.1	Overall conclusions	117
7.2	Future work	119
A	Owens' model for human blood	120
A.1	Governing equations	120
A.2	Analytical solution of Owens' model in Couette flow	122
A.3	Derivatives	123
A.4	Implementation of Owens' model	125
A.4.1	Validation of Owens' model	125
A.5	Velocity profile	126
B	Weighted residual form of $\nabla_x \cdot \mathbf{S} = 0$	128
C	Nanoindentation test to characterize the elastic modulus of PDMS membrane	132
C.1	Experimental Method	133
C.2	Results and discussions	134
C.3	Conclusions	135
D	Stability analysis of pressure driven flow of a viscoelastic fluid through a deformable channel	136
D.1	Governing equations	136
D.2	Base state	139
D.3	Linear stability analysis	139

D.4	Results and Discussions	142
D.4.1	Code validation	142
D.5	Conclusions	143
Bibliography		144

List of Tables

2.1	Constitutive functions in the general conformation tensor model for the different types of constitutive equations used in this work.	16
3.1	Meshes considered in the current study.	32
3.2	Maximum mesh converged value of Wi , and the limiting Wi for the three fluid models, for computations carried out with the M2 and M3 meshes, at two values of α	36
5.1	Meshes considered in the current study.	83
A.1	Comparison of different components of conformation tensor.	126

List of Figures

1.1	Geometry of the 2D collapsible channel; the segment BC is an elastic membrane. Here, Q is the flow rate, p_e is the external pressure on the membrane, p_d is the pressure on the wall at the downstream boundary, W is the width of the channel, L the length of the deformable membrane, and h is the minimum height of the gap between the bottom wall of the channel and the deformable membrane.	7
2.1	Mapping between different domains	19
3.1	Geometry of the 2D collapsible channel; the segment BC is an elastic membrane.	27
3.2	The deformed shape of the flexible wall for the steady flow of a Newtonian fluid in the 2D collapsible channel, at various values of the dimensionless membrane tension ratio α . Lines denote the result of the current FEM simulation, while the symbols are the reported results of Luo and Pedley [1995].	30
3.3	Meshes M1 (a), M2 (b) and M3 (c), considered in the current study.	31
3.4	Contour plots of the largest eigenvalues (m_3) of the conformation tensor at $Wi = 0.1$ for: (a) Oldroyd-B, (b) FENE-P, and (c) Owens models, at a tension ratio $\alpha = 30$	33
3.5	Contour plots of the smallest eigenvalues (m_1) of the conformation tensor at $Wi = 0.1$ for: (a) Oldroyd-B, (b) FENE-P, and (c) Owens models, at a tension ratio $\alpha = 30$	34
3.6	Maximum value of the largest eigenvalue (m_3) and minimum value of the smallest eigenvalue (m_1) in the entire flow domain, for the Owens model, as a function of Wi at two different values of tension ratio $\alpha = 30$ (a, b), and $\alpha = 45$ (c, d).	35
3.7	Limiting Weissenberg number for the Oldroyd-B, FENE-P and Owens models at different tension ratios α	36

3.8	Profile of M_{xx} across the narrowest channel gap for the Oldroyd-B, FENE-P and Owens models, for a range of Weissenberg numbers, at $\alpha = 45$. The distance from the bottom channel is scaled by the narrowest gap width h of the particular model.	37
3.9	Contours of axial velocity (v_x) in the flow domain, for (a) Newtonian (red), Oldroyd-B (green) and FENE-P (blue) fluids, and (b) Newtonian (red) and Owens (blue) fluids, at $Wi = 0.01$ and $\alpha = 45$	38
3.10	Molecular extension rate $\dot{\epsilon}_M$ for (a) Oldroyd-B, (b) FENE-P, and (c) Owens models, at $Wi = 0.1$ and $\alpha = 30$	39
3.11	Molecular shear rate $\dot{\gamma}_M$ for (a) Oldroyd-B, (b) FENE-P, and (c) Owens models, at $Wi = 0.1$ and $\alpha = 30$	40
3.12	Locations of the maximum eigenvalue m_3 , the maximum molecular shear and extension rates $\dot{\gamma}_M$ and $\dot{\epsilon}_M$, and the maximum local Weissenberg number \widetilde{Wi} , for the Owens model, at $\alpha = 45$, for various values of the Weissenberg number Wi . Curved lines indicate the shape of the flexible membrane at the lowest and highest value of Wi	41
3.13	The deformed shape of the flexible wall for the steady flow of Oldroyd-B, FENE-P and Owens model fluids in a 2D collapsible channel, compared with the profile for a Newtonian fluid, with $Re = 1.0$ and $\beta = 0.0071$, at (a) various values of α for $Wi = 0.01$, and (b) various values of Wi for $\alpha = 45$	42
3.14	Pressure and normal components of stress on the flexible wall for the Newtonian, Oldroyd-B, FENE-P and Owens models at $\alpha = 45$ and $Wi = 0.01$, with $Re = 1.0$ and $\beta = 0.0071$. T_n is the normal component of total stress, P is the pressure, τ_n^s is the normal component of viscous stress and τ_n^p is the normal component of elastic stress.	44
3.15	Dependence of the pressure profile along the flexible membrane on Wi and α , for the Oldroyd-B ((a) and (d)), FENE-P ((b) and (e)) and Owens models ((c) and (f)), respectively. The symbols in (d)–(f) are for a Newtonian fluid. Note that $\alpha = 45$ in (a)–(c) and $Wi = 0.01$ in (d)–(f). All other parameters are as in Fig. 3.14.	46

3.16	(a) The contribution of the microstructure to the total viscosity, η_p , for the Owens model and FENE-P fluids in steady shear flow as a function of local Weissenberg number \widetilde{Wi} , at a constant value of the relaxation time λ_0 . (b) Pressure profile along the flexible membrane for Newtonian fluids with a range of viscosities. The profiles for an Owens model fluid and a FENE-P fluid, with $Wi = 0.1$ and $\alpha = 45$, are also displayed.	48
3.17	(a) Pressure drop ΔP in the channel for the Oldroyd-B, FENE-P and Owens models at different Wi , for $\alpha = 45$, $Re = 1.0$ and $\beta = 0.0071$. Note that for a Newtonian fluid, $\Delta P = 7474.0$. The curves terminate at the limiting Weissenberg number for each model. (b) Dependence of pressure drop on tension ratio for the three viscoelastic fluids, at $Wi = 0.01$, compared to the dependence of ΔP on α for a Newtonian fluid.	49
3.18	Dependence of the narrowest channel gap h on: (a) α , and (b) Wi . The narrowest gap is scaled by the channel width W in (a), and by the gap for a Newtonian fluid in (b). Note that $\alpha = 45$ in (b).	51
3.19	Dependence of the axial component of the conformation tensor M_{xx} on Wi , for (a) Oldroyd-B, (b) FENE-P, and (c) Owens models, at $\alpha = 45$, and dependence of M_{xx} on α , for (d) Oldroyd-B, (e) FENE-P, and (f) Owens models, at $Wi = 0.01$	53
3.20	Dependence of the total tangential shear stress on the membrane ($\tau_t^s + \tau_t^p$) on Wi , for (a) Oldroyd-B, (b) FENE-P, and (c) Owens models, at $\alpha = 45$, and dependence of ($\tau_t^s + \tau_t^p$) on α , for (d) Oldroyd-B, (e) FENE-P, and (f) Owens models, at $Wi = 0.01$	55
4.1	The contribution of the microstructure to the total viscosity, η_p , for the FENE-P fluid in steady shear flow as a function of local Weissenberg number \widetilde{Wi} , at a constant value of the relaxation time λ_0	59
4.2	Minimum value of the smallest eigenvalue (m_1) and maximum value of the largest eigenvalue (m_3) in the entire flow domain, for a FENE-P model, as a function of Wi at $\alpha = 45$ and $b_M = 100$	60
4.3	Minimum value of the smallest eigenvalue (m_1) and maximum value of the largest eigenvalue (m_3) in the entire flow domain, for the FENE-P model at different finite extensibility b_M	61
4.4	Comparison of contours of axial velocity (v_x) in the domain at tension ratio of 45 for Newtonian (black line) and different values of b_M for the FENE-P model, $b_M=100$ (red dashed line), $b_M=50$ (blue dots) and $b_M=2$ (thin green line) at $Re = 1.0$ and $\beta = 0.0071$	62

4.5	(a) The deformed shape of the flexible wall for the steady flow of the FENE-P model fluid in a 2D collapsible channel, compared with the profile for a Newtonian fluid, with $Re = 1.0$ and $\beta = 0.0071$, at various values of b_M for $\alpha = 45$ and $Wi = 0.1$ and (b) comparison of the narrowest channel gap between the flexible wall and bottom wall at various values of b_M for varying Wi	63
4.6	Dependence of the pressure profile along the flexible membrane on Wi for the FENE-P model at various values of b_M . Here the vertical lines with the same colour as the pressure profile indicate the position of the narrowest channel gap for the corresponding cases.	64
4.7	Dependence of the pressure drop in the channel on Wi for the FENE-P model at various values of b_M . Note that for a Newtonian fluid, $\Delta P = 7474.0$	64
4.8	Pressure profile along the flexible membrane for Newtonian fluids with a range of viscosities, and the pressure profile for a FENE-P fluid with $Wi = 0.1$ and $b_M = 2, 10$ and 100 . The values $\eta = 0.0523, 0.0205$ and 0.0156 Pa s are the calculated values of reduced viscosity, respectively, at $b_M = 100, 10$ and 2 , at the location of the maximum \widetilde{Wi} under the flexible membrane.	65
4.9	Dependence of the axial component of the conformation tensor M_{xx} on b_M for a fixed value of $Wi = 0.1$	66
4.10	Dependence of the axial component of the conformation tensor M_{xx} on Wi , for (a) $b_M=100$, (b) $b_M=10$ and (c) $b_M=2$	67
4.11	Dependence of the total tangential shear stress on the membrane $\tau_t^s + \tau_t^p$ on b_M for a fixed value of $Wi = 0.1$	68
4.12	Dependence of the total tangential shear stress on the membrane ($\tau_t^s + \tau_t^p$) on Wi , for (a) $b_M=100$, (b) $b_M=10$ and (c) $b_M=2$	69
5.1	Geometry of the domain.	71
5.2	Couette flow of a Newtonian fluid past an incompressible finite thickness neo-Hookean solid.	74
5.3	Comparison of FEM simulation with the analytical solution for different values of Γ . Lines denote the analytical solution reported by Gkanis and Kumar [2003], while symbols are results of the current FEM formulation.	75
5.4	Comparison of the shape of the flexible wall predicted by the finite thickness elastic solid model, for different values of wall thickness, with the results of Luo et al. [2007] for an elastic beam model. Circles denote the elastic beam model, while the lines are the results of the current FEM formulation.	77

5.5	(a) Extrapolation to $t = 0$ of the flexible wall shape obtained from the finite thickness elastic solid model, for $t = 0.01 W$, $t = 0.05 W$, and $t = 0.1 W$. (b) Comparison of the shape of the flexible wall predicted by the finite-thickness solid model (symbols) with the prediction of the zero-thickness membrane model (solid line). (c) Extrapolation of average tension acting in the elastic solid to the limit of zero wall thickness.	78
5.6	The contribution of the microstructure to the total viscosity, η , for the Owens model and FENE-P fluids in steady shear flow as a function of Weissenberg number \widetilde{Wi} . The inset shows the shear rate dependence of viscosity in the Owens model, fitted to the experimental results for blood reported by Chien [1970], and the predictions of the FENE-P model for $b_M = 2$ and $\lambda_0 = 0.263$. . .	80
5.7	Meshes considered in the current study. (a) M1, (b) M2 and (c) M3, for $t = 0.4W$.	83
5.8	Minimum value of the smallest eigenvalue (m_1) and maximum value of the largest eigenvalue (m_3) in the entire flow domain, for the Oldroyd-B ((a) and (d)), FENE-P ((b) and (e)), and Owens model ((c) and (f)), as a function of Wi at $\Gamma = 4.95 \times 10^{-5}$ and $P_e = 0.04$ for $t = 0.4W$	84
5.9	Profile of M_{xx} across the narrowest channel gap for the Oldroyd-B, FENE-P and Owens models, for a range of Weissenberg numbers, at $\Gamma = 1.98 \times 10^{-4}$. The distance from the bottom channel is scaled by the narrowest gap width Δy_{max} (see Fig. 5.13(a) for a definition) of the particular model.	86
5.10	Maximum mesh converged value of Wi , and the limiting Wi for the three fluid models, for computations carried out with the M2 mesh, at $P_e = 0.04$ and $t = 0.4W$ for different values of Γ	87
5.11	Contours of axial velocity (v_x) in the flow domain, for Newtonian (black), Oldroyd-B (red), FENE-P (blue) and Owens (green) fluids at $P_e = 0.04$, $t = 0.4W$ and $\Gamma = 1.98 \times 10^{-4}$ for two different values of Weissenberg number (a) $Wi = 0.1$ and (b) $Wi = 0.5$	88
5.12	The shape of the fluid-solid interface in a 2D collapsible channel for the Oldroyd-B ((a) and (d)), FENE-P ((b) and (e)) and Owens models ((c) and (f)), compared with the profile for a Newtonian fluid. Note that Wi is 0.1 in (a)–(c) and Γ is 4.95×10^{-4} in (d)–(f). In (a)–(c) different symbols represent different values of Γ (\square : 4.95×10^{-5} , \circ : 1.98×10^{-4} , \star : 3.0×10^{-4} , $+$: 3.96×10^{-4} , \times : 4.95×10^{-4} and \triangle : 6.6×10^{-4}). Lines with the same colour as the symbols represent the predictions of a Newtonian fluid for identical values of Γ	90

5.13	(a) Schematic diagram for defining the position of maximum deformation ($\Delta x_{max}, \Delta y_{max}$). (b) Dependence of ($\Delta x_{max}, \Delta y_{max}$) on Γ at a fixed value of $Wi = 0.1$, and (c) on Wi at a fixed value of $\Gamma = 4.95 \times 10^{-4}$. In (b) and (c) the arrows indicate the direction of increasing Γ and Wi , respectively. The range of Wi for the Oldroyd-B, FENE-P and Owens models are 0.01-1.508, 0.01-2.372 and 0.01-7.9, respectively.	92
5.14	Dependence of the pressure profile along the flexible membrane on Wi and Γ , for the Oldroyd-B ((a) and (d)), FENE-P ((b) and (e)) and Owens models ((c) and (f)), respectively. The lines in (a)–(c) are for a Newtonian fluid. Note that $\Gamma = 1.98 \times 10^{-4}$ in (d)–(f) and $Wi = 0.1$ in (a)–(c).	93
5.15	Dependence of pressure drop ΔP in the channel for the Oldroyd-B, FENE-P and Owens models on (a) Γ at a fixed value of $Wi=0.1$ and (b) Wi at $\Gamma = 1.98 \times 10^{-4}$. Note that for a Newtonian fluid, $\Delta P = 0.1$. The curves terminate at the limiting Weissenberg number for each model.	95
5.16	Dependence of the axial component of the conformation tensor M_{xx} on Γ , for (a) Oldroyd-B, (b) FENE-P, and (c) Owens models, at $Wi = 0.1$, and dependence of M_{xx} on Wi , for (d) Oldroyd-B, (e) FENE-P, and (f) Owens models, at $\Gamma = 4.95 \times 10^{-4}$	97
5.17	Dependence of the tangential component of stress $\tau_t^s + \tau_t^p$ on Γ , for (a) Oldroyd-B, (b) FENE-P, and (c) Owens models, at $Wi = 0.1$, and dependence of $\tau_t^s + \tau_t^p$ on Wi , for (d) Oldroyd-B, (e) FENE-P, and (f) Owens models, at $\Gamma = 4.95 \times 10^{-4}$	98
6.1	Schematics of the fabrication process used to produce the collapsible microchannel, (a) spin coating of the SU-8 2035 negative photoresist on a silicon wafer, (b) exposing the photoresist to UV radiation in a standard photolithography process, (c) development to prepare the SU-8 structured mold and (d) inverse cast of the patterned mold made of PDMS upon curing.	102
6.2	Exploded view of the collapsible microchannel fabricated for the present study, (i) design type 1 and (ii) design type 2.	102
6.3	Images of patterned SU-8 mold and PDMS devices for (i) design type 1 ((a) SU-8 mold, (b) close view of the gap between fluid channel and pressure chamber and (c) final PDMS device) and (ii) design type 2 ((a) SU-8 mold for fluid channel, (b) SU-8 mold for pressure chamber and (c) final PDMS device).	104
6.4	Microscopic image of the deformation of the flexible membrane with an application of external pressure $P_e = 85$ kPa for a collapsible microchannel (DT1) with channel width of approximately 0.3 mm.	107

6.5	Dependence of maximum deformation Δz_{\max} of the bottom surface of the flexible membrane on external pressure (P_e) for micro-collapsible channel (DT1) with three different channel widths.	108
6.6	Dependence of maximum deformation Δz_{\max} of the bottom surface of the flexible membrane on width W at three different values of external pressure $P_e = 5, 10$ and 15 kPa obtained from ANSYS simulation.	109
6.7	Microscopic image of the deformation of the flexible membrane with an application of external pressure $P_e = 20$ kPa for collapsible microchannel (DT2) with channel width of approximately 0.5 mm.	110
6.8	Dependence of maximum deformation Δz_{\max} of the bottom surface of the flexible membrane on external pressure (P_e) for micro-collapsible channel (DT2) with different channel widths, approximately $0.22, 0.5, 1.0, 2.0, 3.0$ and 4.0 mm.	111
6.9	Comparison of experimental results with the 2D simulation results.	112
6.10	Experimental setup for carrying out pressure drop measurements.	112
6.11	Dependence of pressure drop Δp on flow rate Q for two different widths.	113
6.12	FEM prediction of fluid-solid interface profile at different flow rate.	114
A.1	Flow domain and boundary conditions for the Couette flow	126
A.2	Blunting of the parabolic profile.	127
B.1	Geometry of the solid domain.	129
B.2	Comparison of formulations FEM-N and FEM-C with the ANSYS plain-strain model for three different values of G : (a) 24000 Pa, (b) 12000 Pa, and (c) 6000 Pa.	131
C.1	Load-displacement curves for PDMS membrane with thickness of 0.05 mm	134
C.2	Dependence of reduced elastic modulus E_r and Young's modulus of PDMS membrane on thickness.	135
D.1	Geometry of the pressure driven viscoelastic fluid flow interacting with elastic solid layer	137
D.2	Eigenspectrum for varicose mode with $H = 5, k = 0.8$ and $Re = 100$ for different values of Γ . Inset compares the positive C_i values of our simulation with the reported C_i values by Gaurav and Shankar [2010].	143

Chapter 1

Introduction

Simulating blood transportation through the human cardiovascular system numerically is an intense area of research [Robertson et al., 2008], since cardiovascular diseases are one of the major threats in the modern world. Blood supplies oxygen and nutrients to tissues and is transported from the ventricles of the heart to capillaries in organs and tissues of the body by the vessels known as arteries. Different body activities require constant maintenance of blood pressure in the human body. In response to the varying flow rate and external forces, an artery changes its diameter to keep the pressure constant and any deviation from this expected response can cause an increase in blood pressure or a localized reduction in blood flow. The reduction in blood flow causes unnatural growth in the arterial wall thickness by facilitating the deposition of cholesterol on the arterial wall. The thickening of the artery wall promotes cardiovascular diseases, such as stenosis or arteriosclerosis, circulatory disorders and kidney failure. This immense importance of blood flow in the human body has motivated many researchers to understand and model the mechanism in both healthy and pathological cases.

The aim of this work is to lay a foundation for the study of blood flow in small blood vessels by considering the viscoelastic nature of blood and the elastic nature of blood vessel walls. In this introduction, we first present brief overviews of blood rheology, artery wall modelling and fluid-structure interaction. Often many researchers have modelled the phenomenon of artery wall constriction and expansion by studying flow through collapsible channels and tubes. A brief literature survey of flow through collapsible channels is presented. In order to validate our fluid-structure interaction model through experiments, we have made use of a microfluidic device which we describe briefly. Finally, an outline of this work concludes the introduction.

1.1 Blood rheology and modelling

Blood is a concentrated suspension of multiple components, with a complex rheological behaviour, that interacts with the walls of blood vessels both chemically and mechanically to give rise to an intricate fluid-structure interaction. Consequently, obtaining a quantitative description of physiological blood circulation requires a thorough in-depth insight into the blood rheology, along with the flow dependence on the architectural and mechanical properties of the vascular system. Typically the flow of blood in small vessels, such as arterioles, venules, and capillaries is referred to as the *microcirculation*, while flow in larger arteries is referred to as the *macrocirculation*. From the fluid mechanics viewpoint, the distinction between the micro and macrocirculation is generally based on the Reynolds number, Re . Microcirculation corresponds to flows where Re is small, and inertial forces can be neglected; while macrocirculation corresponds to flows where inertial forces are significant. Although blood flow in micro and macrocirculation share a fundamental common feature: the interaction between blood and vessel walls, there are still significant differences that require a completely different approach to model each of them. For instance, in the medium to large arteries of the macrocirculation, since Reynolds numbers are high, tube diameters large and blood can be considered to be a Newtonian fluid, it has been well accepted that the Navier-Stokes equations can be successfully used to predict blood flow [Robertson et al., 2008]. Most studies in the literature on fluid-structure interaction issues in the context of blood flow so far have been focused on the macrocirculation. The viscoelastic property of blood was first measured by Thurston [1972]. Parameters such as plasma viscosity, red blood cell deformability, aggregation, and hematocrit cumulatively reflect the effects of blood viscoelasticity. The shear thinning behaviour of blood is well established [Baskurt and Meiselman, 2003; Popel and Johnson, 2005; Robertson et al., 2008]. At low shear rates the apparent viscosity is high. This apparent viscosity decreases with increasing shear and approaches a minimum value under high shear forces [Chien, 1975; Merrill, 1969; Rand et al., 1964]. It is clear that models for blood flow in the microcirculation cannot ignore the particulate nature of blood which leads to non-Newtonian behaviour at low shear rates. This necessitates the consideration of its shear thinning, viscoelastic and thixotropic nature [Baskurt and Meiselman, 2003; Cristini and Kassab, 2005; Popel and Johnson, 2005; Robertson et al., 2008; Sequeira and Janela, 2007]. To the best of our knowledge, so far there have been no studies of fluid-structure interaction issues associated with the flow of viscoelastic fluids in vessels with compliant walls. The present

research aims to examine the flow of a variety of model viscoelastic fluids in a simple two-dimensional collapsible channel. It is hoped that this preliminary study will lay the foundation for understanding the interaction of more realistic models of blood and blood vessels.

The shear thinning behaviour of blood has its origins in the tendency of red blood cells to aggregate into linear arrays, termed rouleaux, in which they are arranged like stacks of coins. These aggregates also interact with each other to form three-dimensional structures. Since reduced shear favours aggregation of red blood cells, the viscosity of blood increases significantly at low shear rates. However, with increasing shear rate, the size of the aggregates diminishes, leading to a reduction in the viscosity. To date, a range of models has been proposed for describing the rheological behaviour of blood [Anand et al., 2003; Moyers-Gonzalez et al., 2008a; Owens, 2006; Quemada, 1993, 1999; Sun and Kee, 2001; Williams et al., 1993; Yeleswarapu et al., 1998]. Models that account for the viscoelastic nature of blood are typically generalized Maxwell models. In these models, the relaxation time and shear viscosity depend on a structural variable that describes the aggregation/disaggregation of red blood cells. The structural variable typically obeys an evolution equation. Among the various available models, the recent models proposed by Owens and co-workers [Moyers-Gonzalez et al., 2008a; Owens, 2006] use a micro-structural framework based on transient polymer network theory to derive the evolution equation for the structural variable. Apart from the appeal of the rigorous foundation for the derivation of the evolution equation, predictions of the models developed by Owens and co-workers also compare very well with a range of experimental observations of the rheological behaviour of blood [Fang and Owens, 2006; Moyers-Gonzalez et al., 2008b; Owens, 2006]. Owens' original model [Owens, 2006] was derived in the context of homogeneous flows. In order to take into account complex blood flow phenomenon such as the Fåhræus [Fåhræus, 1929] and Fåhræus and Lindqvist [Fåhræus and Lindqvist, 1931] effects, Owens and co-workers recently have extended their model to treat non-homogeneous flows [Moyers-Gonzalez et al., 2008a]. In this study, we have adopted Owens' original homogeneous flow model [Owens, 2006] as the benchmark model to study the flow of blood in a compliant channel. As in the case of other models for viscoelastic fluids derived from kinetic theory for homogeneous flows, the homogeneous flow model can be applied to non-homogeneous flows by simply treating the time derivative of stress as a substantial derivative rather than a partial derivative. This assumption is justified by assuming that the velocity gradients

do not vary significantly on the length scale of the microstructure. Since this is a preliminary study of fluid-structure interaction issues in the context of viscoelastic fluids, we have considered the simpler of the two Owens models for blood. Further, since to the best of our knowledge no viscoelastic model has been examined in this geometry previously, we have also computed the flows of two other viscoelastic fluids, namely, the Oldroyd-B and FENE-P fluids, which are also derived on the microscopic scale for homogeneous flows, and commonly used to compute complex non-homogeneous flows. Henceforth in this paper, whenever we refer to Owens' model, we indicate the homogeneous flow model.

1.2 Artery wall rheology and modelling

In the arterial vascular network, as one moves from the aorta to the capillary beds of individual organs, the number of arteries becomes larger and the wall thickness to diameter ratio also becomes larger (approximately 0.125 in aorta and 0.4 in arterioles). The aorta is the largest artery which has its origin in the heart, while arterioles, the smallest arteries, carry blood to very thin capillaries in which the exchange of oxygen, nutrients and metabolites between blood and tissues takes place. There are four major components which determine the viscoelastic behaviour of the artery walls, smooth muscle cells, elastin, viscous ground substance and collagen [Hayashi, 2003; Kalita and Schaefer, 2008]. The inelastic and viscoelastic behaviour of the artery walls remote from the heart is due to the decrease in the ratio of elastin to collagen [Kalita and Schaefer, 2008]. In the histological structure of the artery wall, three layers can be distinguished, in order from the inner most to the outer most: an intima, a media and an adventitia [Holzapfel, 2003; Kalita and Schaefer, 2008; Quarteroni et al., 2000]. The media is the thickest layer of the artery wall which is rich in elastin and smooth muscle cells and is considered as the most significant layer responsible for the elastic properties of the artery wall [Holzapfel, 2003].

Stephen Hales first considered the elasticity of artery walls. and invented the Windkessel (air kettle) theory. Lumped models or 0D models based on the Windkessel model or modified versions of it are represented by electrical circuits, consisting of a parallel capacitor and a resistor, [Stergiopoulos et al., 1999]. Simple 0D or 1D models are easy to use for numerical computations, however their applicability in predicting physiological phenomena is restricted, since these models usually neglect the essential properties of the artery walls, such as nonlinear elasticity. On the other hand some

2D models (such as a Koiter shell) which considers some of the basic features of the artery wall are promising in their prediction of physiological phenomena. A detailed description of different artery wall models can be found in Kalita and Schaefer [2008]. A nonlinear Koiter shell model represents the artery wall as a thin structural wall, although artery walls are thick and heterogeneous over the thickness. Quarteroni et al. [2000] have used the equation of a thin rod to represent the artery wall behaviour in their fluid-structure interaction studies. Canic and Mikelic [2003] and Canic et al. [2006] proposed a linearly viscoelastic cylindrical axisymmetric Koiter shell model for artery wall modelling. This model shows excellent agreement with the experimental results. However the models for artery walls in the microcirculation where artery wall thickness to vessel diameter ratio is much larger, cannot ignore the non-zero thickness of the artery wall. In the present study we have represented the artery wall as an incompressible neo-Hookean solid with finite-thickness.

1.3 Fluid-structure interaction

Fluid flow within a flexible structure is regulated by the stresses imposed upon the structure by both the fluid and any external forces. Thus, the rheological properties of both the fluid and the structure significantly influence the fluid flow in the system. The viscous and elastic stresses and fluid pressure exerted on the boundaries of the flexible wall cause its deformation. Due to the deformation of the flexible structures, the flow domain and flow field alters and gives rise to an intricate fluid-structure interaction problem which requires the solution of a free-boundary problem. Here the location of the boundary is not known *a priori* and its evolution completely depends on the dynamical balance between the fluid flow and structural movement. It is well known that the numerical simulation of free boundary flows of Newtonian fluids is a very challenging task. Incorporation of viscoelastic fluid and structure in the free-boundary problem introduces additional variables and nonlinearities. Although there has been significant progress on addressing the challenges of the fluid-structure interaction problem, most of the research in this area has dealt with Newtonian fluids. Also, the elastic nature of the artery wall has not been addressed accurately. To our knowledge, no model has been developed to simultaneously consider the elastic nature of a thick artery wall and the non-Newtonian character of blood. The most significant and innovative aspect of this research project is the development of a fluid-structure interaction model capable of describing the flow of shear thinning, viscoelastic blood

through an elastic artery.

Several techniques have been proposed for the numerical solution of fluid-structure interaction problems. The Immersed Boundary Method developed by Peskin [1977], originally developed to study fluid motion in the heart, was successfully used to model a variety of fluid-structure interaction phenomena (e.g. platelet aggregation during blood clotting [Fogelson, 1984], aquatic animal locomotion [Fauci, 1988], suspended particles in three-dimensional Stokes flow [Fogelson and Peskin, 1988], and three-dimensional heart motion [Peskin and McQueen, 1989], peristaltic pumping of solid particles [Fauci, 1992], fluid dynamics of the inner ear [Beyer, 1992], sperm motility in the presence of boundaries [Fauci and McDonald, 1995], bacterial swimming [Dillon et al., 1995], biofilm processes [Dillon et al., 1996], myogenic response of the arteriolar wall [Arthurs et al., 1998], spinning of elastic filament in a viscous incompressible fluid [Lim and Peskin, 2004], biofilm growth [Duddu et al., 2008], blood flow in a compliant vessel [Kim et al., 2009], flow-induced deformation of three-dimensional capsules [Sui et al., 2008, 2010]). In the Immersed Boundary Method, usually the action of the boundary on the fluid arises from a body force included in the Navier-Stokes equations, and the boundary, as a consequence of the no-slip condition, is required to move at the local fluid velocity. Generally fluids are described by Eulerian formulations, whereas structures are expressed by Lagrangian formulations. While solving for the combined case some kind of mixed description known as the Arbitrary Lagrangian Eulerian (ALE) formulation is employed frequently to account for the domain deformability [Bathe et al., 1995; Bathe and Zhang, 2004; Bathe et al., 1999; Quarteroni et al., 2000]. The ALE-finite element method is based on mapping the deformed computational domain to a convenient fixed reference domain by means of a mapping that satisfies elliptic equations [Christodoulou and Scriven, 1992; deSantos, 1991] or the deformation equations of a pseudo-solid [DE Almeida, 1999; Sackinger et al., 1996a]. To compute Newtonian free surface flow problems ALE-FEM is efficient and effective [Christodoulou and Scriven, 1992; Sackinger et al., 1996a]. Carvalho and Scriven [1997] proposed a fluid-structure interaction formulation to solve roll cover deformation in roll coating flows, where the rubber roll cover was modelled as an incompressible Mooney-Rivlin solid. In order to solve the problem of blood flow in the microcirculation, we decided to use the finite thickness neo-Hookean solid model which would account for the effect of the shear stress on membrane shape [Carvalho, 2003; Carvalho and Scriven, 1997] and realistic constitutive equations for blood [Fang and Owens, 2006; Owens, 2006].

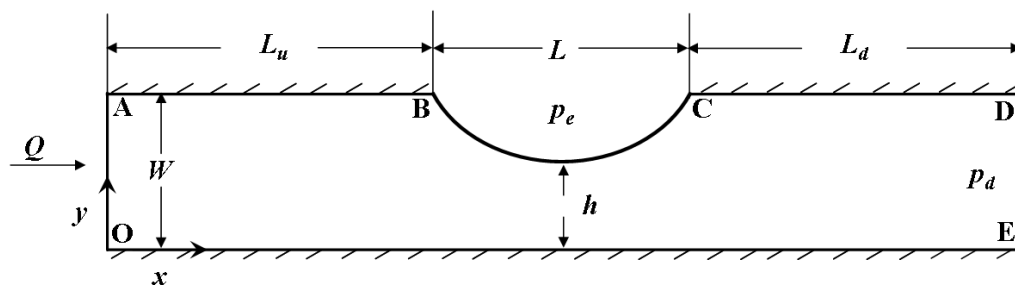


Figure 1.1: Geometry of the 2D collapsible channel; the segment BC is an elastic membrane. Here, Q is the flow rate, p_e is the external pressure on the membrane, p_d is the pressure on the wall at the downstream boundary, W is the width of the channel, L the length of the deformable membrane, and h is the minimum height of the gap between the bottom wall of the channel and the deformable membrane.

1.4 Flow in collapsible channels

Laboratory experiments performed on flow through collapsible tubes have demonstrated the complex and nonlinear nature of the dynamics of such a system, with a multiplicity of self-excited oscillations [Bertram, 1982, 1986, 1987; Bertram and Castles, 1999; Bertram and Elliott, 2003; Bertram and Godbole, 1997; Bertram et al., 1990, 1991; Brower and Scholten, 1975; Conrad, 1969]. The earliest and simplest theoretical models of collapsible-tube flow were lumped-parameter [Katz et al., 1969] and one dimensional models [Jensen, 1990; Shapiro, 1977], followed by two-dimensional models. The simplest numerical model discussed so far in the literature, that captures some of the rich behaviour observed in these experiments, is a 2D model with fluid flowing in a rigid parallel sided channel, where part of one wall is replaced by a membrane under tension (Fig. 1.1). This geometry has been studied extensively in the case of Newtonian fluids, with early models treating the flexible wall as an elastic membrane of zero thickness, with stretching along the flow direction and bending stiffness of the membrane neglected [Heil and Jensen, 2003; Lowe and Pedley, 1995; Luo and Pedley, 1995, 1996; Rast, 1994]. While initial studies appeared to suggest that in the range of Reynolds numbers and transmural pressures considered, a converged numerical solution could only be achieved for relatively large values of membrane tension [Luo and Pedley, 1995; Rast, 1994], Luo and Pedley [1996] subsequently found that with the

help of an algorithm capable of time dependent simulations, converged steady state solutions could be obtained at arbitrary values of membrane tension, for sufficiently small values of the Reynolds number. Interestingly, Luo and Pedley [1996] showed that self-excited oscillations developed when the membrane tension was reduced below a critical value for sufficiently large Reynolds numbers. The membrane model assumes that the bending stiffness and extensibility of the wall in the flow direction can be ignored, and that the movement of the elastic wall is only in the direction normal to the wall. More recently, this basic model has been improved by using a plane strained elastic beam model for the collapsible wall with a Bernoulli-Euler beam, a Timoshenko beam and a 2D-solid model [Cai and Luo, 2003; Liu et al., 2009a; Luo et al., 2007]. It was found that wall stiffness plays a major role in attaining a steady solution, and for very small wall stiffness, the results of the beam model compare favourably with those of the membrane model. Research is also in progress on extending these models to describe 3D compliant tubes [Hazel and Heil, 2003; Jensen and Heil, 2003; Liu et al., 2009a; Marzo et al., 2005; Xie, 2006; Xie and Pasquali, 2003]. Many of the complex dynamical features observed experimentally have been reproduced in these simulations. Attempts to understand the origin of self-excited oscillations have also been performed [Heil and Waters, 2008; Jensen and Heil, 2003]. However, as mentioned earlier, in all these studies the fluid has always been treated as Newtonian. In this work, we focus our attention on the simple 2D model introduced by Pedley and co-workers as the starting point to investigate the behaviour of fluid-structure interaction issues that arise with viscoelastic liquids. Using a step-wise approach, initially the elastic wall has been represented by a zero-thickness membrane model. Subsequently, simulations have been carried out for flow in a two-dimensional collapsible channel by considering the deformable wall to be a finite-thickness incompressible neo-Hookean solid and the channel dimensions to be compatible with those of the microcirculation. Such a study will hopefully form the basis for more sophisticated explorations of fluid-structure interactions in the microcirculation.

1.5 Experiments on flow in a collapsible microchannel

Fascinated by microscale fluid dynamics, many researchers have performed experiments on microfluidic systems to characterize fluid flow in them. Hence over the past

fifteen years, large efforts have been made in developing techniques to fabricate microfluidic systems in silicon, glass, quartz and polymers. However polydimethylsiloxane (PDMS) microfluidic devices, fabricated using a soft lithographic technique, are gaining popularity because of the excellent optical transparency, gas permeability, biocompatibility and elasticity of PDMS [Duffy et al., 1998; Leclerc et al., 2003]. The research work on PDMS microfluidic systems can be broadly divided into two different categories, one where only microchannels are considered for different chemical and pharmaceutical applications [Leclerc et al., 2003; Whitesides, 2006] and the other where microchannels with flexible PDMS membranes (membrane-based micropumps) are employed for controlling fluid flow [Unger et al., 2000; Vestad et al., 2004; Wang and Lee, 2006]. The characterization of fluid flow in microchannels and comparison with conventional theories are well established as evidenced by the work of different researchers [Hrnjak and Tu, 2007; Kandlikar et al., 2005; Kumar et al., 2011; Meinhart et al., 1999; Peiyi and Little, 1983; Pfund et al., 2000; Vijayalakshmi et al., 2009]. Furthermore, studies on membrane-based micropumps have started recently [Hohne et al., 2009; Huang et al., 2009; Irimia et al., 2006; Unger et al., 2000] because of the complicated fabrication process.

In recent years, pneumatically actuated micron size pumps are gaining importance because of their wide use in fluid manipulation in lab-on-a-chip applications (e.g., measuring neutrophil migration [Irimia et al., 2006], precise handling of cell suspensions [Irimia and Toner, 2006], micro filter modulated by pneumatic pressure for cell separation [Huang et al., 2009] and liquid transport and mixing [Weng et al., 2011]). Since moving boundaries or surfaces do pressure work on the working fluid in the most widely reported pneumatic micropumps, they are categorized as reciprocating displacement pumps. The moving boundary performs the action of a piston. PDMS is often used as the diaphragm material for these types of pumps because of its wide range of flexibility [Friend and Yeo, 2010; Fuard et al., 2008; Hohne et al., 2009; Thangawng et al., 2007]. Unger et al. [2000] first demonstrated the power of multilayer soft lithography by fabricating a membrane-based micropump made of elastic polymer. Initially patterned photoresist molds are created for the fluid channel and pressure chamber using soft lithography and individual elastomer layers are cast using these molds. Finally, multilayer pumps consisting of a fluid channel, pressure chamber and flexible membrane are constructed by bonding these different layers using plasma bonding. This micropump drives the working fluid through the channel by the continuous pulsation of the flexible membrane actuated by the pressure chamber. Because of the

relatively lower cost and simpler fabrication approach, multilayer soft lithography has been extensively used to fabricate micropumps for different applications [Hohne et al., 2009; Studer et al., 2004]. The behaviour of this type of micropump is governed by several controlling parameters, such as the viscosity of the flowing fluid, the elasticity of the membrane and dimension of the channel. However in order to investigate fluid-structure interaction in this type of micropump, it is necessary to first introduce the conventional theory for predicting the experimentally observed fluid flow behaviour.

The length scale at which fluid flow occurs in microfluidic devices is entirely different from the large-scale flows that are familiar to most industrial engineers. Fluid flowing in a conventional microfluidic channel with characteristic length scale in the sub-millimeter range, is identified by low velocity and hence small Reynolds numbers. Thus in order to understand fluid flow phenomenon at the microscale, successful development of fabricated microfluidic devices is necessary. It is widely acknowledged that the experimental observations conducted in *macroscale* channels can be well predicted by the Navier-Stokes equation. Experimental research efforts in the area of microscale fluid flow have considered various flow rates, different fluids, different cross-sectional geometries (circular, rectangular, triangular, trapezoidal, hexagonal, etc.) to obtain friction factor versus pressure drop measurements and compare them with the prediction of conventional theory. However, discrepancies have been reported in the literature while comparing the experimental data of pressure drop occurring in microchannel flow devices with the predictions of conventional theories [Hrnjak and Tu, 2007; Judy et al., 2002; Kandlikar et al., 2005; Kohl et al., 2005; Meinhart et al., 1999; Peiyi and Little, 1983; Peng et al., 1995; Pfahler et al., 1989; Pfund et al., 2000; Vijayalakshmi et al., 2009]. The discrepancy is related to the different degrees of surface roughness, inaccurate measurements of channel dimensions and unexplained corrections for inlet and exit losses [Celata et al., 2009; Kumar et al., 2011; Steinke and Kandlikar, 2006]. Thus, in order to describe fluid flow in microchannels with the help of conventional theories, much effort is still required in fabricating microfluidic devices effectively. As mentioned earlier most people these days accept the validity of continuum mechanics for describing microscale flow, however it is the approximations used to simplify and hence solve the Navier-Stokes equations that are questionable. To the best of our knowledge, most of the experiments on flow through a collapsible tube [Bertram, 1982, 1986, 1987; Bertram and Castles, 1999; Bertram and Elliott, 2003; Bertram and Godbole, 1997; Bertram et al., 1990, 1991; Brower and Scholten, 1975; Conrad, 1969] were carried out in large diameter tubes (13-15 mm) for high Reynolds number (>100). In the microcirculation, arterioles

have a diameter in the range of 100 to 300 μm . To the best of our knowledge, there is no evidence in the literature of the use of a collapsible microchannel. In this study, we investigate the fluid flow in a collapsible microchannel made of PDMS. To characterize the elastic properties of PDMS, initially the deformation of the thin PDMS membrane is measured without fluid flow in the channel. Upon establishing the PDMS properties, fluid is introduced in the channel and different parameters are studied.

The plan of the thesis is as follows. The finite element formulation of the governing equations for the viscoelastic fluids and incompressible neo-Hookean solid are presented in Chapter 2. The results for the flow of the three viscoelastic fluids in a two-dimensional channel partly bounded by a zero-thickness membrane under constant tension is presented in Chapter 3. Chapter 4 represents the influence of shear thinning on viscoelastic fluid-structure interaction in a two-dimensional collapsible channel. Chapter 5 presents steady viscoelastic flow in a two-dimensional channel in which part of one wall is replaced by a deformable finite thickness elastic solid. The experimental results on micro-collapsible channel are reported in Chapter 6. Finally, concluding remarks are drawn in Chapter 7.

Chapter 2

Finite Element Formulation for the Interaction of a Viscoelastic Fluid and a Finite-Thickness Elastic Wall

In this chapter, the computational method for solving the interaction of viscoelastic fluids with an incompressible neo-Hookean solid model is presented. The governing equations are discretized using the finite element method and the corresponding weighted residuals and Jacobian matrices are also discussed.

It is well known that in medium-to-large arteries, such as the coronary arteries (medium) and the abdominal aorta (large), the Navier-Stokes equations for an incompressible viscous fluid are a good model for blood flow [Robertson et al., 2008]. However, it is clear that in models for blood flow in the microcirculation, where the flow rates are low, one cannot ignore the rheological behaviour of blood as a shear-thinning, viscoelastic fluid [Baskurt and Meiselman, 2003; Cristini and Kassab, 2005; Popel and Johnson, 2005; Sequeira and Janela, 2007]. A Newtonian constitutive equation is not completely adequate for the description of viscoelastic fluids because of the shear rate dependence of viscosity and the presence of elasticity. Viscoelastic fluids are mainly characterized by the Weissenberg number (Wi), which is the ratio of the characteristic time scale of the fluid to that of the flow. To model complex viscoelastic fluids a constitutive equation is generally used to obtain the polymer contribution to the Cauchy stress. The choice of constitutive equation is made to balance computational efficiency, thermodynamic consistency of the models, and microstructural insight. Most of the constitutive equations are either macroscopic models (conformation tensor based models, rate-type models [Bird et al., 1987a,b]) or mesoscopic models

(stochastic differential equations based on bead-spring or bead-rod models [Bird et al., 1987a,b]). The elastic stress tensor obtained by considering a macroscopic model does not incorporate the detailed microstructural description of the flow. However, finer details of the microstructure can be acquired by using mesoscopic models. Computational models based on a conformation tensor are less expensive computationally than models based on more detailed microstructural representations of the liquid based on bead-spring-rod models (e.g., stochastic methods such as CONFFESSIT [Feigl et al., 1995], the Adaptive Lagrangian Particle method [Gallez et al., 1999], and Brownian configuration fields Hulsen et al. [1997]). Recently viscoelastic flows in complex geometries have been successfully modelled with a conformation tensor model for polymer solutions [Bajaj et al., 2008; Pasquali and Scriven, 2002, 2004; Xie, 2006; Xie and Pasquali, 2004].

In conformation tensor based models, microstructural features of polymer solutions can be represented by an independent variable, the conformation tensor (\mathbf{M}), which gives the microstructural state of a polymer molecule, and which is related to the polymer contribution to the stress through an algebraic constitutive equation [Guenette et al., 1992; Pasquali, 2000; Pasquali and Scriven, 2002]. The conformation tensor is used to represent the microstructural state of the complex fluid, and leads to insight into the stretch and orientation of the microstructure. Once the configuration and the configurational distribution function is known the stress can be evaluated.

Over the last two decades, the use of the finite element method has dominated the solution of viscoelastic flow problems. Several methods of solving the partial differential equations for such flows have been proposed. Baaijens [1998] provides an extensive review on various developments of finite element techniques used to solve viscoelastic flows. Additional stability issues arising from the coupling of the momentum equation with the hyperbolic constitutive equation are addressed by employing the so-called elastic viscous split stress (EVSS) formulation of Rajagopalan et al. [1990]. Several successive variations have been proposed along the lines of the EVSS method: the DEVSS (Discrete Elastic Viscous Split Stress) [Guenette et al., 1992], DEVSS-G (Discrete Elastic Viscous Split Stress with interpolated velocity gradient) [Guénette and Fortin, 1995], DAVSS-G (Discrete Adaptive Elastic Viscous Stress Split with interpolated velocity gradient) [Sun et al., 1999] and DEVSS-TG/SUPG (Discrete Elastic Viscous Split Stress-Traceless Gradient, Streamline Upwind Petrov-Galerkin) [Pasquali and Scriven, 2002]. Furthermore, as is well known, most viscoelastic computations based on the conformation tensor break down numerically at some limiting value of the Weissenberg

number due the development of large stresses, and stress gradients in narrow regions of the flow domain. Recently, an important contribution for improving the convergence of viscoelastic flow at high Weissenberg number has been addressed by Fattal and Kupferman [2004, 2005], who developed the so-called Log-Conformation method. It is worth noting, however, that the log-conformation tensor method has so far been mainly applied to confined flows [Afonso et al., 2009; Coronado et al., 2007; Damanik et al., 2010; Gu ette et al., 2008; Hulsen et al., 2005], and to our knowledge, there are very few studies of free surface flows with this method [Fortin et al., 2010; Tom e et al., 2009].

The shape of the collapsible wall, deforming due to both the fluid and any external forces, is unknown a priori and describing its evolution is a part of the solution. Several methods have been developed to locate the unknown boundaries while solving simultaneously the velocity, pressure and stress field in the fluid domain. The volume of fluid (VOF) [Hirt and Nichols, 1981; Maronnier et al., 2003], boundary element method (BEM) [Kaur and Leal, 2009; Rallison and Acrivos, 1978; Stone and Leal, 1990] and the marker-and-cell (MAC) [Harlow and Welch, 1965] are boundary-mapping techniques which are available to compute the free surface shape. These methods are computationally cheaper than domain-mapping methods because they do not need to solve internal mesh points. However, these methods are not suitable for the description of a free surface where deformation is large, as the boundary shapes produced by them are not smooth mathematical curves and often subjected to high errors. On the other hand, domain-mapping methods such as elliptic mesh generation [Benjamin, 1994; Christodoulou and Scriven, 1992; deSantos, 1991; Pasquali and Scriven, 2002] and domain deformation [DE Almeida, 1995, 1999; Lynch and O Neill, 1980; Sackinger et al., 1996b] have been used successfully to solve several complex free surface flow problems [Bajaj et al., 2008; Pasquali and Scriven, 2002, 2004; Xie, 2006; Xie and Pasquali, 2004]. In this work, a boundary fitted finite element based elliptic mesh generation method [Benjamin, 1994; Christodoulou and Scriven, 1992; deSantos, 1991] has been used to simulate viscoelastic fluids. A DEVSS-TG/SUPG finite element method has been used here to solve for the fluid velocity and stress fields, and the shape of the fluid boundary using a numerical algorithm which was developed originally by Pasquali and Scriven [2004].

The model formulation used here follows the seminal work of Carvalho and Scriven [1997] who proposed a fluid-structure interaction formulation to solve roll cover deformation in roll coating flows, with the rubber roll cover modelled as incompressible

neo-Hookean and Mooney-Rivlin solids. The constitutive equations of all the viscoelastic fluids considered here are written in conformation tensor form [Pasquali and Scriven, 2004]. As is well known, it is possible to map the well known Oldroyd-B and FENE-P models, which are typically written as constitutive equations for the polymer contribution to stress, to equivalent conformation tensor models. The original model by Owens [Owens, 2006] leads to a multi-mode model for the contribution of red blood cells to the stress. However, with a view to obtaining a tractable model, Owens also proposed a single mode model, that is believed to capture the contribution of the aggregates containing the largest fraction of red blood cells. In order to incorporate the Owens model into the numerical algorithm mentioned above, we have rewritten the single mode constitutive equation for the stress in terms of an equivalent conformation tensor expression.

2.1 Governing equations

2.1.1 Governing equations for fluid

The equations of motion for steady, incompressible flow in the absence of body forces are:

$$\nabla \cdot \mathbf{v} = 0 \quad (2.1)$$

$$\rho \mathbf{v} \cdot \nabla \mathbf{v} = \nabla \cdot \mathbf{T} \quad (2.2)$$

where ρ is the density of the liquid, \mathbf{v} is the velocity, ∇ denotes the gradient. The Cauchy stress tensor is $\mathbf{T} = -p\mathbf{I} + \boldsymbol{\tau}^s + \boldsymbol{\tau}^p$, where p is the pressure, \mathbf{I} is the identity tensor, $\boldsymbol{\tau}^s$ is the viscous stress tensor and $\boldsymbol{\tau}^p$ is the elastic stress tensor. The viscous stress tensor is $\boldsymbol{\tau}^s = 2\eta_s \mathbf{D}$, where η_s is the solution viscosity and $\mathbf{D} = \frac{1}{2}(\nabla \mathbf{v} + \nabla \mathbf{v}^T)$ is the rate of strain tensor.

Pasquali and Scriven [2002] derived an expression for the rate of change of conformation due to internal processes. Considering molecular stretch, rotation and relaxation as independent processes, taking the vorticity as the average rate of rotation of microstructural molecules, and using isotropy and representation theorems, the transport

equation of the conformation tensor can be written as [Pasquali and Scriven, 2002]:

$$\begin{aligned} \mathbf{0} = & \mathbf{v} \cdot \nabla \mathbf{M} - \underbrace{2\xi \frac{\mathbf{D} : \mathbf{M}}{\mathbf{I} : \mathbf{M}} \mathbf{M}}_{\text{molecular stretching}} - \underbrace{\zeta \left(\mathbf{M} \cdot \mathbf{D} + \mathbf{D} \cdot \mathbf{M} - 2 \frac{\mathbf{D} : \mathbf{M}}{\mathbf{I} : \mathbf{M}} \mathbf{M} \right)}_{\text{molecular relative rotation}} \\ & - \underbrace{\mathbf{M} \cdot \mathbf{W} - \mathbf{W}^T \cdot \mathbf{M}}_{\text{solid-body rotation}} + \frac{1}{\lambda_0} \underbrace{\left(g_0 \mathbf{I} + g_1 \mathbf{M} + g_2 \mathbf{M}^2 \right)}_{\text{molecular relaxation}} \end{aligned} \quad (2.3)$$

where \mathbf{M} is the dimensionless conformation tensor, $\mathbf{W} = \frac{1}{2}(\nabla \mathbf{v} - \nabla \mathbf{v}^T)$ is the vorticity tensor, λ_0 is the characteristic relaxation time of the polymer, $\xi(\mathbf{M})$ represents the polymer resistance to stretching along the backbone, $\zeta(\mathbf{M})$ represents the polymer resistance to rotation with respect to neighbours and $g_0(\mathbf{M})$, $g_1(\mathbf{M})$ and $g_2(\mathbf{M})$ define the rate of relaxation of polymer segments.

The elastic stress tensor (τ^P) is obtained from the conformation tensor (\mathbf{M}) by (Pasquali and Scriven [2002]):

$$\tau^P = 2(\xi - \zeta) \frac{(\mathbf{M} - \mathbf{I})}{\mathbf{I} : \mathbf{M}} \mathbf{M} : \frac{\partial a}{\partial \mathbf{M}} + 2\zeta(\mathbf{M} - \mathbf{I}) \cdot \frac{\partial a}{\partial \mathbf{M}} \quad (2.4)$$

where $a(\mathbf{M})$ is the Helmholtz free energy per unit mass of the polymeric liquid. The constitutive functions ($\xi(\mathbf{M})$, $\zeta(\mathbf{M})$, $g_0(\mathbf{M})$, $g_1(\mathbf{M})$, $g_2(\mathbf{M})$ and $a(\mathbf{M})$) whose forms depend on the type of the constitutive relation chosen, are listed in Table 2.1 for the viscoelastic fluids (the Oldroyd-B, the FENE-P and Owens models) used in the present work. G_p is the polymer elastic modulus and b_M is the finite extensibility parameter.

Table 2.1: Constitutive functions in the general conformation tensor model for the different types of constitutive equations used in this work.

Model	$\xi(\mathbf{M})$	$\zeta(\mathbf{M})$	$g_0(\mathbf{M})$	$g_1(\mathbf{M})$	$g_2(\mathbf{M})$	$a(\mathbf{M})$
Oldroyd-B	1	1	-1	1	0	$\frac{G_p}{2} \text{tr} \mathbf{M}$
FENE-P	1	1	-1	$\frac{b_M - 1}{b_M - \frac{\text{tr} \mathbf{M}}{3}}$	0	$\frac{3G_p(b_M - 1)}{2} \ln \left(\frac{b_M - 1}{b_M - \frac{\text{tr} \mathbf{M}}{3}} \right)$
Owens' Model	1	1	-1	1	0	$\frac{G_p}{2} \text{tr} \mathbf{M}$

2.1.1.1 Viscoelastic fluid models

The three different conformation tensor based constitutive models used in this work are described below.

- **Infinitely extensible molecules (Oldroyd-B model)** Using the values of constitutive functions ($\xi = 1, \zeta = 1, g_0 = -1, g_1 = 1, g_2 = 0$) as listed in Table 2.1, the evolution equation of the dimensionless conformation tensor for the Oldroyd-B model becomes

$$\mathbf{v} \cdot \nabla \mathbf{M} - \nabla \mathbf{v}^T \cdot \mathbf{M} - \mathbf{M} \cdot \nabla \mathbf{v} = -\frac{1}{\lambda_0} \{\mathbf{M} - \mathbf{I}\} \quad (2.5)$$

The elastic stress for the Oldroyd-B model represented by the dimensionless conformation tensor takes the form,

$$\boldsymbol{\tau}^P = \frac{\eta_{p,0}}{\lambda_0} \{\mathbf{M} - \mathbf{I}\} \quad (2.6)$$

where $\eta_{p,0}$ is the contribution of the micro-structural elements to the zero shear rate viscosity, and λ_0 is the constant characteristic relaxation time of the microstructure.

- **Finitely extensible molecules (FENE-P model)** As shown in the Table 2.1, the constitutive functions for FENE-P model are $\xi = 1, \zeta = 1, g_0 = -1, g_1 = (b_M - 1)/(b_M - \frac{\text{trM}}{3}), g_2 = 0$. The evolution equation of the dimensionless conformation tensor for the FENE-P model is

$$\mathbf{v} \cdot \nabla \mathbf{M} - \nabla \mathbf{v}^T \cdot \mathbf{M} - \mathbf{M} \cdot \nabla \mathbf{v} = -\frac{1}{\lambda_0} \left\{ \frac{b_M - 1}{b_M - \frac{\text{trM}}{3}} \mathbf{M} - \mathbf{I} \right\} \quad (2.7)$$

The finite extensibility parameter b_M is defined as the ratio of the maximum length squared of the microstructural element to its average length squared at equilibrium. For the FENE-P model, the dependence of elastic stress on the dimensionless conformation tensor is well known [Pasquali and Scriven, 2004]; it takes the form,

$$\boldsymbol{\tau}^P = \frac{\eta_{p,0}}{\lambda_0} \left\{ \frac{b_M - 1}{b_M - \frac{\text{trM}}{3}} \mathbf{M} - \mathbf{I} \right\} \quad (2.8)$$

- **Owens blood model [Owens, 2006]** The Owens blood model [Owens, 2006] was originally presented in terms of a constitutive equation for the elastic stress and has not yet been translated into conformation tensor form and studied in complex flows. A conformation tensor version of the Owens model can be derived straightforwardly,

$$\mathbf{v} \cdot \nabla \mathbf{M} - \nabla \mathbf{v}^T \cdot \mathbf{M} - \mathbf{M} \cdot \nabla \mathbf{v} = -\frac{1}{\lambda} \{\mathbf{M} - \mathbf{I}\} \quad (2.9)$$

and the constitutive equation for polymer stress is given by,

$$\boldsymbol{\tau}^P = \frac{\eta_{p,0}}{\lambda_0} \{\mathbf{M} - \mathbf{I}\} \quad (2.10)$$

It is interesting to note that the elastic stress Eq. (2.10) maintains the same form for Owens' model as in the Oldroyd-B model (Eq. (2.6)). However, the *constant* relaxation time λ_0 in Eq. (2.5) is replaced by a *function* λ in Eq. (2.9), representing the relaxation time of the elastic stress due to blood cell aggregates. λ depends on the average size of the blood cell aggregates, n , which is controlled by the competition of spontaneous aggregation and flow-induced disaggregation. We assume here $n = n_{st}(\dot{\gamma})$ as we are solving for steady flows. This choice preserves the viscoelastic and shear thinning character of blood but does not capture its thixotropic behaviour [Owens, 2006]. This simplification makes it unnecessary to solve an additional equation for the variation of n in the flow domain. Under this assumption, the relaxation time λ is

$$\lambda = \left(\frac{\lambda_H}{\eta_{p,\infty}} \right) \eta_p(\dot{\gamma}) \quad (2.11)$$

where, λ_H is the relaxation time of individual blood cell aggregates, $\eta_{p,\infty}$ is the infinite shear-rate viscosity, and $\eta_p(\dot{\gamma})$ is their contribution to blood viscosity given by the Cross model,

$$\eta_p(\dot{\gamma}) = \eta_{p,0} \left(\frac{1 + \theta_1 \dot{\gamma}^m}{1 + \theta_2 \dot{\gamma}^m} \right) \quad (2.12)$$

where m is a power law index, and the ratio of parameters θ_1 and θ_2 satisfies the expression, $\theta_1/\theta_2 = \eta_{p,\infty}/\eta_{p,0}$ [Owens, 2006]. The values of all model parameters are reported in Chapter 3 and Chapter 5.

2.1.2 Governing equations for the solid

Fig. 2.1 displays schematically the approach adopted by Carvalho and Scriven [1997] while solving roll coating flow considering fluid-structure interaction. Although the fluid and solid domains are represented as distinct domains, they are coupled at the interface and the response of the solid is strongly affected by the response of the fluid, and vice versa. The fluid domain (Ω_F) is mapped by the elliptic mesh generation method [Benjamin, 1994; Christodoulou and Scriven, 1992; deSantos, 1991] to a reference domain (Ω_{0F}), where the fluid equations are solved. The deformed solid domain

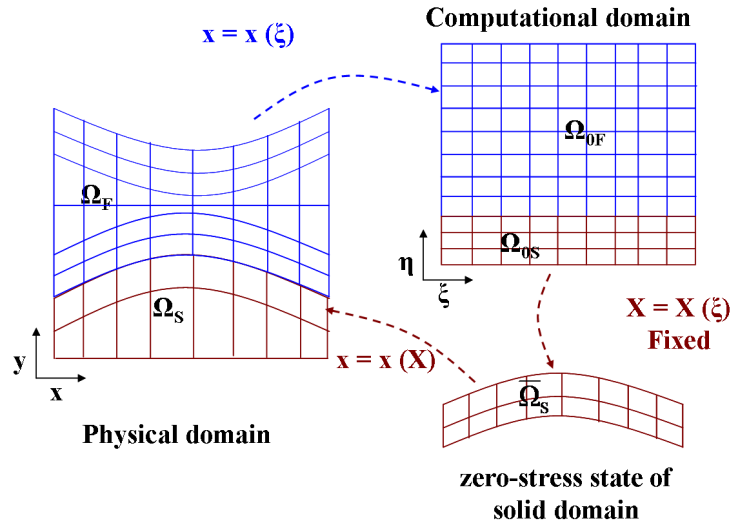


Figure 2.1: Mapping between different domains

(Ω_S) is mapped to the stress-free domain $(\bar{\Omega}_S)$ where the equations for the solid wall are solved. Interestingly, the solution of the wall equations itself constitutes a mapping, and is consequently not solved separately. The mapping from the computational domain (Ω_{0S}) to the zero-stress configuration $(\bar{\Omega}_S)$ is known and it only requires a change of domain of integration. If the acceleration and body forces are neglected, the equilibrium equation in the current (deformed) configuration is simply

$$\nabla_{\mathbf{X}} \cdot \mathbf{S} = \mathbf{0} \quad (2.13)$$

where \mathbf{S} is the first Piola-Kirchhoff stress tensor and is related to the Cauchy stress tensor $(\boldsymbol{\sigma})$ through

$$\mathbf{S} = \mathbf{F}^{-1} \cdot \boldsymbol{\sigma} \quad (2.14)$$

where \mathbf{F} is the deformation gradient tensor which relates the undeformed state $[\mathbf{X} = (X, Y, Z)]$ to the deformed state $[\mathbf{x} = (x, y, z)]$ and can be expressed as,

$$\mathbf{F} = \frac{\partial \mathbf{x}}{\partial \mathbf{X}} \quad (2.15)$$

The Cauchy stress tensor for a neo-Hookean material can be expressed as

$$\boldsymbol{\sigma} = -\pi\mathbf{I} + G\mathbf{B} \quad (2.16)$$

where π is a pressure-like scalar function, G is the shear modulus and \mathbf{B} is the left Cauchy-Green tensor which is expressed as $\mathbf{B} = \mathbf{F} \cdot \mathbf{F}^T$

2.1.3 Mesh generation technique for moving boundaries

In the FEM, interface tracking can be achieved using many methods. To compute free surface flows, the unknown physical domain is mapped onto a fixed reference computational domain. This mapping ($\mathbf{x} = \mathbf{x}(\boldsymbol{\xi})$) connects the known and the unknown domains. As shown in Fig. 2.1, the unknown physical domain is denoted by the position vector \mathbf{x} and the reference domain by $\boldsymbol{\xi}$. In complex geometries the physical domain cannot be mapped onto a simpler, quadrangular reference domain. In these situations, it is usually convenient to subdivide the physical domain into subdomains and then map each subdomain of the physical domain onto a separate subdomain of the computational domain. Here we use a boundary fitted finite element based elliptic mesh generation method [Benjamin, 1994; Christodoulou and Scriven, 1992; deSantos, 1991; Pasquali and Scriven, 2002] which involves solving the following elliptic differential equation for the mapping:

$$\nabla \cdot (\tilde{\mathbf{D}} \cdot \nabla \boldsymbol{\xi}) = \mathbf{0} \quad (2.17)$$

where, $\boldsymbol{\xi}$ is a vector of positions in the computational domain and the dyadic, $\tilde{\mathbf{D}}$, is a function of $\boldsymbol{\xi}$, analogous to a diffusion coefficient, which controls the spacing of the coordinate lines [Benjamin, 1994].

To solve the above set of governing equations ((2.1), (2.2), (2.3) and (2.17)) with the DEVSS-TG/SUPG finite element method an additional equation is required whose solution gives the interpolated velocity gradient, \mathbf{L} . Pasquali and Scriven [2002] introduced the following equation to keep \mathbf{L} traceless:

$$\mathbf{L} - \nabla \mathbf{v} + \frac{1}{\text{tr}\mathbf{I}}(\nabla \cdot \mathbf{v})\mathbf{I} = \mathbf{0} \quad (2.18)$$

In the transport equations the rate of strain tensor (\mathbf{D}) and vorticity tensor (\mathbf{W}) are

calculated from this interpolated velocity gradient (\mathbf{L}) as follows:

$$\mathbf{D} = \frac{1}{2}(\mathbf{L} + \mathbf{L}^T); \mathbf{W} = \frac{1}{2}(\mathbf{L} - \mathbf{L}^T) \quad (2.19)$$

Pasquali and Scriven [2002] proposed a modified expression for the viscous stress tensor as a stabilization term to the momentum equation, which is as follows:

$$\boldsymbol{\tau}^s = \eta_s(\mathbf{L} + \mathbf{L}^T) + \eta_a(\nabla \mathbf{v} + \nabla \mathbf{v}^T - \mathbf{L} - \mathbf{L}^T) \quad (2.20)$$

where η_a is a numerical parameter, whose value has no effect on the solution of the problem as long as $\eta_a \equiv \eta_s + \eta_{p,0}$ [Bajaj et al., 2008; Pasquali and Scriven, 2002].

2.1.4 Finite element formulation of the problem

2.1.4.1 Weighted residual form of governing equations for fluid

The coupled set of transport equations for mass, momentum, interpolated velocity gradient and conformation tensor along with the mesh equations is:

$$0 = \nabla \cdot \mathbf{v} \quad (2.21)$$

$$\mathbf{0} = \rho \mathbf{v} \cdot \nabla \mathbf{v} - \nabla \cdot \mathbf{T} \quad (2.22)$$

$$\mathbf{0} = \mathbf{L} - \nabla \mathbf{v} + \frac{1}{\text{tr} \mathbf{I}}(\nabla \cdot \mathbf{v})\mathbf{I} \quad (2.23)$$

$$\mathbf{0} = \mathbf{v} \cdot \nabla \mathbf{M} - 2\xi \frac{\mathbf{D} : \mathbf{M}}{\mathbf{I} : \mathbf{M}} \mathbf{M} - \zeta \left(\mathbf{M} \cdot \mathbf{D} + \mathbf{D} \cdot \mathbf{M} - 2 \frac{\mathbf{D} : \mathbf{M}}{\mathbf{I} : \mathbf{M}} \mathbf{M} \right) \quad (2.24)$$

$$- \mathbf{M} \cdot \mathbf{W} - \mathbf{W}^T \cdot \mathbf{M} + \frac{1}{\lambda} (g_0 \mathbf{I} + g_1 \mathbf{M} + g_2 \mathbf{M}^2) \quad (2.25)$$

$$\mathbf{0} = \nabla \cdot (\tilde{\mathbf{D}} \cdot \nabla \xi) \quad (2.26)$$

$$(2.27)$$

The weighted residual form of governing equations is obtained by multiplying the governing equations with appropriate weighting functions and then integrating over

the flow domain, as follows:

$$r^{c,\alpha} = \int_{\Omega_F} \psi_c^\alpha \nabla \cdot \mathbf{v} d\Omega_F \quad (2.28)$$

$$\mathbf{r}^{m,\alpha} = \int_{\Omega_F} \psi_m^\alpha (\rho \mathbf{v} \cdot \nabla \mathbf{v} - \nabla \cdot \mathbf{T}) d\Omega_F \quad (2.29)$$

$$\mathbf{R}^{L,\alpha} = \int_{\Omega_F} \psi_L^\alpha \left(\mathbf{L} - \nabla \mathbf{v} + \frac{1}{tr \mathbf{I}} (\nabla \cdot \mathbf{v}) \mathbf{I} \right) d\Omega_F \quad (2.30)$$

$$\begin{aligned} \mathbf{R}^{M,\alpha} = \int_{\Omega_F} \psi_M^\alpha \left(\mathbf{v} \cdot \nabla \mathbf{M} - 2\xi \frac{\mathbf{D} : \mathbf{M}}{\mathbf{I} : \mathbf{M}} \mathbf{M} - \zeta \left(\mathbf{M} \cdot \mathbf{D} + \mathbf{D} \cdot \mathbf{M} - 2 \frac{\mathbf{D} : \mathbf{M}}{\mathbf{I} : \mathbf{M}} \mathbf{M} \right) \right. \\ \left. - \mathbf{M} \cdot \mathbf{W} - \mathbf{W}^T \cdot \mathbf{M} + \frac{1}{\lambda} (g_0 \mathbf{I} + g_1 \mathbf{M} + g_2 \mathbf{M}^2) \right) d\Omega_F \end{aligned} \quad (2.31)$$

$$\mathbf{r}^{x,\alpha} = \int_{\Omega_F} \psi_x^\alpha \nabla \cdot \tilde{\mathbf{D}} \cdot \nabla \xi d\Omega_F \quad (2.32)$$

Here, Ω_F is the unknown physical fluid domain, $\psi_c^\alpha, \dots, \psi_x^\alpha$ are sets of scalar weighting functions defined in the physical domain, and $r^{c,\alpha}, \dots, \mathbf{r}^{x,\alpha}$ are the weighted residuals of the equations. The first superscript (c, \dots, x) on the residual denotes the relevant equation and second superscript α varies from 1 to the number of independent weighting functions to be chosen for a particular equation.

The second order derivatives in Eqs. (2.29) and (2.32) are reduced to first order derivatives by applying the divergence theorem and integrating by parts. The resulting equations are

$$\mathbf{r}^{m,\alpha} = \int_{\Omega_F} \psi_m^\alpha \rho \mathbf{v} \cdot \nabla \mathbf{v} d\Omega_F + \int_{\Omega_F} \nabla \psi_m^\alpha \cdot \mathbf{T} d\Omega_F - \int_{\Gamma_F} \psi_m^\alpha (\mathbf{n} \cdot \mathbf{T}) d\Gamma_F \quad (2.33)$$

$$\mathbf{r}^{x,\alpha} = \int_{\Gamma_F} (\mathbf{n} \cdot \tilde{\mathbf{D}} \cdot \nabla \xi) \psi_x^\alpha d\Gamma_F - \int_{\Omega_F} (\nabla \psi_x^\alpha \cdot \tilde{\mathbf{D}} \cdot \nabla \xi) d\Omega_F \quad (2.34)$$

where Γ_F is the boundary of the physical fluid domain and \mathbf{n} is the outward pointing normal to the boundary.

Each independent variable ($\mathbf{x}, p, \mathbf{v}, \mathbf{L}, \mathbf{M}$) of above mentioned equations is represented by finite element basis functions as:

$$\mathbf{x} \equiv \mathbf{x}^\beta \phi_{\mathbf{x}}^\beta, \quad p \equiv p^\beta \phi_p^\beta, \quad \mathbf{v} \equiv \mathbf{v}^\beta \phi_{\mathbf{v}}^\beta, \quad \mathbf{L} \equiv \mathbf{L}^\beta \phi_{\mathbf{L}}^\beta, \quad \mathbf{M} \equiv \mathbf{M}^\beta \phi_{\mathbf{M}}^\beta \quad (2.35)$$

where ϕ^β are the basis functions, $\mathbf{x}^\beta, \dots, \mathbf{M}^\beta$ are the unknown coefficients and β is a dummy index ranging from 1 to the number of basis functions for different independent variables. Galerkin weighting functions are used in Eqs. (2.28), (2.29), (2.30) and (2.32),

i.e. $\psi_c = \phi_p$, $\psi_m = \phi_v$, $\psi_L = \phi_L$ and $\psi_x = \phi_x$. The Streamline-Upwind Petrov-Galerkin method is used for the weighting function in the conformation transport Eq. (2.31), $\psi_M = \phi_M + h^u \mathbf{v} \cdot \nabla \phi_M$, where h^u is the upwind parameter. The upwind parameter h^u is chosen as the characteristic element size. In all our simulations h^u was always less than 0.01.

2.1.4.2 Weighted residual form of the equilibrium equation for solid

The weighted residual form of Eq. (2.13) is obtained by multiplying the governing equations with appropriate weighting functions and then integrating over the current domain. The formulation of the fluid-structure interaction problem posed here follows the procedure introduced previously by Carvalho and Scriven [1997] in their examination of roll cover deformation in roll coating flows. However, it turns out that the weighted residual form of Eq. (2.13) used in their finite element formulation is incorrect. While the error does not lead to significant discrepancies for small deformations, it is serious for large deformations. The correct form of the weighted-residual equation is presented here and validated in Appendix B against predictions by the commercial software package ANSYS-11.0 for the deformation of a simple beam fixed at its edges. The deformation of the solid in the current configuration (Ω_S) is written in the zero-stress configuration ($\bar{\Omega}_S$). A construction of the mapping $\mathbf{X} = \mathbf{X}(\boldsymbol{\xi})$ from computational domain (Ω_{0S}) to zero-stress configuration ($\bar{\Omega}_S$) is required to integrate this equation in the computational domain (Ω_{0S}). This is a known mapping and it requires a change of domain of integration. The Jacobian of this transformation is denoted by $|\mathbf{J}^*|$. The weak form of the equilibrium equation is

$$\begin{aligned} \int_{\bar{\Omega}_S} \nabla_{\mathbf{x}} \cdot \mathbf{S} \cdot \phi d\bar{\Omega}_S &= \mathbf{0} \\ \Rightarrow - \int_{\bar{\Omega}_S} \nabla_{\mathbf{x}} \phi \cdot \mathbf{S} d\bar{\Omega}_S + \int_{\bar{\Gamma}_S} \phi (\mathbf{N} \cdot \mathbf{S}) d\bar{\Gamma}_S &= \mathbf{0} \end{aligned} \quad (2.36)$$

The weighted residual form of the x-position, y-position and incompressibility in the reference domain can be expressed as,

$$R_i^x = - \int_{\Omega_{0S}} \left[\frac{\partial \phi_i}{\partial X} S_{Xx} + \frac{\partial \phi_i}{\partial Y} S_{Yx} \right] |\mathbf{J}^*| d\Omega_{0S} + \int_{\Gamma_{0S}} \phi_i (\mathbf{N} \cdot \mathbf{S})_x \left(\frac{d\bar{\Gamma}_S}{d\Gamma_{0S}} \right) d\Gamma_{0S} \quad (2.37)$$

$$R_i^y = - \int_{\Omega_{0S}} \left[\frac{\partial \phi_i}{\partial X} S_{Xy} + \frac{\partial \phi_i}{\partial Y} S_{Yy} \right] |\mathbf{J}^*| d\Omega_{0S} + \int_{\Gamma_{0S}} \phi_i (\mathbf{N} \cdot \mathbf{S})_y \left(\frac{d\bar{\Gamma}_S}{d\Gamma_{0S}} \right) d\Gamma_{0S} \quad (2.38)$$

$$R_i^{p^*} = \int_{\Omega_{0s}} \left[\frac{\partial x}{\partial X} \frac{\partial y}{\partial Y} - \frac{\partial x}{\partial Y} \frac{\partial y}{\partial X} - 1 \right] \chi_i |\mathbf{J}^*| d\Omega_{0s} \quad (2.39)$$

The weighting functions ϕ_i are bi-quadratic, and χ_i are piecewise linear discontinuous.

2.1.5 Boundary conditions

Appropriate boundary conditions are needed to solve the governing equations. The momentum and mesh equations for the fluid (Eqs. (2.2) and (2.17)) and equilibrium equation for the solid (Eq. (2.13)) are elliptic in nature, thus boundary conditions must be specified on all boundaries. Since the equation for the conformation tensor (Eq. (2.3)) is hyperbolic in nature, boundary conditions are only required at the inflow boundaries. Xie and Pasquali [2004] have shown that the entrance boundary condition $\mathbf{v} \cdot \nabla \mathbf{M} = \mathbf{0}$ is appropriate when the flow is fully developed at the inlet. The continuity equation and the velocity gradient equation don't need any boundary conditions. More specific boundary conditions pertaining to different problems are described in chapters 3-5.

2.1.6 Solution procedure with Newton's method

Newton's method with analytical Jacobian is applied to solve the non-linear equations, Eqs. (2.28)–(2.31) and (2.37)–(2.39). Initially a 2D structured mesh is generated utilizing a code developed by Scriven's group at the University of Minnesota. The weighted residual ($\mathbf{R} = r^{c,\alpha}, \mathbf{r}^{m,\alpha}, \mathbf{R}^{L,\alpha}, \mathbf{R}^{M,\alpha}, \mathbf{r}^{x,\alpha}, R_i^x, R_i^y$ and $R_i^{p^*}$) form of the equations and the Jacobian matrix (\mathbf{J}), which represents the analytical derivative of the residual equations and their boundary conditions with respect to the basis function coefficients, are solved.

$$\delta \mathbf{u} = \mathbf{u}_{k+1} - \mathbf{u}_k \quad (2.40)$$

$$\mathbf{J} \delta \mathbf{u} = -\mathbf{R} \quad (2.41)$$

where \mathbf{u}_{k+1} is the solution vector ($\mathbf{v}, p, \mathbf{x}, \mathbf{L}, \mathbf{M}$) at the current Newton iteration and \mathbf{u}_k is the solution vector at the previous Newton iteration. The residual vector and Jacobian matrix is assembled and the linear system of equations is solved by a frontal solver [DE Almeida, 1995; Duff et al., 1989; Pasquali, 2000]. The final solution is obtained when the residual and update norms approach a convergence criterion. The details of

the analytical Jacobian entries for viscoelastic fluids have been provided by Pasquali [2000], whereas the analytical Jacobian entries for the solid can be found in Carvalho [1996].

2.2 Conclusion

In this chapter, a computational method to solve steady two-dimensional viscoelastic fluid-elastic solid interaction has been described. The rheological behaviour of the viscoelastic fluids has been described in terms of a conformation tensor model and the finite-thickness solid wall by a neo-Hookean solid model. A DEVSS-TG/SUPG mixed finite element method for discretizing the mesh equation and transport equations, together with the solution technique proposed by Carvalho and Scriven [1997] for calculating deformation of a finite thickness solid has been employed.

Chapter 3

Viscoelastic flow in a two-dimensional collapsible channel

3.1 Introduction

In this chapter¹, we compute the flow of three viscoelastic fluids in a two-dimensional channel partly bounded by a tensioned membrane, a benchmark geometry for fluid-structure interactions. The computational method developed in chapter 2 is used to solve this problem.

As mentioned previously, laboratory experiments on flow through collapsible tubes have shown complex and nonlinear dynamics, with a multiplicity of self-excited oscillations [Bertram, 1986; Bertram et al., 1990]. The simplest numerical model in the literature that captures part of this rich behaviour is that of a fluid flowing in a 2D rigid parallel sided channel, where part of one wall is replaced by a tensioned membrane (Fig. 3.1). This geometry has been studied extensively in the case of Newtonian fluids, with the flexible wall treated as an elastic membrane of zero thickness, with the stretching and the bending stiffness of the membrane along the flow direction neglected [Heil and Jensen, 2003; Lowe and Pedley, 1995; Luo and Pedley, 1995, 1996; Rast, 1994]. There have been no studies of fluid-structure interaction issues associated with the flow of viscoelastic fluids in vessels with compliant walls. This work aims to study the flow of model viscoelastic fluids in a simple two-dimensional collapsible channel as a preliminary study of the behaviour that might arise when more realistic models of blood

¹This chapter has been published as, Chakraborty, D., Bajaj, M., Yeo, L., Friend, J., Pasquali, M., and Prakash, J. R. (2010). Viscoelastic flow in a two-dimensional collapsible channel. *J. Non-Newton. Fluid Mech.*, 165:12041218.

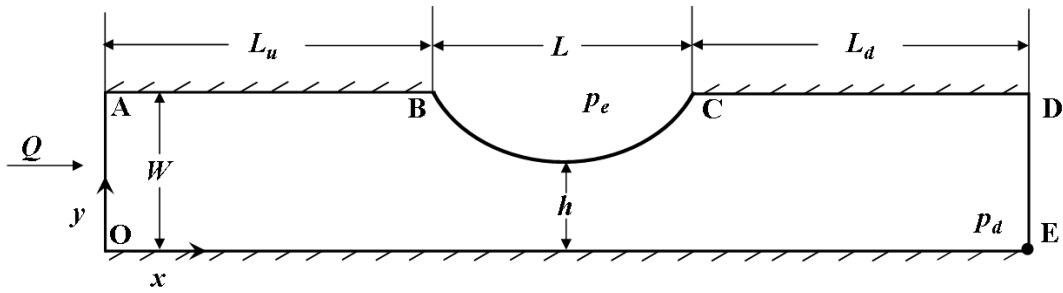


Figure 3.1: Geometry of the 2D collapsible channel; the segment BC is an elastic membrane.

and blood vessels are simulated under conditions in which the viscoelastic character of blood and the elastic nature of blood vessel walls become important. Here, we use the simple 2D geometry, with a zero thickness membrane, to study fluid-structure interaction in viscoelastic liquids. We restrict our attention to $Re = 1$, since we are interested in the microcirculation.

This chapter is organized as follows. Section 3.2 presents the flow domain, boundary conditions, dimensionless numbers and choice of parameter values. Section 3.3 compares the results of viscoelastic and Newtonian fluid computations, and Section 3.4 summarises our conclusions.

3.2 Problem formulation

In units of channel width W , the dimensions of the channel are $L_u = 7W$, $L = 5W$, and $L_d = 7W$ (Fig. 3.1). As in Luo and Pedley [1995], the tension in the flexible wall is constant and the shape of the flexible part is governed by the normal force acting on it. h denotes the *minimum* channel width between the deformed membrane and the bottom wall (Fig. 3.1).

3.2.1 Boundary conditions

The governing equations for the present problem have already been discussed in chapter 2. However, in order to solve the present problem, appropriate boundary conditions are needed. We prescribe the following boundary conditions:

1. At the upstream boundary, a fully developed velocity profile is specified in the

form, $v_x = f(y)$, and $v_y = 0$. Since, for all the Wi considered here, the upstream velocity profiles for the Oldroyd-B and FENE-P fluids do not differ significantly from that for a Newtonian fluid, a Newtonian velocity profile is used. However, because of the strongly shear thinning nature of the Owens model fluid, we use a fully developed velocity profile obtained by analytically solving the flow of a power-law fluid in a channel. The power-law index used is that exhibited by the Owens model (with the current parameter values) in a simple shear flow.

2. No slip boundary conditions ($\mathbf{v} = \mathbf{0}$) are applied on the rigid walls.
3. At the flexible wall,
 - (a) On the *momentum* equation (Eq. (2.2)), we impose (i) $\mathbf{t} \cdot \mathbf{v} = 0$, where \mathbf{t} is the unit tangent to the flexible wall, and, (ii) a force balance in the normal direction through the traction boundary condition:

$$\mathbf{nn} : \mathbf{T} = -p_e + \chi \nabla_{II} \cdot \mathbf{n} \quad (3.1)$$

where, \mathbf{n} is the unit normal to the flexible wall, ∇_{II} denotes the surface gradient operator, p_e is the external pressure and χ is the fixed tension in the flexible wall.

- (b) On the *mapping* equation (Eq. (2.17)), we impose (i) $\mathbf{n} \cdot \mathbf{v} = 0$ in the normal direction, and, (ii) a uniform node distribution in the tangential direction.
4. At the downstream boundary, the fully developed flow boundary condition is imposed, $\mathbf{n} \cdot \nabla \mathbf{v} = \mathbf{0}$.
5. At the upstream inflow, the conformation tensor does not change along the streamlines because the flow is fully developed [Pasquali and Scriven, 2002; Xie and Pasquali, 2004]. Thus,

$$\mathbf{v} \cdot \nabla \mathbf{M} = \mathbf{0} \quad (3.2)$$
6. The pressure of the fluid at the downstream boundary, p_d , is set equal to zero on the bottom wall (at location E in Fig. 3.1).

3.2.2 Dimensionless numbers and choice of parameter values

Non-dimensionalization of the governing equations and boundary conditions yields the following dimensionless numbers:

$$Re = \frac{\rho W U_0}{\eta_0}; \quad \beta = \frac{\eta_s}{\eta_0}; \quad Wi = \frac{\lambda_0 U_0}{W}; \quad Ca = \frac{\eta_0 U_0}{\chi}; \quad P_d = \frac{(p_e - p_d)W}{\eta_0 U_0} \quad (3.3)$$

where, U_0 is the average inlet velocity, Ca is analogous to a capillary number, β is the viscosity ratio, Wi is the *inlet* Weissenberg number, P_d is the dimensionless transmural pressure difference, and $\eta_0 = \eta_s + \eta_{p,0}$ is the zero shear rate solution viscosity. (For a Newtonian fluid, η_0 is just the constant Newtonian viscosity). It is convenient to define a *local* Weissenberg number $\widetilde{Wi} = \lambda_0 \dot{\gamma}$, which measures the non-dimensional shear rate anywhere in the flow.

Luo and Pedley [1995] used the dimensionless ratio, $\alpha = Ca/Ca^*$ to represent the influence of membrane tension, where Ca^* is a reference dimensionless tension (defined with $\chi = 1.610245$ N/m). In order to compare our predictions for Newtonian fluids at $Re = 1$ [Luo and Pedley, 1995], we also index membrane tension by α (in the range $\alpha = 15\text{--}64$), and we use the same value of the dimensionless transmural pressure difference, $P_d = 9.3 \times 10^4$.

For the Owens model, the best agreement with triangular step shear rate experimental data [Bureau et al., 1980] occurs when parameters $\eta_{p,0} = 0.14$ Pa s, $\eta_{p,\infty} = 0.004$ Pa s, $\theta_2 = 7.2$, $m = 0.6$, and $\lambda_H = 0.145$ s [Owens, 2006]. Interestingly, this choice of parameters neglects the solvent (or plasma) viscosity, and consequently yields an upper convected Maxwell" rather than an "Oldroyd-B" type model. Later work [Fang and Owens, 2006; Moyers-Gonzalez et al., 2008a] introduced a solvent contribution ($\eta_s = 0.001$ Pa s), and modified the remaining parameters depending on the specific comparison of model predictions with experiments. Importantly, in steady homogeneous flows, specification of the parameters above also sets the expression of the relaxation time $\lambda(\dot{\gamma})$. Here we vary λ_H to control the inlet Weissenberg number (since $\lambda_0 = \frac{\eta_{p,0}}{\eta_{p,\infty}} \lambda_H$), while keeping the values of the other parameters [Owens, 2006], augmented with the plasma viscosity $\eta_s = 0.001$ Pa s.

To attain $Re = 1$, we set $\rho = 1054$ kg/m³ (as in Owens [2006]), $U_0 = 1.338 \times 10^{-2}$ m/s, $W = 10^{-2}$ m and $\eta_0 = 0.141$ Pa s. This yields a viscosity ratio $\beta = 0.0071$ (which signifies that the fluid is predominantly elastic). The FENE-P parameter b_M is set to 100.

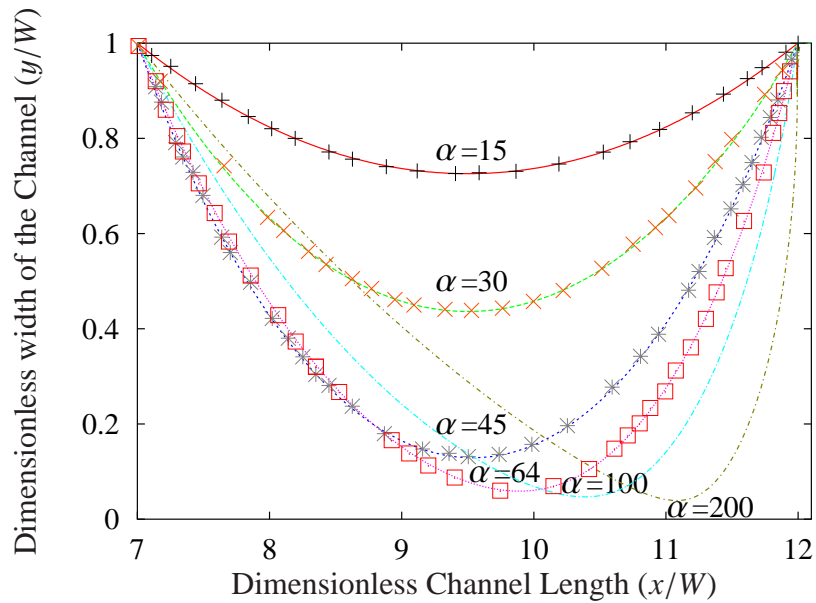


Figure 3.2: The deformed shape of the flexible wall for the steady flow of a Newtonian fluid in the 2D collapsible channel, at various values of the dimensionless membrane tension ratio α . Lines denote the result of the current FEM simulation, while the symbols are the reported results of Luo and Pedley [1995].

3.3 Results and Discussions

3.3.1 Code validation

We compare our prediction of membrane shapes for a Newtonian fluid to those of Luo and Pedley [1995] (a similar comparison was reported earlier in Xie and Pasquali [2003]). The difference between external p_e and outlet p_a pressures is one of the parameters that determines the velocity and stress fields in the channel [Luo and Pedley, 1995, 1996]. In Newtonian flow, our downstream boundary condition is equivalent to that used by Luo and Pedley [1995]; to allow direct comparison, we use the same downstream channel length as used by them.

Fig. 3.2 shows the profile of the membrane at different values of α . Our results are in excellent agreement with Luo and Pedley [1995]. Notably, Luo and Pedley [1995] reported that steady states could be computed directly only at high membrane tension—i.e., low $\alpha < 64$ at $Re = 1$ [Luo and Pedley, 1995]—whereas time dependent simulations were necessary to compute steady solutions at higher α (for sufficiently small Re) [Luo

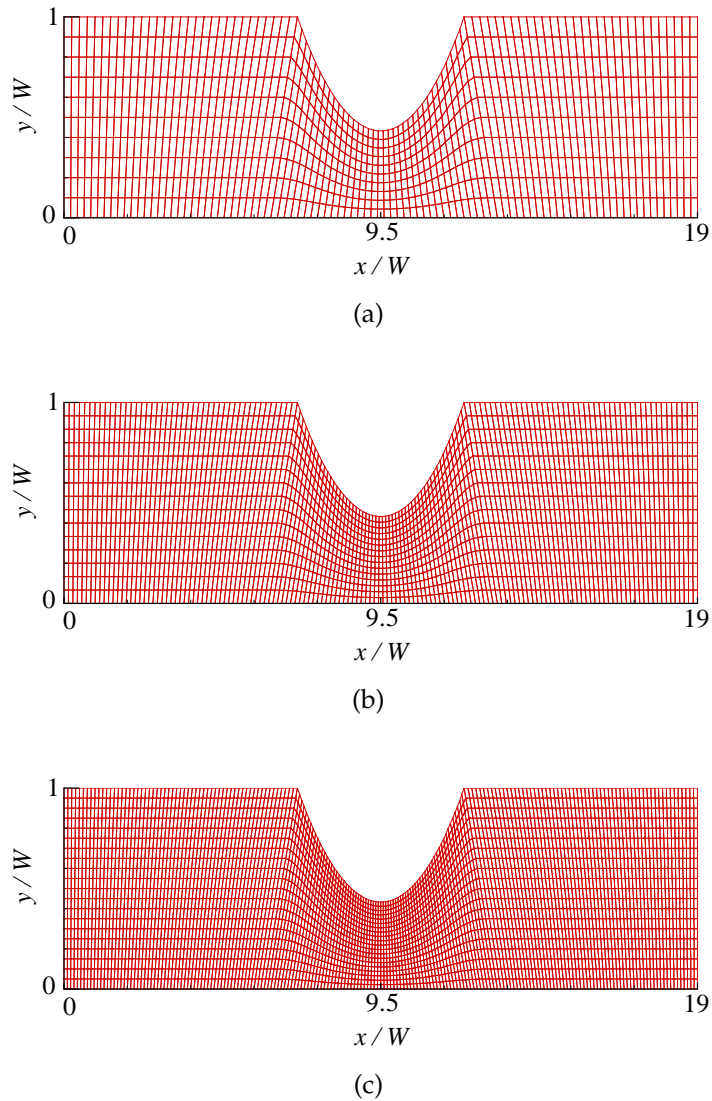


Figure 3.3: Meshes M1 (a), M2 (b) and M3 (c), considered in the current study.

and Pedley, 1996]. Our fully-coupled algorithm shows no such convergence limits at $Re = 1$; profiles for $\alpha = 100$ and 200 are displayed in Fig. 3.2. This demonstrates the robustness of the present simulation technique.

3.3.2 Mesh convergence and the limiting Weissenberg number

Viscoelastic flows are notoriously difficult to compute; therefore, here we study mesh convergence over a range of parameters, particularly to establish whether the collapsible channel flow suffers from the high Weissenberg number problem.

Computations are performed with three different meshes (M1, M2 and M3) (Fig. 3.3

Table 3.1: Meshes considered in the current study.

Mesh	Number of elements	Number of nodes	Degrees of freedom for fully coupled macroscopic simulations ($\mathbf{x}, \mathbf{v}, p, \mathbf{M}, \mathbf{L}$)
M1	950	4011	27342
M2	2145	8897	60455
M3	3800	15621	105972

and Table 3.1).

The invariants of the conformation dyadic, \mathbf{M} are a good indicator of mesh convergence; its eigenvalues m_i represent the square stretch ratios along the principal directions of stretching m_i for an ensemble of molecules [Pasquali and Scriven, 2002, 2004]. Previous studies of viscoelastic flows based on conformation tensor formulations of the Oldroyd-B and FENE-P models have shown that the breakdown of numerical computations coincides with the smallest eigenvalue becoming negative in some regions of the flow domain [Bajaj et al., 2008; Pasquali and Scriven, 2002]. There have been some recent developments where the problem of the lack of positive definiteness of \mathbf{M} have been addressed, and solutions proposed [Balci et al., 2011; Fattal and Kupferman, 2004, 2005; Lozinski and Owens, 2003]. However, in the present instance, since a conventional conformational tensor formulation has been used, we encounter numerical problems similar to those seen in earlier studies, as described in greater detail shortly.

Figs. 3.4 and 3.5 show the contour plots of the largest (m_3) and smallest (m_1) eigenvalues for the Oldroyd-B, FENE-P and Owens models, at $Wi = 0.1$ and $\alpha = 30$. They indicate that the molecules experience varying extents of stretching and contraction as they flow in the channel and below the collapsible wall. For all the models, the largest eigenvalue is highest below the collapsible wall at the minimum gap location (Fig. 3.4). (The magnitude varies from model to model). The smallest eigenvalue is positive everywhere in the flow domain (Fig. 3.5, $Wi = 0.1$).

Raising Wi yields higher maximum m_3 and lower minimum m_1 across the flow domain, as shown in Fig. 3.6 for the Owens model at $\alpha = 30$ and $\alpha = 45$. Whereas the maximum m_3 grows smoothly with Wi and results on various meshes overlap (Fig. 3.6 (b) and (d)), the plots of minimum m_1 show clearly the breakdown of each mesh (Fig. 3.6 (a) and (c)) Even though we have not carried out computations with a

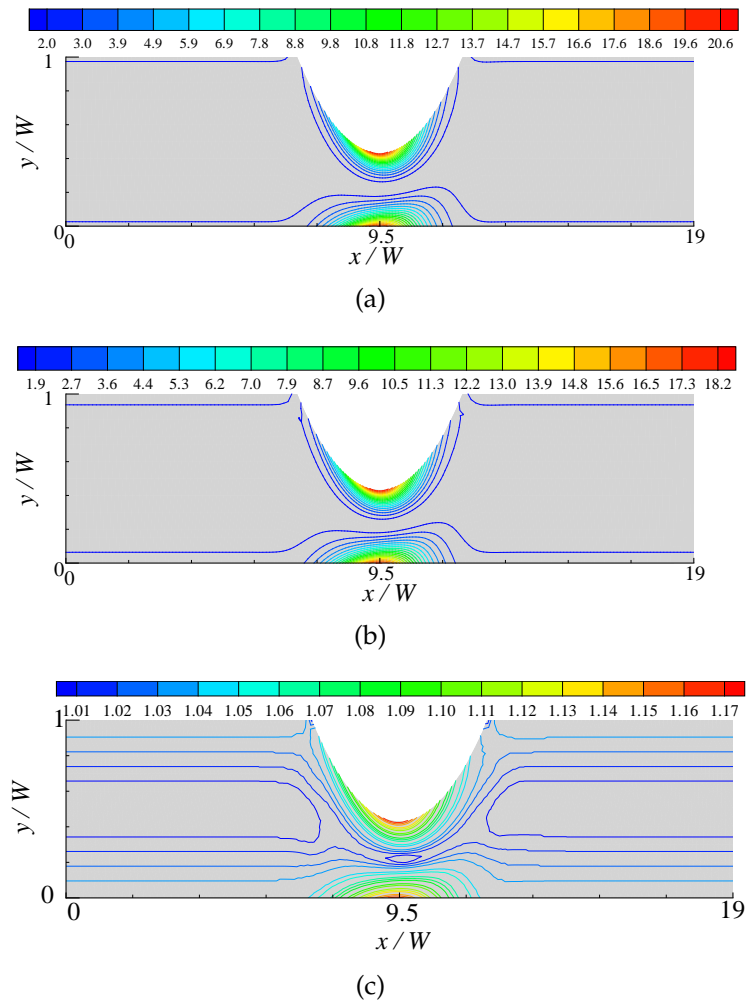


Figure 3.4: Contour plots of the largest eigenvalues (m_3) of the conformation tensor at $Wi = 0.1$ for: (a) Oldroyd-B, (b) FENE-P, and (c) Owens models, at a tension ratio $\alpha = 30$.

mesh finer than M3, the sudden change of slope of the curves in Fig. 3.6 (c) suggests that M3 mesh is yielding inaccurate results at $Wi \gtrsim 0.5$ at $\alpha = 45$. Unless otherwise specifically stated, all computations reported hereafter were performed on M3.

On any mesh, computations can be performed at Wi beyond the limit of mesh convergence, until a limiting Weissenberg number, beyond which computations fail because the minimum value of m_1 becomes negative (which is unphysical)—this is clearly visible in Fig. 3.6 (a) and (c). As has been observed in previous studies [Bajaj et al., 2008; Pasquali and Scriven, 2002], the maximum attainable value of Wi increases with mesh refinement; for example, in the Owens model at $\alpha = 45$, the limiting value of the Weissenberg number is $Wi = 0.75$ on M2 and $Wi = 0.9$ on M3. Fig. 3.6 (a) and (c) shows that the tension ratio affects the limiting Weissenberg number (because it affects

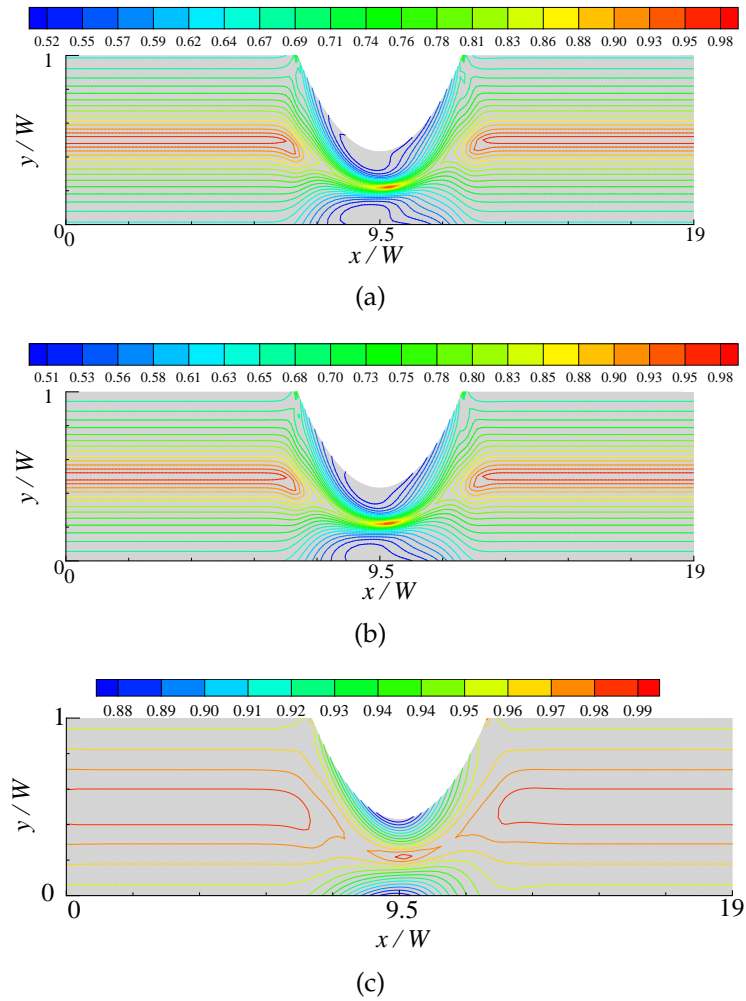


Figure 3.5: Contour plots of the smallest eigenvalues (m_1) of the conformation tensor at $Wi = 0.1$ for: (a) Oldroyd-B, (b) FENE-P, and (c) Owens models, at a tension ratio $\alpha = 30$.

the minimum gap); For the Owens model, the limiting Weissenberg number (on M3) decreases from $Wi = 7.0$ at $\alpha = 30$ to $Wi = 0.9$ at $\alpha = 45$.

The decrease of the minimum eigenvalue below zero coincides with a step increase in the maximum eigenvalue (Fig. 3.6 (b) and (d)). This value is much higher for $\alpha = 45$ than for $\alpha = 30$ because (as in the Newtonian case, Fig. 3.2) the minimum gap h decreases with increasing α , leading to a more dramatic “squeezing” of the fluid, and a consequently greater stretching of the molecules in the gap.

Computations with the Oldroyd-B and FENE-P models yield qualitatively similar behaviour; the limiting Wi values are reported in Table. 3.2 for $\alpha = 30$ and $\alpha = 45$.

Fig. 3.7 shows the dependence of the limiting Weissenberg number on the tension ratio for the three different fluid models. In general, the limiting Weissenberg numbers

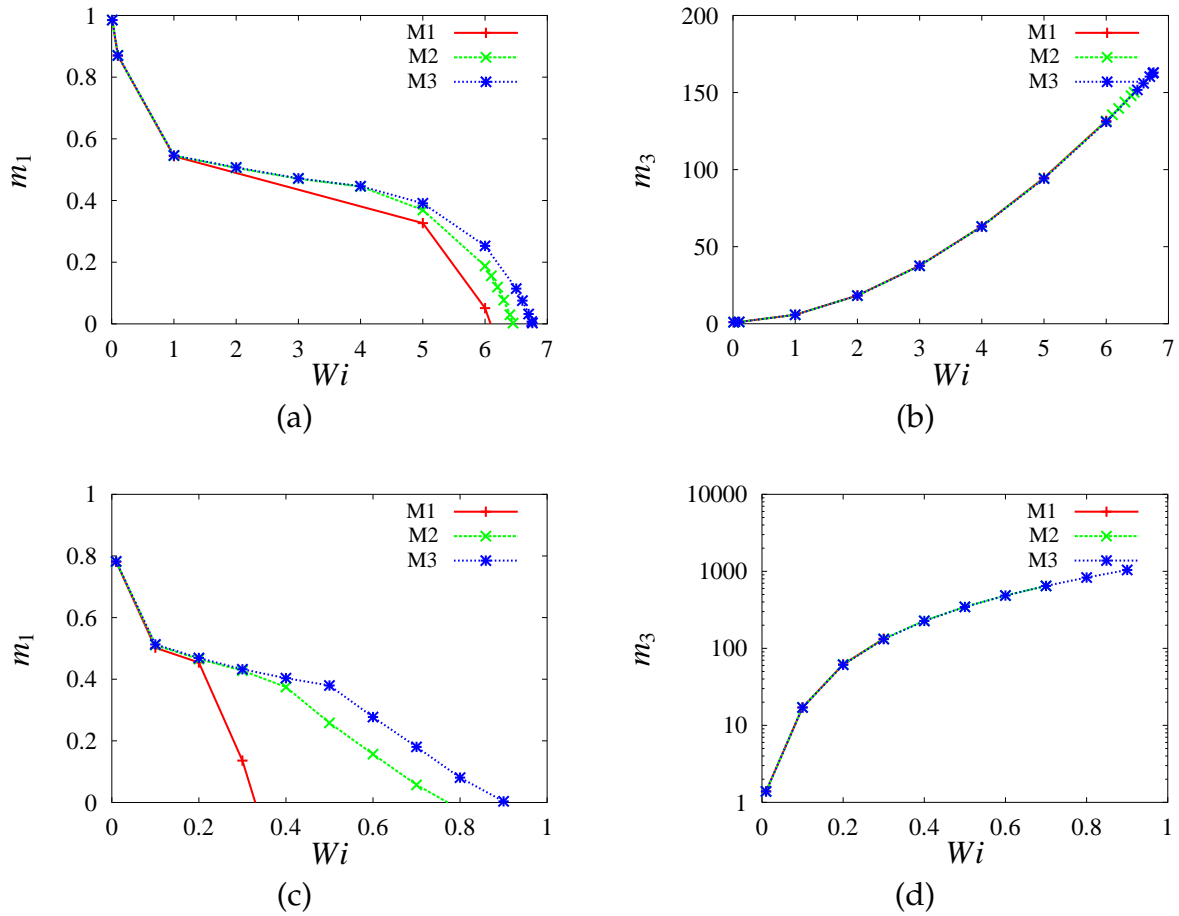


Figure 3.6: Maximum value of the largest eigenvalue (m_3) and minimum value of the smallest eigenvalue (m_1) in the entire flow domain, for the Owens model, as a function of Wi at two different values of tension ratio $\alpha = 30$ (a, b), and $\alpha = 45$ (c, d).

follow the trend Owens > FENE-P > Oldroyd-B until a tension ratio $\alpha \approx 50$, where there is an interesting crossover, and the limiting Weissenberg number for the Owens model becomes smaller than that for the FENE-P model.

Fig. 3.8 shows the profile of M_{xx} (mean streamwise molecular stretch) across the minimum gap at $\alpha = 45$ for a range of Weissenberg numbers and all three fluid models. Clearly, with increasing Wi , M_{xx} grows almost symmetrically, from a relatively low value in the middle of the gap, to a significantly larger value near the bottom (rigid) and top (flexible) walls. In the Oldroyd-B and Owens models, M_{xx} is unbounded. Conversely, the FENE-P model has an upper bound for the maximum M_{xx} , which

Table 3.2: Maximum mesh converged value of Wi , and the limiting Wi for the three fluid models, for computations carried out with the M2 and M3 meshes, at two values of α .

	$\alpha = 30$				$\alpha = 45$			
	Converged Wi		Limiting Wi		Converged Wi		Limiting Wi	
	M2	M3	M2	M3	M2	M3	M2	M3
Oldroyd-B	0.2	0.43	0.42	0.44	0.02	0.04	0.06	0.07
FENE-P	0.32	0.45	0.50	0.53	0.2	0.27	0.25	0.27
Owens	4.0	5.0	6.45	6.76	0.3	0.5	0.75	0.9

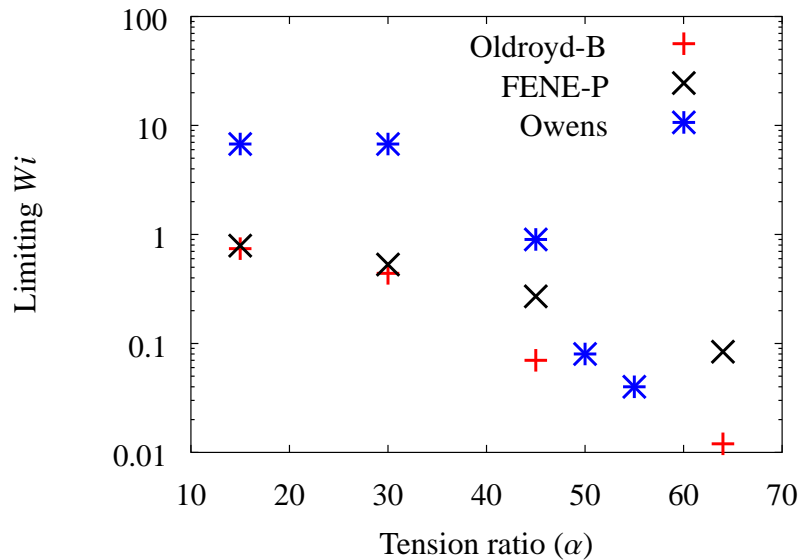


Figure 3.7: Limiting Weissenberg number for the Oldroyd-B, FENE-P and Owens models at different tension ratios α .

for $b_M = 100$ is 300. This upper bound for the FENE-P model limits the M_{xx} cross-stream gradient near the walls; such saturation is not present in the M_{xx} profiles for the Oldroyd-B and Owens models, which display steep gradients near the walls. Interestingly, of the three fluid models, the FENE-P model shows the highest stretch in the center of the gap.

Before examining the effect of fluid behaviour on flow characteristics, it is important to note that both the Oldroyd-B and Owens models predict an unbounded conformation tensor and extensional viscosity in a steady, homogeneous extensional flow, whereas

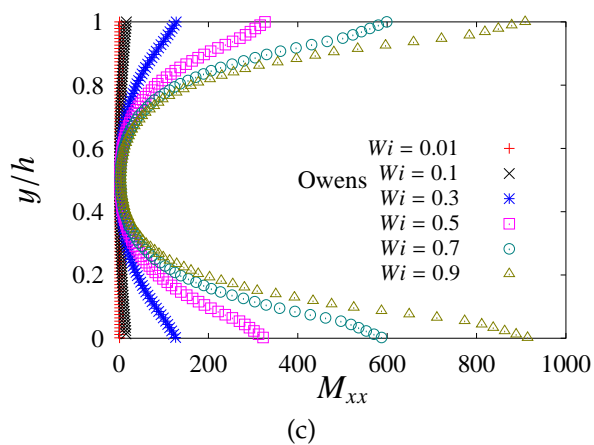
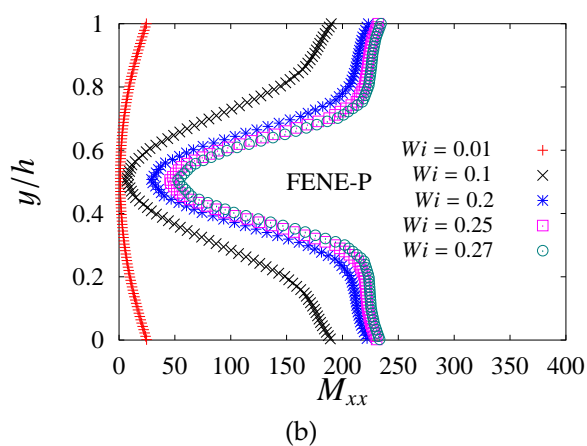
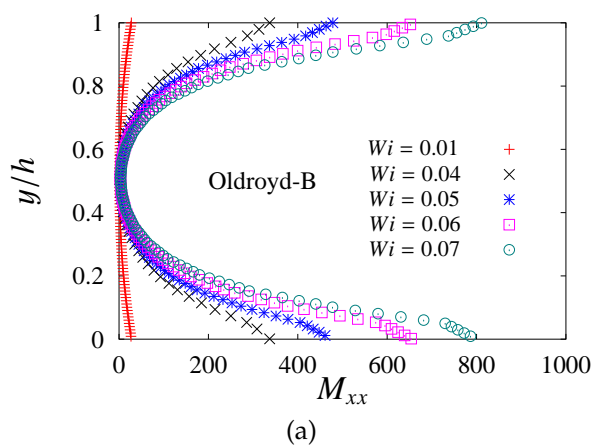


Figure 3.8: Profile of M_{xx} across the narrowest channel gap for the Oldroyd-B, FENE-P and Owens models, for a range of Weissenberg numbers, at $\alpha = 45$. The distance from the bottom channel is scaled by the narrowest gap width h of the particular model.

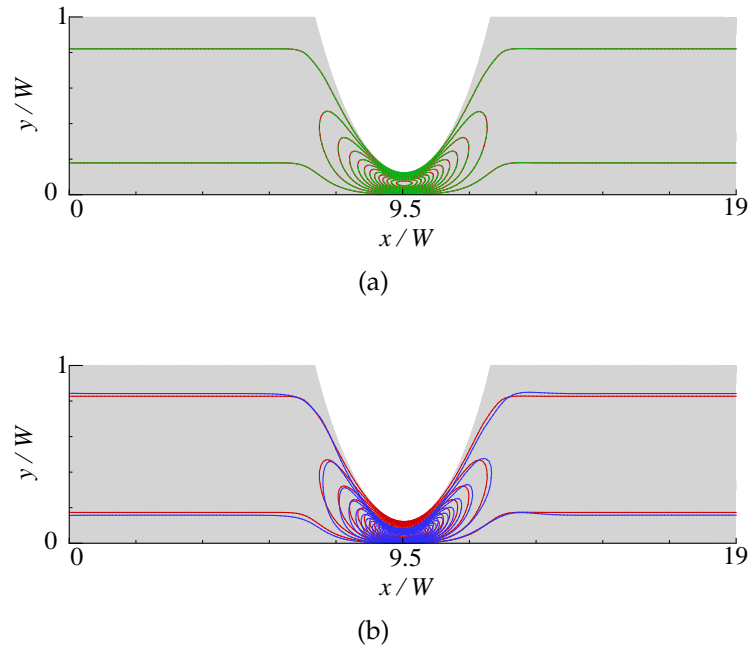


Figure 3.9: Contours of axial velocity (v_x) in the flow domain, for (a) Newtonian (red), Oldroyd-B (green) and FENE-P (blue) fluids, and (b) Newtonian (red) and Owens (blue) fluids, at $Wi = 0.01$ and $\alpha = 45$.

the FENE-P model has a bound on these quantities. Moreover, the Oldroyd-B model predicts constant viscosity in steady shear flow, whereas the FENE-P and Owens models are shear thinning.

3.3.3 Velocity fields and molecular shear and extension rates

Fig. 3.9 compares the velocity contours predicted for a Newtonian fluid with the contours predicted for the Oldroyd-B, FENE-P and Owens model fluids at $Wi = 0.01$ and $\alpha = 45$. While the fields for the Newtonian, Oldroyd-B and FENE-P fluids do not differ to any significant degree from each other at this value of Wi (Fig. 3.9 (a)), the velocity profile for the Owens model displays a slight difference from the Newtonian profile (Fig. 3.9 (b)). Interestingly, this apparently slight difference in the velocity field between the different models becomes greatly amplified when viewed from the perspective of *molecular* deformation rates, as elaborated below.

Arguing that the invariants of the rate of strain cannot serve as indicators of the type of flow because they do not carry any information on whether molecules are being strained persistently along the same axes, or are rotating with respect to the

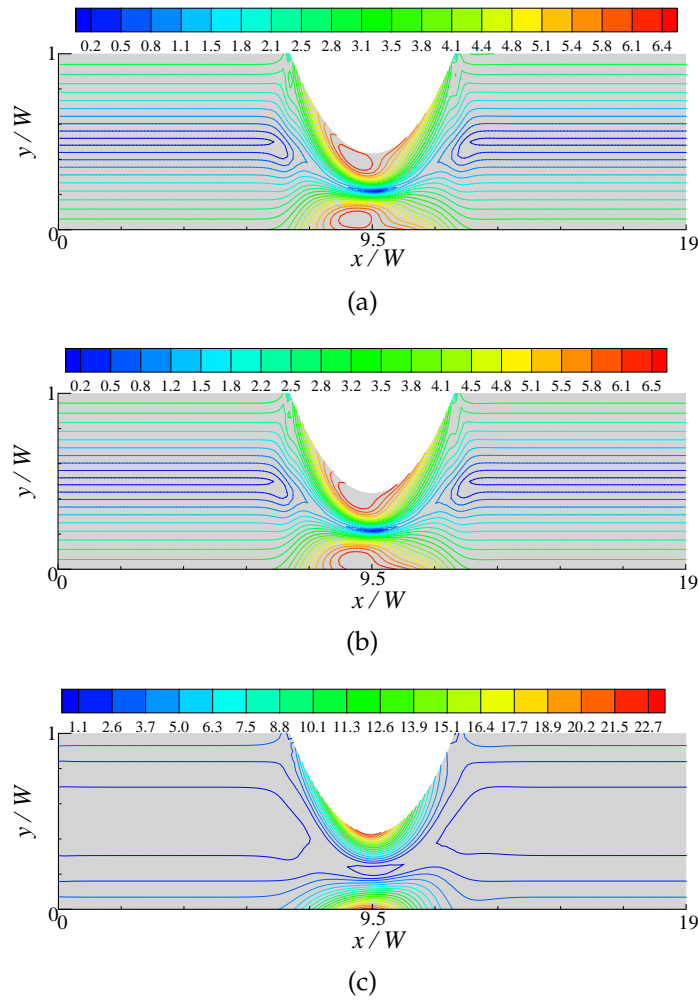


Figure 3.10: Molecular extension rate $\dot{\epsilon}_M$ for (a) Oldroyd-B, (b) FENE-P, and (c) Owens models, at $Wi = 0.1$ and $\alpha = 30$.

principal axes of the rate of strain, Pasquali and Scriven [2004] introduced the molecular extension and shear rates as being more appropriate measures for obtaining insight into the coupling between the flow and molecular behaviour. These deformation rates are defined as,

$$\dot{\epsilon}_M \equiv \mathbf{m}_3 \mathbf{m}_3 : \mathbf{D} \quad \text{and} \quad \dot{\gamma}_M = | \mathbf{m}_1 \mathbf{m}_3 : \mathbf{D} | \quad (3.4)$$

where, $\dot{\epsilon}_M$ is the mean ensemble molecular extension rate, $\dot{\gamma}_M$ is the mean ensemble molecular shear rate, and, as mentioned earlier, the eigenvectors \mathbf{m}_3 and \mathbf{m}_1 are associated with the largest and smallest eigenvalue of \mathbf{M} , respectively. In regions of flow where $\dot{\epsilon}_M > 0$, molecular segments are being stretched along their direction of preferred stretch and orientation and the flow is working against the molecular relaxation processes. On the other hand, a large $\dot{\gamma}_M$ indicates that the rate of strain is

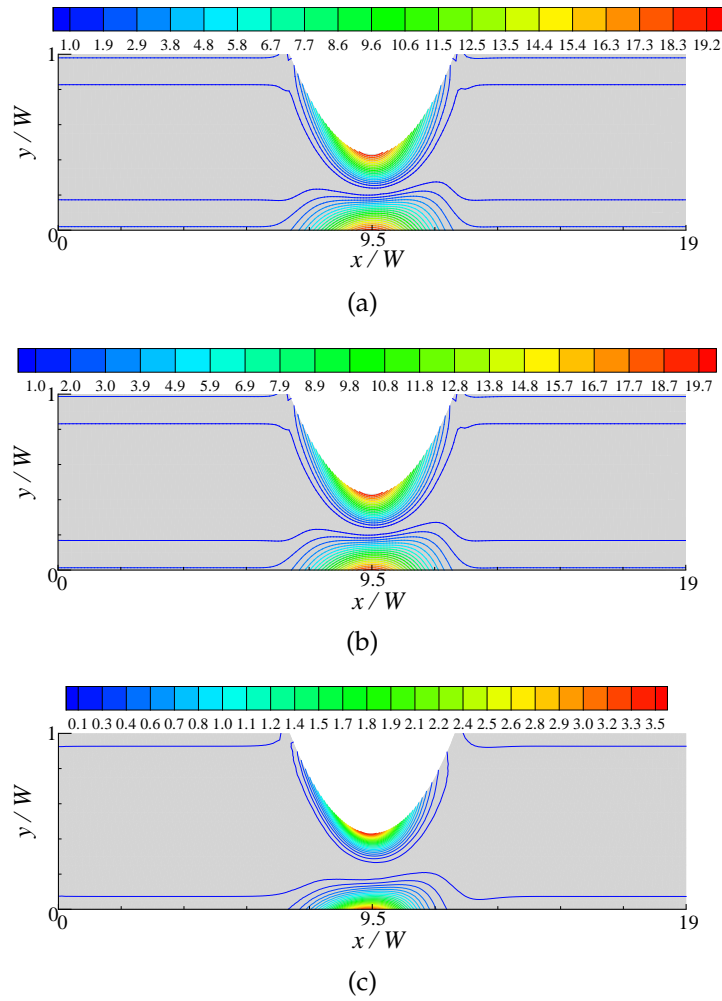


Figure 3.11: Molecular shear rate $\dot{\gamma}_M$ for (a) Oldroyd-B, (b) FENE-P, and (c) Owens models, at $Wi = 0.1$ and $\alpha = 30$.

deforming molecules aligned along one of the principal directions of the conformation tensor, in a direction orthogonal to their orientation.

Figs. 3.10 and 3.11 display contours of molecular extension and shear rate for the Oldroyd-B, FENE-P and Owens fluids at $\alpha = 30$ and $Wi = 0.1$. Fig. 3.10 indicates that $\dot{\epsilon}_M$ is of the same order of magnitude for the Oldroyd-B and FENE-P models, and the contour lines appear similar to each other. However, both the contours and the maximum value for the Owens model are significantly different, with the maximum value being greater by roughly a factor of 3. With regard to $\dot{\gamma}_M$, on the other hand, while the contour lines are similar in all the fluid models, the maximum values for the Oldroyd-B and FENE-P models are roughly greater than that for the Owens model by a factor of 6 (Fig. 3.11).

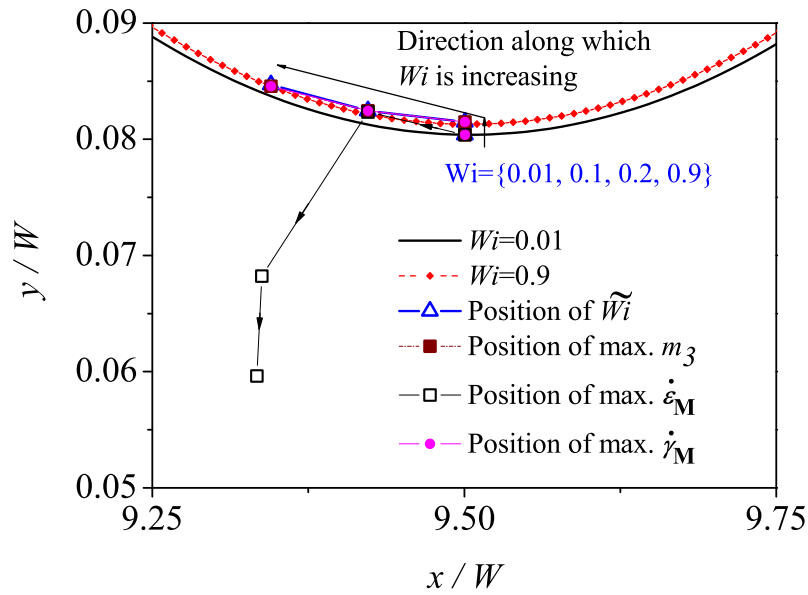


Figure 3.12: Locations of the maximum eigenvalue m_3 , the maximum molecular shear and extension rates $\dot{\gamma}_M$ and $\dot{\epsilon}_M$, and the maximum local Weissenberg number \tilde{Wi} , for the Owens model, at $\alpha = 45$, for various values of the Weissenberg number Wi . Curved lines indicate the shape of the flexible membrane at the lowest and highest value of Wi .

A comparison of the contour lines for the largest eigenvalue m_3 (displayed in Fig. 3.4) with the contour lines for $\dot{\gamma}_M$ (Fig. 3.11), suggests a strong correlation between the two sets of figures. Indeed, the ordering of the magnitudes between the three models, with the values for the Oldroyd-B and FENE-P models being greater than that for the Owens model, is similar in both figures. A more detailed examination of this correlation is afforded by Fig. 3.12, which shows the location of the maximum values of m_3 , $\dot{\gamma}_M$, $\dot{\epsilon}_M$, and the local Weissenberg number \tilde{Wi} , for the Owens model at $\alpha = 45$, for a range of Wi . For all values of the Weissenberg number, the maximum values of m_3 , $\dot{\gamma}_M$ and \tilde{Wi} coincide with each other, and are located just below the collapsible channel, as suggested by the contour lines in Fig. 3.4 and Fig. 3.11 for the former two variables. Note that the location appears to move slightly upstream with increasing Wi . On the other hand, the location of the maximum value of $\dot{\epsilon}_M$ starts close to the

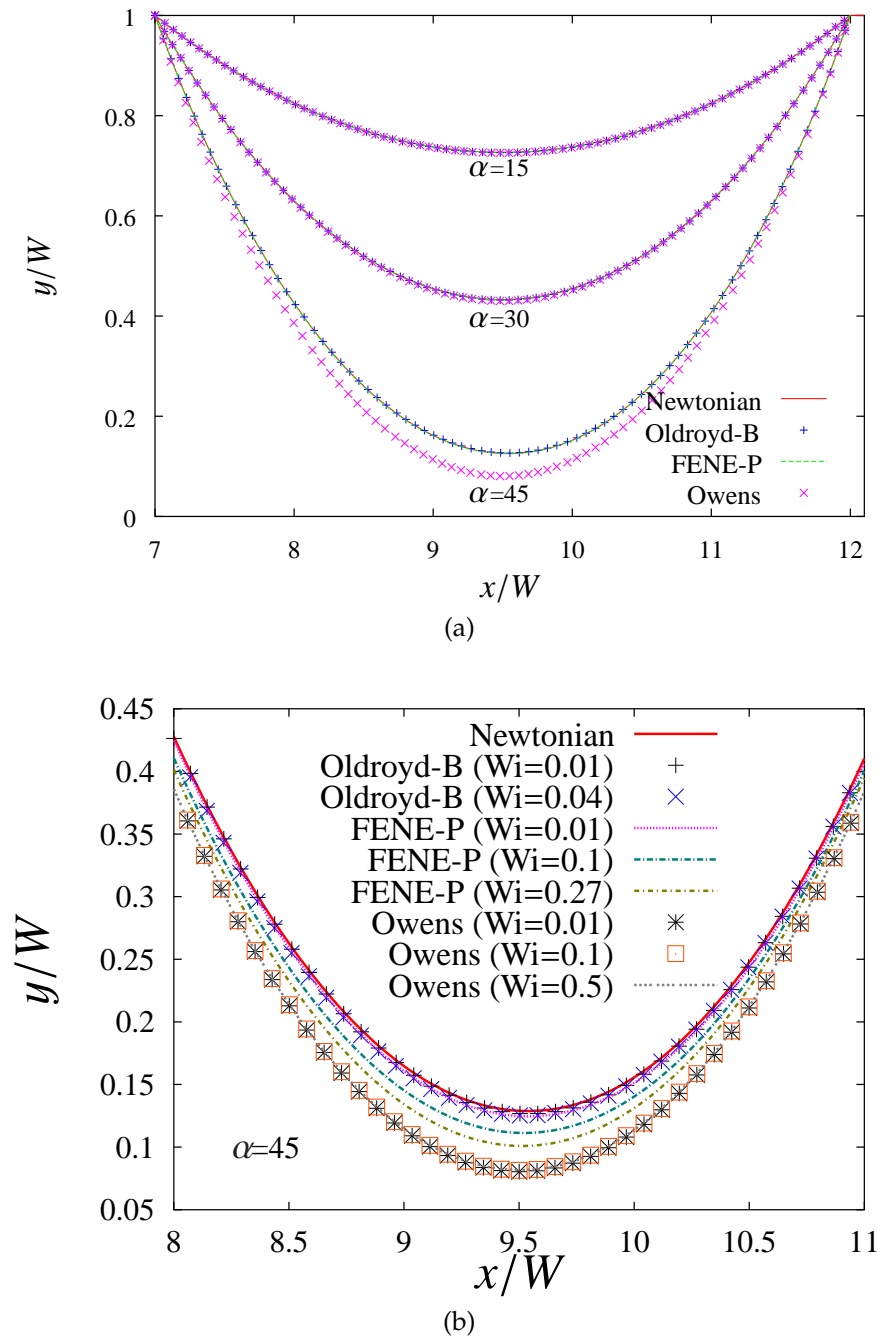


Figure 3.13: The deformed shape of the flexible wall for the steady flow of Oldroyd-B, FENE-P and Owens model fluids in a 2D collapsible channel, compared with the profile for a Newtonian fluid, with $Re = 1.0$ and $\beta = 0.0071$, at (a) various values of α for $Wi = 0.01$, and (b) various values of Wi for $\alpha = 45$.

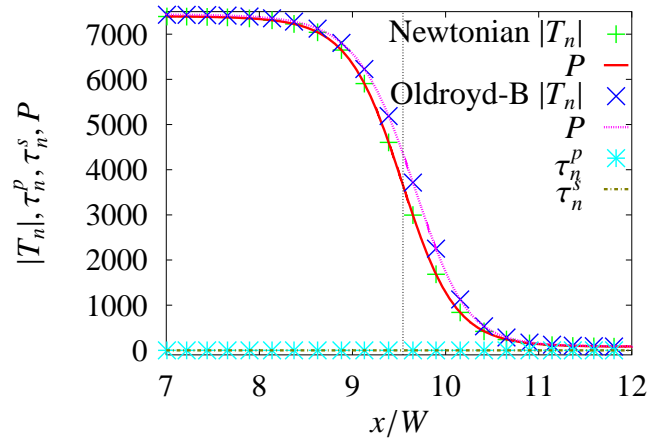
bottom of the collapsible membrane for small values of Wi , but moves away towards the bulk flow with increasing Wi . It seems that it is the maximum molecular shear rate below the collapsible membrane rather than the maximum molecular extension rate that determines the magnitude of the largest eigenvalue.

It is appropriate here to revisit Fig. 3.6 (b) and (d) to note the change in the shape of the m_3 versus Wi curve with an increase in α from 30 to 45. While at $\alpha = 30$ the slope of the curve *increases* with increasing Wi , the slope *decreases* with increasing Wi at $\alpha = 45$. The value of m_3 also appears to be levelling off in the latter case. In their examination of the slot coating flow of a viscoelastic fluid, Bajaj et al. [2008] also observed that the maximum m_3 versus Wi curve changes slope and goes through an inflection point with increasing Wi . In that context, it was found that the shape change was related to the fact that the location of the maximum eigenvalue changed from being near a shear-dominated region adjacent to the moving web supporting and transporting the fluid, to being near the extension-dominated region just below the free-surface. In the present instance however, the maximum eigenvalue always appears to be located just below the deformable membrane for all the values of α that we have examined, and coincides with the location of $\dot{\gamma}_M$, as has been demonstrated by Fig. 3.12.

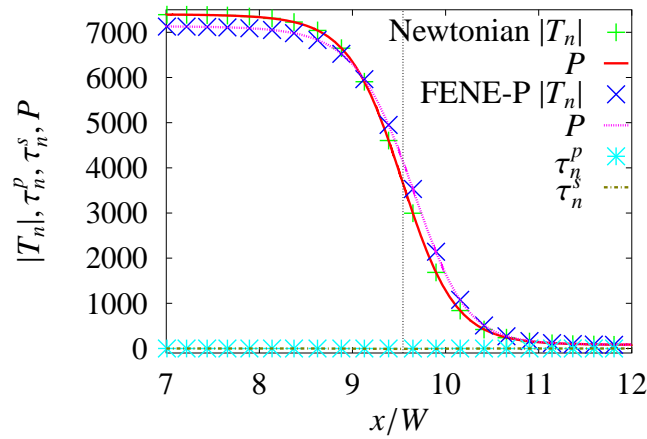
3.3.4 Flexible membrane shape, and pressure and stress fields

In the remainder of this work, we focus our attention on examining the influence of the Weissenberg number Wi and the tension ratio α on the shape of the membrane, and on stress and conformation tensor fields in the channel, for the fixed values of the viscosity ratio β , the transmural pressure P_d , and Reynolds number Re , that have been adopted here. We start by examining the dependence of the shape of the channel on Wi and α , for each of the three viscoelastic fluids, and subsequently attempt to explain the origin of the observed dependence.

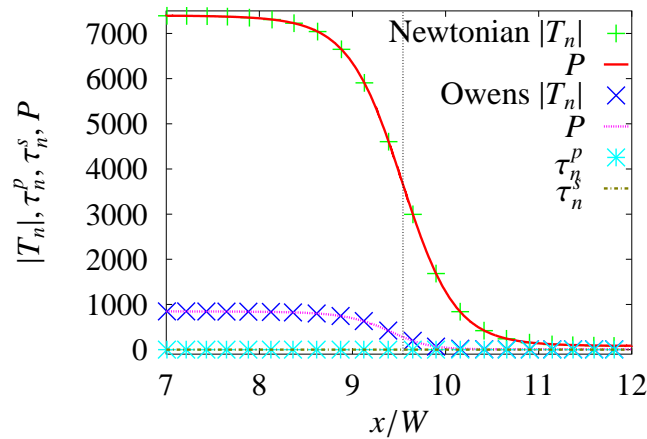
Fig. 3.13 (a) displays the shape of the flexible wall, for the three fluid models, at various values of α , for a fixed value of $Wi = 0.01$, and Fig. 3.13 (b) is a zoomed in view of the membrane shape close to the centre of the membrane, for the three fluids, at various values of Wi , for a fixed value of $\alpha = 45$. It is clear from Fig. 3.13 (a) that on the scale of the figure, the shape of the membrane for the Oldroyd-B and FENE-P models is indistinguishable from the shape of the membrane for a Newtonian fluid at all three values of α ($= 15, 30$ and 45). On the other hand, the shape of the membrane for the Owens model, in the neighbourhood of the centre of the membrane, becomes



(a)



(b)



(c)

Figure 3.14: Pressure and normal components of stress on the flexible wall for the Newtonian, Oldroyd-B, FENE-P and Owens models at $\alpha = 45$ and $Wi = 0.01$, with $Re = 1.0$ and $\beta = 0.0071$. T_n is the normal component of total stress, P is the pressure, τ_n^s is the normal component of viscous stress and τ_n^p is the normal component of elastic stress.

clearly distinguishable from that for a Newtonian fluid at $\alpha = 45$. For each of the three fluid models, the curve corresponding to $Wi = 0.01$ in Fig. 3.13 (b) is the same as that in Fig. 3.13 (a) for $\alpha = 45$. In the case of the Owens model, since the curves for $Wi = 0.1$ and $Wi = 0.5$ coincide with the curve for $Wi = 0.01$, it is clear that the Weissenberg number has negligible influence on the shape of the membrane. While there appears to be a slight change in the shape of the membrane for the Oldroyd-B fluid, the most significant change occurs for the FENE-P model, with the shape approaching that for the Owens model with increasing Weissenberg number. From the nature of the boundary condition on the flexible membrane adopted here (Eq. 3.1), it is clear that the only reason the membrane can change shape as a result of changing either α or Wi is due to a change in the normal stress acting on the membrane. In the present formulation, the shear stress has no influence on membrane shape. It is reasonable therefore to examine the normal stress field on the flexible membrane in order to find the cause of the change (or lack thereof) in the shape of the membrane for the three fluids.

Fig. 3.14 (a)-(c) shows plots of the total non-dimensional normal stress (T_n), and the individual contributions of the non-dimensional pressure (P), the non-dimensional viscous normal stress (τ_n^s), and the non-dimensional elastic normal stress (τ_n^p), for the three viscoelastic fluids, on the flexible membrane as a function of distance along the membrane. The pressure and viscous normal stress for a Newtonian fluid is also displayed on each subfigure for the purpose of comparison. The vertical line indicates the midpoint of the collapsible membrane ($9.5W$), which is the location of the narrowest channel gap for most of the cases. It is immediately apparent that the only contribution to the normal stress is the pressure, since both τ_n^s and τ_n^p are identically zero for all the fluids. This result is entirely consistent with the analytical result derived by Patankar et al. [2002] that any incompressible fluid with a constitutive model of the following form,

$$a_1 \mathbf{D} + a_2 \overset{\vee}{\mathbf{D}} + a_3 \mathbf{T} + a_4 \overset{\vee}{\mathbf{T}} = \mathbf{0} \quad (3.5)$$

will have a zero normal component of extra stress on a rigid body surface. Here, a_1 , a_2 , a_3 , and a_4 are constants or some scalar functions of the invariants of \mathbf{D} and \mathbf{T} , and $\overset{\vee}{\mathbf{D}}$ and $\overset{\vee}{\mathbf{T}}$ represent the upper convected time derivatives of \mathbf{D} and \mathbf{T} . It can be shown that all the viscoelastic fluids considered here belong to the class of fluids described by Eq. (5.15). Since the shape of the flexible membrane is entirely determined by the normal force acting on it, the consequence of zero normal components of extra stress is that only differences in the predictions of pressure on the membrane between one

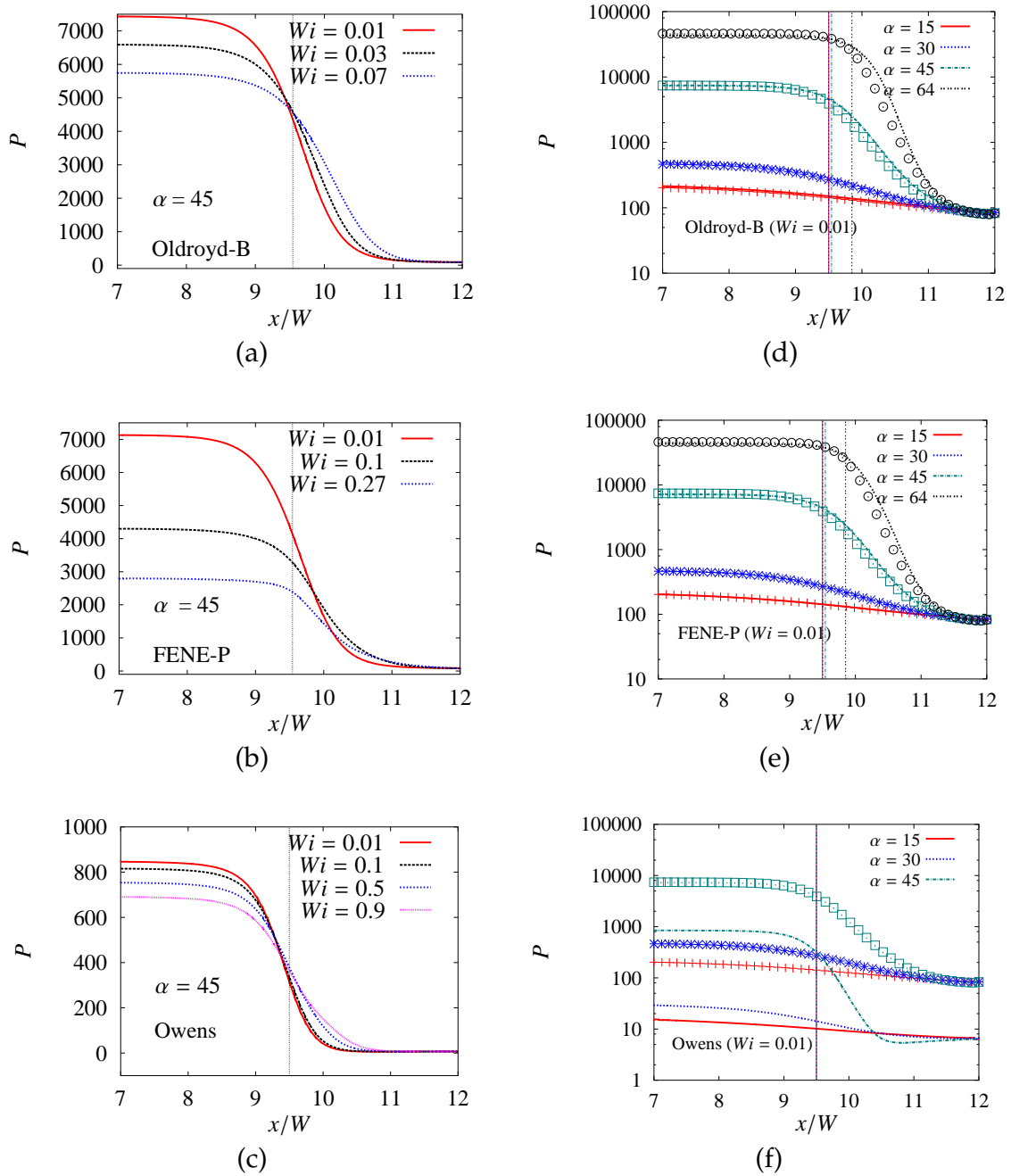


Figure 3.15: Dependence of the pressure profile along the flexible membrane on Wi and α , for the Oldroyd-B ((a) and (d)), FENE-P ((b) and (e)) and Owens models ((c) and (f)), respectively. The symbols in (d)–(f) are for a Newtonian fluid. Note that $\alpha = 45$ in (a)–(c) and $Wi = 0.01$ in (d)–(f). All other parameters are as in Fig. 3.14.

model and another are responsible for any differences in the prediction of the shape of the membrane. Clearly, at $\alpha = 45$, the pressure exerted by the Oldroyd-B and FENE-P fluids along the membrane is nearly identical to that exerted by a Newtonian fluid, while the pressure exerted by an Owens model fluid is significantly lower. This difference is responsible for the difference observed earlier in the predicted membrane shape in Fig. 3.13 (a). The origin of the pressure difference predicted by the different models is examined in greater detail after first discussing the results in Fig. 3.15.

The two sets of plots in Fig. 3.15 display the dependence of the pressure profile on Wi and α for all the three viscoelastic fluids. From Fig. 3.15 (a)–(c) it can be seen that an increase in Wi leads to a decrease in the pressure upstream of the narrowest gap in the channel, while causing a modest increase in the pressure downstream of the narrowest gap. In each of the subfigures, data is presented until the limiting Weissenberg number for the respective model. Fig. 3.15 (d)–(f) reveals that the pressure increases uniformly across the entire channel with an increase in α . Both the Oldroyd-B and FENE-P fluids closely mirror the increase in pressure observed for a Newtonian fluid (represented by the symbols). On the other hand, as seen earlier in Fig. 3.14 (c), the pressure prediction in the Owens model is below the Newtonian value at all values of α . The increase in pressure is not surprising since the narrowest channel gap decreases with increasing α (see Fig. 3.13 (b)). Note that results are reported in Fig. 3.15 (f) for the Owens model for a maximum value of $\alpha = 45$. This is discussed further subsequently.

We now examine the possible origin of the differences in the prediction of pressure by the different models. Since the Oldroyd-B and the FENE-P models predictions of pressure are close to that for a Newtonian fluid at $Wi = 0.01$, it can be conjectured that the elasticity of the fluid accounted for by these two models does not play a significant role in determining the pressure. Since the Owens model at the same value of Wi predicts a significantly lower pressure, it seems reasonable to expect that the shear thinning behaviour of the Owens model is the source of this difference. In order to examine this hypothesis further, we have plotted in Fig. 3.16 (a), the FENE-P and Owens models predictions of the microstructure's contribution to viscosity (η_p) as a function of the local Weissenberg number \widetilde{Wi} , in a steady shear flow, at a constant value of λ_0 . For the values of U_0 and W chosen here, this value of λ_0 corresponds to an inlet Weissenberg number of 0.1. The dependence of η_p on $\dot{\gamma}$ for a FENE-P model in steady shear flow has been derived previously [Bird et al., 1987b].

For the Owens model, the dependence of η_p on $\dot{\gamma}$ in steady shear flow is given by Eq. (2.12). Since the parameters in the Cross model are fixed for all the computations

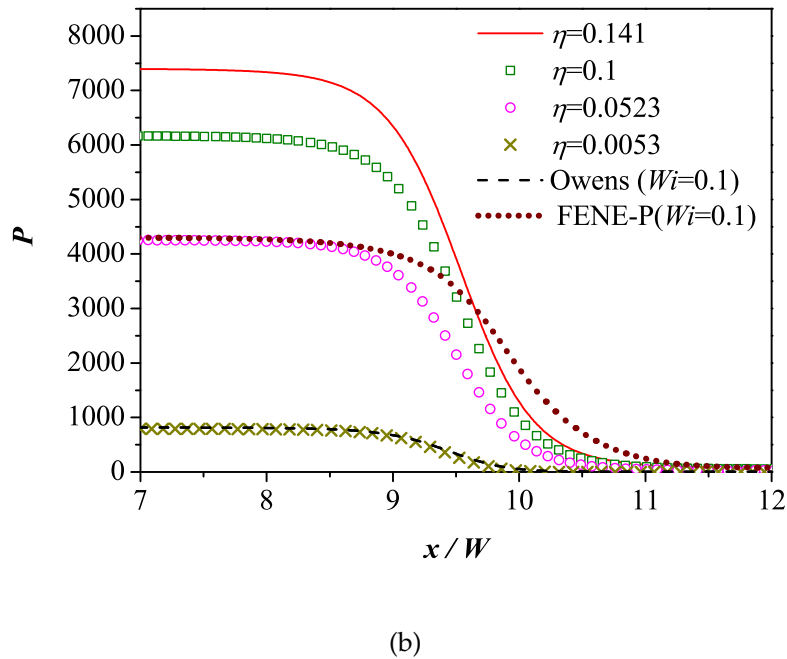
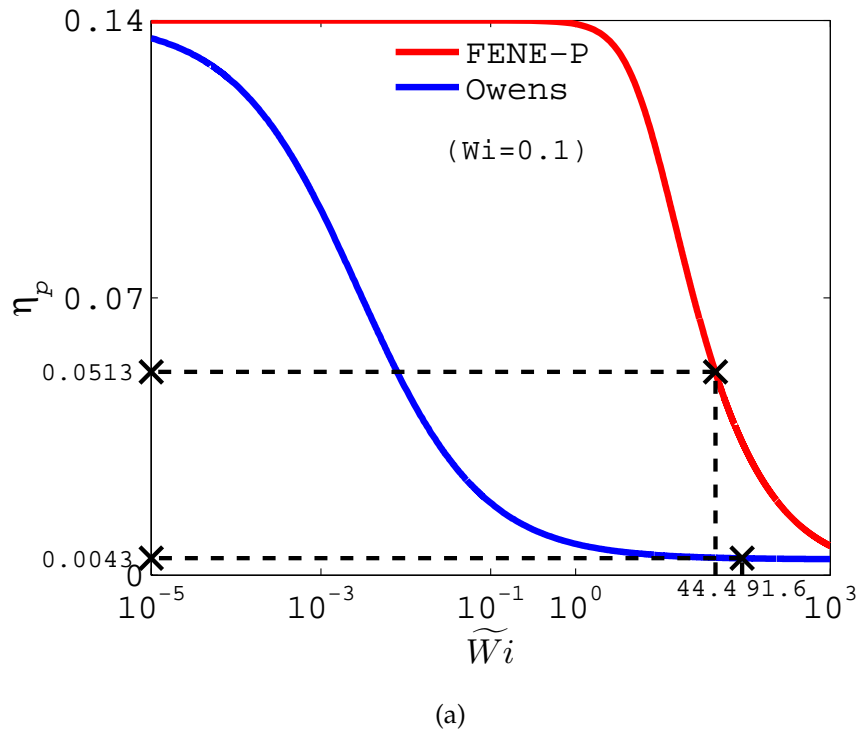
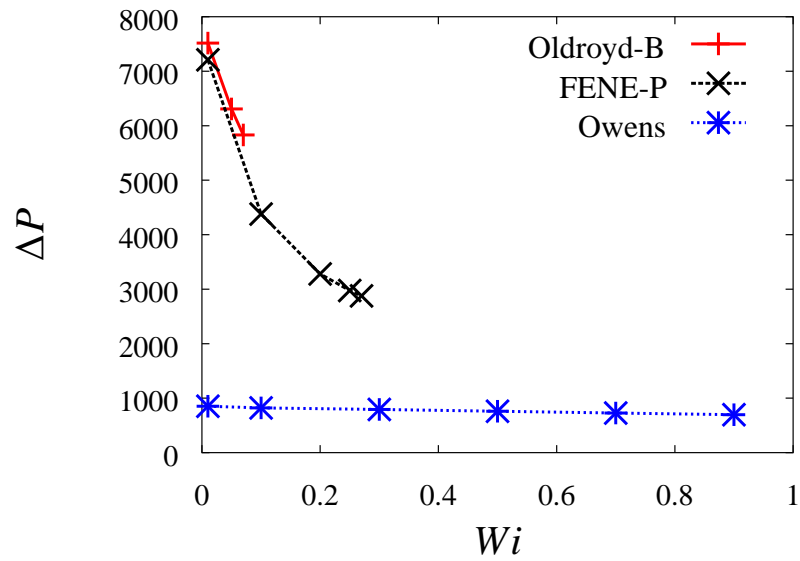
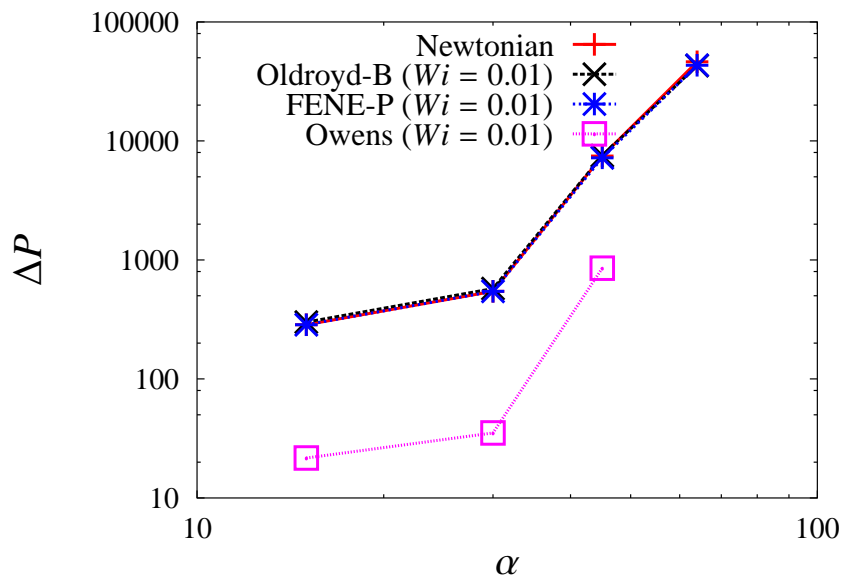


Figure 3.16: (a) The contribution of the microstructure to the total viscosity, η_p , for the Owens model and FENE-P fluids in steady shear flow as a function of local Weissenberg number \widetilde{Wi} , at a constant value of the relaxation time λ_0 . (b) Pressure profile along the flexible membrane for Newtonian fluids with a range of viscosities. The profiles for an Owens model fluid and a FENE-P fluid, with $Wi = 0.1$ and $\alpha = 45$, are also displayed.



(a)



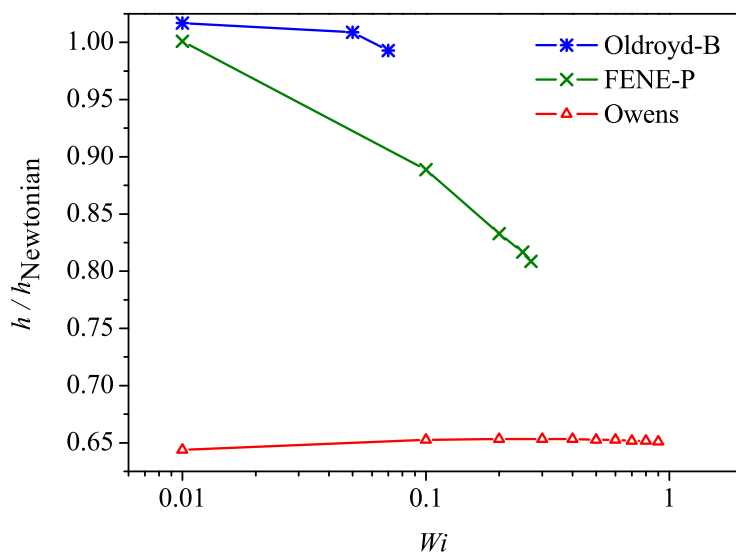
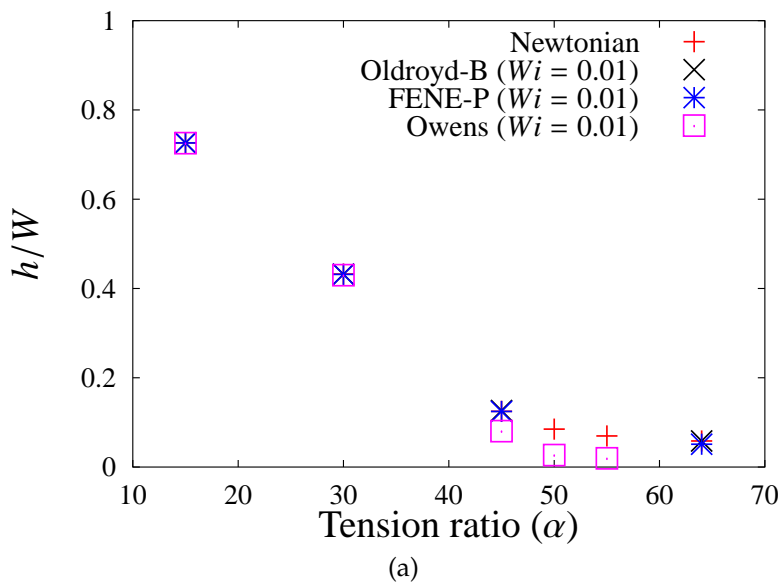
(b)

Figure 3.17: (a) Pressure drop ΔP in the channel for the Oldroyd-B, FENE-P and Owens models at different Wi , for $\alpha = 45$, $Re = 1.0$ and $\beta = 0.0071$. Note that for a Newtonian fluid, $\Delta P = 7474.0$. The curves terminate at the limiting Weissenberg number for each model. (b) Dependence of pressure drop on tension ratio for the three viscoelastic fluids, at $Wi = 0.01$, compared to the dependence of ΔP on α for a Newtonian fluid.

carried out here, the functional dependence of η_p on $\dot{\gamma}$ is the same in all the cases considered here. However, since the profile in Fig. 3.16 (a) for the Owens model is plotted as a function of the local Weissenberg number \widetilde{Wi} , it will vary for different values of λ_0 .

For the parameters in the Owens model adopted here (chosen by Owens [Owens, 2006] to get agreement with the experimental results of Bureau et al. [1980]), it is clear from Fig. 3.16 (a) that the onset of shear thinning occurs at really small values of \widetilde{Wi} . If shear thinning is the sole cause for the reduced prediction of pressure on the membrane in a channel flow, then a Newtonian fluid with viscosity equal to the effective viscosity in the Owens model, would predict the same value of pressure as the Owens model. By scanning the flow field in the channel, the maximum value of $\widetilde{Wi} = \lambda_0 \dot{\gamma}$ (which occurs just below the collapsible membrane) for an inlet Weissenberg number $Wi = 0.1$ and $\alpha = 45$, was found to be $\widetilde{Wi} = 91.6$. As indicated in Fig. 3.16 (a) for the Owens model, this corresponds to a reduced viscosity of $\eta_p = 0.0043$ at the location of the maximum shear rate. In Fig. 3.16 (b), the pressure profile along the flexible membrane predicted by the Owens model at $Wi = 0.1$ and $\alpha = 45$, has been compared with pressure profiles predicted for Newtonian fluids with a wide range of viscosity values. Of these, the profile for a Newtonian fluid with a viscosity $\eta_0 = \eta_p + \eta_s = 0.0043 + 0.001 = 0.0053$ Pa s is nearly identical to that for the Owens model, strongly supporting the validity of our hypothesis. Fig. 3.16 (a) indicates that even the FENE-P fluid suffers considerable shear thinning at $Wi = 0.1$. By following a procedure similar to that for the Owens model, we find that the maximum value of \widetilde{Wi} , at $Wi = 0.1$ and $\alpha = 45$, for a FENE-P fluid flowing in the channel is 44.4. This corresponds to $\eta_p = 0.0513$. As can be seen in Fig. 3.16 (b), the pressure profile on the flexible membrane for a Newtonian fluid with $\eta_0 = 0.0523$ is fairly similar to that for a FENE-P fluid. In particular, the value for the maximum pressure on the membrane is nearly identical.

The identification of shear thinning as the main factor responsible for the predicted pressure profile is also helpful in understanding the dependence of the pressure drop ΔP in the channel, on the inlet Weissenberg number, depicted in Fig. 3.17 (a). (Note that the curves terminate at the limiting Wi for each model). Clearly, the lack of any change in the pressure drop with Wi for an Owens model fluid is related to the fact that at these Weissenberg numbers, nearly all the shear thinning that can occur has occurred, and there is consequently no change in the viscosity with increasing Wi . The fairly rapid decrease in pressure drop for a FENE-P fluid is related to the significant shear thinning that sets in at Weissenberg numbers greater than 0.1 (which correspond to



(b)

Figure 3.18: Dependence of the narrowest channel gap h on: (a) α , and (b) Wi . The narrowest gap is scaled by the channel width W in (a), and by the gap for a Newtonian fluid in (b). Note that $\alpha = 45$ in (b).

$\widetilde{Wi} \geq 1$). Interestingly, the modest decrease in ΔP with increasing Wi observed for the Oldroyd-B fluid must be attributed to the fluid's elasticity, since the Oldroyd-B fluid does not shear thin. Unfortunately, the breakdown of the Oldroyd-B model at very low values of Wi prevents a more thorough examination of the dependence of ΔP on Wi . It is worth noting that the dependence of membrane shape on Wi observed earlier in Fig. 3.13 (b), namely, the lack of change in membrane shape for the Owens model, and the significant change in shape for the FENE-P model, can also be understood in the context of the shear thinning behaviour of these two fluids. The increase in ΔP with α displayed in Fig. 3.17 (b) is clearly the result of the narrowing of the channel gap with increasing α . The coincidence of the curves for the Oldroyd-B and FENE-P fluids with that for a Newtonian fluid is because the viscosities of these fluids are nearly identical at $Wi = 0.01$.

The dependence on α of the narrowest channel gap (scaled by the width of the channel) predicted for the three viscoelastic models, is compared with that for a Newtonian fluid in Fig. 3.18 (a). The rate at which the narrowest gap decreases with increasing α appears to slow down for $\alpha \geq 50$ in the case of Newtonian, Oldroyd-B and FENE-P models. While the behaviour of the Owens model coincides with that of the other fluids until approximately $\alpha = 45$, the gap continues to decrease until it becomes extremely narrow. Indeed, the gap becomes so small for $\alpha \geq 50$ that we have been unable to compute the shape of the membrane for any values of $\alpha > 55$. On the other hand, no difficulty was encountered in computing the membrane shape for the Oldroyd-B and FENE-P models for all the values of α explored here (up to $\alpha = 64$). The difficulty of numerically solving the Owens model for $\alpha \geq 50$ is the likely cause for the change in the dependence of the limiting Weissenberg number on α , observed earlier at these values of α in Fig. 3.7. In Fig. 3.18 (b), the dependence on Wi of the narrowest channel gap scaled by the value of the gap for a Newtonian fluid, $h/h_{\text{Newtonian}}$, is displayed. The differences observed between the three viscoelastic fluids can be understood in terms of the differences in the degree of shear thinning exhibited by these fluids, using arguments similar to those proposed above in the context of Fig. 3.17 (a).

The behaviour observed in Fig. 3.7 can be explained using Fig. 3.18 (b). It is clear that even at $Wi = 0.01$ for $\alpha = 45$ the narrowest channel gap predicted by the Owens model becomes very small and this gap decreases rapidly with the further increase in the value of α . However, for all other models (Newtonian, Oldroyd-B and FENE-P) the rate at which the narrowest gap decreases with increasing α appears to slow down for $\alpha \geq 50$.

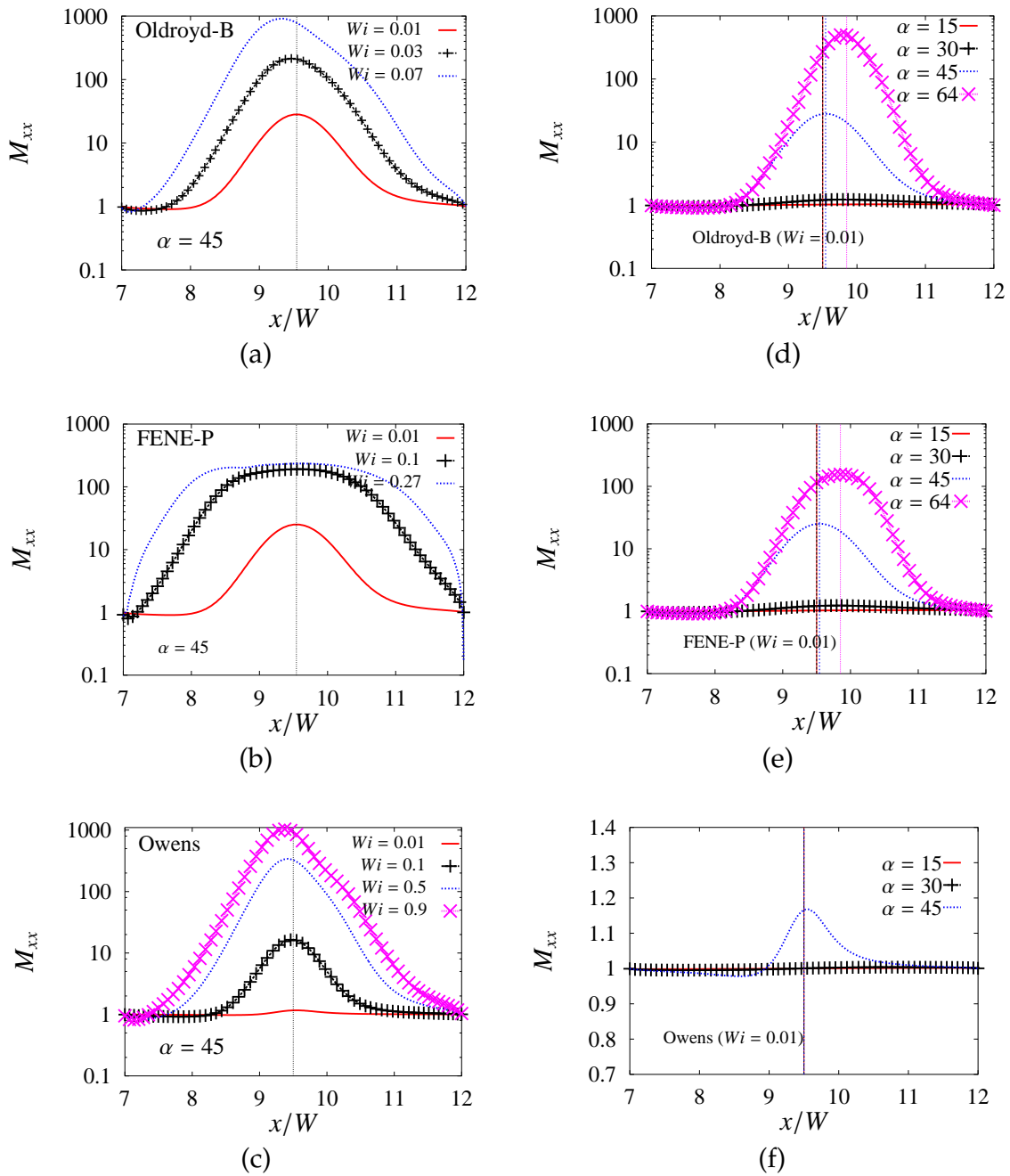


Figure 3.19: Dependence of the axial component of the conformation tensor M_{xx} on Wi , for (a) Oldroyd-B, (b) FENE-P, and (c) Owens models, at $\alpha = 45$, and dependence of M_{xx} on α , for (d) Oldroyd-B, (e) FENE-P, and (f) Owens models, at $Wi = 0.01$.

Fig. 3.19 (a)–(c) displays the dependence of the axial component of the conformation tensor M_{xx} along the flexible membrane on Wi , and Fig. 3.19 (d)–(f) displays its dependence on α . As expected, an increase in Wi or in α leads to an increase in the degree of stretching experienced by the micro-structural elements, with the maximum stretching occurring near the narrowest channel gap (indicated by the vertical lines). Since both the Oldroyd-B and Owens constitutive equations are based on Hookean dumbbell models, there is no upper bound on M_{xx} . Interestingly, the FENE-P model predicts that close to the limiting Weissenberg number, the micro-structural elements are nearly fully stretched for a fairly significant fraction of the length of the flexible membrane. For large values of α , the shape of the curves in Fig. 3.19 (d) and (e) appear to reflect the asymmetry in the shape of the membrane, which was seen to occur earlier for Newtonian fluids in Fig. 3.2. Interestingly, Fig. 3.19 (f) suggests that the value of M_{xx} in the Owens model is much less sensitive to the value of α compared to the Oldroyd-B and FENE-P fluids, and remains nearly unchanged from its equilibrium value. This can be attributed to the extensive shear thinning experienced by the fluid, leading to a significant reduction in the local relaxation time. The same argument can also be used to understand the differences in the relative magnitudes of the maximum eigenvalue m_3 for the three viscoelastic fluids, that was displayed earlier in Fig. 3.4.

The manner in which the presence of a flexible wall has been treated in this work, through a zero-thickness membrane that is coupled to the fluid only through the normal force, is a particularly simple representation of the fluid-structure interaction problem that underlies flow in a collapsible channel. It is reasonable to expect that the shear force on the membrane will also play a significant role in determining the shape of the membrane. With a view to examining the magnitude of shear forces on the membrane, we have computed the tangential shear stress along the length of the membrane surface. The dependence of the shear stress on both Wi and α , for the three different viscoelastic fluids, is displayed in Fig. 3.20 (a)–(f). It is immediately apparent from Fig. 3.20 (a)–(c) that, while the common feature between the three fluids is the decrease in tangential shear stress with an increase in Wi , there are striking differences in the extent of the decrease. While the Oldroyd-B model fluid suffers a relatively modest decrease in the shear stress near the narrowest channel gap, the FENE-P model fluid experiences a significant decrease. In the case of the Owens model, there is hardly any difference in the shear stress for the different Weissenberg numbers. As has been argued in a number of instances above, it is straightforward to relate these differences in behaviour to the different degrees of shear thinning experienced by the fluids, at the Weissenberg

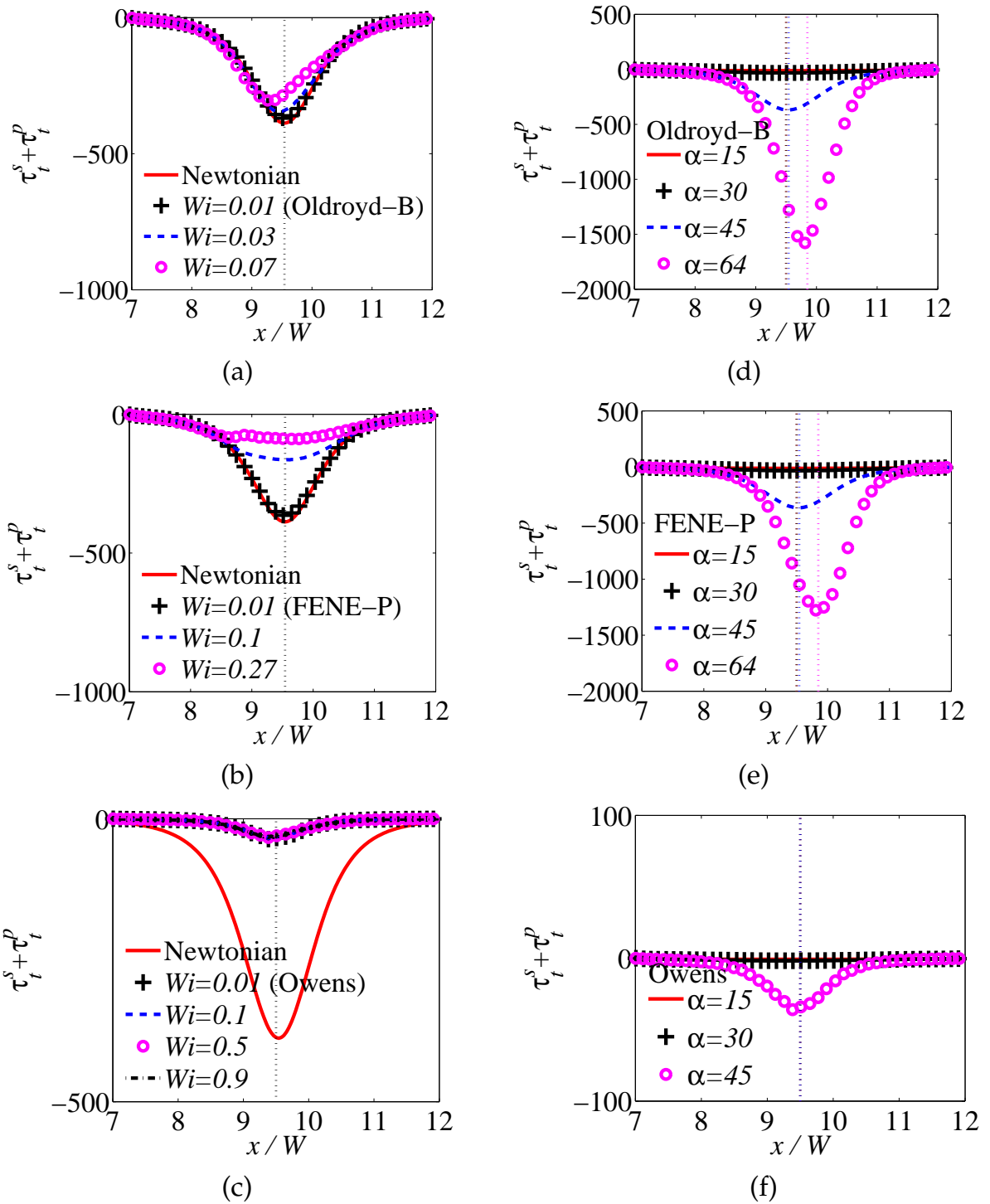


Figure 3.20: Dependence of the total tangential shear stress on the membrane ($\tau_t^s + \tau_t^p$) on Wi , for (a) Oldroyd-B, (b) FENE-P, and (c) Owens models, at $\alpha = 45$, and dependence of ($\tau_t^s + \tau_t^p$) on α , for (d) Oldroyd-B, (e) FENE-P, and (f) Owens models, at $Wi = 0.01$.

numbers examined in Fig. 3.20 (a)–(c). For all the fluids, at $Wi = 0.01$, the tangential shear stress appears to increase in absolute value with an increase in α , as can be seen from Fig. 3.20 (d)–(f). While the values for the Oldroyd-B and FENE-P models are approximately equal to each other, the shear stress prediction by the Owens model is significantly lower. At this value of Wi , the FENE-P model fluid does not undergo much shear thinning, and as a result, both the pressure (see Fig. 3.15 (d)–(f)) and the shear stress are similar for the Oldroyd-B and FENE-P models.

In general, even though there are significant differences in the shear stresses predicted by the different models, this is not reflected in the predicted shape of the membrane (see Fig. 3.13) because of the boundary condition adopted here. It would be extremely interesting to compare the predictions of the three fluid models with more realistic boundary conditions, where the influence of the shear stress is taken into account, since we can anticipate that significant differences in the predicted shape of the membrane will emerge. This is the problem studied in Chapter 5.

3.4 Conclusions

The aim of this chapter was to examine the differences that arise when three different viscoelastic fluids interact with the deformable membrane on the channel wall. Each of the three model viscoelastic fluids that have been chosen, namely, the Oldroyd-B, the FENE-P and Owens models, has unique features that distinguish it from the others. These differences lead to differences in the predictions of the various properties, and in many instances, the source of the difference can be traced back to a particular characteristic of the viscoelastic fluid. The most significant findings of this part are the following:

1. There is a limiting Weissenberg number Wi for each of the fluids beyond which computations fail. The value of Wi at which simulations breakdown coincides with the value at which the smallest eigenvalue of the conformation tensor becomes negative somewhere in the flow field.
2. For the Oldroyd-B and Owens models, the breakdown of numerical computations is accompanied by the axial component of the conformation tensor M_{xx} assuming large values at the top and bottom walls, close to the location in the channel where the gap between the walls is the narrowest.

3. The maximum deformation of the micro-structural elements occurs at a point just below the deformable membrane at the narrowest gap in the channel, and the location of this point coincides with the location of the maximum shear rate.
4. The shape of the deformable membrane, and its dependence on Wi and tension ratio α , is entirely determined by the pressure on the membrane surface, and by the changes in pressure that occur as a result of changes in these parameter values.
5. The key determinant of the pressure in the channel is the effective viscosity of the viscoelastic fluid at the location of the maximum shear rate. This result has been established for the FENE-P and Owens models (see Fig. 3.16 (b)) by showing that a Newtonian fluid with viscosity equal to the effective viscosity has nearly the same pressure profile as the viscoelastic fluid.
6. While it has been difficult to discern any noticeable influence of the elasticity of the fluid on the various properties, the degree of shear thinning exhibited by the fluid has a dramatic effect on all the properties. Thus, for instance, the observed dependence on Wi and α , of the pressure drop in the channel, the width of the narrowest gap, and the tangential shear stress on the membrane surface, can be understood by considering the extent of shear thinning experienced by the fluids at the relevant values of these parameters.
7. The significant differences that arise amongst the three viscoelastic fluids in the predicted value of the tangential shear stress on the membrane surface, has no influence on the shape of the deformable membrane in the present model because of the boundary condition adopted in this work, whereby only changes in the normal stress on the membrane can lead to changes in the shape. A more accurate model for the deformable membrane would account for the effect of the shear stress on membrane shape.

Chapter 4

The influence of shear thinning on viscoelastic fluid-structure interaction in a two-dimensional collapsible channel

4.1 Introduction

In chapter 3 it was shown that viscoelastic fluids behave similarly to Newtonian fluids, provided that the viscosity of the two fluids at the location of the maximum shear rate in the channel is the same. However, the influence of the degree of shear thinning of the viscoelastic fluid was not examined systematically. The finite extensibility parameter b_M , in the FENE-P model controls the extent of shear thinning experienced by the fluid, and is consequently a convenient parameter for examining the influence of shear thinning. In this chapter², we compute numerically the steady flow of a viscoelastic FENE-P fluid in a two-dimensional collapsible channel (Fig. 3.1). We use the same flow domain, boundary conditions, computational method, dimensionless numbers and parameter values as discussed in chapter 3. However, in order to delineate the role of shear thinning on the nature of the fluid-structure interaction, we compute the flow of a FENE-P model fluid for various values of b_M . The FENE-P parameter b_M is set in the range 2–100.

²Most of the results of this chapter has been published as, Debadi Chakraborty and J. Ravi Prakash, Influence of Shear Thinning on Viscoelastic Fluid-Structure Interaction in a Two-Dimensional Collapsible Channel, Ind. Eng. Chem. Res., ASAP publication, DOI:10.1021/ie200173b, 2011.

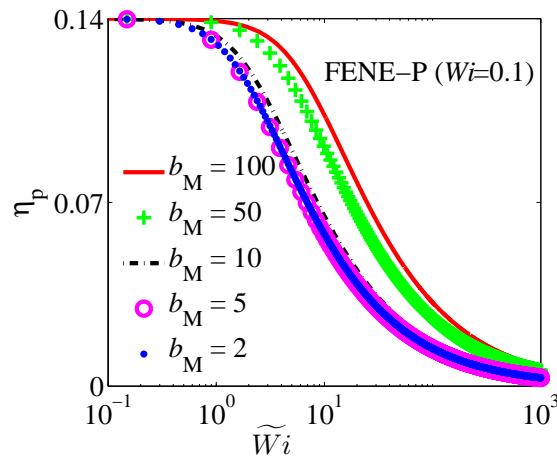


Figure 4.1: The contribution of the microstructure to the total viscosity, η_p , for the FENE-P fluid in steady shear flow as a function of local Weissenberg number \widetilde{Wi} , at a constant value of the relaxation time λ_0 .

Here various predictions of the FENE-P fluid model, along with a comparison of predictions for a Newtonian fluid, is presented. Finally, concluding remarks are drawn in the last section.

4.2 Results and discussion

A comparison of the predictions of the current formulation for a Newtonian fluid with those of Luo and Pedley [1995] has been carried out by Chakraborty et al. [2010]. Predictions of the profile of the membrane at different values of α , were shown to be in excellent agreement with the reported results of Luo and Pedley [1995].

Before we present results for the various relevant variables, it is appropriate here to show the dependence of the FENE-P model's predictions of the microstructure's contribution to viscosity η_p on the local Weissenberg number \widetilde{Wi} , in a steady shear flow, at a constant value of λ_0 for different values of b_M . As is evident from Fig. 4.1, the FENE-P model undergoes increasing shear thinning with decreasing values of the finite extensibility parameter b_M . Note that the values of U_0 and W chosen here, this value of λ_0 corresponds to an inlet Weissenberg number of 0.1. The dependence of η_p on $\dot{\gamma}$ for a FENE-P model in steady shear flow has been derived previously [Bird et al., 1987b]. In this section, we examine the effect of varying b_M on other properties such as

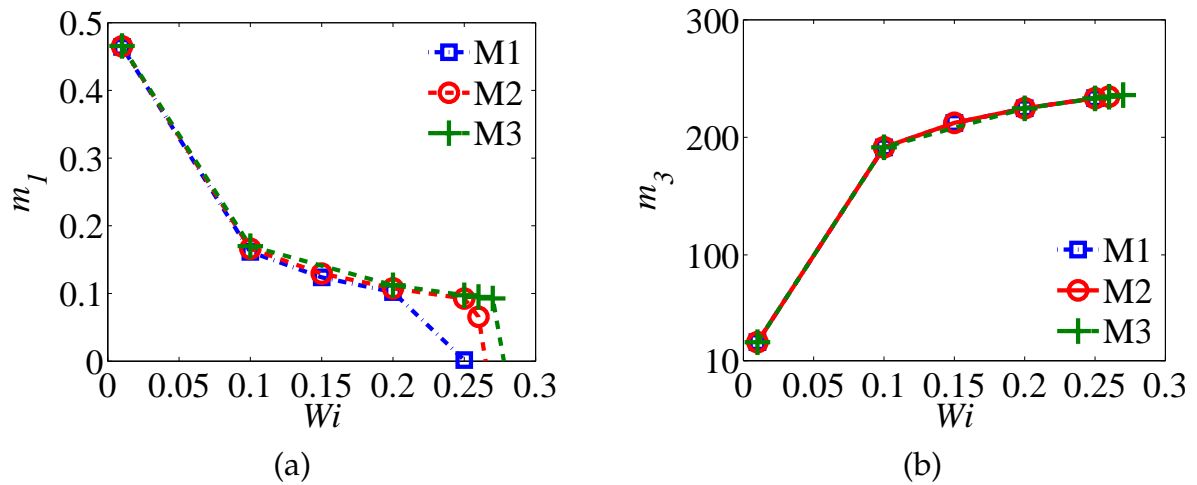


Figure 4.2: Minimum value of the smallest eigenvalue (m_1) and maximum value of the largest eigenvalue (m_3) in the entire flow domain, for a FENE-P model, as a function of Wi at $\alpha = 45$ and $b_M = 100$.

the limiting Weissenberg number, the shape of the membrane and pressure profile in the channel.

4.2.1 Mesh convergence and the limiting Weissenberg number

Since most viscoelastic computations break down numerically at some limiting value of the Weissenberg number due to the development of large stresses, it is essential to ensure mesh convergence over a range of parameters. Three different meshes (M1, M2 and M3), with number of elements 2145, 3008 and 3800 respectively, have been considered here for examining the convergence of the numerical computations. A convenient set of variables with which to examine the convergence of numerical computations of viscoelastic fluids are the invariants of the conformation dyadic, \mathbf{M} . Previous studies have revealed that invariably the breakdown of viscoelastic computations coincides with the smallest eigenvalue becoming negative, and the largest eigenvalue assuming significantly large values in some regions of the flow domain [Bajaj et al., 2008; Pasquali and Scriven, 2002]. The magnitude of the maximum in m_3 and the minimum in m_1 , in the entire flow domain, is displayed in Fig. 4.2 as a function of Wi , for the FENE-P model, at $\alpha = 45$ and $b_M = 100$. The value of Wi at which mesh convergence no longer exists can be clearly located in Fig. 4.2 (a) for the minimum eigenvalue m_1 . As has

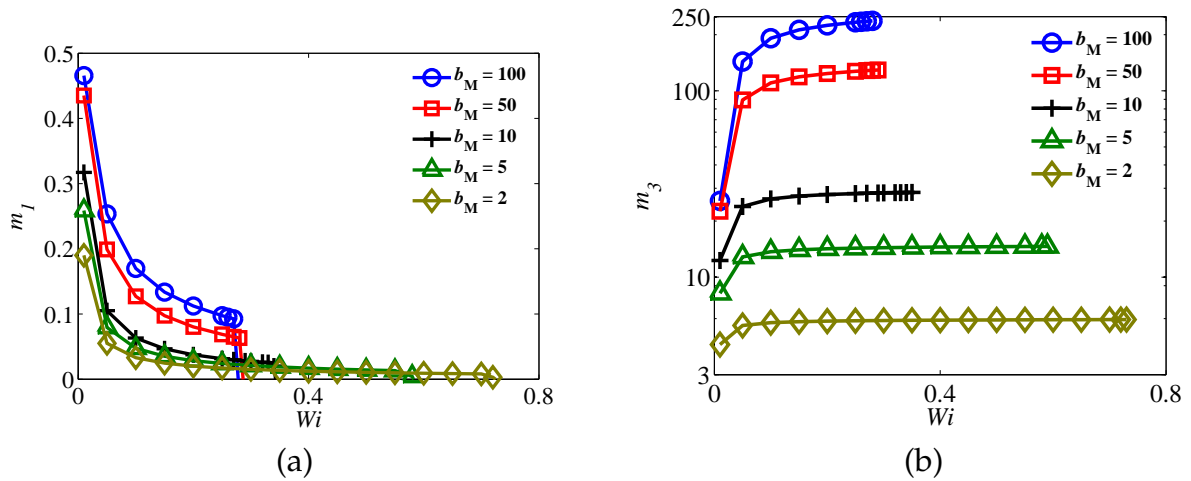


Figure 4.3: Minimum value of the smallest eigenvalue (m_1) and maximum value of the largest eigenvalue (m_3) in the entire flow domain, for the FENE-P model at different finite extensibility b_M .

been observed in previous studies [Bajaj et al., 2008; Pasquali and Scriven, 2002], the maximum attainable value of Wi increases with mesh refinement; for example, in the FENE-P model at $\alpha = 45$ and $b_M = 100$, the limiting value of the Weissenberg number is $Wi = 0.26$ on M2 and $Wi = 0.27$ on M3. Unless otherwise specifically stated, we have used the M3 mesh in all the remaining computations carried out in this work.

Fig. 4.3 examines the dependence of the limiting Weissenberg number (which is the value at which the curves terminate), on the finite extensibility parameter b_M . Both figures indicate that the limiting Weissenberg number increases with decreasing b_M . Thus shear thinning enhances the computability of the viscoelastic fluid by decreasing the value of m_3 and delaying the value of Wi at which m_1 becomes negative.

4.2.2 Flow field and flexible membrane shape

To examine the behaviour of a viscoelastic liquid in this flow domain we compare the velocity contours predicted by a Newtonian fluid with the predictions of the FENE-P model. Fig. 4.4 compares the velocity profile prediction at $Wi = 0.1$ for different values of b_M . It is clear that the Newtonian and FENE-P fluids do not show any significant differences between them for $b_M = 100$ at $Wi = 0.1$. The prediction of the FENE-P model for lower values of b_M , on the other hand, displays some difference from the Newtonian

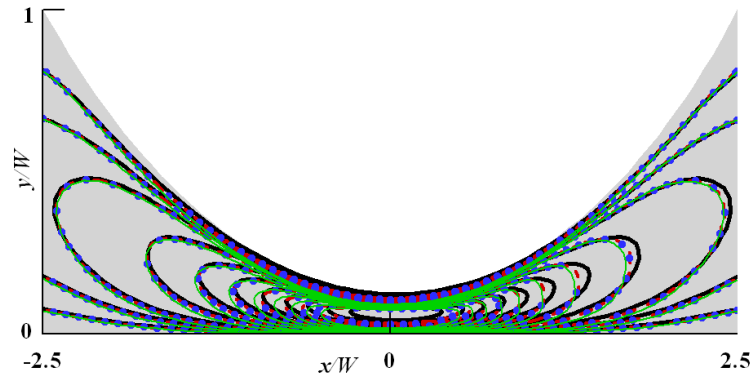


Figure 4.4: Comparison of contours of axial velocity (v_x) in the domain at tension ratio of 45 for Newtonian (black line) and different values of b_M for the FENE-P model, $b_M=100$ (red dashed line), $b_M=50$ (blue dots) and $b_M=2$ (thin green line) at $Re = 1.0$ and $\beta = 0.0071$.

velocity profile, which must arise since different values of b_M imply different degrees of shear thinning.

In the remainder of this section, we focus our attention on examining the influence of the Weissenberg number Wi and the finite extensibility b_M on the shape of the membrane, for the fixed values of the viscosity ratio β , the transmural pressure P_d , and the Reynolds number Re , that have been adopted here. The dependence of the shape of the channel on Wi and b_M is shown in Fig. 4.5 (a) which is a zoomed in view of the membrane shape close to the centre of the membrane, for the FENE-P model fluid, at various values of b_M , for a fixed value of $Wi = 0.1$. Shear thinning leads to a departure from the Newtonian shape. The influence of shear thinning and viscoelasticity on the extent of deformation of the membrane can be seen more clearly in Fig. 4.5 (b) which reveals the effect of Weissenberg number (Wi) on the narrowest channel gap scaled by the value for a Newtonian fluid for various values of b_M . The value of the narrowest channel gap is seen to be decreasing with increase in Wi at fixed values of b_M , while at a fixed Wi , $h/h_{\text{Newtonian}}$ decreases with decreasing b_M . It is clear that both these parameters have a similar effect on changes in the membrane shape since they both have a similar effect on the viscosity of the fluid, as evident from Fig. 4.1.

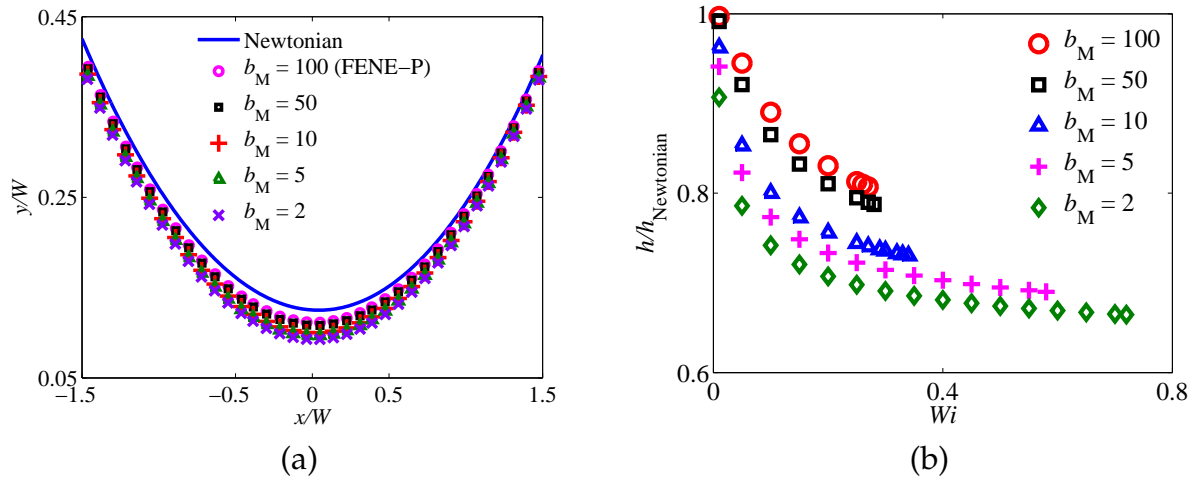


Figure 4.5: (a) The deformed shape of the flexible wall for the steady flow of the FENE-P model fluid in a 2D collapsible channel, compared with the profile for a Newtonian fluid, with $Re = 1.0$ and $\beta = 0.0071$, at various values of b_M for $\alpha = 45$ and $Wi = 0.1$ and (b) comparison of the narrowest channel gap between the flexible wall and bottom wall at various values of b_M for varying Wi

4.2.3 Pressure and stresses

From the nature of the boundary condition on the flexible membrane adopted here (3.1), it is clear that the only reason the membrane can change shape as a result of changing either b_M or Wi , is if there is a change in the normal stress acting on the membrane. Patankar et al. [2002] have shown analytically that the contribution from the elastic and viscous stresses to the component of stress normal to the surface of a rigid body, for a wider class of fluids, is zero. A similar result has also been observed by Chakraborty et al. [2010] in a 2D collapsible channel for the flow of incompressible Oldroyd-B, FENE-P and Owens model fluids, where they showed that the normal component of stress on the membrane wall is solely due to pressure. This is also confirmed in the present simulations, where we find that the normal component of stress on the wall is solely due to pressure for all values of b_M .

Fig. 4.6 displays the pressure profile along the flexible membrane for the FENE-P model at various values of b_M . It is clear that both increasing the value of Wi and decreasing the value of b_M , decreases the pressure on the membrane upstream of the narrowest section of the channel. Fig. 4.7 shows the overall pressure drop (ΔP) across the channel for the FENE-P model for different values of b_M with varying Wi . The

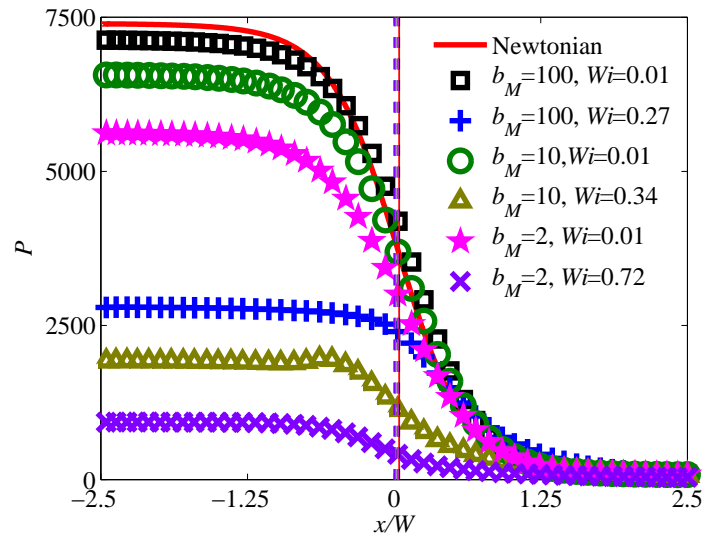


Figure 4.6: Dependence of the pressure profile along the flexible membrane on Wi for the FENE-P model at various values of b_M . Here the vertical lines with the same colour as the pressure profile indicate the position of the narrowest channel gap for the corresponding cases.

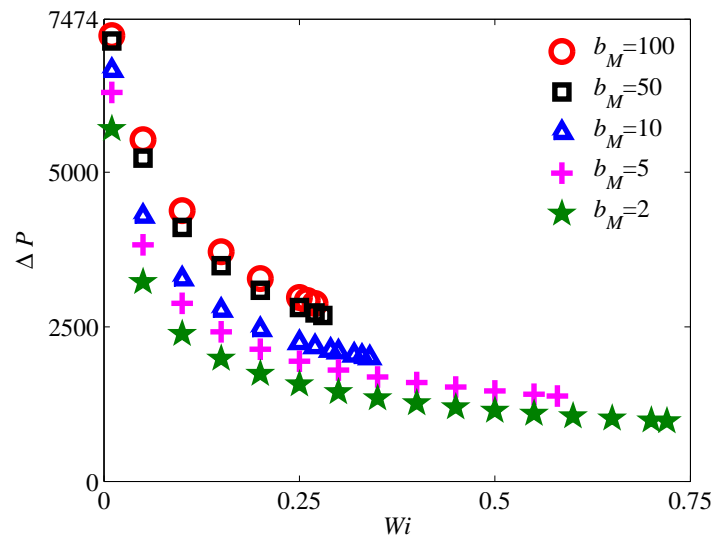


Figure 4.7: Dependence of the pressure drop in the channel on Wi for the FENE-P model at various values of b_M . Note that for a Newtonian fluid, $\Delta P = 7474.0$.

decrease in pressure drop is significant with increase in Wi and with decrease in b_M . This decrease in pressure and pressure drop is clearly attributable to the decrease in the viscosity of the fluid in the channel due to shear thinning. In turn, the decrease in

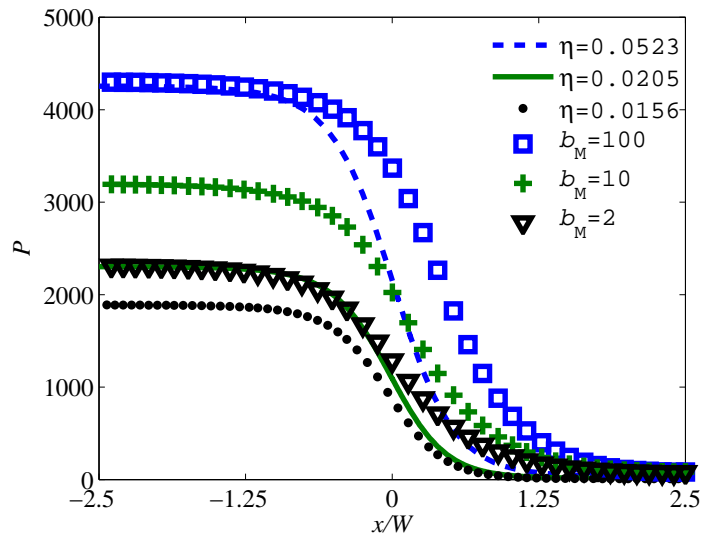


Figure 4.8: Pressure profile along the flexible membrane for Newtonian fluids with a range of viscosities, and the pressure profile for a FENE-P fluid with $Wi = 0.1$ and $b_M = 2, 10$ and 100 . The values $\eta = 0.0523, 0.0205$ and 0.0156 Pa s are the calculated values of reduced viscosity, respectively, at $b_M = 100, 10$ and 2 , at the location of the maximum \widetilde{Wi} under the flexible membrane.

pressure is the source of change in membrane shape seen earlier in Fig. 4.5.

If shear thinning is the primary cause for the reduced prediction of pressure on the membrane in a channel flow, then a Newtonian fluid with viscosity equal to the effective viscosity in the FENE-P model, would predict a similar value of pressure to that of the FENE-P model. We find the maximum value of $\widetilde{Wi} = \lambda_0 \dot{\gamma}$ (which occurs just below the collapsible membrane) by scanning the flow field in the channel for different values of b_M for an inlet Weissenberg number $Wi = 0.1$. Subsequently, utilizing Fig. 4.1, the corresponding reduced viscosity is obtained at that particular value of b_M . In Fig. 4.8, the pressure profile along the flexible membrane predicted by the FENE-P model at $Wi = 0.1$ for different values of b_M , has been compared with pressure profiles predicted for Newtonian fluids with a range of viscosity values obtained from the above mentioned procedure. We find that the maximum value of \widetilde{Wi} , at $Wi = 0.1$ and $b_M = 100$, for a FENE-P fluid flowing in the channel is 44.4 . This corresponds to $\eta_p = 0.0513$. As can be seen in Fig. 4.8, the pressure profile on the flexible membrane for a Newtonian fluid with $\eta_0 = 0.0523$ is fairly similar to that for a FENE-P fluid. In particular, the value for the maximum pressure on the membrane is nearly identical. The pressure profiles

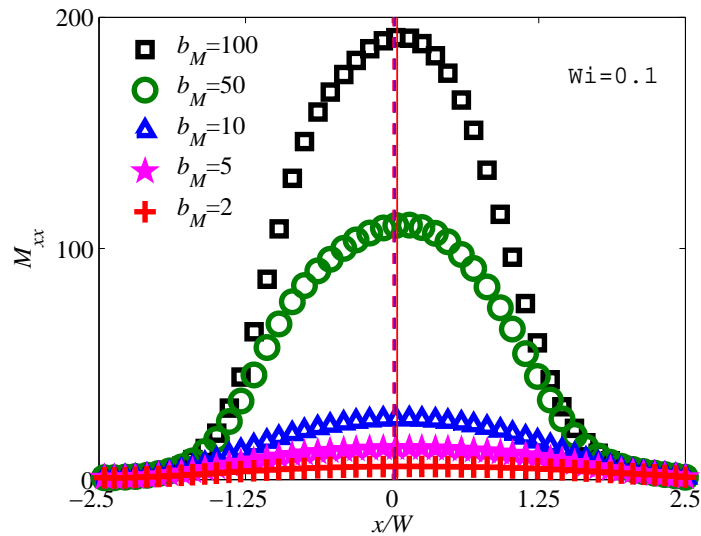


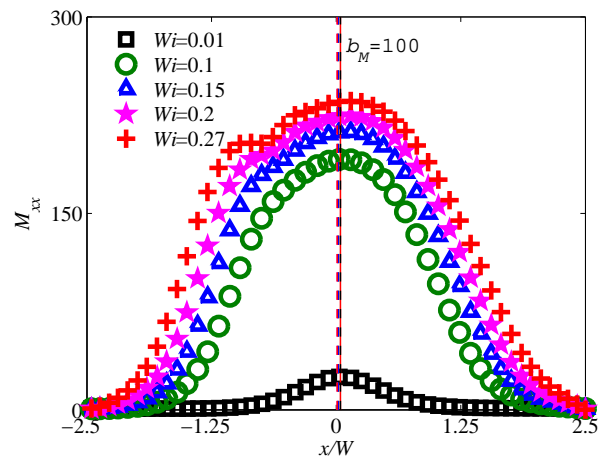
Figure 4.9: Dependence of the axial component of the conformation tensor M_{xx} on b_M for a fixed value of $Wi = 0.1$.

for a FENE-P fluid at other values of b_M also show the same trend as the pressure profile of a Newtonian fluid calculated at the respective reduced viscosity.

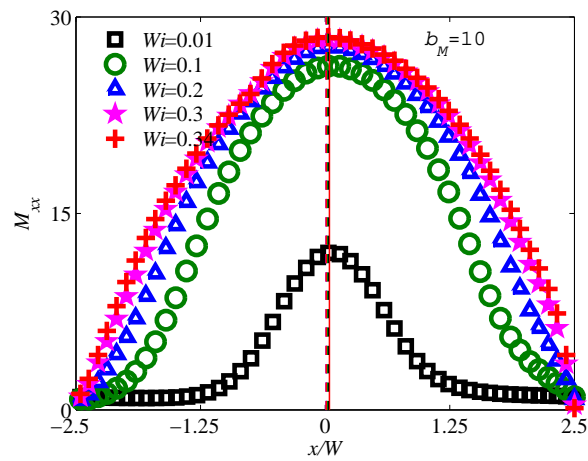
We now explore the influence of viscoelasticity, by examining the behaviour of the axial component of the conformation tensor M_{xx} along the membrane wall. Fig. 4.9 displays the dependence on b_M , while Fig. 4.10 displays the dependence on Wi . The value of M_{xx} is maximum near the narrowest region of the channel and increases with both Wi and b_M . This signifies that the FENE-P fluid is experiencing the maximum stretching near the narrowest region of the channel. The value of b_M imposes an upper bound to the mean stretchability of the spring in the FENE-P model and restricts the maximum value for M_{xx} .

Fig. 4.11 shows the dependence of the shear stress on b_M for the FENE-P fluid at a fixed value of Wi , while Fig. 4.12 explores the effect of Wi at various values of b_M . It is immediately apparent from these figures that the common feature is a decrease in tangential shear stress with an increase in Wi and a decrease in b_M . This is clearly due to the reduction of viscosity in the channel that accompanies the change in these parameters.

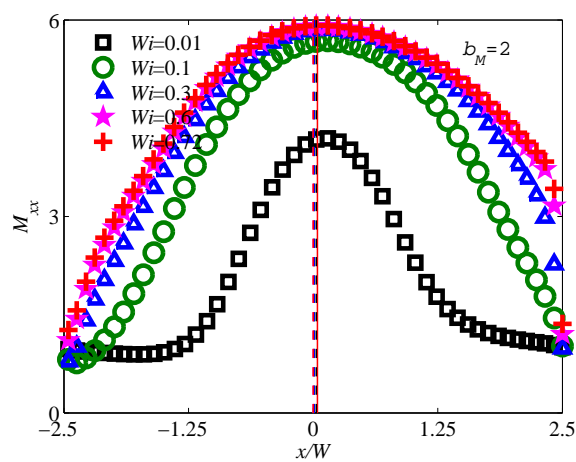
The significant differences in the shear stresses predicted by the FENE-P model at different values of b_M has no effect on membrane shape under the present set of boundary conditions, since the influence of shear stresses exerted by the fluid on the flexible membrane cannot be taken into account. Future advancement of this work



(a)



(b)



(c)

Figure 4.10: Dependence of the axial component of the conformation tensor M_{xx} on Wi , for (a) $b_M=100$, (b) $b_M=10$ and (c) $b_M=2$.

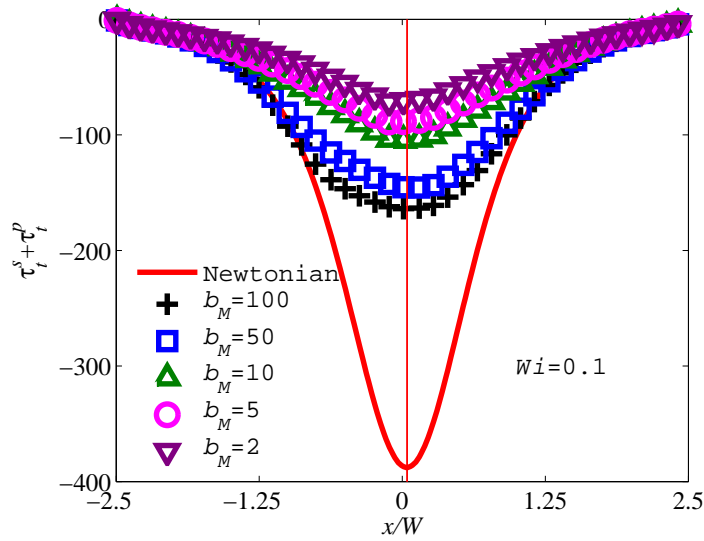


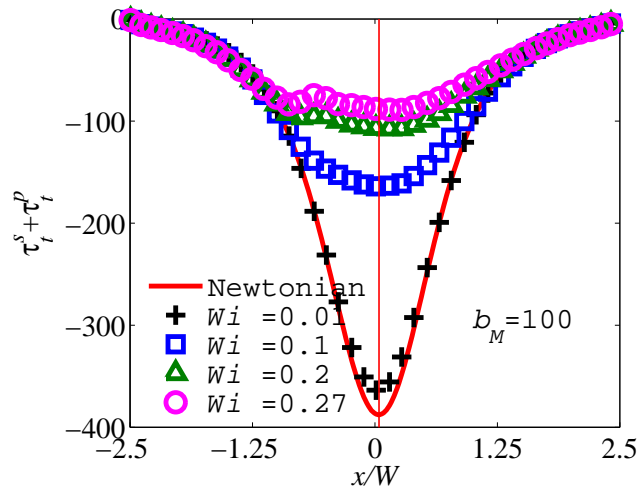
Figure 4.11: Dependence of the total tangential shear stress on the membrane $\tau_t^s + \tau_t^p$ on b_M for a fixed value of $Wi = 0.1$

requires a more realistic implementation of boundary conditions, which is the focus of Chapter 5.

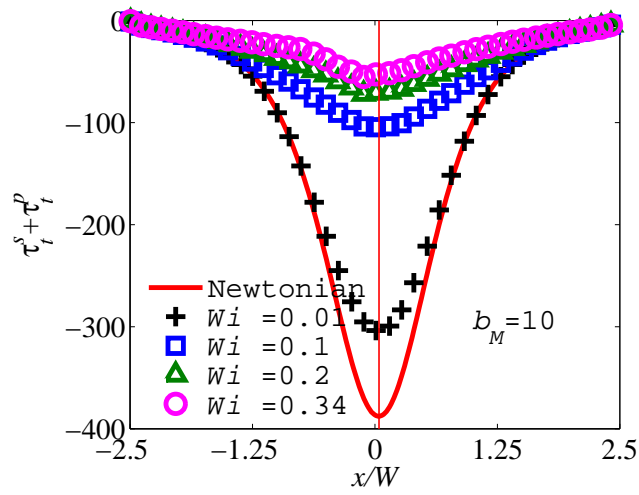
4.3 Conclusions

The extent of shear thinning is shown to be a key factor in determining the nature of the fluid-structure interaction. The most significant conclusions of this work are the following:

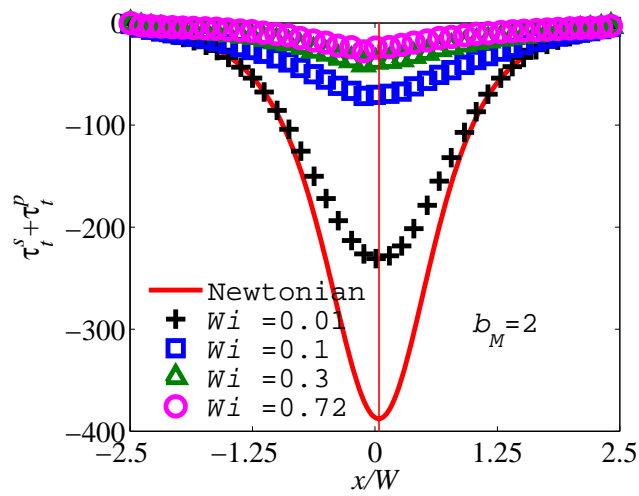
1. There is a limiting Weissenberg number Wi at each value of b_M for the FENE-P fluid beyond which computations fail. The limiting value of Wi increases with the decrease in the value of b_M .
2. The shape of the deformable membrane, and its dependence on Wi and b_M , is entirely determined by the pressure on the membrane surface.
3. The pressure drop, molecular conformation tensor fields, and stresses in the flow domain are significantly affected by the extent of shear thinning of the FENE-P fluid.



(a)



(b)



(c)

Figure 4.12: Dependence of the total tangential shear stress on the membrane ($\tau_t^s + \tau_t^p$) on Wi , for (a) $b_M=100$, (b) $b_M=10$ and (c) $b_M=2$.

Chapter 5

Viscoelastic fluid–elastic wall interaction in a two-dimensional collapsible channel

5.1 Introduction

In the earlier chapters, it was found that the significant differences that arise amongst the different viscoelastic fluids in the predicted value of the tangential shear stress on the membrane surface, have no influence on the shape of the deformable membrane, because of the boundary condition adopted in the work. Essentially, it was assumed that the shape of the membrane is governed only by the normal stresses acting on it. In order to use a more realistic model for the collapsible wall, here we use a finite thickness neo-Hookean solid model which accounts for the effect of shear stress on membrane shape. Thus in this chapter, steady viscoelastic flow in a two-dimensional channel in which part of one wall is replaced by a deformable finite thickness elastic solid is studied. Three different viscoelastic fluids have been considered—the Oldroyd-B model, the FENE-P model, and the Owens model for blood. The elastic wall is modelled as an incompressible neo-Hookean solid. The model formulation used here follows the seminal work of Carvalho and Scriven [1997] who proposed a fluid-structure interaction formulation to solve roll cover deformation in roll coating flows, with the rubber roll cover modelled as incompressible neo-Hookean and Mooney-Rivlin solids. We choose channel dimensions to be compatible with the microcirculation. The computational method developed in chapter 2 is used to solve this problem.

The plan of the chapter is as follows. The problem formulation, with details of the

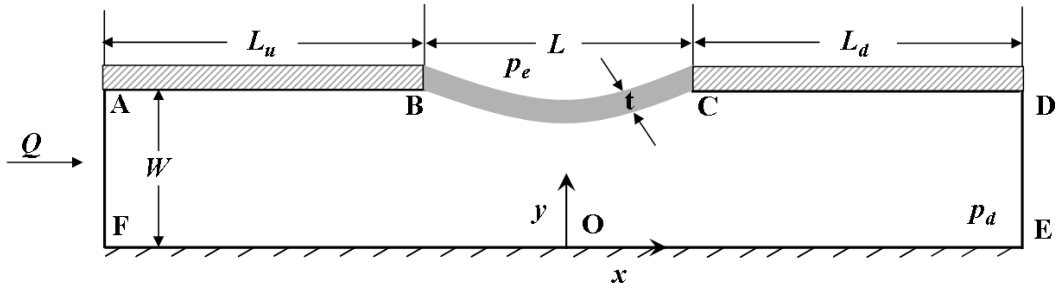


Figure 5.1: Geometry of the domain.

governing equations for the viscoelastic fluids and incompressible neo-Hookean solid, the boundary conditions and the relevant dimensionless variables are presented in Section 5.2. The results of viscoelastic and Newtonian fluid computations are compared in Section 5.3. In particular, the dependence of the shape of the fluid-solid interface, and of the pressure, stress, conformation tensor and velocity fields on the different parameters, is examined. Finally, concluding remarks are drawn in Section 5.4.

5.2 Problem formulation

The geometry of the flow is that of a 2D channel, with one of the walls containing an elastic segment as illustrated in Fig. 5.1. In units of channel width W , the dimensions of the channel are $L_u = 7W$, $L = 5W$, and $L_d = 7W$. The solid wall has a thickness $t = 0.4W$.

5.2.1 Governing Equations

We have nondimensionalized the various physical quantities, by scaling lengths and displacements with W , velocities with GW/η_0 and pressure and stresses with G , where G is the shear modulus of the solid, $\eta_0 (= \eta_s + \eta_{p,0})$ is the zero shear rate solution viscosity, η_s is the solvent viscosity, and $\eta_{p,0}$ is the contribution of the micro-structural elements to the zero shear rate viscosity. (For a Newtonian fluid, η_0 is just the constant Newtonian viscosity). Non-dimensionalization of the governing equations and boundary conditions yields the following dimensionless numbers:

$$Re = \frac{\rho W U_0}{\eta_0}; \quad \beta = \frac{\eta_s}{\eta_0}; \quad Wi = \frac{\lambda_0 U_0}{W}; \quad \Gamma = \frac{\eta_0 U_0}{GW} \quad (5.1)$$

where, Re is the Reynolds number, β is the viscosity ratio, Wi is the *inlet* Weissenberg number, Γ is the dimensionless solid elasticity parameter, ρ is the density of the liquid, U_0 is the average inlet velocity and λ_0 is the constant characteristic relaxation time of the microstructure.

Upon introduction of these dimensionless variables, the governing equations assume the following dimensionless form:

$$\nabla \cdot \mathbf{v} = 0 \quad (\text{Mass balance}) \quad (5.2)$$

$$\frac{Re}{\Gamma} \mathbf{v} \cdot \nabla \mathbf{v} = \nabla \cdot \mathbf{T} \quad (\text{Momentum balance}) \quad (5.3)$$

$$\mathbf{v} \cdot \nabla \mathbf{M} - \nabla \mathbf{v}^T \cdot \mathbf{M} - \mathbf{M} \cdot \nabla \mathbf{v} = -\frac{\Gamma}{Wi} \{f(\text{tr } \mathbf{M}) \mathbf{M} - \mathbf{I}\} \quad (\text{Conformation tensor}) \quad (5.4)$$

$$\mathbf{T} = -P \mathbf{I} + \boldsymbol{\tau}^s + \boldsymbol{\tau}^p \quad (\text{Cauchy stress tensor for viscoelastic fluid}) \quad (5.5)$$

$$\boldsymbol{\tau}^s = \beta(\nabla \mathbf{v} + \nabla \mathbf{v}^T) \quad (\text{Viscous stress tensor}) \quad (5.6)$$

$$\boldsymbol{\tau}^p = (1 - \beta) \frac{\Gamma}{Wi} \{f(\text{tr } \mathbf{M}) \mathbf{M} - \mathbf{I}\} \quad (\text{Elastic stress tensor}) \quad (5.7)$$

$$\nabla_x \cdot \mathbf{S} = 0 \quad (\text{Equation of motion for solid}) \quad (5.8)$$

$$\mathbf{S} = \mathbf{F}^{-1} \cdot \boldsymbol{\sigma} \quad (\text{First Piola-Kirchhoff stress tensor}) \quad (5.9)$$

$$\boldsymbol{\sigma} = -\pi \mathbf{I} + \mathbf{B} \quad (\text{Cauchy stress tensor for a neo-Hookean material}) \quad (5.10)$$

In these equations, \mathbf{v} is the velocity, ∇ denotes the gradient, P is the pressure, \mathbf{I} is the identity tensor, π is a pressure-like scalar function and \mathbf{B} is the left Cauchy-Green tensor, expressed as $\mathbf{B} = \mathbf{F} \cdot \mathbf{F}^T$ and \mathbf{F} is the deformation gradient tensor.

5.2.2 Boundary conditions

We prescribe the following boundary conditions:

1. No slip boundary conditions ($\mathbf{v} = \mathbf{0}$) are applied on the rigid walls.
2. The elastic solid is fixed at both ends (points B and C in Fig. 5.1).
3. At the upstream boundary, a fully developed dimensionless velocity profile $v_x = \Gamma f(y/W)$ is specified. Since, for all the Wi considered here, the upstream velocity profiles for the Oldroyd- B and FENE-P fluids do not differ significantly from that of a Newtonian fluid, a Newtonian velocity profile is used. However, for the Owens model fluid, we use a fully developed velocity profile obtained by analytically solving the flow of a power-law fluid in a channel. This is because of the strongly shear thinning nature of the Owens model fluid which is discussed in more detail subsequently. The power-law index used is that exhibited by the Owens model (with the current parameter values) in a simple shear flow.
4. At the downstream boundary, the fully developed flow boundary condition is imposed, $\mathbf{n} \cdot \nabla \mathbf{v} = \mathbf{0}$ where \mathbf{n} is the unit normal to the outlet.
5. At the upstream inflow, the conformation tensor does not change along the streamlines because the flow is fully developed [Pasquali and Scriven, 2002; Xie and Pasquali, 2004]. Thus,

$$\mathbf{v} \cdot \nabla \mathbf{M} = \mathbf{0} \quad (5.11)$$

6. A force balance and a no-penetration condition are prescribed at the interface between the liquid and solid domain.

$$\mathbf{n} \cdot \mathbf{T} = \mathbf{n} \cdot \boldsymbol{\sigma} \quad \text{and} \quad v_{solid} = v_{fluid} = 0 \quad (5.12)$$

where \mathbf{n} is the unit normal to the deformed solid surface.

7. A force balance is prescribed at the top surface.

$$\mathbf{n} \cdot \boldsymbol{\sigma} = -P_e \mathbf{n} \quad (5.13)$$

where P_e is the dimensionless external pressure.

8. The non-dimensional pressure of the fluid at the downstream boundary, P_d , is set equal to zero.

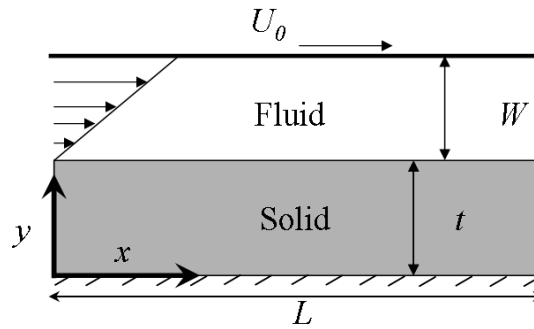


Figure 5.2: Couette flow of a Newtonian fluid past an incompressible finite thickness neo-Hookean solid.

5.3 Results and discussions

A thorough validation of the finite-element code has been carried out by comparing the results of the present formulation with several earlier results obtained in different contexts.

5.3.1 Validation of the finite-element formulation

In order to validate the finite-element formulation used here, results of computations in a variety of different contexts are compared with results reported earlier in the literature.

5.3.1.1 Couette flow past a finite thickness solid

Gkanis and Kumar [2003] have examined the flow of a Newtonian fluid past an incompressible neo-Hookean solid, as shown schematically in Fig. 5.2. The interface between the fluid and solid is located at $y = t$, and a rigid plate located at $z = (W + t)$ moves in the x direction at a constant speed U_0 , giving rise to Couette flow in the fluid domain. The bottom edge of the solid is held fixed. Gkanis and Kumar [2003] have performed a linear stability analysis of this problem in the limit of zero Reynolds number and infinite domain length L , and have shown that the steady state solution of the deformation in the solid produced by the Couette flow is,

$$\boldsymbol{x} = (x, y) = (X + \Gamma Y, Y) \quad (5.14)$$

where Γ is the dimensionless number defined in Eq. (5.1).

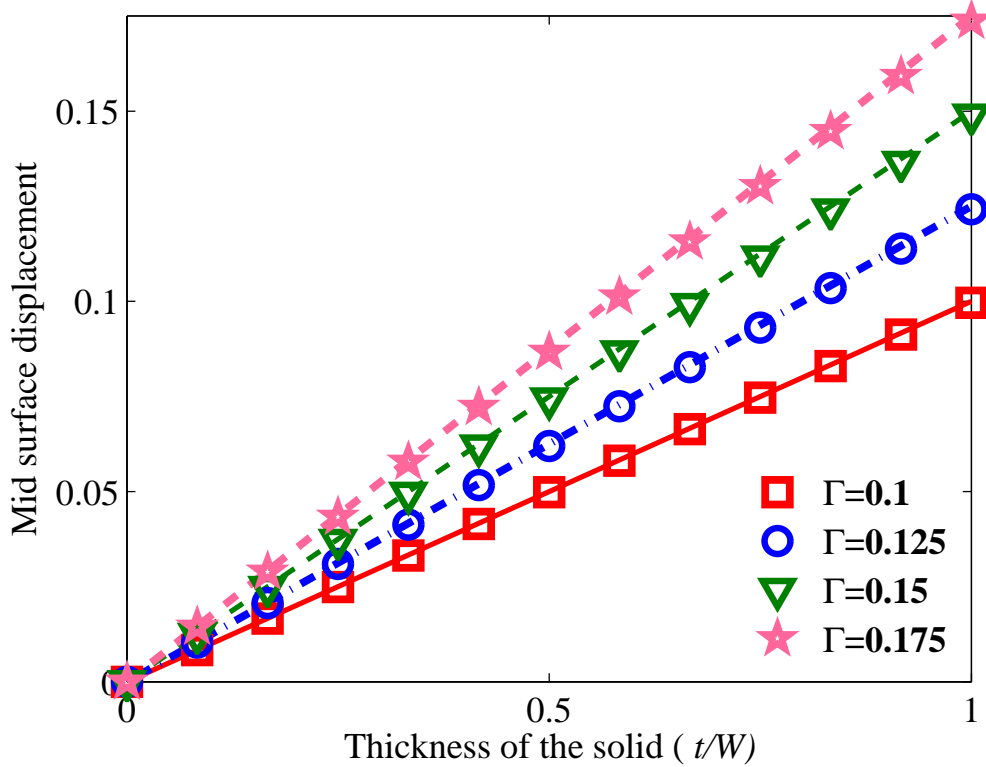


Figure 5.3: Comparison of FEM simulation with the analytical solution for different values of Γ . Lines denote the analytical solution reported by Gkanis and Kumar [2003], while symbols are results of the current FEM formulation.

Computations have been performed to compare predictions for the deformation of the solid domain at $L/2$ with the analytical results of Gkanis and Kumar [2003]. In order to eliminate end effects caused by the fixed ends of the solid and fluid domains in computations, we have varied the length of the domain between 10 to 30 m and ensured that domain length independent predictions are obtained.

The following parameter values have been used: $\rho = 10^{-3} \text{ kg/m}^3$, $\eta_0 = 1 \text{ Pa s}$, $W = 1 \text{ m}$, $t = 1 \text{ m}$ and $U_0 = 10^{-3}$ to 1.75×10^{-3} (in order to keep Re close to zero), and $G = 10^{-2} \text{ Pa}$. This choice of parameter values maintains the value of the dimensionless number Γ in the range 0.1 to 0.175.

The mid-surface displacement of the solid predicted by the finite-element formulation is compared with the analytical solution for different values of Γ , in Fig. 5.3. It is clear that in all cases finite-element results are in excellent agreement with the analytical solution.

5.3.1.2 Two-dimensional collapsible channel flow: Elastic beam model

Luo et al. [2007] have carried out extensive studies of Newtonian fluid flow in a 2D collapsible channel by considering the flexible wall to be a plane-strained elastic beam that obeys Hooke's law. In contrast to the current finite thickness elastic solid model, the beam model does not admit any stress variation across the cross-section of the beam.

For the purposes of comparison, the dimensions of the channel and other parameter values are chosen here to be identical to those used by Luo et al. [2007] in their simulations: $L_u = 5W$, $L = 5W$, $L_d = 30W$, and $U_0 = 0.03$ m/s, $W = 10^{-2}$ m, $\rho = 10^3$ kg/m³, $\eta_0 = 0.001$ Pa s. This choice corresponds to $Re = 300$. Further, we set $G = 11.97$ kPa (which is equivalent to a value of 35.9 kPa for the Young's modulus of an incompressible solid), and $p_e = 1.755$ Pa. The flexible wall thickness is varied in the range $0.01W$ to $0.1W$. The "pre-tension" in the beam is also a variable in the model of Luo et al. [2007]. However, since no such variable exists in the current model, we have restricted our comparison to the results reported by Luo et al. [2007] for cases where the pre-tension in the beam is zero.

Fig. 5.4 compares the prediction of the shape of the flexible wall by the present finite thickness elastic solid model, with the reported results of Luo et al. [2007]. As may be anticipated, while our simulations agree with Luo et al. [2007] for the relatively small deformation that occurs for large membrane thickness t , the Hookean beam model begins to depart from the prediction of the nonlinear neo-Hookean model for the large deformations that occur when the membrane thickness is small.

5.3.1.3 Two-dimensional collapsible channel flow: Zero-thickness membrane model

Simulations have also been performed to compare predictions of the flexible wall shape by the current finite thickness elastic solid model, with predictions by the zero-thickness membrane model of Luo and Pedley [1995], for the flow of a Newtonian fluid. Apart from the simplicity of the zero-thickness membrane model from a constitutive point of view, a fundamental difference between the two models is that while the tension in the flexible wall is prescribed *a priori* in the zero-thickness membrane model, it is part of the solution in the finite thickness elastic solid model. As a result, in order to carry out a comparison, a procedure involving several steps has been invoked.

Firstly, the zero-thickness membrane model has been computed for a pre-determined value of membrane tension equal to 675 N/m, with the following parameter values:

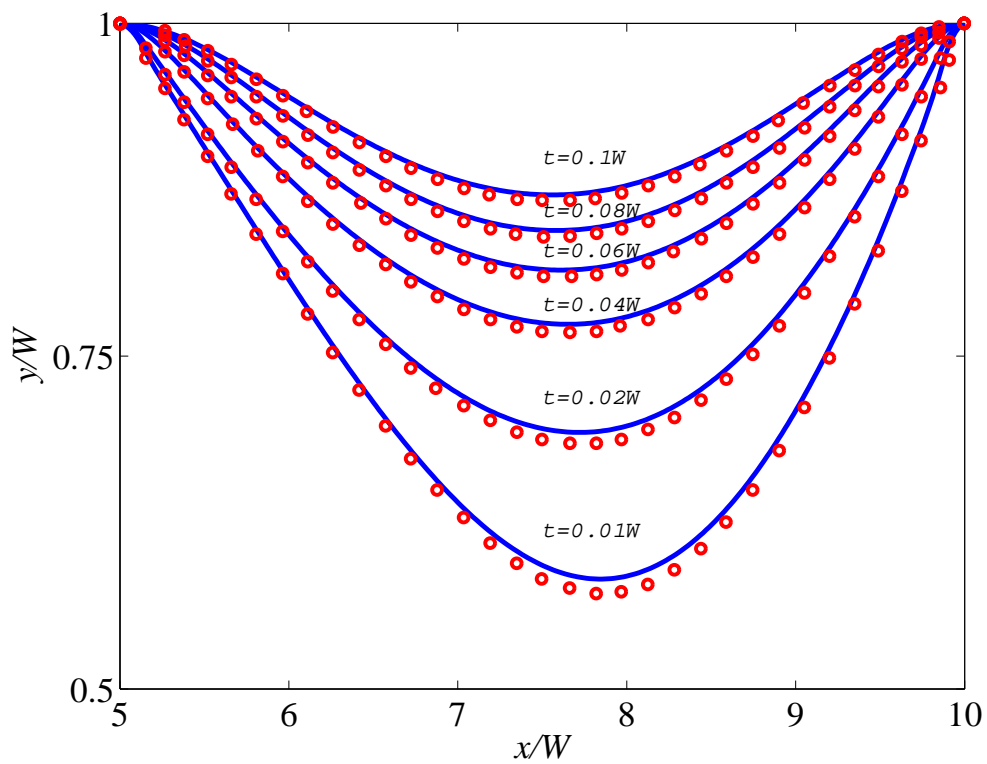


Figure 5.4: Comparison of the shape of the flexible wall predicted by the finite thickness elastic solid model, for different values of wall thickness, with the results of Luo et al. [2007] for an elastic beam model. Circles denote the elastic beam model, while the lines are the results of the current FEM formulation.

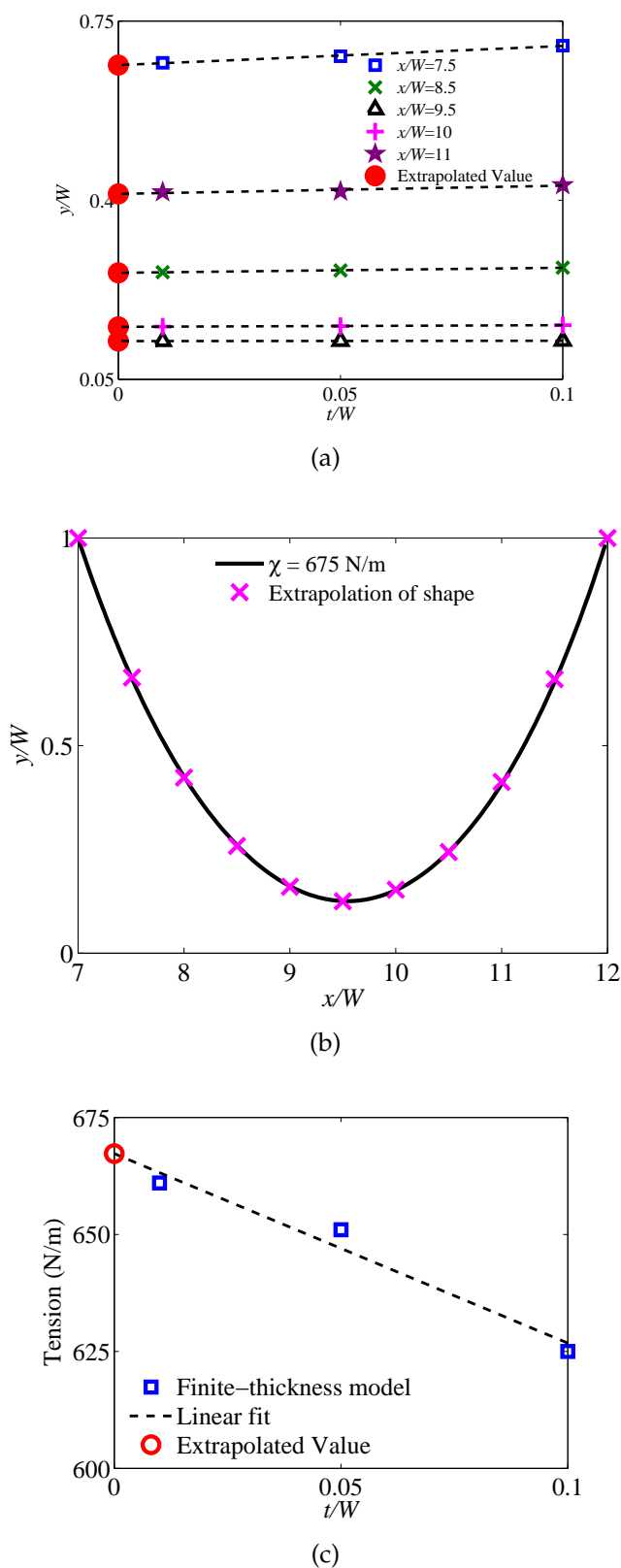


Figure 5.5: (a) Extrapolation to $t = 0$ of the flexible wall shape obtained from the finite thickness elastic solid model, for $t = 0.01 W$, $t = 0.05 W$, and $t = 0.1 W$. (b) Comparison of the shape of the flexible wall predicted by the finite-thickness solid model (symbols) with the prediction of the zero-thickness membrane model (solid line). (c) Extrapolation of average tension acting in the elastic solid to the limit of zero wall thickness.

$Re = 1$, $\rho = 1054 \text{ kg/m}^3$, $U_0 = 1.338 \times 10^{-2} \text{ m/sec}$, $W = 10^{-2} \text{ m}$, $\eta_0 = 0.141 \text{ Pa s}$ and $p_e = 17545 \text{ N/m}^2$. This leads to a prediction of the minimum height of the gap in the channel (beneath the flexible membrane) to be $h/W = 0.125$.

Computations with the finite thickness elastic solid model are then carried out for the same parameter values, for various combinations of flexible wall thickness t , and shear modulus G , such that each combination always leads to the same value of the minimum channel gap height, namely $h/W = 0.125$. It turns out that even though the minimum gap height is the same in both models, the predicted interface shape is not, with the difference increasing with the thickness of the elastic solid. This is clearly a result of the finite thickness of the elastic solid. Consequently, in order to compare the interface shape, an extrapolation procedure has been carried out in which the height of the interface at various locations in the gap, as a function of flexible wall thickness, is extrapolated to the limit of zero wall thickness, as shown in Fig. 5.5 (a). The extrapolated interface shape is then compared with the prediction by the zero-thickness membrane model in Fig. 5.5 (b). Excellent agreement between the two models is obtained.

We still need to evaluate the resultant tension in the finite thickness elastic solid, and examine how it compares with 675 N/m . This is done as follows. First, the tension in the finite thickness solid at a particular location x is estimated by averaging the tangential solid stresses acting across the cross-section at x . An estimate of the overall tension in the solid is then obtained by averaging the tension along the entire length of the flexible solid, for all values of x . The values of the average tension obtained from the finite thickness elastic solid model for $t = 0.01 W$, $t = 0.05 W$, and $t = 0.1 W$ are then extrapolated to $t = 0$, as shown in Fig. 5.5 (c). The extrapolated value of tension (667 N/m) is fairly close to the value of 675 N/m used in the zero-thickness membrane model.

It is appropriate to briefly discuss the fluid models used in the present work before presenting the results, since the differences in behaviour amongst them is essentially due to differences in their rheology.

5.3.2 Fluid models and choice of parameters

Each of the three fluids examined here has distinct qualitative features: (i) The Oldroyd-B fluid is elastic, but does not shear thin. Furthermore, its uniaxial extensional viscosity is unbounded. (ii) The FENE-P fluid is elastic, shear thins, and has a bounded uniaxial extensional viscosity. (iii) The Owens model fluid is elastic and shear thins, but has an

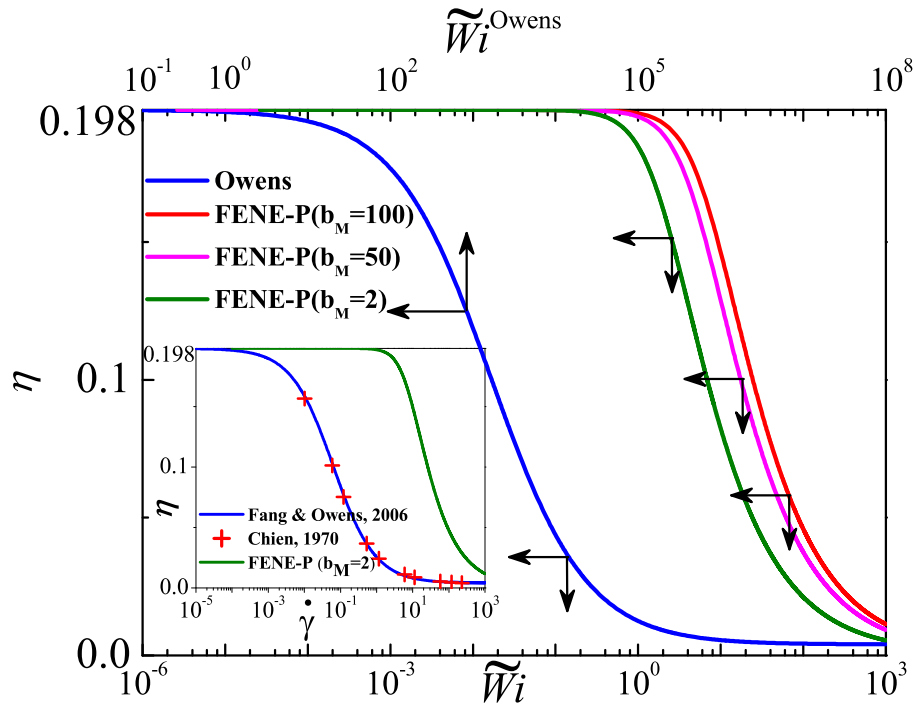


Figure 5.6: The contribution of the microstructure to the total viscosity, η , for the Owens model and FENE-P fluids in steady shear flow as a function of Weissenberg number \widetilde{Wi} . The inset shows the shear rate dependence of viscosity in the Owens model, fitted to the experimental results for blood reported by Chien [1970], and the predictions of the FENE-P model for $b_M = 2$ and $\lambda_0 = 0.263$.

unbounded uniaxial extensional viscosity. Additionally, a notable feature of the Owens model, which belongs to the class of White-Metzner fluids, is that the dependence of viscosity η_p on shear rate $\dot{\gamma}$ can be prescribed arbitrarily through the choice of parameters in the Cross model (see Eq. (2.12)). In particular, the viscosity can be prescribed independently of the relaxation time. In contrast, for the FENE-P model, the dependence of η_p on the shear rate $\dot{\gamma}$ is completely determined by the choice of the parameters, $\eta_{p,0}$, λ_0 , and the finite extensibility parameter b_M . Unlike in the case of the Owens model, no further control can be exerted on the shape of the viscosity function.

The difference in the prediction of viscosity by the FENE-P and Owens models, as a function of the Weissenberg number $\widetilde{Wi} = \lambda_0 \dot{\gamma}$, in steady shear flow, is displayed in

Fig. 5.6. For the Owens model, we set $\eta_{p,0} = 0.197$ Pa s, $\eta_{p,\infty} = 0.003$ Pa s, $\eta_s = 0.001$ Pa s, $\theta_2 = 8$, and $m = 0.75$. These parameter values were chosen by Fang and Owens [2006] to fit experimental data for the steady-state viscosity of blood, as reported by Chien [1970]. The fitted curve and experimental data are reproduced in the inset to Fig. 5.6. Additionally, Fang and Owens [2006] suggest $\lambda_H = 0.004$ s, which leads to $\lambda_0 = 0.263$. In order to compare the two fluid models, we assume that the FENE-P model has the same value of $\eta_{p,0}$ and λ_0 , and that η_s is the same. This assumption is based on the expectation that any choice of viscoelastic model would have to be compatible with known experimental information on the rheology of the fluid, which would, at the least, include a knowledge of the zero shear rate viscosity and the relaxation time. Note that for the FENE-P model, while there is no necessity to prescribe λ_0 when the shear rate dependence of viscosity is expressed in terms of Wi , it is necessary when represented in terms of $\dot{\gamma}$. As is well known, the FENE-P model predicts increasing shear thinning with decreasing values of the finite extensibility parameter b_M . The entire family of curves for the FENE-P model shown in Fig. 5.6, with values of b_M ranging from 100 to 2, does not shear thin as rapidly as the Owens model. In particular, it is clear from the inset that for the parameters recommended by Fang and Owens [2006], the FENE-P model is unable to capture the rapidity with which blood shear thins, even for $b_M = 2$. In all cases, in line with expectation, shear thinning first occurs for the FENE-P fluid when $\widetilde{Wi} \sim O(1)$. For viscoelastic fluids, the onset of shear thinning at $\widetilde{Wi} \sim O(1)$ is an indication that relaxation modes corresponding to time scales larger than λ_0 are responding elastically, while relaxation modes corresponding to smaller times scales are undergoing viscous dissipation. Since the Owens model shear thins at significantly smaller values of \widetilde{Wi} , this suggests that the characteristic time scale below which all modes dissipate energy through viscous dissipation is much larger than λ_0 . As mentioned earlier, λ_0 corresponds to the relaxation time for an aggregate of blood cells, which according to Owens [2006], are typically of a size that represents the greatest proportion of erythrocytes. By defining a Weissenberg number $\widetilde{Wi}^{\text{Owens}}$ for which the Owens model fluid shear thins when it is of $O(1)$ (see the upper horizontal axis of Fig. 5.6), we can estimate that the appropriate relaxation time is of order 10^4 , which must correspond to much larger structures than a typical blood cell aggregate. We do not explore this aspect further here, rather, for the purposes of the present paper, we assume that the FENE-P and Owens models are distinct constitutive models, which have the same zero shear rate material properties, but shear thin significantly differently. As will be discussed in greater detail in the sections below, the difference

between the models leads to significant differences in their behaviour.

For all the computational results reported here, we set $\eta_{p,0}$, $\eta_{p,\infty}$, η_s , θ_2 , and m at the values recommended by Fang and Owens [2006]. However, we vary λ_0 (by varying λ_H) in order to control the inlet Weissenberg number. For the FENE-P fluid, we set $b_M = 100$, which is a value commonly used in simulations. As we are interested in small blood vessels, we choose the width W of the channel to be $100 \mu\text{m}$ and $U_0 = 0.01 \text{ m/s}$, inline with the data reported in Robertson et al. [2008]. The value of Re in small blood vessels is well below 1. We have not seen any significant difference in the profile shape of the collapsible wall for values of Re in the range of 0-1, so we set $Re = 0$ by setting $\rho = 0$.

Deng and Guidoin [1998] have reported the values of Young's modulus for the human artery to be in the range 300-4000 kPa. Zhang and co-workers [Zhang et al., 2004; Zhang and Greenleaf, 2005, 2006a,b] have reported the Young's modulus of the porcine artery to be in the range 110-140 kPa, while using two different values for the external pressure (8 kPa and 9.3 kPa) in their experimental measurements of the Young's modulus. In order to adequately represent the microcirculation, we choose a wide range of values for the external pressure p_e from 1.2 to 16 kPa and G in the range 30 to 400 kPa. Since $P_e = p_e/G$, we keep P_e fixed at a constant value of 0.04 even though both p_e and G are varied. On the other hand, we vary Γ in the range 4.95×10^{-5} to 6.6×10^{-4} . We choose a fixed value of $0.4W$ for thickness of the solid wall (t) as the artery wall thickness to vessel diameter ratio is very high in small blood vessels [Kalita and Schaefer, 2008].

5.3.3 Mesh convergence and the high Weissenberg number problem

Chakraborty et al. [2010] have established that the flow in a collapsible channel with a zero-thickness membrane suffers from the high Weissenberg number problem and have shown that there is a limiting Weissenberg number for each of the fluid models beyond which computations fail. Furthermore, this limiting Wi value has been shown to increase with mesh refinement. Here we study mesh convergence over a range of parameters for the current geometry, using three different meshes M1-M3 for $t = 0.4W$, as illustrated in Fig. 5.7, with the mesh details given in Table 5.1.

In viscoelastic flow, mesh convergence is generally studied by examining the values of the invariants of the conformation dyadic, \mathbf{M} . The eigenvalues m_i of the conformation dyadic represent the square stretch ratios along the principal directions of stretching

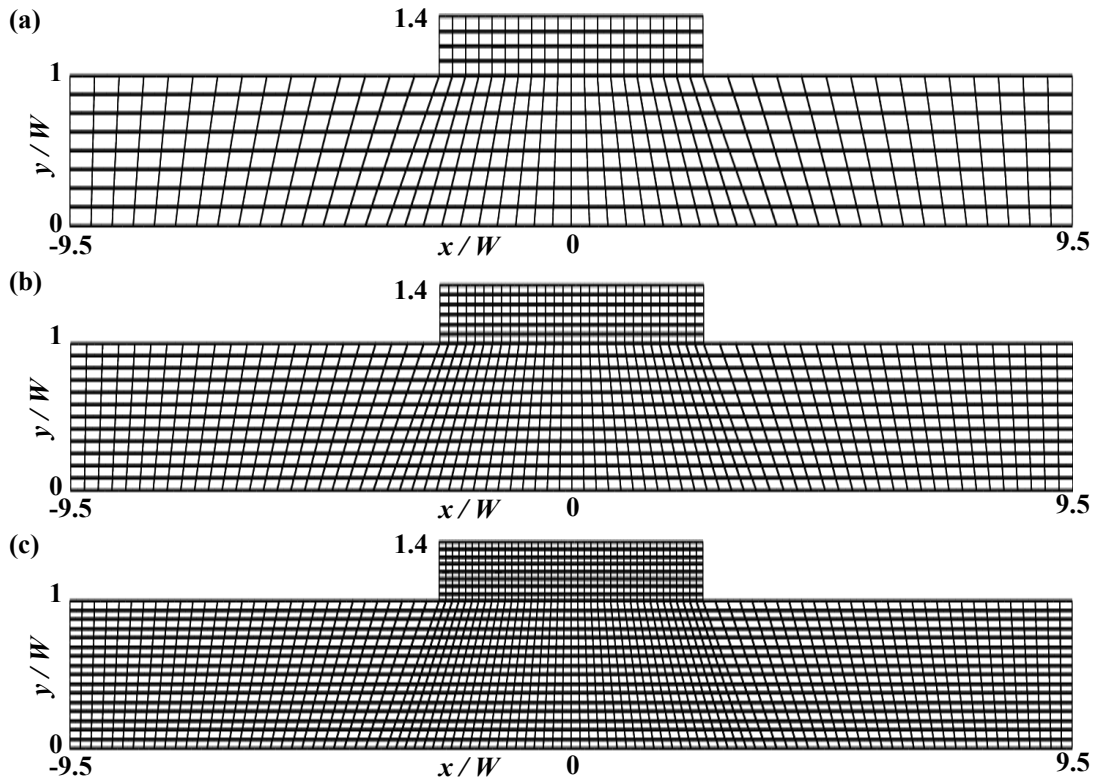


Figure 5.7: Meshes considered in the current study. (a) M1, (b) M2 and (c) M3, for $t = 0.4W$.

Mesh	Number of elements	Number of nodes	Degrees of freedom
M1	400	1705	10972
M2	900	3757	24072
M3	1600	6609	42252

Table 5.1: Meshes considered in the current study.

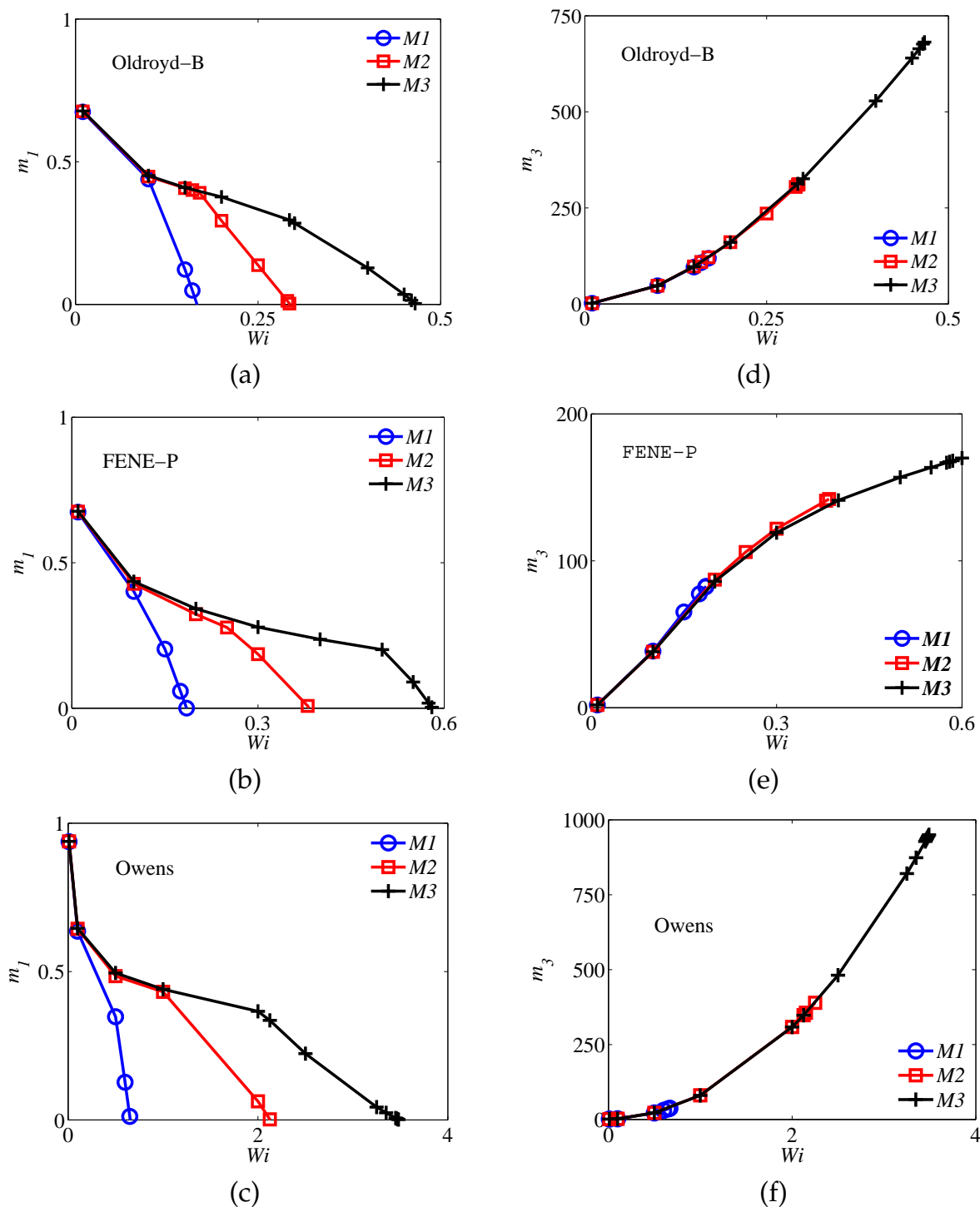


Figure 5.8: Minimum value of the smallest eigenvalue (m_1) and maximum value of the largest eigenvalue (m_3) in the entire flow domain, for the Oldroyd-B ((a) and (d)), FENE-P ((b) and (e)), and Owens model ((c) and (f)), as a function of Wi at $\Gamma = 4.95 \times 10^{-5}$ and $P_e = 0.04$ for $t = 0.4W$.

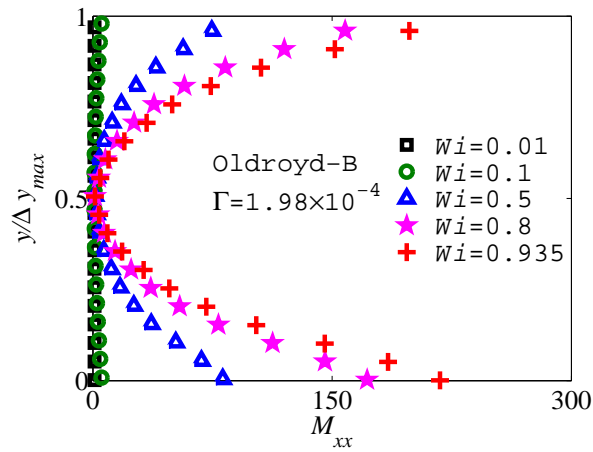
m_i for an ensemble of molecules [Pasquali and Scriven, 2002, 2004]. It has been well established that the breakdown of viscoelastic computations is typically due to the smallest eigenvalue becoming negative in some regions of the flow domain [Bajaj et al., 2008; Chakraborty et al., 2010; Pasquali and Scriven, 2002; Singh and Leal, 1993; Zanden and Hulsen, 1988].

Fig. 5.8 shows the maximum eigenvalue m_3 and minimum eigenvalue m_1 of the conformation tensor as a function of Wi for the Oldroyd-B, FENE-P and Owens fluids at $\Gamma = 4.95 \times 10^{-5}$ and $P_e = 0.04$ for $t = 0.4W$. Fig. 5.8 (a)-(c) clearly exhibits the breakdown of viscoelastic computations at a particular value of Weissenberg number on each mesh, since the minimum value of m_1 becomes negative. This limiting Wi increases with increase in mesh refinement.

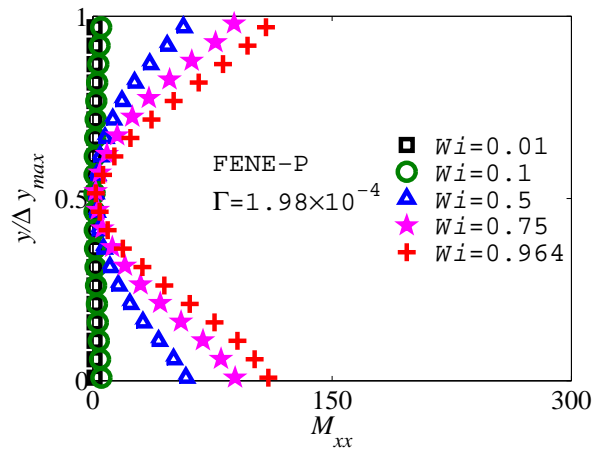
An increase in Wi leads to a higher maximum m_3 and lower minimum m_1 across the flow domain. While the breakdown value of Wi at each mesh can be anticipated from the sudden change of the slope of the curves in the minimum m_1 plots (Fig. 5.8 (a)-(c)), the curves of the maximum m_3 on various meshes overlap with each other (Fig. 5.8 (d)-(f)). The limiting value of Wi on the M2 mesh for the Oldroyd-B, FENE-P and Owens fluids is respectively 0.29, 0.38 and 2.13, while the mesh converged value of Wi for these models is 0.17, 0.20 and 1.0 respectively. In all our analysis, we have ensured that mesh converged values of Wi are used for any particular mesh.

While Fig. 5.8 displays the maximum and minimum eigenvalues in the entire flow field, Fig. 5.9 displays the mean streamwise molecular stretch M_{xx} across the channel at the point where the gap between the flexible and rigid walls is a minimum, for a fixed value of Γ , and increasing values of Wi . With increasing Weissenberg number, M_{xx} grows nearly symmetrically from a relatively low value in the middle of the gap, to a significantly larger value near the bottom (rigid) and top (flexible) walls. Note that in the Oldroyd-B and Owens models, M_{xx} is unbounded due to the infinite extensibility of the Hookean spring in the Hookean dumbbell model which underlies these fluid models. Conversely, the existence of an upper bound to the mean stretchability of the spring in the FENE-P model restricts the maximum value for M_{xx} , which for $b_M = 100$ is 300. The profiles of M_{xx} for the different fluids in Fig. 5.9 clearly reflect this micro-mechanical aspect of the models, and confirm that as in other benchmark problems for non-Newtonian flow, numerical computations in a 2D collapsible channel also fail due to the development of large stresses and stress gradients in certain regions of the flow field, which are related to large changes in the conformations of the molecules.

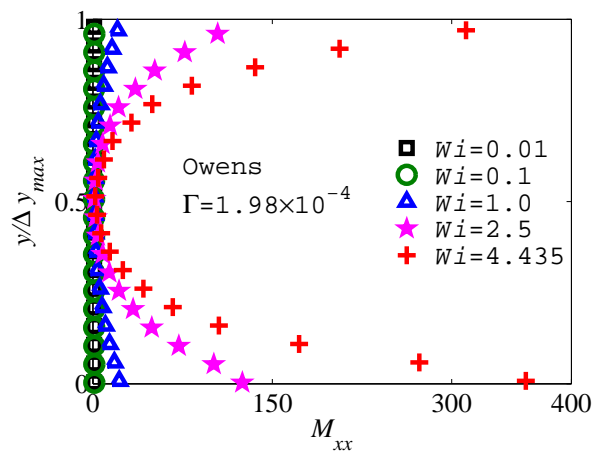
In their earlier study with a zero-thickness membrane, Chakraborty et al. [2010]



(a)



(b)



(c)

Figure 5.9: Profile of M_{xx} across the narrowest channel gap for the Oldroyd-B, FENE-P and Owens models, for a range of Weissenberg numbers, at $\Gamma = 1.98 \times 10^{-4}$. The distance from the bottom channel is scaled by the narrowest gap width Δy_{max} (see Fig. 5.13(a) for a definition) of the particular model.

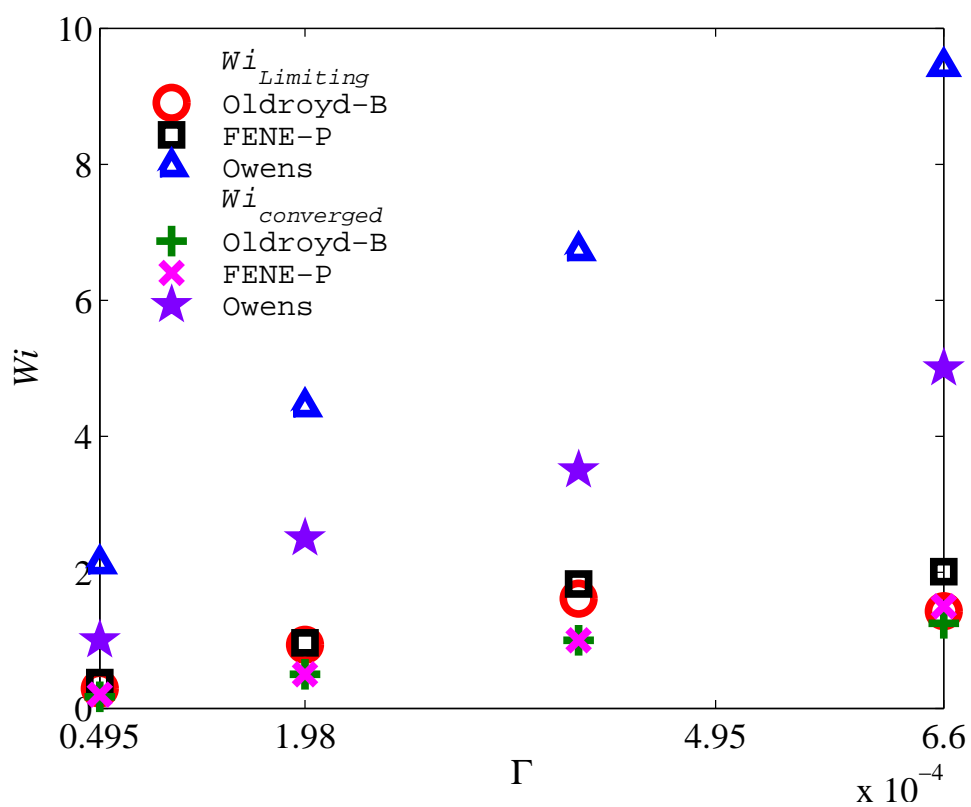


Figure 5.10: Maximum mesh converged value of Wi , and the limiting Wi for the three fluid models, for computations carried out with the M2 mesh, at $P_e = 0.04$ and $t = 0.4W$ for different values of Γ .

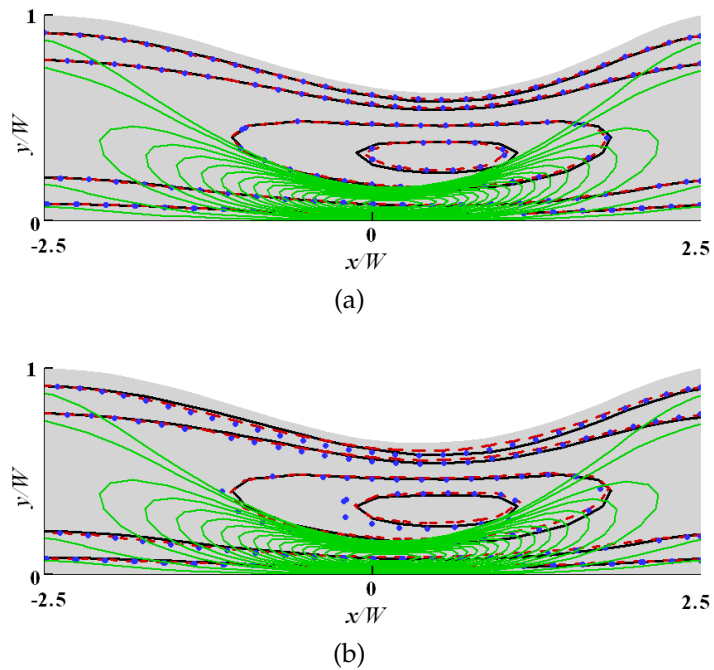


Figure 5.11: Contours of axial velocity (v_x) in the flow domain, for Newtonian (black), Oldroyd-B (red), FENE-P (blue) and Owens (green) fluids at $P_e = 0.04$, $t = 0.4W$ and $\Gamma = 1.98 \times 10^{-4}$ for two different values of Weissenberg number (a) $Wi = 0.1$ and (b) $Wi = 0.5$.

have shown that the extent of collapse of the membrane also has a significant effect on the limiting Weissenberg number. As the gap in the channel becomes narrower with decreasing tension in the membrane, the fluid is 'squeezed' leading to a greater deformation of the molecules, with a concomitant numerical breakdown at smaller values of Wi . The parameter that controls the deformability of the finite thickness wall in the current work is Γ . Fig. 5.10 demonstrates the limiting and the mesh converged values of the Weissenberg number on the M2 mesh for all the values of Γ used in this study. The limiting Weissenberg number increases with an increase in the value of Γ , and follows the trend Owens > FENE-P > Oldroyd-B. The Owens model has the largest gap between the converged and limiting values of Wi . As will be apparent when we discuss the shape of the fluid solid interface in Fig. 5.12, an increase in Γ leads to an increase in the magnitude of the narrowest channel gap, and consequently an increase in the limiting value of Wi .

5.3.4 Velocity fields and interface shape

Fig. 5.11 compares the velocity profile predicted by a Newtonian fluid with those of an Oldroyd-B, FENE-P and Owens' fluid at $P_e = 0.04$, $t = 0.4W$ and $\Gamma = 1.98 \times 10^{-4}$ for two

different values of Wi . The coincidence of the velocity profiles for the Oldroyd-B and FENE-P models with the velocity profile for a Newtonian fluid at $Wi = 0.1$, and the continued coincidence at $Wi = 0.5$ for the Oldroyd-B model suggests that elastic effects do not have a significant influence on the velocity field at these values of Wi . On the other hand, the slight departure of the velocity profile for the FENE-P fluid from the Newtonian velocity profile at $Wi = 0.5$, and the significant departure of the velocity profile for the Owens model, at both values of Wi , indicates that the extent of shear thinning plays a crucial role in determining the velocity profile.

Fig. 5.12 explores the deformation of the finite-thickness solid wall, while interacting with the different fluids. While Fig. 5.12 (a)-(c) investigates the shape of the fluid-solid interface for different values of Γ at $Wi = 0.1$, Fig. 5.12 (d)-(f) examines the dependence of the interface profile on Wi at a fixed value of $\Gamma = 4.95 \times 10^{-4}$. The extraordinary variation in the shape of the elastic solid with varying elasticity parameter Γ is immediately apparent from Fig. 5.12 (a)-(c). In particular, there is a stark contrast in the response of the solid to the flow of different viscoelastic fluids. Except in the case of the Owens model, increasing Γ leads to a movement of the deformable solid from being within the channel (concave downwards) to bulging out of the channel (convex upwards) due to action of the forces exerted by the flowing fluid. At the relatively low value of $Wi = 0.1$ there is no discernible difference between the Newtonian, Oldroyd-B and FENE-P fluids. For the Owens model on the other hand, the elastic solid remains concave downwards for the entire range of Γ values. This behaviour is related to the significant difference in the force field generated in the Owens model fluid due to flow, as discussed shortly.

It is appropriate to note here that in our earlier investigation of viscoelastic flow in a 2D channel with a zero-thickness membrane [Chakraborty et al., 2010], the fluid-solid interface was always observed to be concave downwards for all values of membrane tension. Indeed, in contrast to the situation for a finite thickness solid, with decreasing tension, the zero-thickness membrane moves further into the channel, with a concomitant decrease in the narrowest channel gap.

At a fixed value of elasticity parameter Γ , while Fig. 5.12 (f) indicates that Wi has no effect on the shape of the deformable solid in the case of the Owens model (which remains concave downwards), it has a noticeably different effect for the Oldroyd-B and FENE-P fluids. Both fluids cause the elastic solid to bulge outwards. However, the extent of this bulge decreases more rapidly for the FENE-P fluid with increasing Wi . In the case of the Owens model, at these values of Wi , shear thinning is nearly complete,

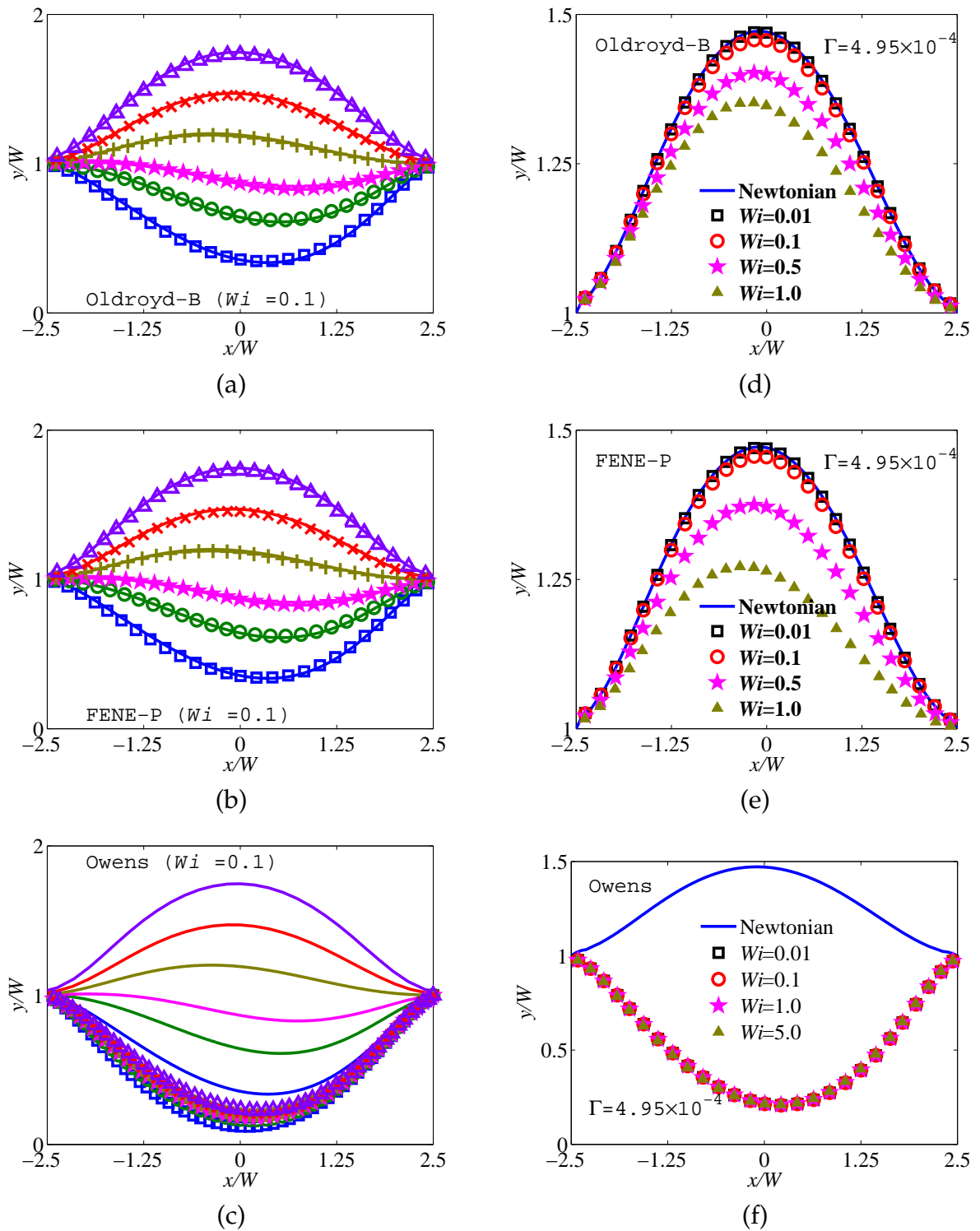


Figure 5.12: The shape of the fluid-solid interface in a 2D collapsible channel for the Oldroyd-B ((a) and (d)), FENE-P ((b) and (e)) and Owens models ((c) and (f)), compared with the profile for a Newtonian fluid. Note that Wi is 0.1 in (a)–(c) and Γ is 4.95×10^{-4} in (d)–(f). In (a)–(c) different symbols represent different values of Γ (\square : 4.95×10^{-5} , \circ : 1.98×10^{-4} , \star : 3.0×10^{-4} , $+$: 3.96×10^{-4} , \times : 4.95×10^{-4} and \triangle : 6.6×10^{-4}). Lines with the same colour as the symbols represent the predictions of a Newtonian fluid for identical values of Γ .

and there is consequently no change discernible in the membrane shape. On the other hand, the onset of shear thinning for the FENE-P model is responsible for the observed variation in the predicted membrane shape from that for an Oldroyd-B fluid.

Fig. 5.12 indicates that the deformation of the solid wall occurs along both axial and vertical directions for all the fluid models, with the extent of movement depending on the values of Γ and Wi . By defining the position of maximum deformation as the point on the elastic solid furthest in the vertical direction from the horizontal surface, this dependence can be examined more systematically. The precise location of the position of maximum deformation is given by the co-ordinate pair $(\Delta x_{max}, \Delta y_{max})$, as shown schematically in Fig. 5.13 (a), which measures the maximum displacement from the centre of the elastic solid when it is horizontal. Fig. 5.13 (b) and (c) tracks the position of maximum deformation for varying Γ and Wi , and correspond to the set of Fig. 5.12 (a-c) and Fig. 5.12 (d-f), respectively. The movement of the elastic solid from being concave downwards to convex upwards in the case of varying Γ , and the downward movement with increasing Wi are clearly captured in this description. The relative immobility of the solid in the case of a flowing Owens model fluid is also clearly revealed.

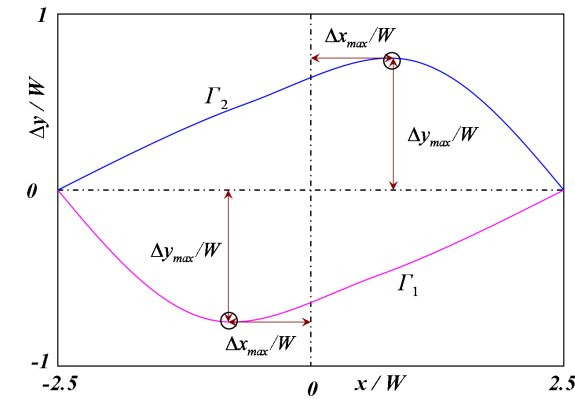
5.3.5 Pressure and stresses

Patankar et al. [2002] have shown analytically that for any constitutive model of the form,

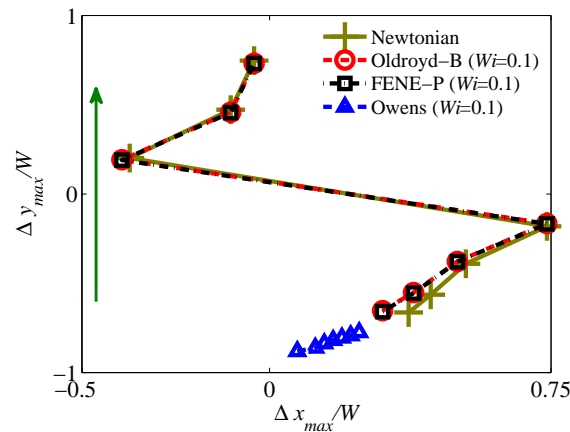
$$a_1 \mathbf{D} + a_2 \overset{\vee}{\mathbf{D}} + a_3 \mathbf{T} + a_4 \overset{\vee}{\mathbf{T}} = \mathbf{0} \quad (5.15)$$

where, a_1, a_2, a_3 , and a_4 are scalar functions of the invariants of \mathbf{D} and \mathbf{T} , and $\overset{\vee}{\mathbf{D}}$ and $\overset{\vee}{\mathbf{T}}$ are the upper convected time derivatives of \mathbf{D} and \mathbf{T} , the *normal component* of extra stress on a rigid body surface will be zero. Chakraborty et al. [2010] have shown numerically that this is true even in the case of flow past a deformable zero-thickness membrane, for all the three viscoelastic fluids considered here. In the present instance as well, we find that the normal component of stress on the elastic wall is solely due to pressure.

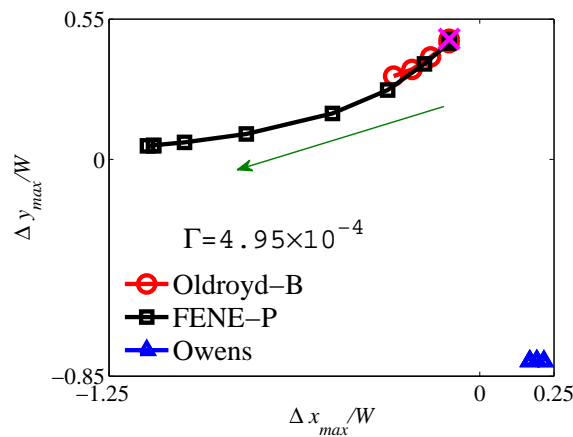
Fig. 5.14 examines the effect of Γ and Wi on the non-dimensional pressure P exerted by the different fluids on the elastic solid. At $Wi = 0.1$, the increase in P with increasing Γ for the Oldroyd-B and FENE-P models is nearly identical to that for a Newtonian fluid, as can be seen from Fig. 5.14 (a) and (b). Notably, for all these fluids, a distinct change occurs in the shape of the pressure profile for $\Gamma > 1.98 \times 10^{-4}$. For values of Γ less than or equal to this value, the pressure profile is relatively constant upstream of the



(a)



(b)



(c)

Figure 5.13: (a) Schematic diagram for defining the position of maximum deformation $(\Delta x_{max}, \Delta y_{max})$. (b) Dependence of $(\Delta x_{max}, \Delta y_{max})$ on Γ at a fixed value of $Wi = 0.1$, and (c) on Wi at a fixed value of $\Gamma = 4.95 \times 10^{-4}$. In (b) and (c) the arrows indicate the direction of increasing Γ and Wi , respectively. The range of Wi for the Oldroyd-B, FENE-P and Owens models are 0.01-1.508, 0.01-2.372 and 0.01-7.9, respectively.

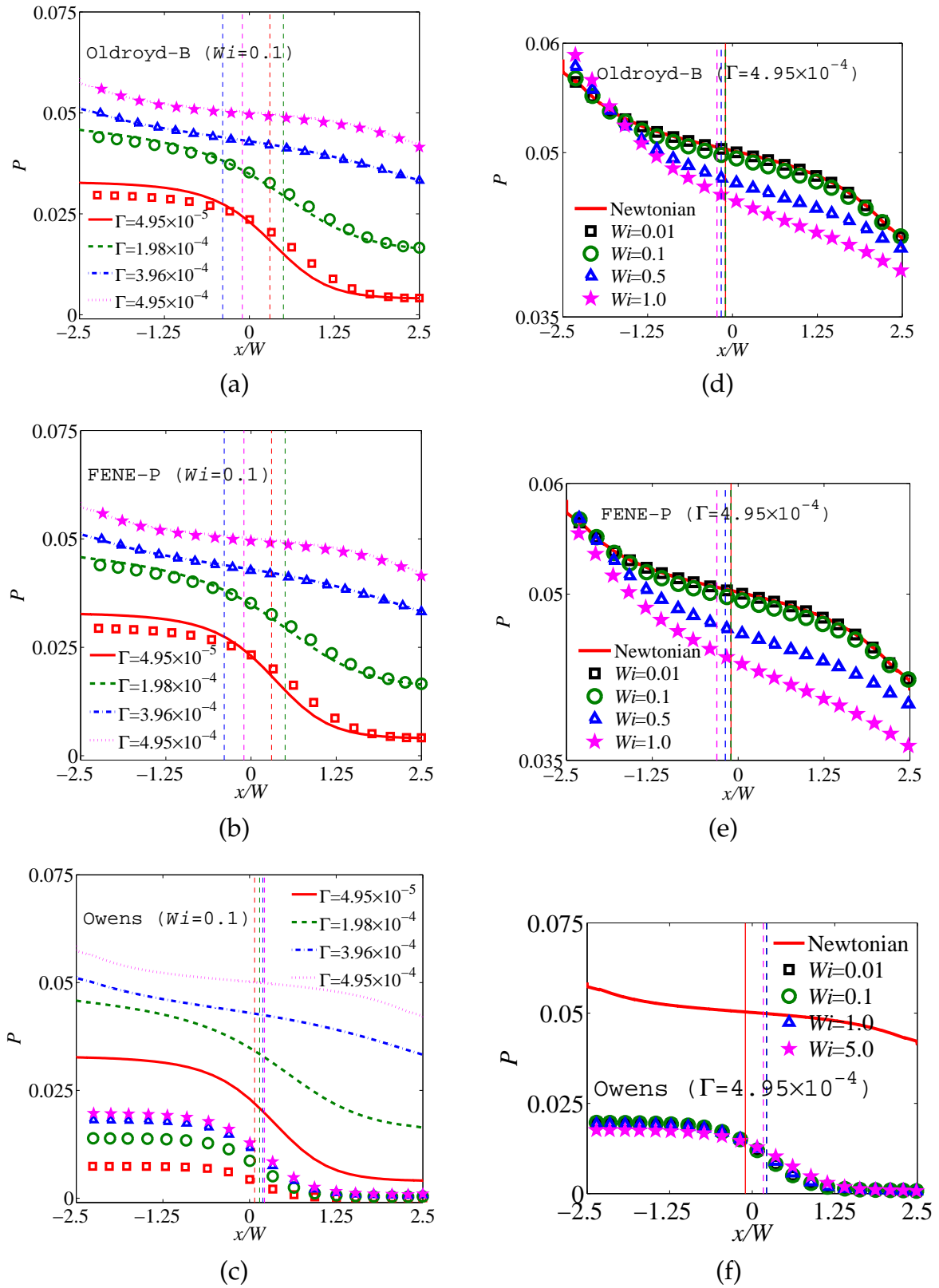


Figure 5.14: Dependence of the pressure profile along the flexible membrane on Wi and Γ , for the Oldroyd-B ((a) and (d)), FENE-P ((b) and (e)) and Owens models ((c) and (f)), respectively. The lines in (a)–(c) are for a Newtonian fluid. Note that $\Gamma = 1.98 \times 10^{-4}$ in (d)–(f) and $Wi = 0.1$ in (a)–(c).

position of maximum deformation, before decreasing relatively rapidly downstream to a constant value. (The vertical lines in the figure denote the x -position of maximum deformation, with the colour coordinated to match the corresponding Γ value). On the other hand, for values of $\Gamma > 1.98 \times 10^{-4}$, the decrease in pressure from the location where the fluid flows under the deformable solid to the location where it exits, is much more uniform. As can be seen from Fig. 5.12 (a) and (b), the change in the shape of the pressure profile is correlated with the change in interface shape that occurs around $\Gamma \sim 3 \times 10^{-4}$, which is approximately the value at which the elastic solid moves from being concave downwards within the channel to bulging outwards from the channel. In the case of the Owens model, even though the pressure increases with increasing Γ , the shape of the pressure profile remains unchanged, since the elastic solid is always concave downwards in shape (see Fig. 5.14 (c) and Fig. 5.12 (c)). Another notable aspect is that the magnitude of pressure at any point along the interface is significantly lower for the Owens model compared to that for all the other fluids. This can be attributed to the significant decrease in viscosity that occurs for the Owens model fluid when it flows under the deformable solid.

Fig. 5.14 (d)-(e) displays the effect of Wi on the pressure profile for a fixed value of $\Gamma = 4.95 \times 10^{-4}$. At this value of Γ , as seen earlier in Fig. 5.12 (d)-(f), for all the values of Wi considered here, the elastic solid bulges outwards from the channel due to interaction with the Oldroyd-B and FENE-P fluids, while it is concave downwards for the flow of an Owens model fluid. In the former two cases, with increasing Wi , there is a clear decrease in the pressure that the fluid exerts on the downstream end of the elastic solid, with the decrease being more substantial for the FENE-P fluid. This correlates with the decrease in the bulge of the elastic solid seen earlier in Fig. 5.12 (d) and (e). For the Oldroyd-B fluid, there also appears to be a slight increase in pressure at the upstream end of the elastic solid. In the case of the Owens model fluid, neither the interface shape nor the pressure profile are significantly altered by the variation in Wi .

A different perspective on fluid pressure in the channel is provided in Fig. 5.15, where the pressure drop ΔP in the channel between the entrance and exit to the region beneath the elastic solid, is displayed. As seen earlier in Fig. 5.12 (a)-(b), with increasing Γ , the interface shape for the Oldroyd-B and FENE-P fluids moves from being concave downwards to convex upwards. Fig. 5.15 (a) shows that this is accompanied by an increase in ΔP . Interestingly, the rate of change of ΔP with Γ has a point of inflection around $\Gamma \sim 3 \times 10^{-4}$, which is approximately the value at which the elastic solid becomes

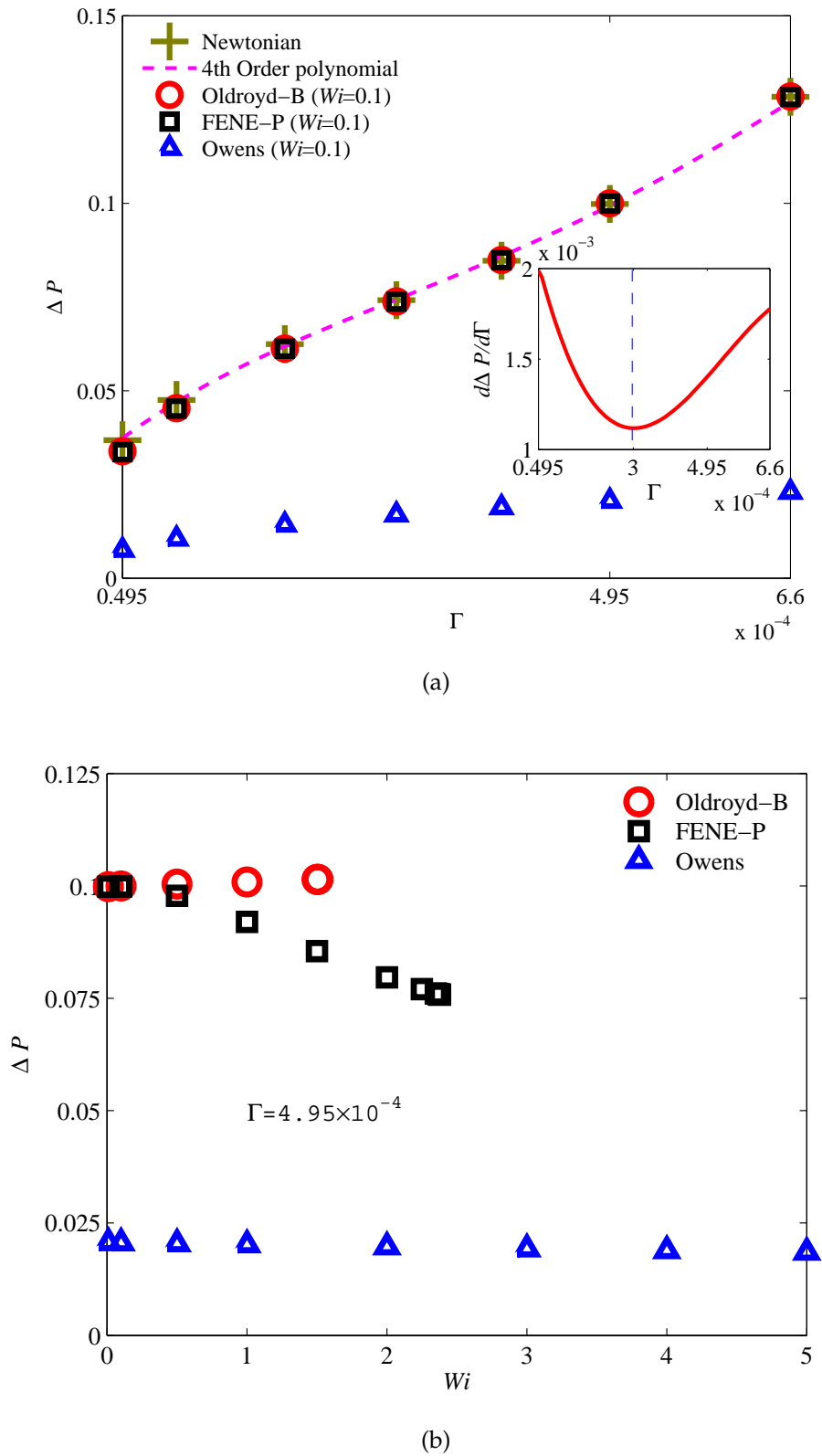


Figure 5.15: Dependence of pressure drop ΔP in the channel for the Oldroyd-B, FENE-P and Owens models on (a) Γ at a fixed value of $Wi=0.1$ and (b) Wi at $\Gamma = 1.98 \times 10^{-4}$. Note that for a Newtonian fluid, $\Delta P = 0.1$. The curves terminate at the limiting Weissenberg number for each model.

horizontal (see Fig. 5.12 (a)-(b), and inset to Fig. 5.15 (a)).

A striking manifestation of differences in the prediction of a macroscopic property, because of differences in fluid rheology, is displayed in Fig. 5.15 (b), where the dependence of pressure drop ΔP on Weissenberg number Wi is plotted. The Owens model fluid has a nearly constant pressure drop because the fluid has undergone significant shear thinning, and has an almost constant viscosity under the deformable elastic solid for all values of Wi . For the Oldroyd-B model on the other hand, which is a constant viscosity fluid, there appears to be a very slight increase in ΔP . Clearly, the decrease in pressure at the downstream end of the channel, is more than made up with the increase at the upstream end. For the FENE-P fluid, the increasing shear thinning with increasing Wi is reflected in Fig. 5.15 (b) with the observed decrease in ΔP .

Fig. 5.16 explores the dependence of the axial component of the conformation tensor M_{xx} , along the flexible wall, on Γ and Wi . Fig. 5.16 (a)-(c) shows that an increase in Γ leads to a decrease in the degree of stretching experienced by the micro-structural elements, and that the value of M_{xx} in the Owens model is much less sensitive to the value of Γ compared to the Oldroyd-B and FENE-P fluids. For the latter two fluids, for values of $\Gamma \lesssim 3 \times 10^{-4}$, the elastic solid is concave downwards. As a result, the M_{xx} profile has a maximum at the location in the channel where the gap is narrowest. As the elastic solid moves out of the channel, there is a significant relaxation in the degree to which the micro-structural elements are stretched.

The correlation between interface shape and M_{xx} profile is more strikingly revealed in Fig. 5.16 (d)-(e), where the dependence of M_{xx} on Wi is explored at a constant value $\Gamma = 4.95 \times 10^{-4}$. Since the interface always bulges outwards for the Oldroyd-B and FENE-P fluids at this value of Γ , the highest stretch occurs at the *inlet* and *outlet* to the deformable region, in contrast to the situation for the Owens model, where the elastic solid is always concave downwards, and consequently, the maximum stretch is always at the location of the narrowest gap.

Finally, the dependence of the total shear stress on the elastic solid, $\tau_t^s + \tau_t^p$, on the parameters Γ and Wi , is examined in Fig. 5.17 for the three viscoelastic fluids. Once again, there is close parallel between the shape of the fluid-solid interface and the shear stress on the wall. Indeed, the shear stress profiles are either concave downwards or convex upwards in complete synchrony with the interface shape. In contrast to the zero-thickness membrane model, where the shear stress on the membrane has no influence on membrane shape because of the use of a boundary condition that only accounts for the influence of the normal stress, in the present model, both the pressure

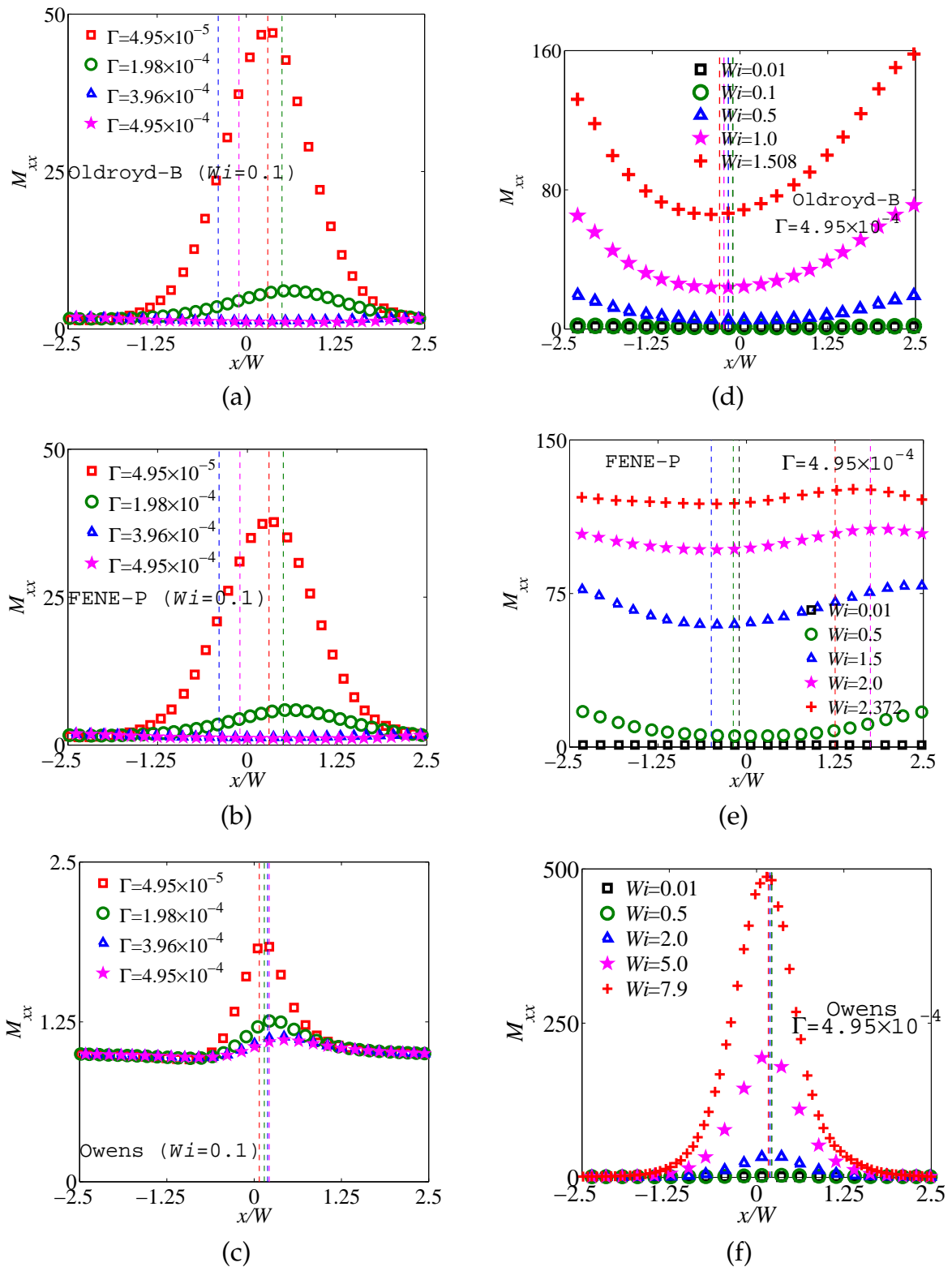


Figure 5.16: Dependence of the axial component of the conformation tensor M_{xx} on Γ , for (a) Oldroyd-B, (b) FENE-P, and (c) Owens models, at $Wi = 0.1$, and dependence of M_{xx} on Wi , for (d) Oldroyd-B, (e) FENE-P, and (f) Owens models, at $\Gamma = 4.95 \times 10^{-4}$.

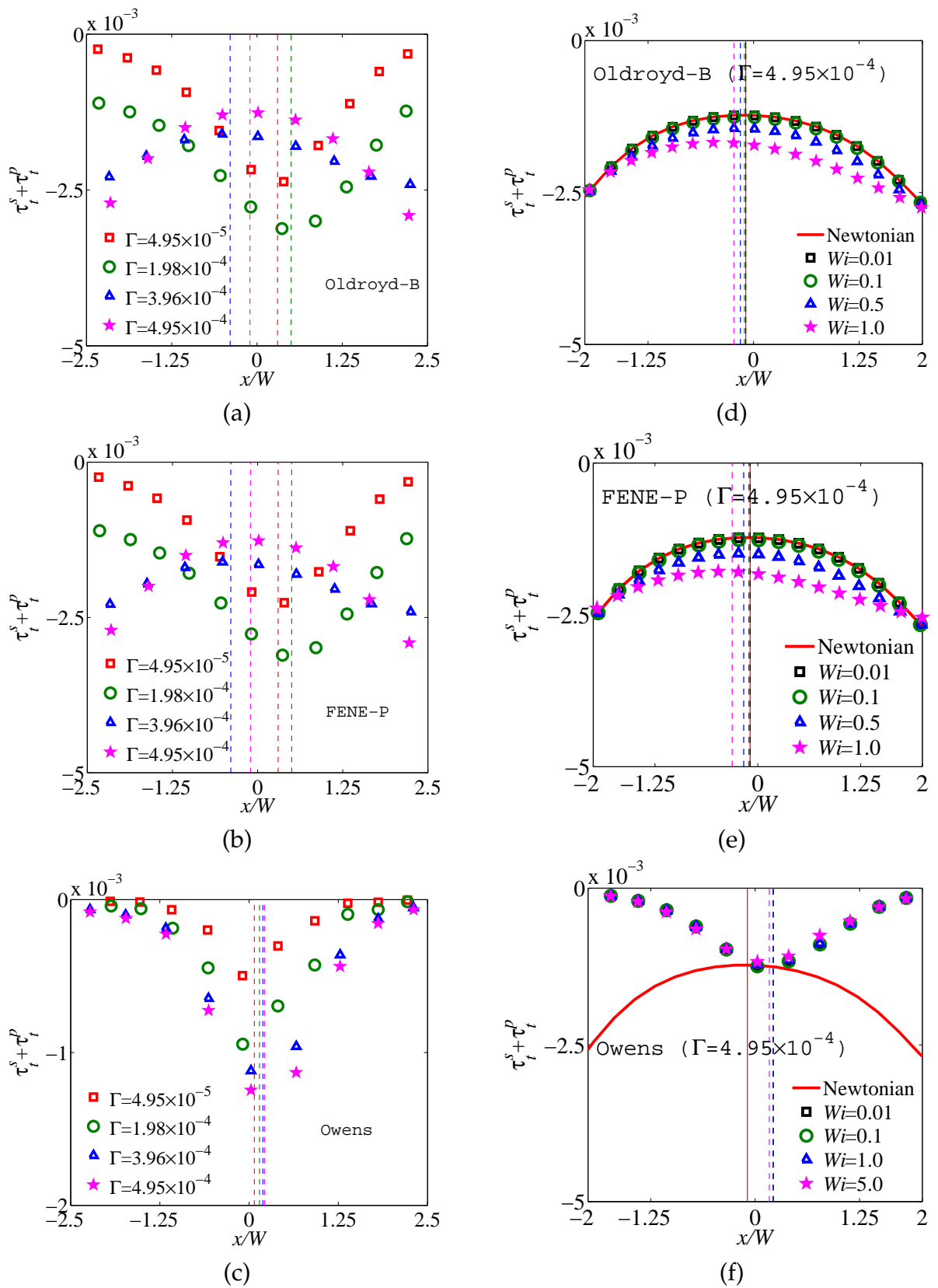


Figure 5.17: Dependence of the tangential component of stress $\tau_t^s + \tau_t^p$ on Γ , for (a) Oldroyd-B, (b) FENE-P, and (c) Owens models, at $Wi = 0.1$, and dependence of $\tau_t^s + \tau_t^p$ on Wi , for (d) Oldroyd-B, (e) FENE-P, and (f) Owens models, at $\Gamma = 4.95 \times 10^{-4}$.

and the shear stress are responsible for the membrane shape. As a result, a much greater variety of interface shapes is observed for a finite thickness elastic solid.

5.4 Conclusions

In order to use a more realistic model for the collapsible wall, the zero-thickness membrane model has been replaced by a finite-thickness incompressible neo-Hookean solid which accounts for the effect of shear stress on membrane shape. A modified version of Carvalho's fluid-structure interaction formulation [Carvalho and Scriven, 1997] together with the DEVSS-TG/SUPG mixed finite element method is used to solve for the fluid velocity, stress field and deformation of the solid wall. We have found significant differences in the fluid-solid interface profiles from the Newtonian fluids for all values of Γ for the Oldroyd-B, FENE-P and Owens models.

1. We have found a limiting Weissenberg number which is very sensitive to viscoelastic models and depends on dimensionless solid elasticity parameter Γ .
2. The axial component of the conformation tensor M_{xx} has a large value for both the Oldroyd-B and Owens models near the maximum deformed position of the fluid-solid interface. This can be attributed to the breakdown of numerical computations.
3. The shape of the membrane as a function of a membrane elasticity parameter Γ , and of the Weissenberg number Wi has been studied, and the change in shape has been used as an indication of the extent of fluid-structure interaction.

Chapter 6

Collapsible microchannel

6.1 Introduction

Experiments on flow through a collapsible tube [Bertram, 1982, 1986, 1987; Bertram and Castles, 1999; Bertram and Elliott, 2003; Bertram and Godbole, 1997; Bertram et al., 1990, 1991; Brower and Scholten, 1975; Conrad, 1969] were carried out in large diameter tubes (13-15 mm) at high Reynolds numbers (>100) and the theory for predicting the Newtonian fluid flow in collapsible macrochannels/macrotubes is well established [Hazel and Heil, 2003; Heil and Jensen, 2003; Liu et al., 2009a; Luo and Pedley, 1995, 1996; Marzo et al., 2005]. However, to the best of our knowledge none of the studies have used a collapsible microchannel. In this chapter, we investigate fluid flow in a collapsible microchannel made of PDMS (approximate length 30 mm and width $200\mu\text{m}$). Initially, to characterize the elastic behaviour of PDMS, the deformation of the thin PDMS membrane is measured without fluid flow in the channel. Upon establishing the PDMS properties, fluid is introduced in the channel. We have used two-dimensional Navier-Stokes equations to predict the behaviour of the fluid flow, however special care has been taken to eliminate the effect of the third dimension. In this study, measurements of the deformation of the PDMS membrane having different widths has been performed in addition to the finite element analysis to extract the elastic modulus of the PDMS membrane from the load-displacement data.

This chapter is organized as follows. Section 6.2 presents the microfabrication process employed to fabricate the collapsible microchannel. Section 6.3 compares the experimental results with the simulation, and Section 6.4 summarises our conclusions.

6.2 Method

6.2.1 Design of a PDMS collapsible microchannel

Optical transparency, gas permeability, biocompatibility and elasticity of PDMS polymers, makes them suitable for studying several phenomena in the microcirculation [Duffy et al., 1998; Leclerc et al., 2003]. The fabrication of microfluidics channels using PDMS has been done following the standard microfabrication method [Duffy et al., 1998; Unger et al., 2000]. Fig. 6.1 schematically shows the microfabrication process to produce a collapsible microchannel. The mold for the PDMS collapsible microchannel is created by standard photolithography technique. The photomask for the mold is designed by AUTOCAD software and a laser quartz photomask is prepared by printing in a chromium deposited quartz plate (420 000 dpi/600 nm). To prepare the mold, we have used SU-8 (SU-8 2035, MicroChem, Newton MA USA) negative photoresist. Initially, the SU-8 photoresist was spin coated on a cleaned silicon wafer to achieve an approximate thickness of 100 to 200 μm by varying spinning speed. The photoresist film was then prebaked (soft baked) (at 65°C for 10 min and 95°C for 120 min) on a hot plate. For high aspect-ratio mold multiple layers of SU-8 are spin coated and subsequently prebaked. After the soft baking process, the SU-8 covered wafer with mask atop was exposed to UV radiation with a wavelength of 350–400 nm for 60 s. To enhance the cross-linking in the exposed portions of the SU-8 a two-stage postexposure bake procedure (65°C for 1 min and 95°C for 20 min) was then used. The wafer was developed by keeping it in a MicroChem SU-8 developer solution for 20 min. The dimension of the mold was confirmed by taking several measurements with a profilometer.

Once the mold is created, PDMS (Dow and Corning Sylgard 184) which is a two-part system, is mixed in the ratio of cross-linker: siloxane equal to 1:10 and is then kept in a vacuum chamber to remove the bubbles generated during mixing. It is well established that the changes in mixing ratio and curing procedure can alter the rigidity of the PDMS significantly [Friend and Yeo, 2010; Fuard et al., 2008; Hohne et al., 2009]. Hence, we strictly followed the mixing ratio and curing procedure to keep the rigidity of the PDMS channel the same when making different devices. PDMS was then poured over the mold and cured at 70°C for two hours in an oven yielding an inverse cast of the patterned mold. The PDMS structure was then peeled away from the mold and holes were punched to provide for inlet and outlet ports and outlets for a pressure sensor. The PDMS channels are oxidized in a plasma cleaner for 2 min and then bonded with another piece of PDMS.

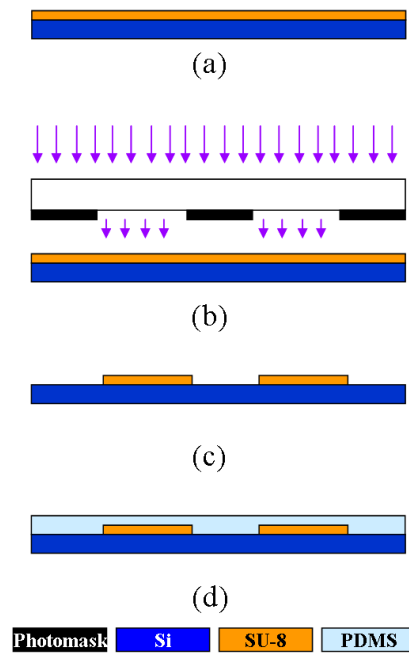


Figure 6.1: Schematics of the fabrication process used to produce the collapsible microchannel, (a) spin coating of the SU-8 2035 negative photoresist on a silicon wafer, (b) exposing the photoresist to UV radiation in a standard photolithography process, (c) development to prepare the SU-8 structured mold and (d) inverse cast of the patterned mold made of PDMS upon curing.

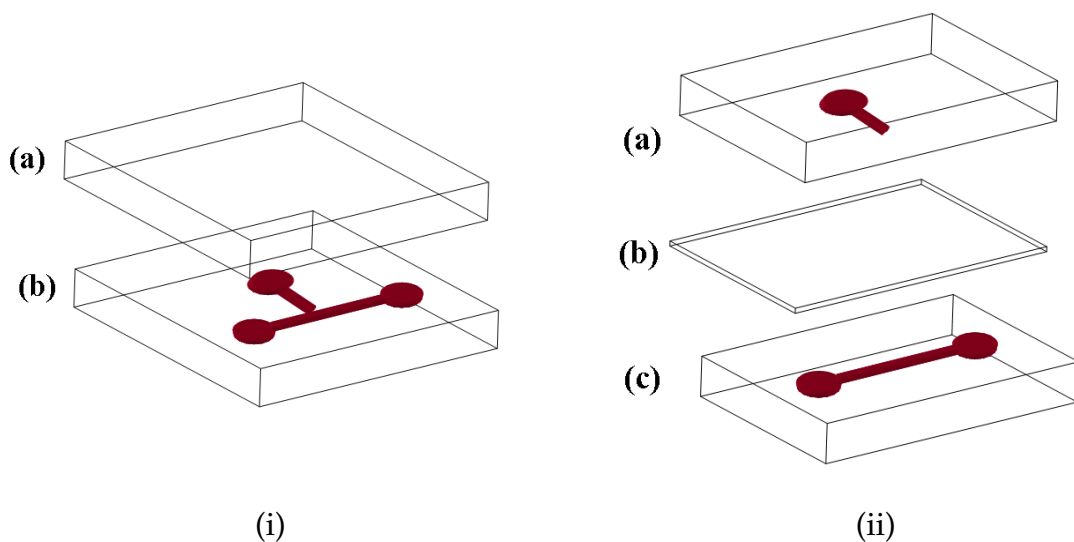


Figure 6.2: Exploded view of the collapsible microchannel fabricated for the present study, (i) design type 1 and (ii) design type 2.

Fig. 6.2 shows two different designs for fabricating collapsible microchannels. In one type of design (device type one, DT1) a single casted PDMS structure contains the fluid channel, pressure chamber and flexible membrane, where as in the other type (DT2), the fluid channel, pressure chamber and flexible membrane are separately cast. In DT1 the width of the channel (W) is decided by the spin coated thickness of the SU-8, while this thickness decides the height (H) of the channel for DT2. The width of the DT1 devices are limited because of the challenges in making a high thickness SU-8 mold.

Fig. 6.3 shows the images of the mold and final devices which are fabricated using the two different approaches adopted in the present study. While following the fabrication process for DT1 we have successfully fabricated collapsible microchannels of three different widths, approximately 0.3, 0.45 and 0.67 mm. In these types of devices the thin PDMS membrane structure is developed due to the maintenance of a gap of approximately $80\ \mu\text{m}$ between the fluid channel and pressure chamber. It was not possible to generate an SU-8 mold of thickness more than 0.67 mm, since the gap did not develop properly which in turn limited the width of the channel to 0.67 mm. However, we have successfully fabricated collapsible microchannels of six different widths, approximately 0.22, 0.5, 1.0, 2.0, 3.0 and 4.0 mm using the fabrication process for DT2.

6.2.2 Analytical solution for pressure drop

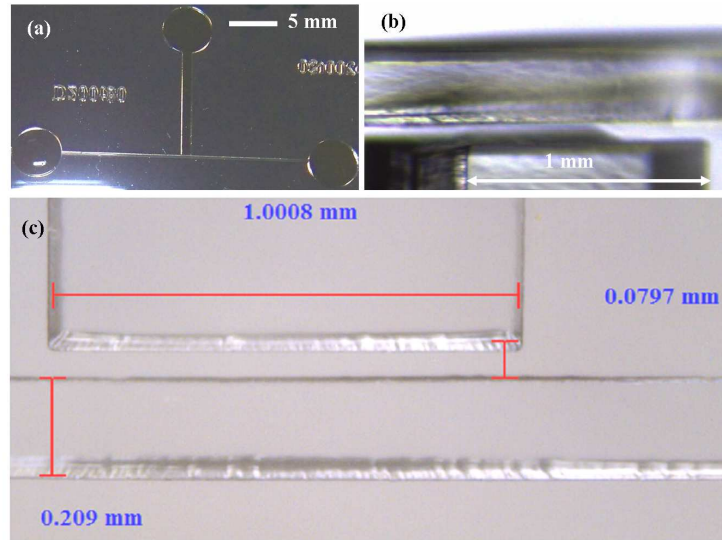
The equations of motion for steady, incompressible flow in the absence of body forces are:

$$\nabla \cdot \mathbf{v} = 0 \quad (6.1)$$

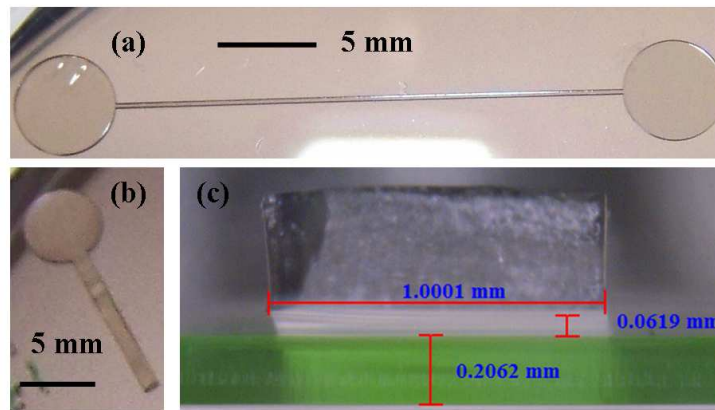
$$\rho \mathbf{v} \cdot \nabla \mathbf{v} = \nabla \cdot (-p\mathbf{I} + \boldsymbol{\tau}) \quad (6.2)$$

where ρ is the density of the liquid, \mathbf{v} is the velocity, ∇ denotes the gradient, p is the pressure, \mathbf{I} is the identity tensor, $\boldsymbol{\tau}$ is the viscous stress tensor. For a Newtonian fluid, the viscous stress tensor is $\boldsymbol{\tau} = 2\eta\mathbf{D}$, where η is the viscosity of the liquid and $\mathbf{D} = \frac{1}{2}(\nabla\mathbf{v} + \nabla\mathbf{v}^T)$ is the rate of strain tensor.

In general, fluid flow in a microchannel is characterized by low Reynolds numbers [Squires and Quake, 2005]. In a fully developed steady Poiseuille flow through a long, straight, rigid rectangular microchannel, the velocity field cannot depend on the



(a)



(b)

Figure 6.3: Images of patterned SU-8 mold and PDMS devices for (i) design type 1 ((a) SU-8 mold, (b) close view of the gap between fluid channel and pressure chamber and (c) final PDMS device) and (ii) design type 2 ((a) SU-8 mold for fluid channel, (b) SU-8 mold for pressure chamber and (c) final PDMS device).

flow direction (x), while only its x component can be non-zero. These simplifying assumptions on the Navier-Stokes equations result in the following equation (x direction only).

$$0 = -\frac{\partial p}{\partial x} + \eta \left(\frac{\partial^2 v_x}{\partial y^2} + \frac{\partial^2 v_x}{\partial z^2} \right) \quad (6.3)$$

The analytical solution of the equation 6.3 is straightforward for a channel with circular cross section (Hagen and Poiseuille flow), while an approximate solution is obtained as a Fourier sum for the flow in a channel with a rectangular cross-section which is the frequently encountered shape especially in microfluidics [Bruus, 2008; Mortensen et al., 2005; White, 1991]. The velocity profile in a rectangular microchannel is given by

$$v_x = \frac{4H^2\Delta p}{\pi^3\eta L} \sum_{n,odd}^{\infty} \frac{1}{n^3} \left[1 - \frac{\cosh(n\pi\frac{y}{H})}{\cosh(n\pi\frac{W}{2H})} \right] \sin(n\pi\frac{z}{H}) \quad (6.4)$$

where L is the length of the channel, W is the width of the channel, Δp is the total pressure drop and H is the height of the channel. The flow rate Q can be obtained upon integration of equation 6.4 along the width and height of the channel [Bruus, 2008; White, 1991],

$$Q = \frac{H^3W\Delta p}{12\eta L} \left[1 - \sum_{n,odd}^{\infty} \frac{192H}{n^5\pi^5W} \tanh(n\pi\frac{W}{2H}) \right] \quad (6.5)$$

In the worst case, i.e. when $H = W$, the approximate value of Q considering only the first term of the series gives an error of 13% in comparison to the value including all the terms in the series.

6.2.3 ANSYS formulation

The incompressible neo-Hookean model described in Section 2.1.2 is only valid for a two-dimensional geometry. However, to solve in a three-dimensional geometry, we have considered the ANSYS plain strain model for a compressible neo-Hookean solid. Here we briefly present the ANSYS formulation for simulating rubber-like materials which undergo large deformations and are termed hyperelastic solids. The geometrical transformations in this type of material are described in terms of the deformation gradient tensor (\mathbf{F}). Hyperelastic materials are described by a strain-energy density function or a elastic potential function \widehat{W} . This quantity is a function of strain tensors and its derivative with respect to a strain component determines the corresponding stress component. This stress can be obtained as

$$\widehat{\mathbf{S}} = 2 \frac{\partial \widehat{W}}{\partial \mathbf{C}} \quad (6.6)$$

where $\widehat{\mathbf{S}}$ is the second Piola-Kirchoff stress tensor and \mathbf{C} is the right Cauchy-Green strain tensor which is expressed as $\mathbf{C} = \mathbf{F}^T \cdot \mathbf{F}$.

The strain energy potential for the neo-Hookean material can be expressed as

$$\widehat{W} = \frac{G}{2} (I_1 - 3) + \frac{1}{d} (J - 1)^2 \quad (6.7)$$

where I_1 is the first invariant of the right Cauchy-Green deformation tensor which can be expressed as $I_1 = \text{tr}(\mathbf{C})$. In the above equation, G is the initial shear modulus of the material, d is the material incompressibility parameter and J which is the ratio of the deformed elastic volume over the undeformed volume of material expressed as $J = \det(\mathbf{F})$.

If the acceleration and body forces are negligible, the equilibrium equation in the current (deformed) configuration is simply

$$\nabla_x \cdot \boldsymbol{\sigma} = \mathbf{0} \quad (6.8)$$

where $\boldsymbol{\sigma}$ is the Cauchy stress tensor which is related to the second Piola-Kirchoff stress tensor as $\boldsymbol{\sigma} = J^{-1} \mathbf{F} \cdot \widehat{\mathbf{S}} \cdot \mathbf{F}^T$.

6.3 Results and discussions

6.3.1 Deformation of the PDMS membrane without fluid flow

Initially, to characterize the elastic properties of PDMS, the deformation of the thin PDMS membrane was measured without fluid flow in the channel. One of the major aims of the present study is to compare the experimental results with the two-dimensional computational model developed here. It is consequently important to fabricate a collapsible microchannel which can display two-dimensional features. One of the possible means of reducing the dimensionality is to make the third dimension (width of the channel in this case) very large compared to the other dimensions. In this type of collapsible microchannel, however, the value of width at which two-dimensional behaviour can be observed is not known *a priori*. Thus collapsible microchannels for three different widths, approximately 0.3, 0.45 and 0.67 mm were fabricated. The deformation of the thin PDMS membrane with the applied external pressure was captured by microvideography using a Dino-Lite–Digital Microscope.

Fig. 6.4 displays the deformed shape of the membrane for an external pressure of 85 kPa. The deformation of the membrane is extracted from such images. Fig. 6.5 shows the maximum deformation (Δz_{\max}) of the flexible membrane in the three collapsible

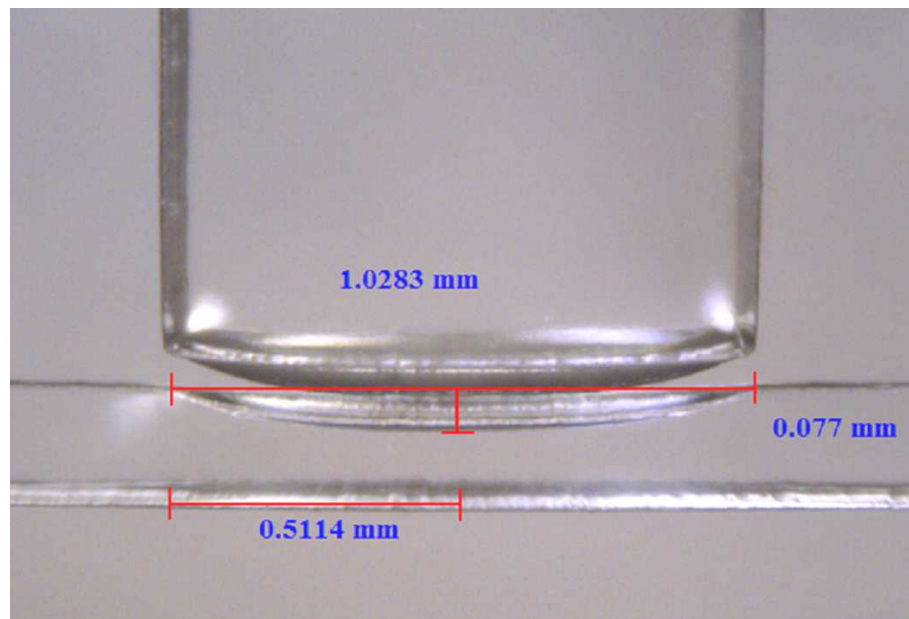


Figure 6.4: Microscopic image of the deformation of the flexible membrane with an application of external pressure $P_e = 85$ kPa for a collapsible microchannel (DT1) with channel width of approximately 0.3 mm.

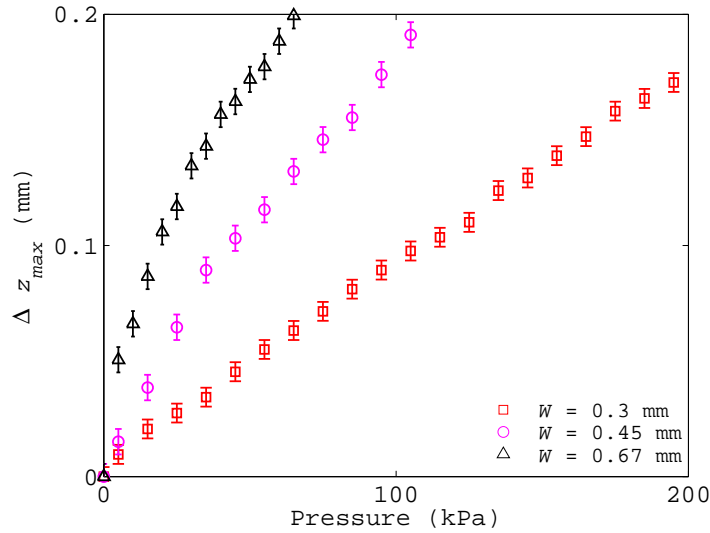


Figure 6.5: Dependence of maximum deformation Δz_{max} of the bottom surface of the flexible membrane on external pressure (P_e) for micro-collapsible channel (DT1) with three different channel widths.

microchannels with applied external pressure. As may be expected, the increase in the width of the channel alleviates the end effects imposed by the fixed ends of the flexible membrane at the two extremes of the channel width. However, the two-dimensional behaviour cannot be derived from the deformation in these devices.

To get an idea of the approximate value of W at which the importance of the width in the third dimension diminishes, finite element analysis was performed with a standard simulation tool for elastic analysis namely, the structural mechanics module of ANSYS. Only the thin PDMS membrane was simulated by considering a finite-thickness rectangular membrane with a fixed thickness of $60 \mu\text{m}$ and a length of 1 mm and varying widths (0.2, 0.5, 1.0, 2.0, 3.0 and 4.0 mm). Since ANSYS does not converge for the incompressible case, i.e. when the Poisson ratio (ν) is 0.5, we have carried out simulations at $\nu = 0.495$. All the edges were kept fixed and an external pressure applied on the top surface of these membranes, while keeping the pressure on the bottom surface at zero. Nanoindentation tests were used to evaluate the values of Young's modulus for the PDMS membranes, and values in the range of 1.2 to 2.2 MPa were obtained. A detailed description of the nanoindentation test results can be found in Appendix C. The thin PDMS membrane is modelled as a nearly incompressible

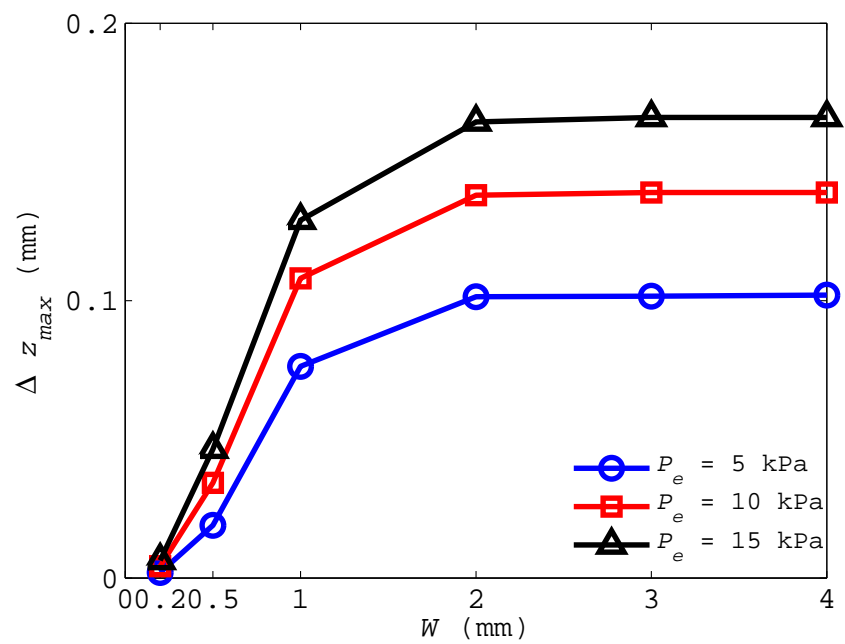


Figure 6.6: Dependence of maximum deformation Δz_{max} of the bottom surface of the flexible membrane on width W at three different values of external pressure $P_e = 5, 10$ and 15 kPa obtained from ANSYS simulation.

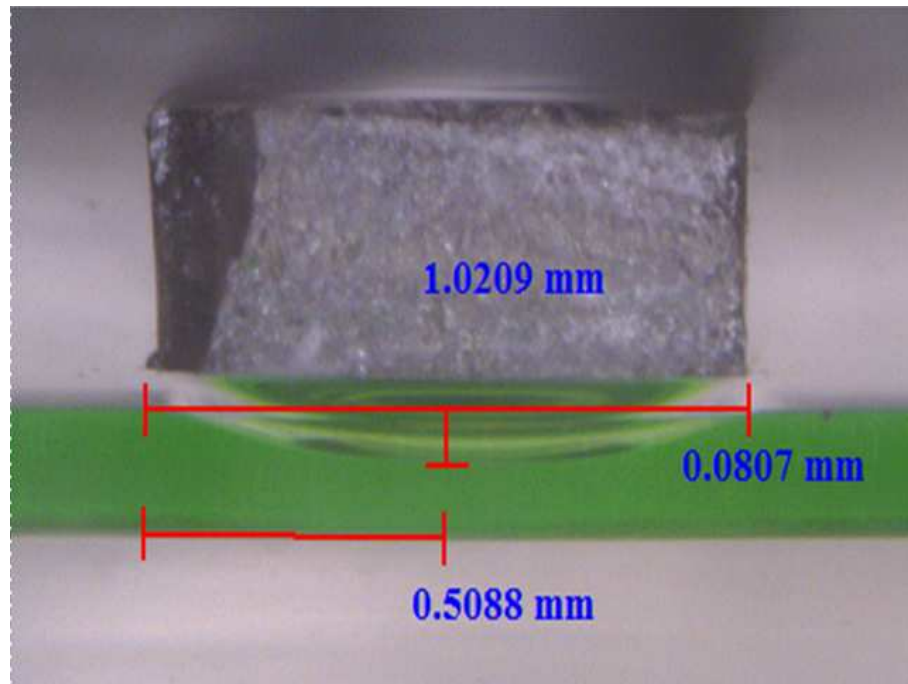


Figure 6.7: Microscopic image of the deformation of the flexible membrane with an application of external pressure $P_e = 20$ kPa for collapsible microchannel (DT2) with channel width of approximately 0.5 mm.

non-linear neo-Hookean elastic material with Young's modulus of $E = 2$ MPa and a Poisson ratio of $\nu = 0.495$. The maximum deformation of the bottom surface of the flexible PDMS membrane is extracted from the simulation at different pressures. Fig. 6.6 clearly shows the appearance of 2D behaviour, starts at around $W = 2$ mm.

It is now clear from the preliminary ANSYS simulation that at least a width of $W = 2$ mm is required to neutralize the influence of the third dimension. However, we are constrained with the present technique of device fabrication DT1, since the width of the DT1 devices are limited because of the challenges in making high aspect-ratio SU-8 mold using standard photolithography. It is essential to find an alternative method to make devices which have higher width values. As mentioned in the section 6.2.1, the DT2 devices can have higher widths. However we found it difficult to observe the membrane deformation using DT2. We then devised a new post-casting technique to make the viewing transparent, in order to explore DT2 micro-collapsible channels to see the appearance of 2D behaviour as suggested by the ANSYS simulation. Fig. 6.7 shows the deformed shape of the membrane with a width of 0.5 mm for an external

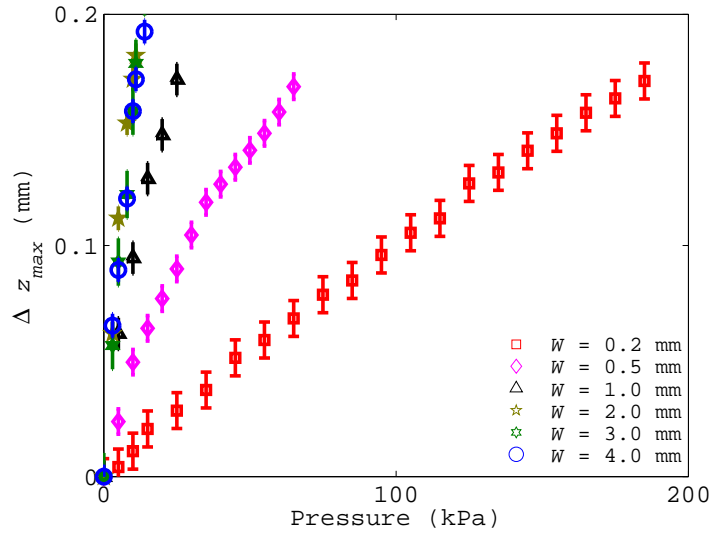


Figure 6.8: Dependence of maximum deformation Δz_{\max} of the bottom surface of the flexible membrane on external pressure (P_e) for micro-collapsible channel (DT2) with different channel widths, approximately 0.22, 0.5, 1.0, 2.0, 3.0 and 4.0mm.

pressure of 20 kPa.

Fig. 6.8 displays the maximum deformation (Δz_{\max}) of the flexible membrane in these six collapsible microchannels with applied external pressure. It is clearly visible from Fig. 6.8 that the two-dimensional deformation pattern is starting at around $W = 2$ mm.

We now compare our experimental results with the 2D simulation results for an incompressible neo-Hookean material. Simulations are carried out considering a 2D beam of length 1 mm and thickness $60 \mu\text{m}$, which is fixed at both the ends and deforms due an external pressure acting on the top edge. In all the simulations, the value of p_e was varied according to the experimental value and different values of Young's modulus for the solid were assumed. It can be seen from the Fig. 6.9 that the deformation behaviour predicted using $E = 1.95$ MPa is approximately in agreement with the experimental results at lower values of deformation, whereas, a value of $E = 1.5$ MPa is more appropriate for higher deformation values.

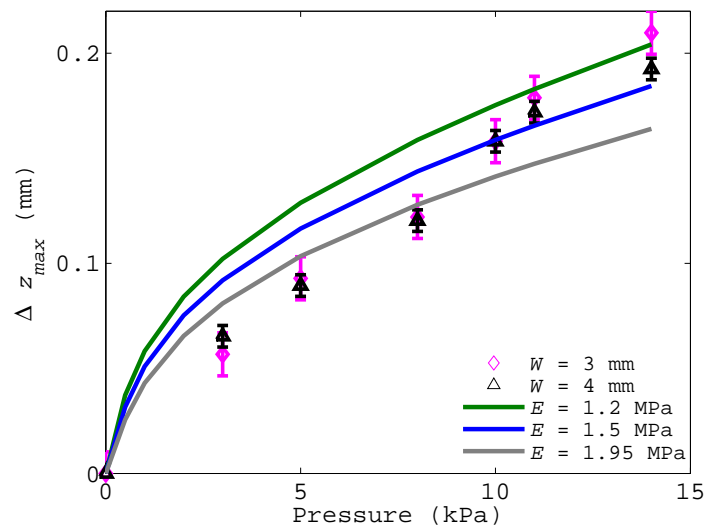


Figure 6.9: Comparison of experimental results with the 2D simulation results.

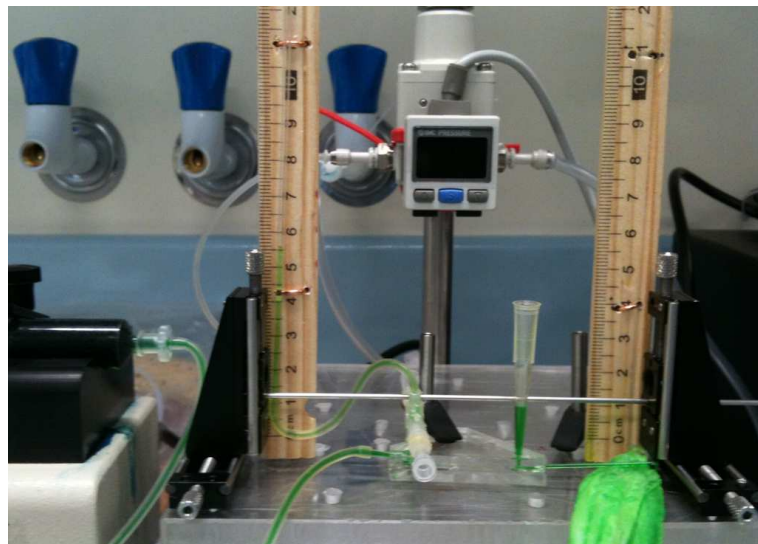


Figure 6.10: Experimental setup for carrying out pressure drop measurements.

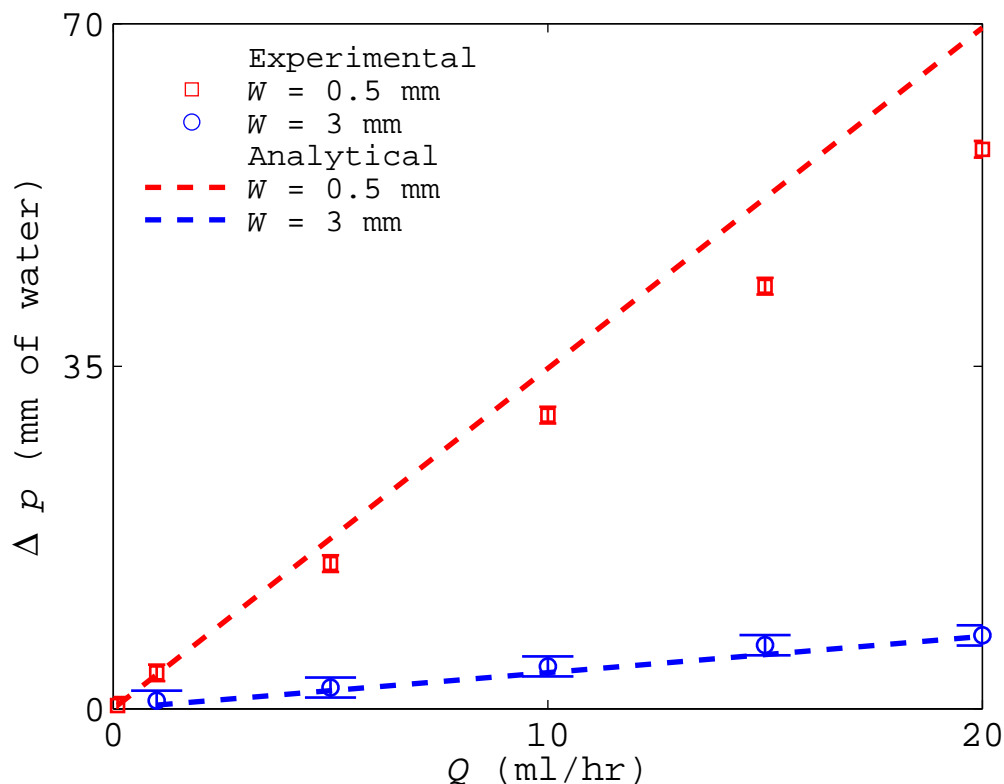


Figure 6.11: Dependence of pressure drop Δp on flow rate Q for two different widths.

6.3.2 Deformation of the PDMS membrane with fluid flow

Fig. 6.10 shows the microfluidics setup designed for carrying out pressure drop measurements together with the microimaging for membrane deformation. A syringe pump, which is connected to the channel inlet, is used to supply fluid at constant flow rate to the collapsible microchannel. The pressure drop in the channel can be calculated from the difference in fluid column height (pressure head) indicated by the small tubes connected to the channel at the inlet and outlet pressure ports.

It is very important to measure the pressure drop in the channel to characterize the flow within a collapsible microchannel. As shown in Fig. 6.11, the measured pressure drop using the present experimental setup is compared with the analytical values derived from Eqs. 6.5 for two different widths (0.5 and 3.0 mm) of the channel. The measured experimental Δp agrees well with the analytical solution. The variation in the channel pressure drop with flow rate follows the linear behaviour of theoretical profiles

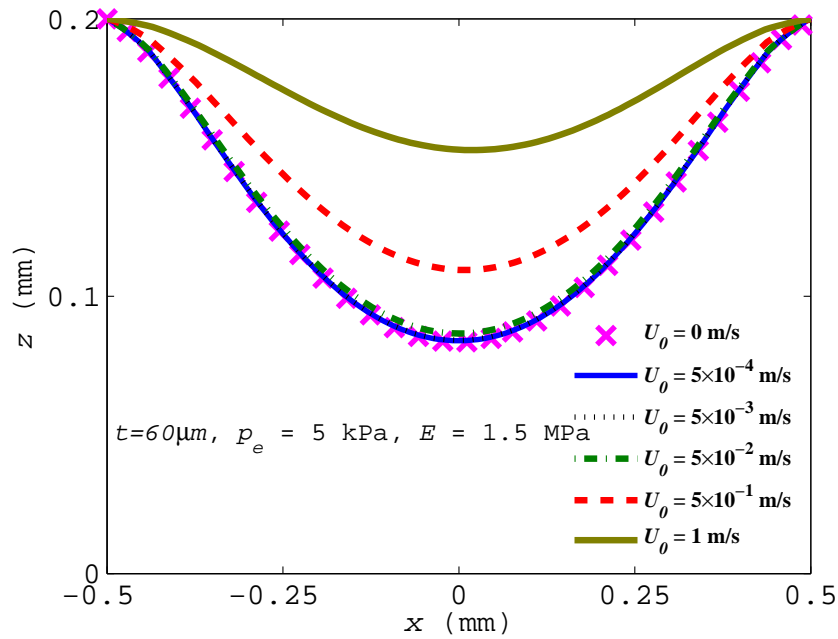


Figure 6.12: FEM prediction of fluid-solid interface profile at different flow rate.

at low flow rates. Although in the experimental data, the dependence of ΔP on Q appears largely linear, a departure of the experimental data from the analytical solution is evident at higher values of flow rate for the channel having a width of 0.5 mm. Because of the flexible nature of PDMS channel deformation can occur at higher flow rates and this deformation can change the cross-sectional area of the microchannel [Gervais et al., 2006; Hardy et al., 2009; Holden et al., 2003]. While deriving the Eqs. 6.5 it was assumed that the channel cross-section did not experience any change due to the pressure applied by the flowing fluid. The departure from the linear theoretical profile in predicting pressure drop in the channel of 0.5 mm width can be attributed to the channel deformation occurring at higher flow rate. However for the 3 mm width channel, the deformation has negligible effect as evidenced from the pressure drop profile.

Preliminary experiments are carried out on 3.0 mm width channel to see the evidence of fluid-structure interaction in the collapsible microchannel. While keeping the external pressure fixed at $p_e = 5$ kPa, flow rates are varied in the range of $Q = 1 - 60$ ml/hr, which corresponds to average inlet velocity U_0 in the range of 4.4×10^{-4} to 2.6×10^{-2} . We have not encountered any significant departure in the fluid-solid interface profile.

In order to identify the reason behind this type of behaviour, we have carried out FEM simulation considering a collapsible channel of height $200\ \mu\text{m}$. The geometry of the flow is that of a 2D channel, with one of the walls containing an elastic segment. The membrane has a finite thickness of $60\ \mu\text{m}$. The channel has a height of $H = 200\ \mu\text{m}$ and a total length of $L = 29\ \text{mm}$. To mimic the experimental flow, we set $\rho = 1000\ \text{kg/m}^3$, $H = 200\ \mu\text{m}$ and $\eta_0 = 0.001\ \text{Pa s}$ and vary U_0 in the range of 5.0×10^{-4} to $1\ \text{m/s}$. As can be seen from the Fig. 6.12, any noticeable departure in interface shape cannot be observed for the inlet velocity U_0 varying in the range of 5.0×10^{-4} to $5.0 \times 10^{-2}\ \text{m/s}$. This result strongly supports our experimental results. A total pressure drop of approximately $0.2\ \text{kPa}$ has been measured at $Q = 60\ \text{ml/hr}$ which is very much less than the external pressure of $p_e = 5\ \text{kPa}$ acting on the flexible membrane. Thus the normal force as well as the shear force exerted by the fluid on the solid surface is not changing much with the set of parameter values considered in the present case. Further analysis is required to see the deformation of the flexible membrane caused by the flowing fluid. One possibility is to use a very high viscosity fluid. In addition to the increase in total pressure drop, the shear stress acting on the solid surface can be increased significantly with the high viscosity fluid. Another option is to increase the flexibility of the PDMS membrane so that it can display the similar type of deformation even at lower values of external pressure. These directions will be pursued in future work.

6.4 Conclusions

Experiments have been carried out in a micro-collapsible channel made of polydimethylsiloxane (PDMS) that mimics the numerically simulated geometry. To characterize the elastic properties of PDMS, the deformation of the thin PDMS membrane is measured without fluid flow in the channel. Upon establishing the PDMS properties, fluid is introduced in the channel and different parameters are studied. The most significant conclusions of this work are the following:

1. The influence of the third dimension has been eliminated successfully with the use of a proper device fabrication technique. A simple simulation carried out using the commercial software ANSYS has revealed the channel widths at which the third dimension is important.
2. The observed value of the elastic modulus for the PDMS membrane agrees well with the nanoindentation test results.

3. The load-displacement curve predicted by the FEM simulation agrees well with the experimental data.
4. Preliminary studies carried for the flow of a Newtonian fluid in the collapsible microchannel show promising trends for the applicability of our simulation method.

Chapter 7

Overall conclusions and future work

7.1 Overall conclusions

The aim of this work has been to understand the role of viscoelasticity on flow in a two-dimensional collapsible channel using a numerical method based on a fluid-structure interaction formulation. At present, there are no models in the literature that simultaneously account for the elastic nature of the collapsible wall and the non-Newtonian rheology of the flowing fluid. In this study, for the first time, a viscoelastic fluid-structure interaction model has been developed that accounts for a viscoelastic fluid and a finite thickness elastic wall, and the resulting governing equations are solved with a sophisticated finite element method. Three different viscoelastic fluid models have been considered - the Oldroyd-B, the FENE-P and Owens model for blood. The rheological behaviour of the viscoelastic fluids is described in terms of a conformation tensor model. Initially the collapsible wall is considered as a zero-thickness membrane model. Subsequently the collapsible wall is modelled as an incompressible neo-Hookean solid. The mesh equation and transport equations are discretized by using the DEVSS-TG/SUPG mixed finite element method. The computational method developed in this work is validated by comparing with the available analytical and numerical results. Experiments in collapsible microchannels have also been performed. The three distinct parts of this project are zero-thickness membrane model, finite-thickness model and collapsible microchannel.

1. **Viscoelastic flow in a 2D channel with zero-thickness membrane model:** Since the focus has been on modelling flows at low Reynolds number, a fixed value of $Re = 1$ has been used in all the computations. Each of the three model viscoelastic fluids that have been chosen, namely, the Oldroyd-B, the FENE-P and Owens

models, has unique features that distinguish it from the others. The predicted flow patterns are compared to those of a Newtonian liquid. We find that computations fail beyond a limiting Weissenberg number. Flow fields and membrane shape differ significantly because of the different degree of shear thinning and molecular extensibility underlying the three different microstructural models.

The flow of a FENE-P fluid for various values of finite extensibility parameter b_M has also been studied numerically to delineate the role of shear thinning on the nature of the fluid-structure interaction in this benchmark geometry. The influence of viscoelasticity and shear thinning on flow patterns and stress profiles is examined and comparisons with Newtonian predictions are reported. The existence of a limiting Weissenberg number beyond which computations fail is demonstrated. The extent of shear thinning is shown to be a key factor in determining the nature of the fluid-structure interaction.

2. **Viscoelastic flow in a 2D channel with finite-thickness solid model:** We have introduced a new geometry, whose central feature is the existence of fluid-structure interaction, into the lexicon of standard benchmark non-Newtonian flow computations. The role that the presence of a deformable membrane plays in the development of a complex flow field in the channel has been examined, and the relationship of the upper limit to the Weissenberg number to molecular conformations at various locations in the flow domain, has been delineated. The shape of the membrane as a function of a membrane elasticity parameter Γ , and of the Weissenberg number Wi has been studied, and the change in shape has been used as an indication of the extent of fluid-structure interaction. The nature of the coupling between macroscopic observables such as velocity, stress and conformation fields, and various rheological features of the three viscoelastic fluid models used in this study, has been explored in some detail.
3. **Collapsible microchannel:** Experiments show that the channel width W perpendicular to the flow must be significant in order for wall effects to be negligible (an assumption that is made in the 2D simulation). As a consequence, the commercial software ANSYS has been used to develop a full 3D model of the channel which captures the deformation of the flexible membrane in the absence of flow. Deformation patterns observed for higher W channels agree well with the ANSYS prediction. The elastic properties of PDMS have been extracted by comparing

the load-displacement curves obtained from the FEM simulations with the experiments. Preliminary comparison has been made between simulations and experiments for the flow of a Newtonian fluid in the collapsible microchannel.

7.2 Future work

There are many aspects of the fluid-structure interaction problem for viscoelastic flows in two dimensional collapsible channels that have not been examined in our work, and which are important to examine in order to obtain a more complete understanding.

1. In terms of the fluid model, the use of a constitutive model that accounts for thixotropy is an important feature, since the aggregation of blood cells in regions of low shear rate can lead to rheological properties that depend locally on microstructural dynamics. The Owens model in its most general form does account for thixotropy [Owens, 2006]. Thixotropy leads to rheological properties that depend locally on microstructural dynamics.
2. Even though there exists an upper limit to the Weissenberg number at which computations fail for each mesh, we have not encountered, in our admittedly limited simulations, a situation where this upper limit has not changed with mesh refinement. It would be interesting to see if the use of a log-conformation tensor formalism leads to much higher upper limits to the Weissenberg numbers for all the models.
3. The multiple modes of instabilities that arise for flow in collapsible channels, and the rich behaviour that occurs in unsteady flows, has been extensively investigated for Newtonian fluids. We hope that the present work provides a starting point for similar studies in the context of viscoelastic fluids.
4. Further study is required to achieve a comprehensive understanding of experimental aspects of the flow of blood in collapsible microchannels.

Appendix A

Owens' model for human blood

A.1 Governing equations

As mentioned earlier, the Oldroyd-B, FENE-P and Owens' models are used in this work. The origins of the Oldroyd-B and FENE-P models are well known and consequently are not discussed here further. We will discuss briefly, however, the new constitutive equation for whole human blood derived by Owens [2006]. Owens used ideas drawn from temporary polymer network theory to model the aggregation and disaggregation of erythrocytes in normal human blood at different shear rates. Each erythrocyte is represented by a dumbbell. The model exhibits shear-thinning, viscoelasticity and thixotropy and its predictions agree reasonably closely with experimental observations that have been carried out in certain benchmark flows [Bureau et al., 1980]. The basic equation (for homogeneous flow) derived by Owens [2006] to describe the elastic stress tensor for blood is:

$$\boldsymbol{\tau}^P + \lambda \left(\frac{\partial \boldsymbol{\tau}^P}{\partial t} - (\nabla \mathbf{v})^T \cdot \boldsymbol{\tau}^P - \boldsymbol{\tau}^P \cdot \nabla \mathbf{v} \right) = N_0 k_B T \lambda \dot{\boldsymbol{\gamma}} \quad (\text{A.1})$$

A conformation tensor version of the Owens model can be derived straightforwardly,

$$\frac{\partial \mathbf{M}}{\partial t} + \mathbf{v} \cdot \nabla \mathbf{M} - \nabla \mathbf{v}^T \cdot \mathbf{M} - \mathbf{M} \cdot \nabla \mathbf{v} = -\frac{1}{\lambda} \{\mathbf{M} - \mathbf{I}\} \quad (\text{A.2})$$

and the constitutive equation for elastic stress is given by,

$$\boldsymbol{\tau}^P = \frac{\eta_{P,0}}{\lambda_0} \{\mathbf{M} - \mathbf{I}\} \quad (\text{A.3})$$

where

$$\begin{aligned}\lambda &= \frac{n\lambda_H}{1 + g_n n \lambda_H} \\ \frac{dn}{dt} &= -\frac{1}{2}b(\dot{\gamma})(n - n_{st})(n + n_{st} - 1) \\ b(\dot{\gamma}) &= \frac{a(\dot{\gamma})N_0}{n_{st}(n_{st} - 1)} \\ g_n n &= \frac{1}{2}b(\dot{\gamma})n(n - 1) + a(\dot{\gamma})N_0\end{aligned}\tag{A.4}$$

$$n_{st} = \frac{\eta_{p,0}}{\eta_\infty} \left(\frac{1 + \theta_1 \dot{\gamma}^{m^*}}{1 + \theta_2 \dot{\gamma}^{m^*}} \right) \left(1 + \frac{3}{2}a(\dot{\gamma})N_0\lambda_H \right)\tag{A.5}$$

here $\dot{\gamma}$ is the rate of strain tensor $(\nabla \mathbf{v} + (\nabla \mathbf{v})^T)$, $\dot{\gamma}$ is the shear rate $(+\sqrt{(1/2)\dot{\gamma} : \dot{\gamma}})$, $a(\dot{\gamma})$ is the aggregation rate, $b(\dot{\gamma})$ is the disaggregation rate, g_n is the disaggregation coefficient, n is the average aggregate size, n_{st} is the steady state value of n at a given shear rate, N_0 is the number of red blood cells per unit volume, m^* , θ_2 and $\theta_1 = \theta_2 \eta_\infty / \eta_{p,0}$ are the Cross model parameters, with $\eta_{p,0}$ and $\eta_\infty = N_0 k_B T \lambda_H$ being the zero and infinite shear-rate red blood cell viscosities, respectively.

The exact form of the functions $a(\dot{\gamma})$ and $b(\dot{\gamma})$ are not known either experimentally or theoretically. All RBC aggregates will break up at sufficiently high shear rate and thus $a(\dot{\gamma}) \rightarrow 0$ as $\dot{\gamma} \rightarrow \infty$. Owens shows that with increase in shear rate, the function $a(\dot{\gamma})N_0$ attains a maximum at some critical shear rate and then decays to zero. However, Owens restricted his calculations to a linear form for $a(\dot{\gamma})N_0$, which we follow. Owens [2006] found the best agreement with the experimental data of Bureau et al. [1980] occurred for the choice of parameters $\eta_{p,0} = 0.14$ Pa s, $\eta_\infty = 0.004$ Pa s, $\theta_2 = 7.2$, $m^* = 0.6$, $\lambda_H = 0.145$ s and $aN_0 = 2(1 + \dot{\gamma})$.

With these parameter values, Eq. (A.4) and (A.5) can be rewritten for steady state as:

$$g_{n_{st}} n_{st} = 3(1 + \dot{\gamma})\tag{A.6}$$

$$n_{st} = \frac{\eta_{p,0}}{\eta_\infty} \left(\frac{1 + \theta_1 \dot{\gamma}^{m^*}}{1 + \theta_2 \dot{\gamma}^{m^*}} \right) \{1 + 3(1 + \dot{\gamma})\lambda_H\}\tag{A.7}$$

A.2 Analytical solution of Owens' model in Couette flow

Motivated from the derivation of the analytical solution for the Oldroyd-B model in Bird et al. [1987a] we describe here an analytical solution of Owens' model in Couette flow. For Newtonian fluids in Couette flow, there is a only one non-zero component of stress, i.e. the transverse shear stress (τ_{yx}). But this is not the case for viscoelastic flows. The most general form that the stress tensor [Bird et al., 1987a] can have for a simple shear flow is given below:

$$\boldsymbol{\tau}^P = \begin{pmatrix} \tau_{xx}^P & \tau_{yx}^P & 0 \\ \tau_{yx}^P & \tau_{yy}^P & 0 \\ 0 & 0 & \tau_{zz}^P \end{pmatrix}$$

In simple shear flow, the rate of strain tensor ($\dot{\gamma}$) will have the following form:

$$\dot{\gamma} = \nabla \mathbf{v} + (\nabla \mathbf{v})^T = \begin{pmatrix} 0 & 1 & 0 \\ 1 & 0 & 0 \\ 0 & 0 & 0 \end{pmatrix} \dot{\gamma}_{yx}$$

Here shear rate ($\dot{\gamma}$) is same as $\dot{\gamma}_{yx}$ provided $\dot{\gamma}_{yx} \geq 0$. Now the upper convected time derivative of the stress tensor ($\boldsymbol{\tau}_{(1)}^P$) for steady flow can be expressed as follows [Bird et al., 1987a]:

$$\boldsymbol{\tau}_{(1)}^P = - \begin{pmatrix} 2\tau_{yx}^P & \tau_{yy}^P & 0 \\ \tau_{yy}^P & 0 & 0 \\ 0 & 0 & 0 \end{pmatrix},$$

so, that equation A.1 can be written as:

$$\begin{pmatrix} \tau_{xx}^P & \tau_{yx}^P & \tau_{zx}^P \\ \tau_{yx}^P & \tau_{yy}^P & \tau_{zy}^P \\ \tau_{zx}^P & \tau_{zy}^P & \tau_{zz}^P \end{pmatrix} - \lambda \dot{\gamma} \begin{pmatrix} 2\tau_{yx}^P & \tau_{yy}^P & 0 \\ \tau_{yy}^P & 0 & 0 \\ 0 & 0 & 0 \end{pmatrix} = N_0 k_B T \lambda \begin{pmatrix} 0 & 1 & 0 \\ 1 & 0 & 0 \\ 0 & 0 & 0 \end{pmatrix} \dot{\gamma}.$$

For a two dimensional geometry this equation becomes,

$$\begin{pmatrix} \tau_{xx}^P & \tau_{yx}^P \\ \tau_{yx}^P & \tau_{yy}^P \end{pmatrix} - \lambda \dot{\gamma} \begin{pmatrix} 2\tau_{yx}^P & \tau_{yy}^P \\ \tau_{yy}^P & 0 \end{pmatrix} = N_0 k_B T \lambda \begin{pmatrix} 0 & 1 \\ 1 & 0 \end{pmatrix} \dot{\gamma}$$

After solving this equation we can get the following expressions for the different

components of stresses.

$$\tau_{yx}^p = N_0 k_B T \lambda \dot{\gamma} \quad \tau_{xx}^p = 2N_0 k_B T \lambda^2 \dot{\gamma}^2$$

Once we calculate the values of stresses we can easily calculate the values of the conformation tensor from Eqs. A.3.

A.3 Derivatives

In Owens' model (Owens [2006]) λ depends on shear rate, which in this thesis is calculated from the linearly interpolated velocity gradient (\mathbf{L}). So, to incorporate Owens' model in our FEM code, we need to find out the derivative of λ with respect to the interpolated velocity gradient basis function coefficients (\mathbf{L}_{ij}^β). The strain rate can be expressed in terms of \mathbf{L} as $\dot{\gamma}_{ij} = \mathbf{L} + (\mathbf{L})^T$.

The derivative of the strain rate ($\dot{\gamma}_{ij}$) with respect to the interpolated velocity gradient basis function coefficients (\mathbf{L}_{ij}^β) is,

$$\begin{aligned} \frac{\partial \dot{\gamma}_{ij}}{\partial \mathbf{L}_{kl}^\beta} &= \frac{\partial \mathbf{L}_{ij}}{\partial \mathbf{L}_{kl}^\beta} + \frac{\partial (\mathbf{L}_{ij})^T}{\partial \mathbf{L}_{kl}^\beta} \\ &= (\delta_{ik} \delta_{jl} + \delta_{ik} \delta_{jl}) \times \phi_{\mathbf{L}}^\beta \end{aligned} \quad (\text{A.8})$$

The derivative of shear rate ($\dot{\gamma}$) with respect to the strain rate ($\dot{\gamma}_{ij}$) is,

$$\begin{aligned} \frac{\partial \dot{\gamma}}{\partial \dot{\gamma}_{ij}} &= \frac{\partial \sqrt{\frac{1}{2} \dot{\gamma} : \dot{\gamma}}}{\partial \dot{\gamma}_{ij}} = \frac{\partial \left[\sqrt{\frac{1}{2} \text{tr}(\dot{\gamma}_{ij}^2)} \right]}{\partial \dot{\gamma}_{ij}} \\ &= \frac{1}{2} \left[\frac{1}{2} \text{tr}(\dot{\gamma}_{ij}^2) \right]^{-\frac{1}{2}} \times \frac{\partial \left[\frac{1}{2} \text{tr}(\dot{\gamma}_{ij}^2) \right]}{\partial \dot{\gamma}_{ij}} \\ &= \frac{1}{2} \times \frac{1}{\dot{\gamma}} \times \dot{\gamma}_{ji} \end{aligned} \quad (\text{A.9})$$

The derivative of shear rate ($\dot{\gamma}$) with respect to the interpolated velocity gradient basis function coefficients (\mathbf{L}_{ij}^β) is,

$$\begin{aligned}
\frac{\partial \dot{\gamma}}{\partial L_{kl}^\beta} &= \frac{\partial \dot{\gamma}}{\partial \dot{\gamma}_{ij}} \times \frac{\partial \dot{\gamma}_{ij}}{\partial L_{kl}^\alpha} \\
&= \frac{\dot{\gamma}_{ji}}{2\dot{\gamma}} \times (\delta_{ik}\delta_{jl} + \delta_{ik}\delta_{jl}) \times \phi_L^\beta \\
&= \frac{1}{2\dot{\gamma}} (\dot{\gamma}_{lk} + \dot{\gamma}_{lk}) \times \phi_L^\beta
\end{aligned} \tag{A.10}$$

The derivative of n_{st} with respect to the shear rate ($\dot{\gamma}$) is,

$$\begin{aligned}
\frac{\partial n_{st}}{\partial \dot{\gamma}} &= \frac{\partial}{\partial \dot{\gamma}} \left[\frac{\eta_{p,0}}{\eta_\infty} \left(\frac{1 + \theta\dot{\gamma}^m}{1 + \beta\dot{\gamma}^m} \right) \{1 + 3(1 + \dot{\gamma})\lambda_H\} \right] \\
&= \frac{\eta_{p,0}}{\eta_\infty} \left(\frac{1 + \theta\dot{\gamma}^m}{1 + \beta\dot{\gamma}^m} \right) \frac{\partial}{\partial \dot{\gamma}} \{1 + 3(1 + \dot{\gamma})\lambda_H\} + \frac{\eta_{p,0}}{\eta_\infty} \{1 + 3(1 + \dot{\gamma})\lambda_H\} \frac{\partial}{\partial \dot{\gamma}} \left(\frac{1 + \theta\dot{\gamma}^m}{1 + \beta\dot{\gamma}^m} \right) \\
&= \frac{\eta_{p,0}}{\eta_\infty} \left(\frac{1 + \theta\dot{\gamma}^m}{1 + \beta\dot{\gamma}^m} \right) \times 3\lambda_H + \frac{\eta_{p,0}}{\eta_\infty} \{1 + 3(1 + \dot{\gamma})\lambda_H\} \left(\frac{1 + \theta\dot{\gamma}^m}{1 + \beta\dot{\gamma}^m} \right) \left[\frac{\theta}{1 + \theta\dot{\gamma}^m} - \frac{\beta}{1 + \beta\dot{\gamma}^m} \right] m\dot{\gamma}^{m-1}
\end{aligned} \tag{A.11}$$

The derivative of λ with respect to the shear rate ($\dot{\gamma}$) is,

$$\begin{aligned}
\frac{\partial \lambda}{\partial \dot{\gamma}} &= \frac{\partial}{\partial \dot{\gamma}} \left(\frac{n_{st}\lambda_H}{1 + g_{n_{st}}n_{st}\lambda_H} \right) \\
&= \left(\frac{1}{1 + g_{n_{st}}n_{st}\lambda_H} \right) \lambda_H \frac{\partial n_{st}}{\partial \dot{\gamma}} + \lambda_H n_{st} \frac{\partial}{\partial \dot{\gamma}} \left(\frac{1}{1 + g_{n_{st}}n_{st}\lambda_H} \right) \\
&= \left(\frac{\lambda_H}{1 + 3(1 + \dot{\gamma})\lambda_H} \right) \frac{\partial n_{st}}{\partial \dot{\gamma}} + \lambda_H n_{st} \left[-\{1 + 3(1 + \dot{\gamma})\lambda_H\}^{-2} \right] \times 3\lambda_H \\
&= \frac{\lambda}{n_{st}} \frac{\partial n_{st}}{\partial \dot{\gamma}} - \left(\frac{\lambda_H n_{st}}{1 + 3(1 + \dot{\gamma})\lambda_H} \right) \times \left(\frac{3\lambda_H}{1 + 3(1 + \dot{\gamma})\lambda_H} \right) \\
&= \frac{\lambda}{n_{st}} \frac{\partial n_{st}}{\partial \dot{\gamma}} - \lambda \times \frac{3\lambda}{n_{st}} \\
&= \frac{\lambda}{n_{st}} \left(\frac{\partial n_{st}}{\partial \dot{\gamma}} - 3\lambda \right)
\end{aligned} \tag{A.12}$$

The derivative of $\frac{1}{\lambda}$ with respect to the shear rate ($\dot{\gamma}$) is,

$$\begin{aligned}
\frac{\partial}{\partial \dot{\gamma}} \left(\frac{1}{\lambda} \right) &= \frac{\partial}{\partial \lambda} \left(\frac{1}{\lambda} \right) \times \frac{\partial \lambda}{\partial \dot{\gamma}} \\
&= -\frac{1}{\lambda^2} \frac{\partial \lambda}{\partial \dot{\gamma}} \\
&= \frac{1}{n_{st}} \left(3 - \frac{1}{\lambda} \frac{\partial n_{st}}{\partial \dot{\gamma}} \right)
\end{aligned} \tag{A.13}$$

These derivatives have been incorporated into the Jacobian routine of our FEM code.

A.4 Implementation of Owens' model

In this work Owens' model has been implemented in the FEM code using the conformation tensor based approach. Here all the nonlinear equations are solved with Newton's method with the analytical Jacobian. In general, shear-thinning fluids (such as the White-Metzner fluid) have a power-law viscosity with exponent <1 and exhibit a weakly singular behaviour at zero shear rate. The viscosity in Owens' model does not suffer from such problems (for details see appendix A.1). But the derivative of viscosity with respect to shear rate suffers from this problem (for details see appendix A.3). In Owens' model (Owens [2006]) the relaxation time (λ) depends on the shear rate, which is calculated from a linearly interpolated velocity gradient (L_{ij}^α). So, to incorporate Owens' model in our FEM code, we need to provide the derivative of λ with respect to the interpolated velocity gradient basis function coefficients (ϕ_L^α) for the calculation of the Jacobian matrix. As the values of the Jacobian matrix influence mainly the convergence of the solution, small deviations in its value will not cause any deviation in the final solution. It has been incorporated in the code in such a way that when the value of the shear rate falls below a critical value (here 10^{-6}), the derivative will be calculated from this threshold value. With the implementation of this step, Owens' model works well in all our computations.

A.4.1 Validation of Owens' model

The relaxation time (λ) in the Owens' model is a function of shear rate, whereas the relaxation time for the Oldroyd-B model (λ) is constant. So, these two models should agree with each other in steady simple shear (Couette) flow, i.e. confined flow between two parallel plates of infinite length with one plate moving at some constant velocity. Fig. A.1 shows the flow geometry and boundary conditions for the Couette flow computations. The steady state velocity profile for a Newtonian liquid, $u = U(y/W)$, with W being the distance between two plates is used for Couette flow computations. The flow is generated by imposing a constant velocity, U , to the bottom plate in case of Couette flow.

The analytical solution of Owens' model in Couette flow has been derived in appendix A.2. The flow conditions are $Re = (\rho WV)/\eta = 1$, where fluid density $\rho = 10^3$

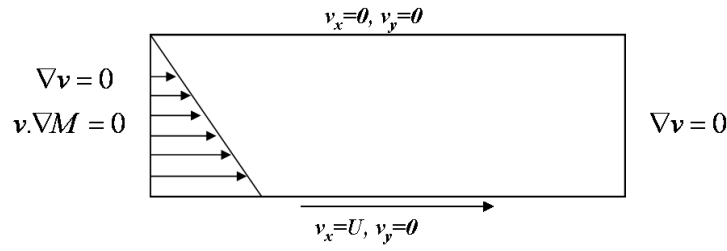


Figure A.1: Flow domain and boundary conditions for the Couette flow

Table A.1: Comparison of different components of conformation tensor.

Components of conformation tensor	Analytical solution	FEM code Oldroyd-B	FEM code Owens' blood model
M_{xx}	1.199	1.199	1.199
M_{yy}	1.0	1.0	1.0
M_{yx}	0.3152	0.3152	0.3152

kg/m³, average velocity $v = 10^{-3}$ m/sec, width of the channel $W=1$ m and total solution viscosity $\eta=1$ Pa s. Here a viscosity ratio ($\beta = \eta_s/(\eta_s + \eta_{p,0})$, where $\eta_{p,0}$ is the polymer contribution and η_s is the solvent contribution to the viscosity of the liquid) of 0.86 has been considered. Table A.1 shows the comparison between the analytical results and the FEM solution results for the Oldroyd-B model and Owens' model. The analytical results and the FEM results agree with each other perfectly.

A.5 Velocity profile

The fully developed velocity profile for a shear thinning power-law fluid can be expressed as follows:

$$u(x) = U_0 \frac{2m+1}{m+1} \left(1 - \left(\frac{y}{h} \right)^{\frac{1+m}{m}} \right) \quad (\text{A.14})$$

where U_0 is the average velocity at the inlet, y is the distance along the height of the channel (h) and m is the power law exponent. We have used a power-law exponent (m) value of 0.59. To check the fully developed velocity profile for this model we have

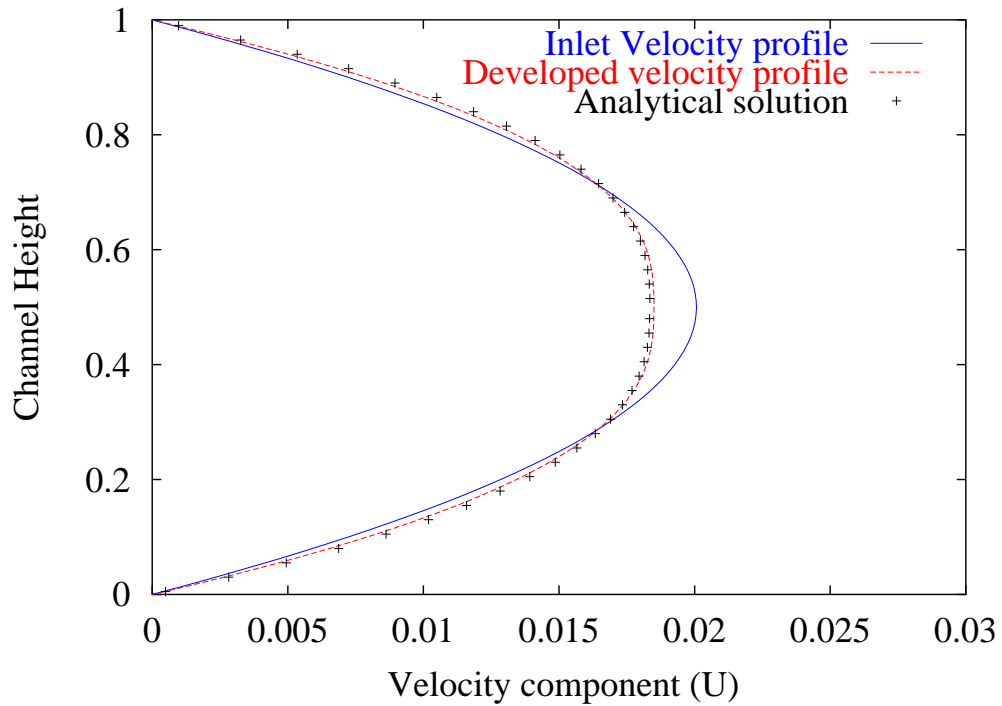


Figure A.2: Blunting of the parabolic profile.

studied a simple case, where flow between two parallel plates is considered and at the inlet a parabolic velocity profile is prescribed. We have found that the prescribed parabolic profile at the inlet is changing and after certain distance along the flow direction blunting of the profile is visible which is shown in the Fig. A.2. Analytical result agrees well with FEM results.

Appendix B

Weighted residual form of $\nabla_{\mathbf{X}} \cdot \mathbf{S} = \mathbf{0}$

The weak form of Eq. (5.8) is,

$$\int_{\bar{\Omega}_S} (\nabla_{\mathbf{X}} \cdot \mathbf{S}) \phi \, d\bar{\Omega}_S = - \int_{\bar{\Omega}_S} (\nabla_{\mathbf{X}} \phi \cdot \mathbf{S}) \, d\bar{\Omega}_S + \int_{\bar{\Gamma}_S} \phi (\mathbf{N} \cdot \mathbf{S}) \, d\bar{\Gamma}_S = \mathbf{0} \quad (\text{B.1})$$

where, $\bar{\Omega}_S$, $\bar{\Gamma}_S$ and \mathbf{N} are the area, arc length and unit normal in the zero-stress configuration, respectively, and ϕ is a weighting function. When written in terms of Cartesian components, the weighted residual form of this equation in the *computational* domain is,

$$R_i^x = - \int_{\Omega_{S0}} \left[\frac{\partial \phi_i}{\partial X} S_{Xx} + \frac{\partial \phi_i}{\partial Y} S_{Yx} \right] |\mathbf{J}^*| \, d\Omega_{S0} + \int_{\Gamma_{S0}} \phi_i (\mathbf{N} \cdot \mathbf{S})_x \left(\frac{d\bar{\Gamma}_S}{d\Gamma_{S0}} \right) \, d\Gamma_{S0} \quad (\text{B.2})$$

$$R_i^y = - \int_{\Omega_{S0}} \left[\frac{\partial \phi_i}{\partial X} S_{Xy} + \frac{\partial \phi_i}{\partial Y} S_{Yy} \right] |\mathbf{J}^*| \, d\Omega_{S0} + \int_{\Gamma_{S0}} \phi_i (\mathbf{N} \cdot \mathbf{S})_y \left(\frac{d\bar{\Gamma}_S}{d\Gamma_{S0}} \right) \, d\Gamma_{S0} \quad (\text{B.3})$$

Here, $\bar{\Omega}_{S0}$ and $\bar{\Gamma}_{S0}$ are the area and arc length in the computational domain, respectively, $|\mathbf{J}^*|$ is the Jacobian of the transformation from the zero-stress configuration to the computational domain, and ϕ_i are bi-quadratic weighting functions.

We find it convenient to work with dimensional quantities in Appendix B. In terms of the *dimensional* Cauchy stress tensor for a neo-Hookean material, $\boldsymbol{\sigma} = -\pi^* \mathbf{I} + G \mathbf{B}$, the components of the dimensional Piola-Kirchhoff stress tensor \mathbf{S} are,

$$\begin{aligned} S_{Xx} &= -\pi^* \frac{\partial y}{\partial Y} + G \frac{\partial x}{\partial X}; & S_{Yx} &= \pi^* \frac{\partial y}{\partial X} + G \frac{\partial x}{\partial Y} \\ S_{Xy} &= \pi^* \frac{\partial x}{\partial Y} + G \frac{\partial y}{\partial X}; & S_{Yy} &= -\pi^* \frac{\partial x}{\partial X} + G \frac{\partial y}{\partial Y} \end{aligned} \quad (\text{B.4})$$

In their finite-element formulation of the fluid-structure interaction problem, Carvalho

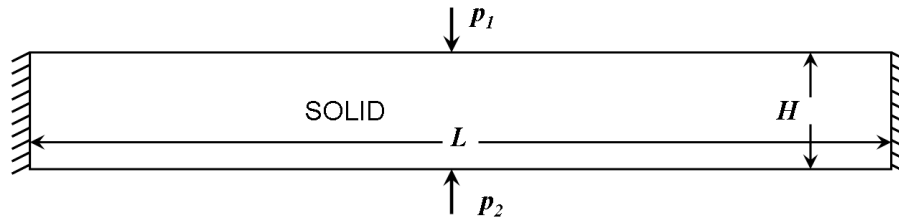


Figure B.1: Geometry of the solid domain.

and Scriven [1997] (see also Carvalho [1996]) have used,

$$R_i^x = - \int_{\Omega_{S0}} \left[S_{Xx} \frac{\partial \phi_i}{\partial X} + S_{Xy} \frac{\partial \phi_i}{\partial Y} \right] |\mathbf{J}^*| d\Omega_{S0} + \int_{\Gamma_{S0}} \phi_i (\mathbf{N} \cdot \mathbf{S})_x \left(\frac{d\bar{\Gamma}_S}{d\Gamma_{S0}} \right) d\Gamma_{S0} \quad (\text{B.5})$$

$$R_i^y = - \int_{\Omega_{S0}} \left[S_{Yx} \frac{\partial \phi_i}{\partial X} + S_{Yy} \frac{\partial \phi_i}{\partial Y} \right] |\mathbf{J}^*| d\Omega_{S0} + \int_{\Gamma_{S0}} \phi_i (\mathbf{N} \cdot \mathbf{S})_y \left(\frac{d\bar{\Gamma}_S}{d\Gamma_{S0}} \right) d\Gamma_{S0} \quad (\text{B.6})$$

in place of Eqs. (B.2) and (B.3). Basically, the positions of the two components S_{Yx} and S_{Xy} have been interchanged.

In order to establish the validity of equations (B.2) and (B.3) and to demonstrate the incorrectness of equations (B.5) and (B.6), we have examined the simple problem of a beam fixed at the edges, with uniform pressure applied on both the top and bottom of the beam, as shown schematically in figure B.1. Essentially, we compare the results of our computations using Eqs. (B.2) and (B.3) (labelled FEM-N), and Eqs. (B.5) and (B.6) (labelled FEM-C), with the results obtained with the ANSYS software package for a plain-strain model.

The following boundary conditions are prescribed,

1. Zero displacements at the left and right edges of the beam.
2. A force balance at the top and bottom of the form,

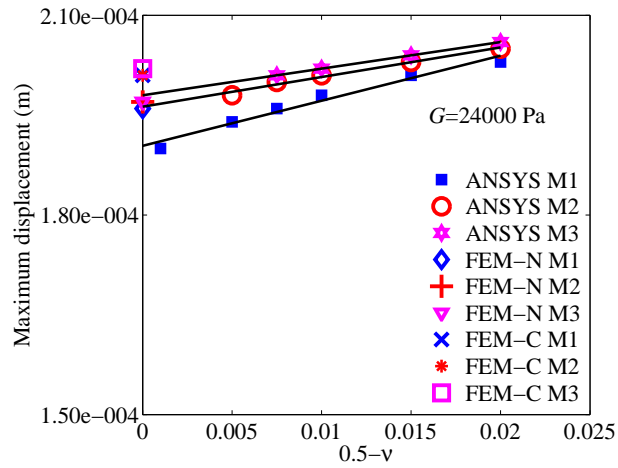
$$\mathbf{n} \cdot \boldsymbol{\sigma} = -p_i \mathbf{n}; \quad i = 1, 2 \quad (\text{B.7})$$

where, \mathbf{n} is the unit normal to the deformed solid surface, and p_1 and p_2 are the dimensional external pressures on the top and bottom of the beam, respectively.

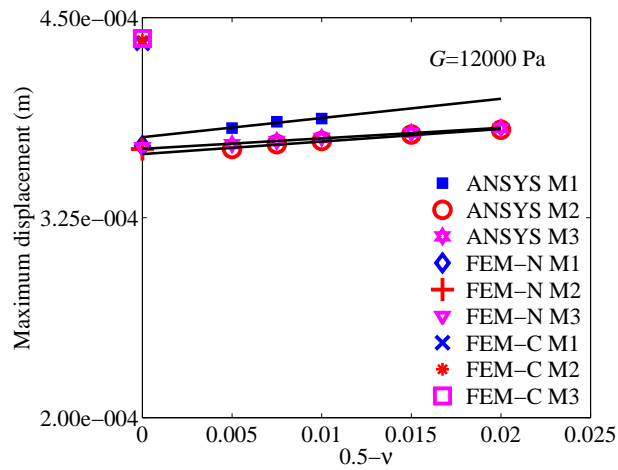
In units of height H , the length of the beam is set at $L = 5H$, with $H = 10^{-3}$ m. The external pressures have been chosen to be $p_1 = 1.1$ N and $p_2 = 1.0$ N, and three different values (6000, 12000 and 24000 Pa) have been used for the shear modulus G . Computations have been performed with three different meshes (M1, M2 and M3) in order to examine mesh convergence.

The formulation of the fluid-structure interaction problem by Carvalho and Scriven [1997] is for the special case of an *incompressible* neo-Hookean material with a Poisson ratio $\nu = 0.5$. On the other hand, the ANSYS plain-strain package is only applicable to *compressible* neo-Hookean materials. Consequently, in order to carry out the comparison with ANSYS, we have obtained predictions with several values of $\nu < 0.5$, and extrapolated the results to $\nu = 0.5$.

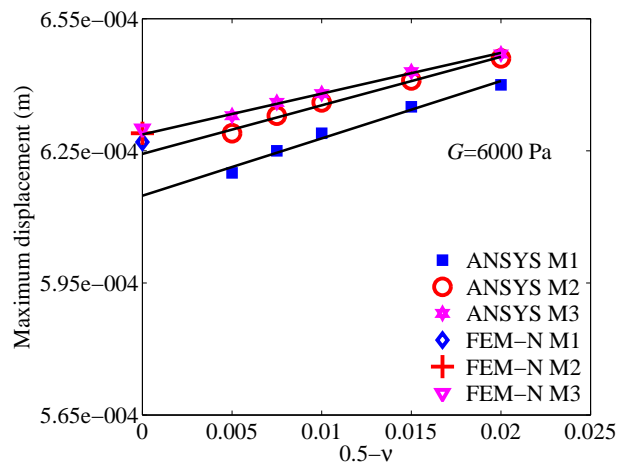
Figure B.2 compares the maximum displacement of the beam obtained with the FEM-N and FEM-C formulations with the ANSYS plain strain model for the three different values of G . In all three cases, mesh converged results obtained with FEM-N agree with the extrapolated mesh converged solution obtained with ANSYS. On the other hand, the mesh converged solution obtained with FEM-C shows differences from the other two approaches. Indeed, while this difference is small at $G = 24000$ Pa, and substantially larger at $G = 12000$ Pa, we are unable to obtain a converged solution with FEM-C at $G = 6000$ Pa.



(a)



(b)



(c)

Figure B.2: Comparison of formulations FEM-N and FEM-C with the ANSYS plain-strain model for three different values of G : (a) 24000 Pa, (b) 12000 Pa, and (c) 6000 Pa.

Appendix C

Nanoindentation test to characterize the elastic modulus of PDMS membrane

The unique properties of polydimethylsiloxane (PDMS), such as optical transparency, gas permeability, biocompatibility and elasticity, make it suitable for the fabrication of microsystems [Duffy et al., 1998; Leclerc et al., 2003; Unger et al., 2000; Whitesides, 2006]. Since the Young's modulus of PDMS can significantly be altered by varying the curing temperature and time and the mixing ratio of silicone base to the curing agent [Friend and Yeo, 2010; Fuard et al., 2008; Hohne et al., 2009; Thangawng et al., 2007], research in measuring the isotropic mechanical properties of PDMS is rapidly growing [Kim et al., 2011; Liu et al., 2009b,c].

Different experimental techniques have been employed to characterize the rigidity of PDMS and the reported value of Young's modulus for PDMS usually falls within 0.05 to 4.0 MPa [Fuard et al., 2008; Thangawng et al., 2007]. Recently, Liu et al. [2009c] have carried out tensile test to establish the thickness dependent hardness and the Young's modulus of the PDMS membranes, which is caused by shear stresses during fabrication of these thin membrane.

The nanoindentation test which has widely been employed for characterizing elastic and plastic properties of hard materials is gaining importance for characterizing mechanical properties of polymeric materials. In a standard nanoindentation test the Young's modulus and hardness of a very thin membrane made of elastic material can easily be obtained from the load displacement data. Carrillo et al. [2005] used a nanoindentation technique to characterize the Young's modulus of PDMS with different degrees of crosslinking.

C.1 Experimental Method

PDMS (Dow and Corning Sylgard 184) samples were prepared by mixing the cross-linker and siloxane in a ratio of 1:10 and were then kept in a vacuum chamber to remove the generated bubbles during mixing. Different thickness PDMS membranes are produced by spin coating glass wafers at different spinning speed and then cured at 70°C for two hours in an oven. The thickness of the PDMS membrane was measured using a surface profiler. By varying the spinning speed in the range of 500 to 2000 rpm, PDMS membranes of thickness in the range of 25 μm to 100 μm are successfully produced.

The nanoindentation test using the TriboIndenter (Hysitron, Inc, Minneapolis, MN) has been performed at room temperature using a Berkovich shaped indenter. 10 μN/s loading and unloading rate, 100 μN peak load and 5 s of hold period have been chosen for load control function. When the tip of the indenter reaches the sample surface, the instrument applies the predefined load and accordingly records the load and displacement data. The hardness and the Young's modulus of a material is then determined from the unloading portion of the load-displacement curve using classical Hertzian contact theory [Johnson, 2003]:

$$H = \frac{F_{\max}}{A} \quad (\text{C.1})$$

$$\frac{1}{E_r} = \frac{1 - \nu^2}{E} + \frac{1 - \nu_i^2}{E_i} \quad (\text{C.2})$$

where H is the hardness of the substrate and F_{\max} is the maximum force applied on the PDMS membrane, A is the projected contact area between the tip and the substrate, ν and E are the Poisson's ratio and the Young's modulus respectively for the test specimen and ν_i and E_i are those for the indenter. The material properties of the diamond indenter are $E_i = 1140$ GPa and $\nu_i = 0.07$. The reduced elastic modulus E_r is calculated using the following expression proposed by Oliver and Pharr [1992],

$$E_r = \frac{S \sqrt{\pi}}{2\beta \sqrt{A}} \quad (\text{C.3})$$

where S is the contact stiffness taken as the initial slope of the unloading section of the load-displacement curve and β is a constant that depends on the geometry of the indenter.

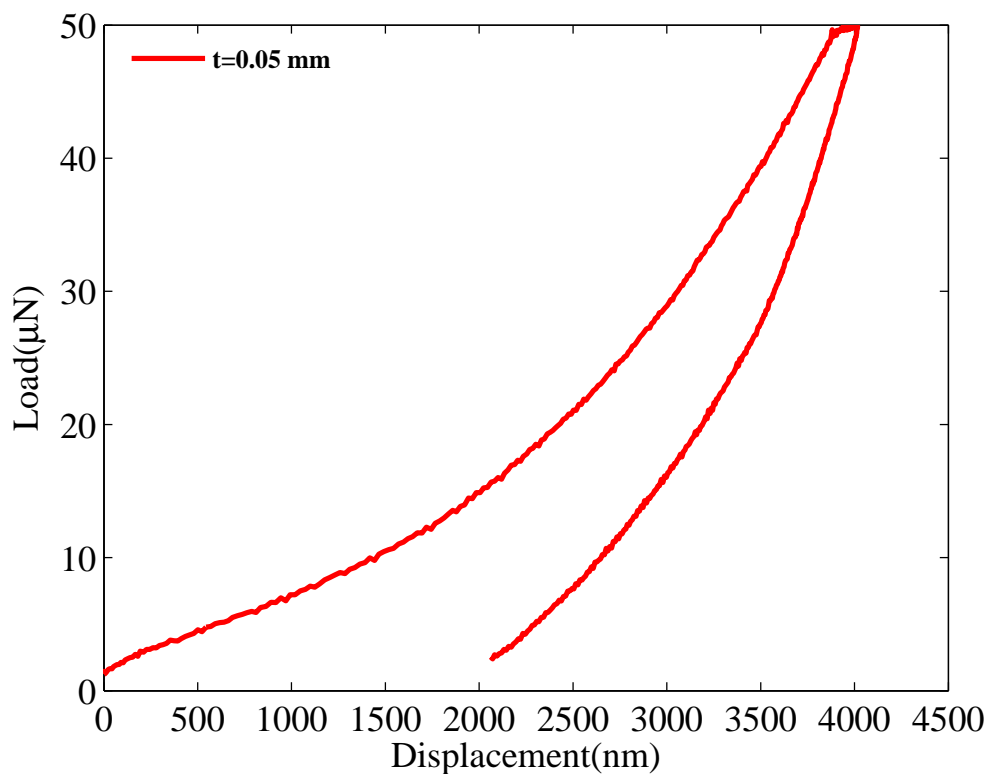


Figure C.1: Load-displacement curves for PDMS membrane with thickness of 0.05 mm

C.2 Results and discussions

Figure C.1 shows the displacement of the indenter in response to the applied load during nanoindentation test on PDMS membrane using quasi-static measurements with the help of a diamond Berkovich-shaped indenter tip in a Hysitron Triboindenter. To confirm the reproducibility of the test data, indentation has been performed on nine different location of a particular sample. We have found similar trends for other PDMS membranes but the penetration depth of the indenter is higher for low thickness PDMS membrane indicating a lower value for Young's modulus as the thickness decreases.

The reduced elastic modulus E_r and Young's modulus of PDMS membrane are calculated using Eqs. (C.2) and (C.3). Fig. C.2 indicates that the Young's modulus of PDMS membranes decreases as the thickness decreases. The results indicate that the nanoindentation test is capable of differentiating the elastic behaviour of a material with varying thickness. All these membranes with different thickness are prepared by varying the spin coating speed while keeping all other parameters, such as curing temperature, PDMS mixing ration and curing time etc., exactly same. As the speed

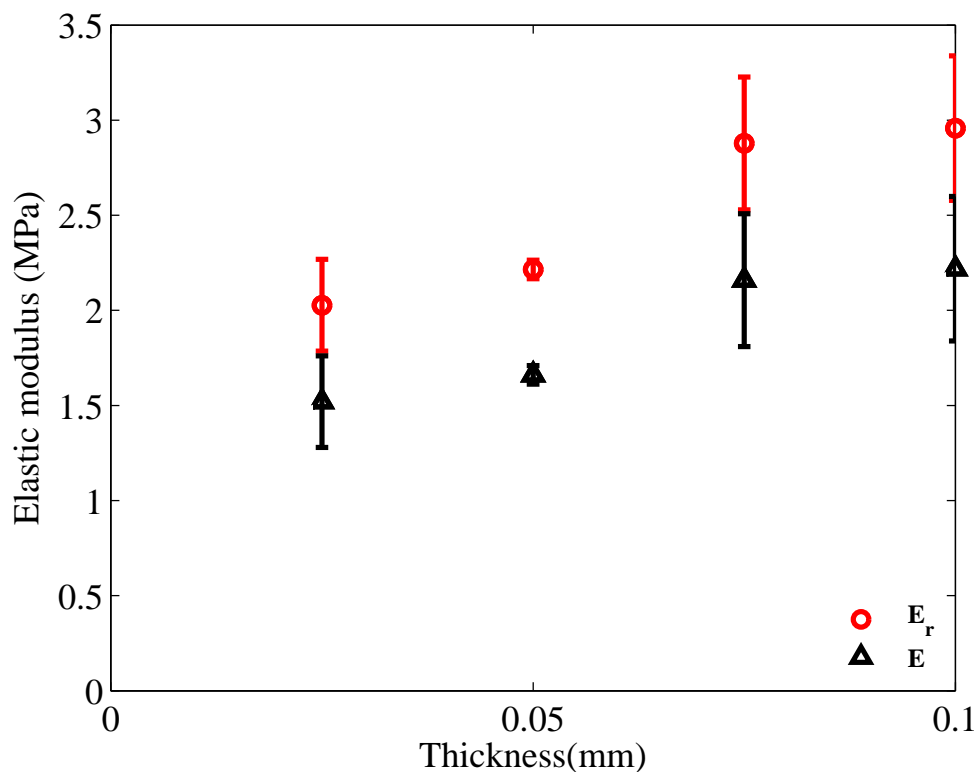


Figure C.2: Dependence of reduced elastic modulus E_r and Young's modulus of PDMS membrane on thickness.

of the spin coating increases the PDMS polymer molecules experience more stretching along the radial direction due to the increase in shear stress value.

C.3 Conclusions

We have demonstrated the thickness dependent Young's modulus of PDMS membranes using a nanoindentation test. The measured values of E agree well with the previously reported values.

Appendix D

Stability analysis of pressure driven flow of a viscoelastic fluid through a deformable channel

D.1 Governing equations

We consider the pressure driven flow of an incompressible viscoelastic fluid flowing through channel lined with a layer of incompressible and impermeable deformable solid. As illustrated in Fig. D.1, the width of the channel is $2W$ and the solid layer has a thickness of HW and is strongly bonded to a rigid surface at $z^* = (2 + H)W$ on top and $z^* = -HW$ below.

The elastic wall is modelled as an incompressible neo-Hookean solid, while the fluid has been considered as an Oldroyd-B fluid. The densities of fluid and solid are assumed to be equal without loss of generality. We have nondimensionalized the various physical quantities, by scaling lengths and displacements with W , velocities with GW/η_0 , time with η_0/G and pressure and stresses with G , where G is the shear modulus of the solid, $\eta_0 (= \eta_s + \eta_{p,0})$ is the zero shear rate solution viscosity, η_s is the solvent viscosity, and $\eta_{p,0}$ is the contribution of the micro-structural elements to the zero shear rate viscosity. For a Newtonian fluid, η_0 is just the constant Newtonian viscosity. Non-dimensionalization of the governing equations and boundary conditions yields the following dimensionless numbers:

$$Re = \frac{\rho W U_0}{\eta_0}; \quad \beta = \frac{\eta_s}{\eta_0}; \quad Wi = \frac{\lambda U_0}{W}; \quad \Gamma = \frac{\eta_0 U_0}{GW} \quad (D.1)$$

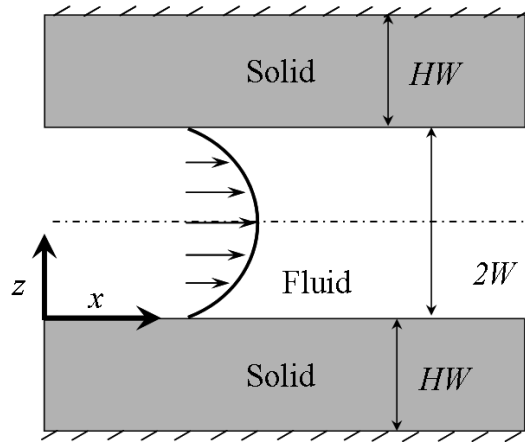


Figure D.1: Geometry of the pressure driven viscoelastic fluid flow interacting with elastic solid layer

where, Re is the Reynolds number, β is the viscosity ratio, Wi is the *inlet* Weissenberg number, Γ is the dimensionless solid elasticity parameter, ρ is the density of the liquid, U_0 is the maximum fluid velocity and λ is the constant characteristic relaxation time of the microstructure. Upon introduction of these dimensionless variables, the governing equations of the fluid assume the following dimensionless form:

$$\nabla \cdot \mathbf{v} = 0 \quad (\text{Mass balance}) \quad (\text{D.2})$$

$$\frac{Re}{\Gamma} \left[\frac{\partial \mathbf{v}}{\partial t} + \mathbf{v} \cdot \nabla \mathbf{v} \right] = \nabla \cdot \mathbf{T} \quad (\text{Momentum balance}) \quad (\text{D.3})$$

$$\mathbf{T} = -P\mathbf{I} + \boldsymbol{\tau}^s + \boldsymbol{\tau}^p \quad (\text{Cauchy stress tensor}) \quad (\text{D.4})$$

$$\boldsymbol{\tau}^s = \beta(\nabla \mathbf{v} + \nabla \mathbf{v}^T) \quad (\text{Viscous stress tensor}) \quad (\text{D.5})$$

In these equations, \mathbf{v} is the fluid velocity, ∇ denotes the gradient, P is the pressure, \mathbf{I} is the identity tensor. The elastic stress for the Oldroyd-B fluid can be given by the following constitutive relation:

$$\frac{We}{\Gamma} \left[\frac{\partial \boldsymbol{\tau}^p}{\partial t} + \mathbf{v} \cdot \nabla \boldsymbol{\tau}^p - (\nabla \mathbf{v})^T \cdot \boldsymbol{\tau}^p - \boldsymbol{\tau}^p \cdot \nabla \mathbf{v} \right] + \boldsymbol{\tau}^p = (1 - \beta) \left[\nabla \mathbf{v} + (\nabla \mathbf{v})^T \right] \quad (\text{D.6})$$

The non-dimensional equations governing the deformation of an incompressible neo-Hookean solid satisfying the momentum and mass conservation equations, are given by

$$\frac{Re\rho_s}{\Gamma\rho} \left[\frac{\partial^2 \mathbf{x}}{\partial t^2} \right] = \nabla_{\mathbf{x}} \cdot \mathbf{S} \quad (\text{D.7})$$

$$\det(\mathbf{F}) = 1 \quad (\text{D.8})$$

$$\mathbf{S} = \mathbf{F}^{-1} \cdot \boldsymbol{\sigma} \quad (\text{First Piola-Kirchhoff stress tensor}) \quad (\text{D.9})$$

$$\boldsymbol{\sigma} = -\pi \mathbf{I} + \mathbf{B} \quad (\text{Cauchy stress tensor for a neo-Hookean material}) \quad (\text{D.10})$$

In these equations, ρ_s is the density of the solid, π is a pressure-like scalar function and \mathbf{B} is the left Cauchy-Green tensor, expressed as $\mathbf{B} = \mathbf{F} \cdot \mathbf{F}^T$. The deformation gradient tensor \mathbf{F} relates the undeformed state [$\mathbf{X} = (X, Y, Z)$] to the deformed state [$\mathbf{x} = (x, y, z)$] and is expressed as:

$$\mathbf{F} = \frac{\partial \mathbf{x}}{\partial \mathbf{X}} \quad (\text{D.11})$$

We prescribe the following boundary conditions:

1. The tangential and normal stress and the velocity continuity condition are prescribed at the interface between the liquid and solid domain.

$$\mathbf{n} \cdot \boldsymbol{\sigma} \cdot \mathbf{n} - \mathbf{n} \cdot \mathbf{T} \cdot \mathbf{n} = \gamma \nabla \cdot \mathbf{n} \quad (\text{D.12})$$

$$\mathbf{n} \cdot \boldsymbol{\sigma} \cdot \mathbf{t} = \mathbf{n} \cdot \mathbf{T} \cdot \mathbf{t} \quad (\text{D.13})$$

$$v_x = \frac{\partial w_x}{\partial t} \quad (\text{D.14})$$

where \mathbf{n} and \mathbf{t} are respectively the normal and tangential unit vectors at the liquid-solid interface and $\gamma = \gamma_i/GW$ is the dimensionless surface tension, with γ_i being the dimensional liquid-solid interface tension. Here v_x is the velocity of the fluid in the x direction and w_x is the deformation of the solid in the x direction.

2. At the fixed surfaces ($z = (2 + H)$ and $z = -H$) zero displacement conditions are specified.

$$\mathbf{x} = \mathbf{X} \quad (\text{D.15})$$

D.2 Base state

In the laminar base state of the present problem, it is assumed that the fluid-solid interface remains flat and the pressure gradient acting on the channel creates an unidirectional flow of fluid in the x direction. Fluid forces acting on the fluid-solid interface produces a nonzero displacement of the solid layer only in the x direction. The base state solution for the dimensionless velocity, viscous and elastic stresses in the fluid layer are given as:

$$\bar{v}_x = 2\Gamma \left(z - \frac{z^2}{2} \right) \quad (\text{D.16})$$

$$\bar{v}_z = 0 \quad (\text{D.17})$$

$$\bar{\tau}_{zz}^s = 0 \quad (\text{D.18})$$

$$\bar{\tau}_{xz}^s = \bar{\tau}_{zx}^s = \beta \frac{\partial \bar{v}_x}{\partial z} \quad (\text{D.19})$$

$$\bar{\tau}_{xx}^s = 0 \quad (\text{D.20})$$

$$\bar{\tau}_{zz}^p = 0 \quad (\text{D.21})$$

$$\bar{\tau}_{xz}^p = \bar{\tau}_{zx}^p = (1 - \beta) \frac{\partial \bar{v}_x}{\partial z} \quad (\text{D.22})$$

$$\bar{\tau}_{xx}^p = \frac{2We(1 - \beta)}{\Gamma} \left(\frac{\partial \bar{v}_x}{\partial z} \right)^2 \quad (\text{D.23})$$

Here the maximum dimensionless velocity has been calculated from the dimensional pressure gradient $\partial p^*/\partial x^*$ acting in the channel. It can be shown that $\Gamma = (W/2G)|\partial p^*/\partial x^*|$ [Gaurav and Shankar, 2010]. The base state solution for the displacement (\mathbf{w}) and pressure field for neo-Hookean solid are given by:

$$\bar{w}_x = X + \Gamma (H^2 - Z^2) + 2\Gamma (H + Z) \quad (\text{D.24})$$

$$\bar{w}_z = Z \quad (\text{D.25})$$

$$\bar{p}_s = \bar{p}(x) + 1 + 4\Gamma^2 \left(\frac{Z^2}{2} - Z \right) \quad (\text{D.26})$$

Here overbar on different quantities indicate its base state value.

D.3 Linear stability analysis

In order to examine the stability behaviour of the present problem, we have performed a temporal linear stability analysis. In this method, a small perturbation is introduced

about the base state to all the dynamical quantities and are substituted in the governing equations and boundary conditions. The resulting equations are then linearized. The perturbations are expressed in the following Fourier form:

$$f' = \tilde{f}(z) \exp[ik(x - ct)] \quad (\text{D.27})$$

where, f' is the perturbation to any variable, $\tilde{f}(z)$ is the complex amplitude function of the disturbance, k is the wavenumber of perturbations and $c (=c_r + ic_i)$ is the complex wavespeed with c_r and c_i being the real and imaginary parts, respectively. The value of c_i governs the stability since even a small initial positive value of c_i will grow with time and make the flow unstable. However, a negative value of c_i always has a stabilizing effect. For the solid equation the perturbation can be expressed as $f' = \tilde{f}(Z) \exp[ik(X - ct)]$. Upon substitution of the perturbation, the linearized governing equations, including the constitutive Eqs. (D.6), for the fluid layer are,

$$\frac{\partial \tilde{v}_z}{\partial z} + ik\tilde{v}_x = 0 \quad (\text{D.28})$$

$$\begin{aligned} \frac{Re}{\Gamma} [ik(\bar{v}_x - c)\tilde{v}_x + (d_z\bar{v}_x)\tilde{v}_z] &= -ik\tilde{p} + \beta \left[\frac{\partial^2 \tilde{v}_x}{\partial z^2} - k^2\tilde{v}_x \right] \\ &+ ik\tilde{\tau}_{xx}^p + \frac{\partial \tilde{\tau}_{xz}^p}{\partial z} \end{aligned} \quad (\text{D.29})$$

$$\begin{aligned} \frac{Re}{\Gamma} [ik(\bar{v}_x - c)\tilde{v}_z] &= -\frac{\partial \tilde{p}}{\partial z} + \beta \left[\frac{\partial^2 \tilde{v}_z}{\partial z^2} - k^2\tilde{v}_z \right] \\ &+ ik\tilde{\tau}_{xz}^p + \frac{\partial \tilde{\tau}_{zz}^p}{\partial z} \end{aligned} \quad (\text{D.30})$$

$$\left[1 + ik(\bar{v}_x - c)\frac{We}{\Gamma} \right] \tilde{\tau}_{zz}^p = 2 \left[ik\frac{We}{\Gamma} \tilde{\tau}_{xz}^p \tilde{v}_z + (1 - \beta) \frac{\partial \tilde{v}_z}{\partial z} \right] \quad (\text{D.31})$$

$$\begin{aligned} \left[1 + ik(\bar{v}_x - c)\frac{We}{\Gamma} \right] \tilde{\tau}_{xz}^p &= \frac{We}{\Gamma} \frac{\partial \bar{v}_x}{\partial z} \tilde{\tau}_{zz}^p - \left[\frac{We}{\Gamma} \frac{\partial \tilde{\tau}_{xz}^p}{\partial z} - ik(1 - \beta + \frac{We}{\Gamma} \tilde{\tau}_{xx}^p) \right] \tilde{v}_z \\ &+ (1 - \beta) \frac{\partial \tilde{v}_x}{\partial z} \end{aligned} \quad (\text{D.32})$$

$$\begin{aligned} \left[1 + ik(\bar{v}_x - c)\frac{We}{\Gamma} \right] \tilde{\tau}_{xx}^p &= -\frac{We}{\Gamma} \frac{\partial \tilde{\tau}_{xx}^p}{\partial z} \tilde{v}_z + 2\frac{We}{\Gamma} \frac{\partial \bar{v}_x}{\partial z} \tilde{\tau}_{xz}^p + \left[2ik(1 - \beta + \frac{We}{\Gamma} \tilde{\tau}_{xx}^p) \right] \tilde{v}_x \\ &+ 2\frac{We}{\Gamma} \tilde{\tau}_{xz}^p \frac{\partial \tilde{v}_x}{\partial z} \end{aligned} \quad (\text{D.33})$$

Eqs. (D.28)- (D.30) can be merged to form a single fourth-order Orr-Sommerfeld-like

equation for \tilde{v}_z .

$$ik \frac{Re}{\Gamma} [(\bar{v}_x - c)(d_z^2 - k^2) - d_z^2 \bar{v}_x] \tilde{v}_z = \beta(d_z^2 - k^2)^2 \tilde{v}_z + k^2 d_z (\tilde{\tau}_{xx}^p - \tilde{\tau}_{zz}^p) - ik(d_z^2 + k^2) \tilde{\tau}_{xz}^p \quad (D.34)$$

Upon substitution of the perturbation, the linearized governing equations for the neo-Hookean solid model are as follows:

$$\frac{\partial \tilde{w}_Z}{\partial Z} + ik \tilde{w}_X + 2ik\Gamma(Z-1) \tilde{w}_Z = 0 \quad (D.35)$$

$$-ik\tilde{p}_s + 4ik\Gamma^2(Z-1) \tilde{w}_Z + 2\Gamma \frac{\partial \tilde{w}_Z}{\partial Z} = k^2 \tilde{w}_X - \frac{\partial^2 \tilde{w}_X}{\partial Z^2} - k^2 c^2 \frac{Re\rho_s}{\Gamma\rho} \tilde{w}_X \quad (D.36)$$

$$\begin{aligned} 2ik\Gamma(1-Z)\tilde{p}_s - \frac{\partial \tilde{p}_s}{\partial Z} - 2\Gamma \frac{\partial \tilde{w}_X}{\partial Z} - 4ik\Gamma^2(Z-1) \tilde{w}_X \\ = k^2 \tilde{w}_Z - \frac{\partial^2 \tilde{w}_Z}{\partial Z^2} - k^2 c^2 \frac{Re\rho_s}{\Gamma\rho} \tilde{w}_Z \end{aligned} \quad (D.37)$$

These equations can be condensed to a single fourth-order, Orr-Sommerfeld-like equation for \tilde{w}_Z :

$$\begin{aligned} d_Z^4 \tilde{w}_Z + 4ik\Gamma(Z-1) d_Z^3 \tilde{w}_Z + \left[6ik\Gamma - k^2 \left(2 + 4\Gamma^2(Z-1)^2 - \frac{Re\rho_s}{\Gamma\rho} c^2 \right) \right] d_Z^2 \tilde{w}_Z \\ - 4k^2\Gamma(Z-1) \left[ik + 2\Gamma - ikc^2 \frac{Re\rho_s}{\Gamma\rho} \right] d_Z \tilde{w}_Z - \left[2ik^3\Gamma \left(1 - \frac{Re\rho_s}{\Gamma\rho} c^2 \right) \right. \\ \left. - k^4 \left(1 + 4\Gamma^2(Z-1)^2 - \frac{Re\rho_s}{\Gamma\rho} (4\Gamma^2 c^2 (Z-1)^2 + c^2) \right) \right] \tilde{w}_Z = 0 \end{aligned} \quad (D.38)$$

The interfacial conditions at the liquid–solid interfaces are linearized by Taylor-expanding the conditions about their respective mean interface positions. The linearized boundary conditions at the liquid–solid interface ($z = 0$) are:

$$\tilde{v}_z = -ikc \tilde{w}_Z \quad (D.39)$$

$$\tilde{v}_x + \tilde{w}_Z (d_z \bar{v}_x)_{z=0} = -ikc \tilde{w}_X \quad (D.40)$$

$$\begin{aligned} \left[8ikWe\Gamma(1-\beta) - 4ik\Gamma^2 + ik + 2\Gamma \right] \tilde{w}_Z + 2\Gamma \frac{\partial \tilde{w}_Z}{\partial Z} + \frac{\partial \tilde{w}_X}{\partial Z} \\ = \beta \frac{\partial \tilde{v}_x}{\partial Z} + \beta ik \tilde{v}_z + \tilde{\tau}_{xz}^p \end{aligned} \quad (D.41)$$

$$-\tilde{p} + 2\beta \frac{\partial \tilde{v}_z}{\partial Z} + \tilde{\tau}_{zz}^p - k^2 \gamma \tilde{w}_Z = -\tilde{p}_s + 2 \frac{\partial \tilde{w}_Z}{\partial Z} \quad (D.42)$$

The boundary condition at the channel centre-line are,

$$\tilde{v}_z = 0, d_z \tilde{v}_x = 0 \quad \text{Varicose modes} \quad (\text{D.43})$$

$$\tilde{v}_x = 0, d_z^2 \tilde{v}_x = 0 \quad \text{Sinuous modes} \quad (\text{D.44})$$

Hence, the linearized boundary conditions at the fixed surface $z = -H$ are:

$$\tilde{w}_z = 0 \quad (\text{D.45})$$

$$\tilde{w}_x = 0 \quad (\text{D.46})$$

The complete set of equations (Eqs. (D.28)- (D.46)) which governs the stability of the present problem are solved for the complex wavespeed c as a function of the parameters $Re, We, \beta, k, \Gamma, H$ and γ .

D.4 Results and Discussions

D.4.1 Code validation

Often a spectral method is employed to solve the eigenvalue problems that arise in hydrodynamic stability. We have used a Chebyshev-tau spectral method for solving the Orr-Sommerfeld equation using expansions in Chebyshev polynomials [Boyd, 2001; Gardner et al., 1989; Orszag, 1971; Weideman and Reddy, 2000]. In the Chebyshev-tau spectral method the fluid velocity field and solid displacement field are expressed in a truncated series of N Chebyshev polynomials. Upon substituting these expressions in to the linearized governing equations and boundary conditions, N equations for the unknown coefficients are obtained. This $N \times N$ matrix is then solved using the *polyeig* eigenvalue solver in MATLAB to get the complete spectrum of eigenvalues c for specified values of other parameters. In order to remove the spurious eigenmodes that may arise, the truncation level N is increased until the genuine modes are accurately identified. We have validated our spectral code with the reported results of Gaurav and Shankar [2010] by considering $\beta = 1.0$ and $Wi = 0$. Fig. D.2 displays the eigenspectrum for $H = 5, k = 0.8$ and $Re = 100$ for different values of Γ . It is clear that unstable modes appear at higher values of Γ and that the number of unstable modes increases with an increase in Γ . In all these cases, we have found good agreement between our results and the reported results of Gaurav and Shankar [2010].

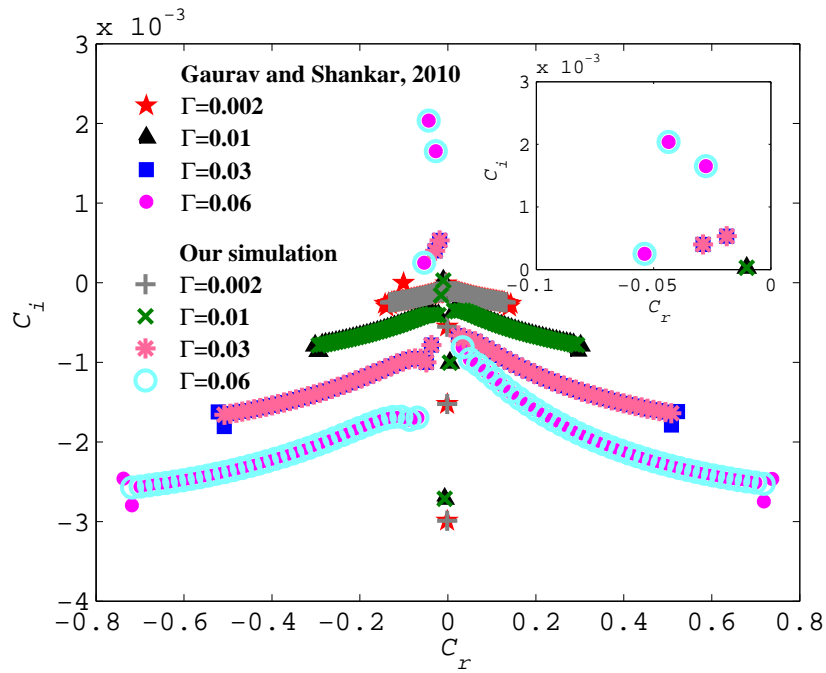


Figure D.2: Eigenspectrum for varicose mode with $H = 5$, $k = 0.8$ and $Re = 100$ for different values of Γ . Inset compares the positive C_i values of our simulation with the reported C_i values by Gaurav and Shankar [2010].

D.5 Conclusions

In this study, we have considered the pressure driven flow of an Oldroyd-B fluid flowing through an channel lined with a layer of an incompressible neo-Hookean solid. A temporal linear stability analysis has been carried out to examine the stability behaviour of the present problem. To check the accuracy of our derivation we have compared our predictions for a Newtonian fluid with the reported results of Gaurav and Shankar [2010]. Preliminary results are promising for future advancement of this study.

Bibliography

- Afonso, A., Oliveira, P., Pinho, F., and Alves, M. (2009). The log-conformation tensor approach in the finite-volume method framework. *J. Non-Newton. Fluid Mech.*, 157(1-2):55–65.
- Anand, M., Rajagopal, K., and Rajagopal, K. R. (2003). A model incorporating some of the mechanical and biochemical factors underlying clot formation and dissolution in flowing blood. *Comp. Math. Meth. Med.*, 5:183–218.
- Arthurs, K. M., Moore, L. C., Peskin, C. S., Pitman, E. B., and Layton, H. E. (1998). Modeling arteriolar flow and mass transport using the immersed boundary method. *J. Comput. Phys.*, No. 2, 147:402–440.
- Baaijens, F. P. T. (1998). Mixed finite element methods for viscoelastic flow analysis: a review. *J. Non-Newton. Fluid Mech.*, 79:361–385.
- Bajaj, M., Prakash, J. R., and Pasquali, M. (2008). A computational study of the effect of viscoelasticity on slot coating flow of dilute polymer solutions. *J. Non-Newton. Fluid Mech.*, 149:104–123.
- Balci, N., Thomases, B., Renardy, M., and Doering, C. R. (2011). Symmetric factorization of the conformation tensor in viscoelastic fluid models. *J. Non-Newton. Fluid Mech.*, 166:546–553.
- Baskurt, O. K. and Meiselman, H. J. (2003). Blood rheology and hemodynamics. *Semin. Thromb. Hemost.*, 29:435–450.
- Bathe, K., Zhang, H., and Wang, M. (1995). Finite element analysis of incompressible and compressible fluid flows with free surfaces and structural interactions. *Comput. Struct.*, 56(2-3):193–213.
- Bathe, K.-J. and Zhang, H. (2004). Finite element developments for general fluid flows with structural interactions. *Int. J. Numer. Methods Eng.*, 60(1):213–232.
- Bathe, K.-J., Zhang, H., and Ji, S. (1999). Finite element analysis of fluid flows fully coupled with structural interactions. *Comput. Struct.*, 72(1):1–16.
- Benjamin, D. F. (1994). *Roll Coating Flows and Multiple Roll Systems*. PhD thesis, University of Minnesota, Minneapolis, MN. (Available from UMI, Ann Arbor, MI, order number 9512679).

- Bertram, C. D. (1982). Two modes of instability in a thick-walled collapsible tube conveying a flow. *J. Biomech.*, 15:223–224.
- Bertram, C. D. (1986). Unstable equilibrium behaviour in collapsible tubes. *J. Biomech.*, 19:61–69.
- Bertram, C. D. (1987). The effects of wall thickness, axial strain and end proximity on the pressure-area relation of collapsible tubes. *J. Biomech.*, 20:863–876.
- Bertram, C. D. and Castles, R. (1999). Flow limitation in uniform thick-walled collapsible tubes. *J. Fluids. Struct.*, 13:399–418.
- Bertram, C. D. and Elliott, N. S. J. (2003). Flow-rate limitation in a uniform thin-walled collapsible tube, with comparison to a uniform thick-walled tube and a tube of tapering thickness. *J. Fluids. Struct.*, 17 (4):541–559.
- Bertram, C. D. and Godbole, S. A. (1997). LDA measurements of velocities in a simulated collapsed tube. *J. Biomech. Eng.-Trans. ASME*, 119:357–363.
- Bertram, C. D., Raymond, C. J., and Pedley, T. J. (1990). Mapping of instabilities during flow through collapsed tubes of differing length. *J. Fluids. Struct.*, 4:125–153.
- Bertram, C. D., Raymond, C. J., and Pedley, T. J. (1991). Application of non-linear dynamics concepts to the analysis of self-excited oscillations of a collapsible tube conveying a flow. *J. Fluids. Struct.*, 5:391–426.
- Beyer, R. (1992). A computational model of the cochlea using the immersed boundary method. *J. Comput. Phys.*, 98(1):145–162.
- Bird, R. B., Armstrong, R. C., and Hassager, O. (1987a). *Dynamics of Polymeric Liquids - Volume 1: Fluid Mechanics*. John Wiley, New York, 2nd edition.
- Bird, R. B., Curtiss, C. F., Armstrong, R. C., and Hassager, O. (1987b). *Dynamics of Polymeric Liquids - Volume 2: Kinetic Theory*. John Wiley, New York, 2nd edition.
- Boyd, J. (2001). *Chebyshev and Fourier Spectral Methods*. Dover, New York, second edition.
- Brower, R. W. and Scholten, C. (1975). Experimental evidence on the mechanism for the instability of flow in collapsible vessels. *Med. Biol. Engrg.*, 13:839–844.
- Bruus, H. (2008). *Theoretical Microfluidics*. Oxford Univ Press, Oxford, 2nd edition.

- Bureau, M., Healy, J., Bourgoïn, D., and Joly, M. (1980). Rheological hysteresis of blood at low shear rate. *Biorheology*, 17:191–203.
- Cai, Z. X. and Luo, X. Y. (2003). A fluid-beam model for flow in a collapsible channel. *J. Fluids. Struct.*, 17:125–146.
- Canic, S. and Mikelic, A. (2003). Effective equations modeling the flow of a viscous incompressible fluid through a long elastic tube arising in the study of blood flow through small arteries. *SIAM J. Applied Dynamical Systems*, 2(3):431–463.
- Canic, S., Tambaca, J., Guidoboni, G., Mikelic, A., Hartley, C. J., and Rosenstrauch, D. (2006). Modeling viscoelastic behavior of arterial walls and their interaction with pulsatile blood flow. *SIAM J. Appl. Math.*, 67(1):164–193.
- Carrillo, F., Gupta, S., Balooch, M., Marshall, S.J., M., G.W., Pruitt, L., and Puttlitz, C. (2005). Nanoindentation of polydimethylsiloxane elastomers: Effect of crosslinking, work of adhesion, and fluid environment on elastic modulus. *J. Mater. Res.*, 20(10):2820–2830.
- Carvalho, M. (2003). Effect of thickness and viscoelastic properties of roll cover on deformable roll coating flows. *Chem. Eng. Sci.*, 58(19):4323–4333.
- Carvalho, M. S. (1996). *Roll coating flows in rigid and deformable gaps*. PhD thesis, University of Minnesota, Minneapolis, MN, USA.
- Carvalho, M. S. and Scriven, L. E. (1997). Flows in forward deformable roll coating gaps: Comparison between spring and plane strain models of roll cover. *J. Comput. Phys.*, 138:449–479.
- Celata, G., Lorenzini, M., Morini, G., and Zummo, G. (2009). Friction factor in micropipe gas flow under laminar, transition and turbulent flow regime. *Int. J. Heat Fluid Flow*, 30(5):814–822.
- Chakraborty, D., Bajaj, M., Yeo, L., Friend, J., Pasquali, M., and Prakash, J. R. (2010). Viscoelastic flow in a two-dimensional collapsible channel. *J. Non-Newton. Fluid Mech.*, 165:1204–1218.
- Chien, S. (1970). Shear dependence of effective cell volume as a determinant of blood viscosity. *Science*, 168:977–979.

- Chien, S. (1975). *Biophysical behavior of red cells in suspension*. In: Surgenor DM, ed. *Red Blood Cell, Vol. 3.* ; 1975:1031-1133. New York, Academic Press.
- Christodoulou, K. N. and Scriven, L. E. (1992). Discretization of free surface flows and other moving boundary problems. *J. Comput. Phys.*, 99:39–55.
- Conrad, W. A. (1969). Pressure-flow relationships in collapsible tubes. *IEEE Trans. Bio-Med. Engrg. BME*, 16:284–295.
- Coronado, O., Arora, D., Behr, M., and Pasquali, M. (2007). A simple method for simulating general viscoelastic fluid flows with an alternate log-conformation formulation. *J. Non-Newton. Fluid Mech.*, 147(3):189–199.
- Cristini, V. and Kassab, G. S. (2005). Computer modeling of red blood cell rheology in the microcirculation: A brief overview. *Ann. Biomed. Eng.*, 33:1724–1727.
- Damanik, H., Hron, J., Ouazzi, A., and Turek, S. (2010). A monolithic FEM approach for the log-conformation reformulation (LCR) of viscoelastic flow problems. *J. Non-Newton. Fluid Mech.*, 165(19-20):1105–1113.
- DE Almeida, V. F. (1995). *Gas-Liquid Counterflow Through Constricted Passages*. PhD thesis, University of Minnesota, Minneapolis, MN. (Available from UMI, Ann Arbor, MI, order number 9615160).
- DE Almeida, V. F. (1999). Domain deformation mapping: Application to variational mesh generation. *SIAM J. Sci. Comput.*, 20:1252–1275.
- Deng, X. and Guidoin, R. (1998). Arteries, veins and lymphatic vessels. In Black, J. and Hastings, G., editors, *Handbook of Biomaterial Properties*, pages 81–105. Chapman & Hall, London.
- deSantos, J. M. (1991). *Two-phase Cocurrent Downflow through Constricted Passages*. PhD thesis, University of Minnesota, Minneapolis, MN. (Available from UMI, Ann Arbor, MI, order number 9119386).
- Dillon, R., Fauci, L., Fogelson, A., and Gaver III, D. (1996). Modeling biofilm processes using the immersed boundary method. *J. Comput. Phys.*, 129(1):57–73.
- Dillon, R., Fauci, L., and Gaver III, D. (1995). A microscale model of bacterial swimming, chemotaxia and substrate transport. *J. Theor. Biol.*, 177(4):325–340.

- Duddu, R., Bordas, S., Chopp, D., and Moran, B. (2008). A combined extended finite element and level set method for biofilm growth. *Int. J. Numer. Methods Eng.*, 74(5):848–870.
- Duff, I. S., Erisman, A. M., and Reid, J. K. (1989). *Direct Methods for Sparse Matrices*. Oxford University Press, Oxford, 1st edition.
- Duffy, D. C., McDonald, J. C., Schueller, O. J. A., and Whitesides, G. M. (1998). Rapid prototyping of microfluidic systems in poly (dimethylsiloxane). *Anal. Chem*, 70(23):4974–4984.
- Fåhræus, R. (1929). The suspension stability of blood. *Physiol. Rev.*, 9:241–274.
- Fåhræus, R. and Lindqvist, T. (1931). The viscosity of blood in narrow capillary tubes. *Am. J. Physiol.*, 96:562–568.
- Fang, J. and Owens, R. G. (2006). Numerical simulations of pulsatile blood flow using a new constitutive model. *Biorheology*, 43:637–660.
- Fattal, R. and Kupferman, R. (2004). Constitutive laws for the matrix-logarithm of the conformation tensor. *J. Non-Newton. Fluid Mech.*, 124:281–285.
- Fattal, R. and Kupferman, R. (2005). Time-dependent simulation of viscoelastic flows at high Weissenberg number using the log-conformation representation. *J. Non-Newton. Fluid Mech.*, 124:23–37.
- Fauci, L.J. and Peskin, C. (1988). A computational model of aquatic animal locomotion. *J. Comput. Phys.*, 77(1):85–108.
- Fauci, L. (1992). Peristaltic pumping of solid particles. *Comput. Fluids*, 21(4):583–598.
- Fauci, L. and McDonald, A. (1995). Sperm motility in the presence of boundaries. *Bull. Math. Biol.*, 57(5):679–699.
- Feigl, K., Laso, M., and Öttinger, H. C. (1995). CONNFESSIT approach for solving a two-dimensional viscoelastic fluid problem. *Macromolecules*, 28:3261–3274.
- Fogelson, A. (1984). A mathematical model and numerical method for studying platelet adhesion and aggregation during blood clotting. *J. Comput. Phys.*, 56(1):111–134.

- Fogelson, A. and Peskin, C. (1988). A fast numerical method for solving the three-dimensional Stokes' equations in the presence of suspended particles. *J. Comput. Phys.*, 79(1):50–69.
- Fortin, A., Kane, A., and Guénette, R. (2010). Numerical simulation of the deformation of drops under simple shear flow. *J. Polym. Eng.*, 30(8):495–521.
- Friend, J. and Yeo, L. (2010). Fabrication of microfluidic devices using polydimethylsiloxane. *Biomicrofluidics*, 4(026502).
- Fuard, D., Tzvetkova-Chevolleau, T., S. Decossas, P. T., and Schiavone, P. (2008). Optimization of poly-di-methyl-siloxane (PDMS) substrates for studying cellular adhesion and motility. *Microelectronic Engineering*, 85:1289–1293.
- Gallez, X., Halin, P., Lielens, G., Keunings, R., and Legat, V. (1999). The adaptive Lagrangian particle method for macroscopic and micro-macro computations of time-dependent viscoelastic flows. *Comput. Meth. Appl. Mech. Eng.*, 180:345–364.
- Gardner, D., Trogdon, S., and Douglass, R. (1989). A modified tau spectral method that eliminates spurious eigenvalues. *J. Comput. Phys.*, 80(1):137–167.
- Gaurav and Shankar, V. (2010). Stability of pressure-driven flow in a deformable neo-Hookean channel. *J. Fluid Mech.*, 659:318–350.
- Gervais, T., El-Ali, J., Gunther, A., and Jensen, K. (2006). Flow-induced deformation of shallow microfluidic channels. *Lab Chip*, 6(4):500–507.
- Gkanis, V. and Kumar, S. (2003). Instability of creeping Couette flow past a neo-Hookean solid. *Phys. Fluids*, 15:2864–2871.
- Guenette, R., Abdelmalek, Z., Fortin, A., Carreau, P., and Grmela, M. (1992). Simulation of viscoelastic flows using a conformation tensor model. *J. Non-Newton. Fluid Mech.*, 45:187–208.
- Guénette, R. and Fortin, M. (1995). A new mixed finite element method for computing viscoelastic flows. *J. Non-Newton. Fluid Mech.*, 60:27–52.
- Guénette, R., Fortin, A., Kane, A., and Héту, J.-F. (2008). An adaptive remeshing strategy for viscoelastic fluid flow simulations. *J. Non-Newton. Fluid Mech.*, 153(1):34–45.

- Hardy, B., Uechi, K., Zhen, J., and Pirouz Kavehpour, H. (2009). The deformation of flexible PDMS microchannels under a pressure driven flow. *Lab Chip*, 9(7):935–938.
- Harlow, F. H. and Welch, J. E. (1965). Numerical calculation of time-dependent viscous incompressible flow. *Phys. Fluids*, 8:2182–2189.
- Hayashi, K. (2003). *Mechanical properties of soft tissues and arterial walls*. In: Holzapfel G. A., Ogden R. W. (eds) *Biomechanics of soft tissue in cardiovascular system*. Springer, New York.
- Hazel, A. L. and Heil, M. (2003). Steady finite-Reynolds-number flows in three-dimensional collapsible tubes. *J. Fluid Mech.*, 486:79–103.
- Heil, M. and Jensen, O. E. (2003). Flows in deformable tubes and channels - theoretical models and biological applications. In Carpenter, P. W. and Pedley, T. J., editors, *Flow Past Highly Compliant Boundaries and in Collapsible Tubes*, pages 15–50. Kluwer, Dordrecht.
- Heil, M. and Waters, S. L. (2008). How rapidly oscillating collapsible tubes extract energy from a viscous mean flow. *J. Fluid Mech.*, 601:199–227.
- Hirt, C. W. and Nichols, B. D. (1981). Volume of fluid (VOF) method for the dynamics of free boundaries. *J. Comput. Phys.*, 39:201–225.
- Hohne, D. N., Younger, J. G., and Solomon, M. J. (2009). Flexible microfluidic device for mechanical property characterization of soft viscoelastic solids such as bacterial biofilms. *Langmuir*, 25(13):7743–7751.
- Holden, M., Kumar, S., Beskok, A., and Cremer, P. (2003). Microfluidic diffusion diluter: Bulging of PDMS microchannels under pressure-driven flow. *J. Micromech. Microeng.*, 13(3):412–418.
- Holzapfel, G. A. (2003). Structural and numerical models for the (visco)elastic response of arterial walls with residual stresses. In Holzapfel, G. A. and Ogden, R. W., editors, *Biomechanics of soft tissue in cardiovascular system*, pages 109–184. Springer, New York.
- Hrnjak, P. and Tu, X. (2007). Single phase pressure drop in microchannels. *Int. J. Heat Fluid Flow*, 28(1 SPEC. ISS.):2–14.
- Huang, S.-B., Wu, M.-H., and Lee, G.-B. (2009). A tunable micro filter modulated by pneumatic pressure for cell separation. *Sens. Actuator B-Chem.*, 142(1):389–399.

- Hulsén, M. A., Fattal, R., and Kupferman, R. (2005). Flow of viscoelastic fluids past a cylinder at high Weissenberg number: Stabilized simulations using matrix logarithms. *J. Non-Newton. Fluid Mech.*, 127:27–39.
- Hulsén, M. A., van Heel, A. P. G., and van den Brule, B. H. A. A. (1997). Simulation of viscoelastic flows using Brownian configuration fields. *J. Non-Newton. Fluid Mech.*, 70:79–101.
- Irimia, D., Liu, S.-Y., Tharp, W., Samadani, A., Toner, M., and Poznansky, M. (2006). Microfluidic system for measuring neutrophil migratory responses to fast switches of chemical gradients. *Lab Chip*, 6(2):191–198.
- Irimia, D. and Toner, M. (2006). Cell handling using microstructured membranes. *Lab Chip*, 6(3):345–352.
- Jensen, O. (1990). Instabilities of flow in a collapsed tube. *J. Fluid Mech.*, 220:623–659.
- Jensen, O. E. and Heil, M. (2003). High-frequency self-excited oscillations in a collapsible-channel flow. *J. Fluid Mech.*, 481:235–268.
- Johnson, K. (2003). *Contact mechanics*. Cambridge University Press, Cambridge, U. K.
- Judy, J., Maynes, D., and Webb, B. (2002). Characterization of frictional pressure drop for liquid flows through microchannels. *Int. J. Heat Mass Transf.*, 45(17):3477–3489.
- Kalita, P. and Schaefer, R. (2008). Mechanical models of artery walls. *Arch. Comput. Method Eng.*, 15:1–36.
- Kandlikar, S., Schmitt, D., Carrano, A., and Taylor, J. (2005). Characterization of surface roughness effects on pressure drop in single-phase flow in minichannels. *Phys. Fluids*, 17(10).
- Katz, A. I., Chen, Y., and Moreno, A. (1969). Flow through a collapsible tube. *Biophys. J.*, 9:1261–1279.
- Kaur, S. and Leal, L. (2009). Three-dimensional stability of a thin film between two approaching drops. *Phys. Fluids*, 21(072101).
- Kim, T., Kim, J., and Jeong, O. (2011). Measurement of nonlinear mechanical properties of PDMS elastomer. *Microelectron. Eng., In Press*.

- Kim, Y., Lim, S., Raman, S., Simonetti, O., and Friedman, A. (2009). Blood flow in a compliant vessel by the immersed boundary method. *Ann. Biomed. Eng.*, 37(5):927–942.
- Kohl, M., Abdel-Khalik, S., Jeter, S., and Sadowski, D. (2005). An experimental investigation of microchannel flow with internal pressure measurements. *Int. J. Heat Mass Transf.*, 48(8):1518–1533.
- Kumar, V., Paraschivoiu, M., and Nigam, K. (2011). Single-phase fluid flow and mixing in microchannels. *Chem. Eng. Sci.*, 66(7):1329–1373.
- Leclerc, E., Sakai, Y., and Fujii, T. (2003). Cell Culture in 3-Dimensional Microfluidic Structure of PDMS (polydimethylsiloxane). *Biomed. Microdevices*, 5(2):109–114.
- Lim, S. and Peskin, C. (2004). Simulations of the whirling instability by the immersed boundary method. *SIAM J. Sci. Comput.*, 25(6):2066–2083.
- Liu, H. F., Luo, X. Y., Cai, Z. X., and Pedley, T. J. (2009a). Sensitivity of unsteady collapsible channel flows to modelling assumptions. *Commun. Numer. Meth. Engng*, 25:483–504.
- Liu, M., Sun, J., and Chen, Q. (2009b). Influences of heating temperature on mechanical properties of polydimethylsiloxane. *Sens. Actuator A-Phys.*, 151(1):42–45.
- Liu, M., Sun, J., Sun, Y., Bock, C., and Chen, Q. (2009c). Thickness-dependent mechanical properties of polydimethylsiloxane membranes. *J. Micromech. Microeng.*, 19(3):035028.
- Lowe, T. W. and Pedley, T. J. (1995). Computation of Stokes flow in a channel with a collapsible segment. *J. Fluids. Struct.*, 9:885–905.
- Lozinski, A. and Owens, R. (2003). An energy estimate for the Oldroyd-B model: theory and applications. *J. Non-Newton. Fluid Mech.*, 112:161–176.
- Luo, X. Y., Calderhead, B., Liu, H. F., and Li, W. G. (2007). On the initial configurations of collapsible tube flow. *Comput. Struct.*, 85:977–987.
- Luo, X. Y. and Pedley, T. J. (1995). A numerical simulation of steady flow in a 2-D collapsible channel. *J. Fluids. Struct.*, 9:149–174.

- Luo, X. Y. and Pedley, T. J. (1996). A numerical simulation of unsteady flow in a 2-D collapsible channel. *J. Fluid Mech.*, 314:191–225.
- Lynch, D. R. and O'Neill, K. (1980). Elastic grid deformation for moving boundary problems in two space dimensions. In Wang, S. Y., Brebbia, C. A., Alonso, C. V., Gray, W. G., and Pinder, G. F., editors, *Proceedings of 3rd International Conference on Finite Elements in Water Resources*, pages 7.111–7.120. University of Mississippi.
- Maronnier, V., Picasso, M., and Rappaz, J. (2003). Numerical simulation of three-dimensional free surface flows. *Int. J. Numer. Meth. Fluids*, 42:697–716.
- Marzo, A., Luo, X., and Bertram, C. (2005). Three-dimensional collapse and steady flow in thick-walled flexible tubes. *J. Fluids. Struct.*, 20:817–835.
- Meinhart, C., Wereley, S., and Santiago, J. (1999). PIV measurements of a microchannel flow. *Exp. Fluids*, 27(5):414–419.
- Merrill, E. W. (1969). Rheology of blood. *Physiol Rev.*, 49:863–888.
- Mortensen, N., Okkels, F., and Bruus, H. (2005). Reexamination of Hagen-Poiseuille flow: Shape dependence of the hydraulic resistance in microchannels. *Physical Review E - Statistical, Nonlinear, and Soft Matter Physics*, 71(5):1–4.
- Moyers-Gonzalez, M. A., Owens, R. G., and Fang, J. (2008a). A non-homogeneous constitutive model for human blood. Part 1. Model derivation and steady flow. *J. Fluid Mech.*, 617:327–354.
- Moyers-Gonzalez, M. A., Owens, R. G., and Fang, J. (2008b). A non-homogeneous constitutive model for human blood. Part III. Oscillatory flow. *J. Non-Newton. Fluid Mech.*, 155:161–173.
- Oliver, W. C. and Pharr, G. M. (1992). An improved technique for determining hardness and elastic modulus using load and displacement sensing indentation experiments. *J. Mater. Res.*, 7:1564–1583.
- Orszag, S. (1971). Accurate solution of the Orr-Sommerfeld stability equation. *J. Fluid Mech.*, 50:689–703.
- Owens, R. G. (2006). A new microstructure-based constitutive model for human blood. *J. Non-Newton. Fluid Mech.*, 140:57–70.

- Pasquali, M. (2000). *Polymer molecules in free surface coating flows*. PhD thesis, University of Minnesota.
- Pasquali, M. and Scriven, L. E. (2002). Free surface flows of polymer solutions with models based on the conformation tensor. *J. Non-Newton. Fluid Mech.*, 108:363–409.
- Pasquali, M. and Scriven, L. E. (2004). Theoretical modelling of microstructured liquids: A simple thermodynamic approach. *J. Non-Newton. Fluid Mech.*, 120:101–135.
- Patankar, N. A., Huang, P. Y., Joseph, D. D., and Hu, H. H. (2002). Normal stresses on the surface of a rigid body in an Oldroyd-B fluid. *ASME J. Fluids Eng.*, 124:279–290.
- Peiyi, W. and Little, W. (1983). Measurement of friction factors for the flow of gases in very fine channels used for microminiature Joule-Thomson refrigerators. *Cryogenics*, 23(5):273–277.
- Peng, X., Peterson, G., and Wang, B. (1995). Frictional flow characteristics of water flowing through rectangular microchannels. *J. Exp. Heat Transfer*, 7(4):249–264.
- Peskin, C. (1977). Numerical analysis of blood flow in the heart. *J. Comput. Phys.*, 25:220–252.
- Peskin, C. and McQueen, D. (1989). A three-dimensional computational method for blood flow in the heart I. Immersed elastic fibers in a viscous incompressible fluid. *J. Comput. Phys.*, 81(2):372–405.
- Pfahler, J., Harley, J., Bau, H., and Zemel, J. (1989). Liquid transport in micron and submicron channels. *Sens. Actuator A-Phys.*, 22(1-3):431–434.
- Pfund, D., Rector, D., Shekarriz, A., Popescu, A., and Welty, J. (2000). Pressure drop measurements in a microchannel. *AIChE Journal*, 46(8):1496–1507.
- Popel, A. S. and Johnson, P. C. (2005). Microcirculation and hemorheology. *Ann. Rev. Fluid Mech.*, 37:43–69.
- Quarteroni, A., Tuveri, M., and Veneziani, A. (2000). Computational vascular fluid dynamics: problems, models and methods. *Computing and Visualization in Science*, 2:163–197.
- Quemada, D. (1993). A non-linear Maxwell model of biofluids: application to normal human blood. *Biorheology*, 30:253–265.

- Quemada, D. (1999). Rheological modelling of complex fluids. IV. Thixotropic and thixoelectric behaviour. Start-up and stress relaxation, creep tests and hysteresis cycles. *Eur. Phys. J. Appl. Phys.*, 5:191–207.
- Rajagopalan, D., Armstrong, R. C., and Brown, R. A. (1990). Finite element methods for calculation of steady viscoelastic flows using constitutive equations with a Newtonian viscosity. *J. Non-Newton. Fluid Mech.*, 36:169–192.
- Rallison, J. and Acrivos, A. (1978). A numerical study of the deformation and burst of a viscous drop in an extensional flow. *J. Fluid Mech.*, 89(1):191–200.
- Rand, P. W., Lacombe, E., Hunt, H. E., and Austin, W. H. (1964). Viscosity of normal human blood under normothermic and hypothermic conditions. *J. Appl. Physiol*, 19:117–122.
- Rast, M. P. (1994). Simultaneous solution of the Navier-Stokes and elastic membrane equations by a finite-element method. *Int. J. Num. Meth. Fluids*, 19:1115–1135.
- Robertson, A. M., Sequeira, A., and Kameneva, M. V. (2008). Hemorheology. In Galdi, G. P., Rannacher, R., Robertson, A. M., and Turek, S., editors, *Hemodynamical Flows: Modeling, Analysis and Simulation (Oberwolfach Seminars)*, pages 63–120. Birkhauser.
- Sackinger, P. A., Schunk, P. R., and Rao, R. R. (1996a). A Newton-Raphson pseudo-solid domain mapping technique for free and moving boundary problems: A finite element implementation. *J. Comput. Phys.*, 125:83–103.
- Sackinger, P. A., Schunk, P. R., and Rao, R. R. (1996b). A Newton-Raphson pseudo-solid domain mapping technique for free and moving boundary problems: a finite element implementation. *J. Comp. Phys.*, 125:83–103.
- Sequeira, A. and Janela, J. (65-87,2007). *An Overview of Some Mathematical Models of Blood Rheology in A Portrait of State-of-the-Art Research at the Technical University of Lisbon*. Springer Netherlands.
- Shapiro, A. H. (1977). Steady flow in collapsible tubes. *J. Biomech. Eng.-Trans. ASME*, 99:126–147.
- Singh, P. and Leal, L. (1993). Finite-element simulation of the start-up problem for a viscoelastic fluid in an eccentric rotating cylinder geometry using a third-order upwind scheme. *Theor. Comput. Fluid Dyn.*, 5:107–137.

- Squires, T. and Quake, S. (2005). Microfluidics: Fluid physics at the nanoliter scale. *Rev. Mod. Phys.*, 77(3):977–1026.
- Steinke, M. and Kandlikar, S. (2006). Single-phase liquid friction factors in microchannels. *Int. J. Therm. Sci.*, 45(11):1073–1083.
- Stergiopoulos, N., Westerhof, B. E., and Westerhof, N. (1999). Total arterial inertance as the fourth element of the windkessel model. *Am. J. Physiol. Heart Circ. Physiol.*, 276(1):H81–H88.
- Stone, H. and Leal, L. (1990). Effects of surfactants on drop deformation and breakup. *J. Fluid Mech.*, 220:161–186.
- Studer, V., Hang, G., Pandolfi, A. and Ortiz, M., Anderson, W., and Quake, S. (2004). Scaling properties of a low-actuation pressure microfluidic valve. *J. Appl. Phys.*, 95(1):393–398.
- Sun, J., Smith, M. D., Armstrong, R. C., and Brown, R. A. (1999). Finite element method for viscoelastic flows based on the discrete adaptive viscoelastic stress splitting and the discontinuous galerkin method: DAVSS-G/DG. *J. Non-Newton. Fluid Mech.*, 86:281–307.
- Sun, N. and Kee, D. D. (2001). Simple shear, hysteresis and yield stress in biofluids. *Can. J. Chem. Eng.*, 79:36–41.
- Thangawng, A. L., Ruoff, R. S., Swartz, M. A., and Glucksberg, M. R. (2007). An ultra-thin PDMS membrane as a bio/micronano interface: fabrication and characterization. *Biomed. Microdevices*, 9(2):587–595.
- Thurston, G. B. (1972). The viscoelasticity of human blood. *Biophysical Journal*, 12:1205–1217.
- Tomé, M. F., Castelo, A., Afonso, A. M., Pinho, F. T., and Alves, M. A. (2009). Application of the log-conformation technique to 3D free surface flows. *Congreso de Métodos Numéricos en Ingeniería, Barcelona*.
- Unger, M. A., Chou, H. P., Thorsen, T., Scherer, A., and Quake, S. R. (2000). Monolithic microfabricated valves and pumps by multilayer soft lithography. *Science*, 288:113–116.

- Vestad, T., Marr, D. W. M., and Oakey, J. (2004). Flow control for capillary-pumped microfluidic systems. *J. Micromech. Microeng.*, 14(11):1503–1506.
- Vijayalakshmi, K., Anoop, K., Patel, H., Harikrishna, P., Sundararajan, T., and Das, S. (2009). Effects of compressibility and transition to turbulence on flow through microchannels. *Int. J. Heat Mass Transf.*, 52(9-10):2196–2204.
- Wang, C. and Lee, G. (2006). Pneumatically driven peristaltic micropumps utilizing serpentine-shape channels*. *J. Micromech. Microeng.*, 16(2):341–348.
- Weideman, J. and Reddy, S. (2000). A MATLAB differentiation matrix suite. *ACM Transactions on Mathematical Software*, 26(4):465–519.
- Weng, C.-H., Lien, K.-Y., Yang, S.-Y., and Lee, G.-B. (2011). A suction-type, pneumatic microfluidic device for liquid transport and mixing. *Microfluidics and Nanofluidics*, 10(2):301–310.
- White, F. (1991). *Viscous fluid flow*. McGraw-Hill, New York, 2nd edition.
- Whitesides, G. M. (2006). The origins and the future of microfluidics. *Nature*, 442:368372.
- Williams, M. C., Rosenblatt, J. S., and Soane, D. S. (1993). Theory of blood rheology based on a statistical mechanics treatment of rouleaux, and comparisons with data. *Int. J. Polym. Mater.*, 21:57–63.
- Xie, X. (2006). *Modeling Viscoelastic Free Surface and Interfacial Flows, with Applications to the Deformation of Droplets and Blood Cells*. PhD thesis, Rice University, Houston, TX.
- Xie, X. and Pasquali, M. (2003). Computing 3D free surface viscoelastic flows. In Mammoli, A. and Brebbia, C. A., editors, *Moving Boundaries VII: Computational Modelling of Free and Moving Boundary Problems*, pages 225–234. WIT press, Southampton, UK.
- Xie, X. and Pasquali, M. (2004). A new, convenient way of imposing open-flow boundary conditions in two- and three-dimensional viscoelastic flows. *J. Non-Newton. Fluid Mech.*, 122:159–176.
- Yeleswarapu, K. K., Kameneva, M. V., Rajagopal, K. R., and Antaki, J. F. (1998). The flow of blood in tubes: theory and experiment. *Mech. Res. Commun.*, 25(3):257–262.
- Zanden, J. and Hulsen, M. (1988). Mathematical and physical requirements for successful computations with viscoelastic fluid models. *J. Non-Newton. Fluid Mech.*, 29:93–117.

- Zhang, X., Fatemi, M., and Greenleaf, J. F. (2004). Inverse method for estimating elastic modulus of arterial walls. *2004 SPIE International Symposium Medical Imaging*, 5368:226–235.
- Zhang, X. and Greenleaf, J. F. (2005). Generation of ring resonant mode for measuring artery elastic modulus. *Medical Imaging 2005, Proceedings of SPIE*, 5750:236–243.
- Zhang, X. and Greenleaf, J. F. (2006a). Estimation of complex arterial elastic modulus from ring resonance excited by ultrasound radiation force. *Ultrasonics*, 44(Suppl 1):e169–e172.
- Zhang, X. and Greenleaf, J. F. (2006b). Noninvasive estimation of local elastic modulus of arteries with the ring resonance measurement. *IEEE International Ultrasonics Symposium, October 3-6, Vancouver, Canada*, pages 1161–1164.

List of publications forming part of, and arising from the thesis**Refereed Journal Papers (International)**

1. Debadī Chakraborty, Mohit Bajaj, Leslie Yeo, James Friend, Matteo Pasquali and J. Ravi Prakash, Viscoelastic flow in a two-dimensional collapsible channel, *Journal of Non-Newtonian Fluid Mechanics*, Volume 165, Issues 19-20, pp. 1204-1218, October 2010.
2. Debadī Chakraborty and J. Ravi Prakash, The influence of shear thinning on viscoelastic fluid-structure interaction in a two-dimensional collapsible channel, *Industrial and Engineering Chemistry Research*, published online, DOI:10.1021/ie200173b, 2011.

Conference Proceedings

1. Debadī Chakraborty and J. Ravi Prakash, Flow of a viscoelastic FENE-P model fluid in a two-dimensional collapsible channel, *CHEMECA 2010*, Adelaide, Australia, 26-29 September, 2010.

Conference Presentation

1. Debadī Chakraborty and J. Ravi Prakash, Influence of Viscoelasticity on Flow in a Two-dimensional Collapsible Channel, 5th Australian-Korean Rheology Conference, 1-4 November 2009, Sydney, Australia.

Conference Posters

1. Debadī Chakraborty, M. Pasquali and J. Ravi Prakash, Viscoelastic flow in a two-dimensional collapsible channel, IMA workshop on Flowing Complex Fluids: Rheological Measurements and Constitutive Modeling, Institute of Mathematics and its Applications at the University of Minnesota, September 14-18, 2009.